



The University of
Nottingham

**Continuous-Flow Hydrothermal and Solvothermal
Synthesis of Inorganic Nanomaterials**

Chris Starkey

**Thesis submitted to the University of Nottingham
for the degree of Doctor of Philosophy**

May 2016

Abstract

Nanomaterials and nanotechnology are presently receiving high levels of interest which is aiding significant advancements to industrial and technological applications. New strategies towards nanoparticle synthesis are needed to produce high quality nanomaterials at industrially viable levels. This thesis presents the continuous flow hydrothermal and solvothermal synthesis (CFHSS) of a range of inorganic nanomaterials produced using a continuous-flow reactor designed at the University of Nottingham. The materials presented herein are currently industrially applicable or projected future trend materials. The aim is to widen the library of materials accessible via this relatively new synthetic strategy. It is mostly concerned with the development of the synthetic protocol towards specific materials and classes of materials, via both chemical and reactor configuration innovations, but additionally yields information about the chemical processes occurring within the reactor and how these can be controlled and exploited. This provides insight into not only the reactor but the field of CFHSS as a whole. Selected materials are subject to application based testing. With a fully industrial scale facility under construction, promising materials are trialled at pilot scale to assess the viability of the transfer of chemistry from laboratory to pilot scale with industrial scale production in mind.

Chapter 1 provides an introduction to nanotechnology and nanomaterials in general, giving background to their unique properties and application. Traditional routes of synthesis are discussed, with particular focus then given to hydrothermal methods and continuous flow reactor design and nanoparticle production.

Chapter 2 presents the characterisation techniques used in this thesis in terms of their theory and application. Application specific testing of the materials is explained in the relevant chapters.

Chapter 3 reports the production of two different metal oxide materials, namely titania and doped titania photocatalysts, and barium strontium titanate nanopowders. Photocatalysis results are reported for the titania nanocrystals, and the barium strontium titanate nanopowders are produced in the first fully hydrothermal continuous flow synthesis at both laboratory and pilot scales to assess their viability for industrial scale production.

Chapter 4 presents the development of the first continuous flow hydrothermal production of metal sulphide nanomaterials, via a general route using thiourea as the sulphur source. Full synthetic details and characterisation are discussed, together with information yielded about the materials and reactor and the implications this may have on future materials synthesis using CFHS and the Nottingham reactor.

Chapter 5 details firstly batch hydrothermal and solvothermal synthesis of lithium iron phosphate materials to investigate the effect of a range of conditions on the reaction pathway and resulting products, followed by a translation of the knowledge learned into continuous flow hydrothermal and solvothermal reactions using the counter-current reactor. Scale up of the synthesis is achieved, together with electrochemical testing of selected products.

Finally, chapter 6 provides general conclusions, summaries and outlooks for future work.

Acknowledgements

It is both a necessity and highly rewarding experience that research is not a solitary pursuit. I have been extremely fortunate throughout the last 3.5 years in my PhD to have worked alongside and had the support of a vast and diverse group of people, in both my academic life and outside of University.

Firstly, I thank my supervisor, Prof Ed Lester. His guidance, unwavering support and unique perspective have enabled me to, what I believe, experience everything a PhD has to offer. Given my approach and attitude towards the PhD process, I feel Ed above all other potential supervisors has been an excellent match. I have benefited not just through academic research, but gaining industrial insight, collaborative and inter-disciplinary working and learning, travel to conferences and undertaking research placements at internationally recognised institutions, and I have been afforded the flexibility to direct my research and build my own researcher portfolio, gaining experience in those topics which interest me. For this I believe I will always be in a better position and will always be grateful.

My co-supervisor Dr Peter Dunne, I thank whole-heartedly. Rarely will I find a more supportive, patient, generous or inspiring colleague with which to not only have had the pleasure to work, but also call a friend. Working with Pete took the PhD from completing an academic qualification, to research becoming an engrossing, enjoyable, encompassing and engaging hobby and interest, and with that, invoking the feelings one can only wish to achieve when one undertakes their job. I thank Pete for also taking the time to aid in the development and finalising of this thesis.

Of course there has been tremendous help from all other group members, academic staff and support staff at Nottingham throughout the years, with particular thanks going to Dr Miquel Gimeno-Fabra, Dr Thomas Huddle and Dr Alexis Munn.

Working with the company Promethean Particles has been an invaluable experience, not only in developing some of the ideas presented in this PhD to industrial concepts and scales, but gaining an insight into the commercial world. Dr Selina Tang and Dr Pete Gooden are particularly thanked for their help, support and many useful discussions.

I was lucky enough to undertake two research placements during my PhD; four weeks at Tohoku University in Japan and five weeks at Sungkyunkwan University in South Korea. For these I thank Prof Tadafumi Adschiri, Prof Seiichi Takami, Prof Jaehoon Kim and Jieun Hwang, in addition to all group members in both research groups. The welcome, help and ongoing support I received during both placements and on returning to Nottingham was and continues to be invaluable. Again I thank Ed for recognising the fantastic opportunity these placements afforded and supporting me in undertaking them.

I thank the EU FP7 funding framework through the SHYMAN Project and the University of Nottingham for generous financial support throughout the PhD.

Finally, one needs support outside of academic study, and I have been fortunate to receive this from family, particularly my incredibly supportive parents, brother, girlfriend Sammy and her parents, friends, housemates and sporting team mates – all have aided in making my PhD time balanced and enjoyable.

Journal Publications Arising from this Work

1. Dunne, P. W., **Starkey, C. L.**, Munn, A. S., Sikder, M., Luebben, O., Shvets, I., Lester, E. H., Transition metal doped anatase nanocrystals: continuous-flow hydrothermal synthesis and photocatalytic activity. *Journal of Environmental Chemical Engineering*, **2016**, In Press, doi:10.1016/j.jece.2016.05.007
2. Dunne, P. W., **Starkey, C. L.**, Munn, A. S., Tang, S. V. Y., Luebben, O., Shvets, I., Ryder, A. G., Casamayou-Boucau, Y., Morrison, L., Lester, E. H., Bench- and pilot-scale continuous-flow hydrothermal production of barium strontium titanate nanopowders. *Chemical Engineering Journal*, **2016**, 289, 433-441.
3. Dunne, P. W., **Starkey, C. L.**, Munn, A. S., Huddle, T. A., Lester, E. H., Continuous-flow supercritical hydrothermal synthesis of inorganic nanomaterials. *Philosophical Transactions of the Royal Society of London A: Mathematical, Physical and Engineering Sciences*, **2015**, 373, 2057.
4. Dunne, P. W., Munn, A. S., **Starkey, C. L.**, Lester, E. H., The sequential continuous-flow hydrothermal synthesis of molybdenum disulphide. *Chemical Communications*, **2015**, 51, 4048-4050.
5. Dunne, P. W., **Starkey, C. L.**, Gimeno-Fabra, M., Lester, E. H., The rapid size- and shape-controlled continuous hydrothermal synthesis of metal sulphide nanomaterials. *Nanoscale*, **2014**, 6 (4), 2406-2418.

Presentation of this Work at Conferences

1. Continuous Flow Hydrothermal & Solvothermal Production of Lithium Iron Phosphate Nanoparticles & Their Electrochemical Performance. *International Solvothermal & Hydrothermal Association Conference 2016, Taiwan. Invited oral presentation. 2016.*
2. Hydro/Solvothermal Batch & Continuous Production of Tailored Nanomaterials: An Investigation into LiFePO₄. *International Solvothermal & Hydrothermal Association Conference 2014, Bordeaux. Poster presentation. 2014.*
3. Continuous Hydrothermal Synthesis of Tailored Metal Sulphide and Metal Phosphate Nanomaterials. *M3 Project Workshop, Sendai, Japan. Oral presentation. 2014.*
4. Continuous Hydrothermal Synthesis of Novel Nanomaterials. *Sustainable Manufacturing of Nanomaterials for Ordered Hybrid Device Structures, Île D'Oléron, France. Flash oral presentation and poster presentation. 2013.*
5. Continuous Hydrothermal Synthesis of LiFePO₄ & Metal Sulphide Nanomaterials. *6th International Conference on Green and Sustainable Chemistry, Nottingham, UK. Poster presentation. 2013.*
6. Small Particles, Large Impact – The Discovery of New Nanomaterials. *University of Nottingham Research Showcase, Nottingham, UK. Poster presentation. 2013.*

Table of Contents

1. Introduction & Background.....	1
1.1. Opening.....	1
1.2. Introduction to Nanoparticles and the Nanoscale	4
1.2.1. Catalytic Properties.....	7
1.2.2. Optical/Electronic Properties.....	8
1.3. The Synthesis of Inorganic Nanomaterials	11
1.3.1. Introduction.....	11
1.3.2. Solid State Reactions	14
1.3.3. Vapour Phase Reactions	15
1.3.4. Solution Phase Reactions.....	16
1.4. Continuous-Flow Hydrothermal & Solvothermal Synthesis	24
1.4.1. Principles and Reactor Design.....	24
1.4.2. Nanomaterials Produced by CFHS.....	38
1.4.3. The Nottingham Counter-Current Reactor	39
1.4.4. The SHYMAN Project	41
1.5. Target Materials of this PhD Project	42
1.6. Aims of this PhD Project	44
2. Materials Characterisation Techniques	46
2.1. X-Ray Diffraction (XRD)	46
2.2. Scanning Electron Microscopy (SEM)	49
2.3. Transmission Electron Microscopy (TEM)	52
2.4. Inductively Coupled Plasma Mass Spectrometry (ICP-MS)	54
2.5. Ultraviolet-Visible Light (UV-Vis) and Fluorescence Spectroscopy	55
2.6. Infra-Red and Raman Spectroscopy	57
2.7. Surface Area Analysis.....	59
3. Metal Oxide Nanoparticles.....	61
3.1. Titania and Transition Metal Doped Titania.....	62
3.1.1. Introduction.....	62
3.1.2. Experimental.....	65

3.1.3.	Results & Discussion.....	68
3.1.4.	Conclusions	82
3.2.	Barium Strontium Titanate ($\text{Ba}_{(1-x)}\text{Sr}_x\text{TiO}_3$)	83
3.2.1.	Introduction.....	83
3.2.2.	Experimental.....	87
3.2.3.	Results & Discussion.....	89
3.2.4.	Conclusions	107
4.	Metal Sulphide Nanomaterials	109
4.1.	Introduction.....	109
4.2.	Experimental	112
4.2.1.	Synthesis	112
4.2.2.	Characterisation	115
4.3.	Results & Discussion	117
4.3.1.	ZnS.....	117
4.3.2.	CdS	126
4.3.3.	PbS.....	131
4.3.4.	CuS	135
4.3.5.	$\text{Fe}_{(1-x)}\text{S}$	140
4.3.6.	Bi_2S_3	142
4.3.7.	MoS_2	146
4.4.	Mechanisms of Metal Sulphide Synthesis by CFHS	153
4.5.	Conclusions.....	158
5.	Lithium Iron Phosphate	163
5.1.	Introduction.....	163
5.2.	Experimental	173
5.2.1.	Batch Hydrothermal & Solvothermal Synthesis	173
5.2.2.	Continuous Flow Hydrothermal & Solvothermal Synthesis	174
5.2.3.	Characterisation	176
5.2.4.	Electrochemical Characterisation	177
5.3.	Results & Discussion	180
5.3.1.	Batch Hydrothermal Synthesis of LFP.....	180

5.3.2.	Batch Solvothermal Synthesis	199
5.3.3.	Summary of Batch Reactions	212
5.3.4.	Continuous-Flow Hydrothermal Synthesis of LFP	215
5.3.5.	Continuous Flow Solvothermal Synthesis of LFP	223
5.3.6.	Pilot-Scale Hydrothermal Production of LFP.....	228
5.3.7.	Electrochemical Testing of CFHS & CFSS LFP.....	230
5.4.	Conclusions.....	240
6.	Conclusions, Summary & Future Work	246
6.1.	Mixed Metal Oxides	246
6.2.	Metal Sulphides	249
6.3.	Lithium Iron Phosphate.....	250
6.4.	Closing Remarks	252
7.	References	255

List of Tables

Table 3.1: Summary of the physical properties of transition metal doped anatase nanocrystals.....	75
Table 3.2: Properties of bench-scale $\text{Ba}_{(1-x)}\text{Sr}_x\text{TiO}_3$ determined by ICP-MS, Raman spectroscopy and XRD. C and T indicate cubic and tetragonal phases, respectively.....	99
Table 3.3: Properties of pilot-scale $\text{Ba}_{(1-x)}\text{Sr}_x\text{TiO}_3$ determined by ICP-MS, Raman spectroscopy and XRD. C and T indicate cubic and tetragonal phases, respectively.....	104
Table 4.1: Details of metal sulphide syntheses performed.....	115
Table 4.2: Phase composition and calculated crystallite diameters, D, of cubic sphalerite (Sph) and hexagonal wurtzite (W) phases of ZnS samples prepared by Method B.....	120
Table 4.3: Phase composition and calculated crystallite diameters, D, of cubic hawleyite (H) and hexagonal greenockite (G) phases of CdS samples prepared by Method B.....	130
Table 5.1: Summary of batch hydrothermal reactions at 180 °C for LFP production.....	180
Table 5.2: Summary of batch hydrothermal reactions at 400 °C for LFP production.....	190
Table 5.3: Summary of batch solvothermal reactions at 180 °C for LFP production.....	199
Table 5.4: Summary of batch solvothermal reactions at 400 °C for LFP production.....	206
Table 5.5: Summary of CFHS reactions at 180 °C for LFP production.....	215
Table 5.6: Summary of CFHS reactions at 400 °C for LFP production.....	216
Table 5.7: Summary of CFSS reactions at 180 °C for LFP production in ethylene glycol.....	223
Table 5.8: Summary of CFSS reactions at 400 °C for LFP production in ethylene glycol.....	224
Table 5.9: The selected LFP products (and synthesis conditions) that were subject to electrochemical testing. AA = ascorbic acid, CA = citric acid, EG = ethylene glycol.....	232

List of Figures

Figure 1.1: Graphic illustrating the increased surface area to volume ratio of smaller (right, nanoscale) material compared to larger (left, bulk) material. Nanoparticles can be viewed as mostly accessible and exploitable surface for novel properties. Image from (Sustainable-nano.com 2013).	6
Figure 1.2: The LaMer model of nanoparticle nucleation and growth.....	12
Figure 1.3: A simplified representation of the phase diagram of water (a) and selected isobaric properties (b).	21
Figure 1.4: Schematic diagram of the reactor configuration typically used by Adschiri <i>et al.</i> for the continuous hydrothermal synthesis of nanoparticles (Adschiri, Kanazawa <i>et al.</i> 1992).	26
Figure 1.5: Schematic of the Nottingham reactor configuration for nanomaterials synthesis using a T-piece mixer (Lester, Blood <i>et al.</i> 2006).	26
Figure 1.6: Steady state concentration map from the pseudofluid models showing the mixing regime in a T-piece mixer acting as a pseudoreactor (Blood, Denyer <i>et al.</i> 2004).	29
Figure 1.7: The patented pipe-in-pipe counter-current continuous hydrothermal and solvothermal reactor designed at The University of Nottingham.....	31
Figure 1.8: The Nottingham counter-current reactor schematic with inset showing the mixing dynamics (a), and the actual system at laboratory scale (b), and pilot scale (c).....	31
Figure 1.9: Diagram demonstrating the orientation of the co-current Confined Jet Reactor designed by Darr <i>et al.</i> at UCL (Gruar, Tighe <i>et al.</i> 2013).....	33
Figure 1.10: A schematic diagram of the continuous flow reactor system used by Kim <i>et al.</i> for the synthesis of metal oxide nanoparticles in supercritical water or methanol. R: supercritical reactor; RH: reactor heater; (Kim, Park <i>et al.</i> 2008).....	36
Figure 1.11: CFD simulations of the three tee reactors (90°, 50° and swirling tee) investigated at the Korea Institute of Science and Technology for the synthesis of LiFePO ₄ nanoparticles (Hong, Kim <i>et al.</i> 2013).....	37
Figure 2.1: A schematic demonstrating the principles and key values associated with XRD. Image from http://physik2.uni-goettingen.de/research/2_hofs/methods/XRD	47
Figure 2.2: Diagram of a scanning electron microscope	51
Figure 2.3: Diagram of a transmission electron microscope	53
Figure 3.1: The structure of anatase viewed along the b- and c-axes.....	63

Figure 3.2: Reaction scheme for the production of transition metal doped anatase nanocrystals.....	66
Figure 3.3: Powder X-ray diffraction patterns of the pure and doped anatase nanocrystals, with red lines indicating anatase TiO ₂ peak positions.....	69
Figure 3.4: TEM images of undoped anatase (a), 1% cobalt doped anatase (b), 1% nickel doped anatase (c), and representative elemental mapping images of a nickel doped anatase sample showing the uniform distribution of the dopant ions (d). Insets show the corresponding HRTEM images and electron diffraction patterns.....	70
Figure 3.5: Nitrogen adsorption-desorption isotherms (a), and pore size distributions obtained by the BJH method (b) of the pure and doped anatase nanocrystals.	71
Figure 3.6: Diffuse reflectance UV-Vis spectra (a) and corresponding Tauc plot (b) of the TiO ₂ , 1% Co:TiO ₂ and 1% Ni:TiO ₂ photocatalyst nanoparticles.	73
Figure 3.7: Results of photocatalytic testing on the degradation of methylene blue under UVA irradiation in the presence of photocatalysts (a), and plot determining the first-order photodegradation rates (b).....	78
Figure 3.8: The BaTiO ₃ perovskite structure, showing in green the Ba ²⁺ in the A position.	84
Figure 3.9: A simplified schematic of the reactor used in the production of Ba _{1-x} Sr _x TiO ₃ with an inset highlighting the counter-current mixing (numbers in brackets indicate flow-rates used at the pilot-scale) (a), and photographs of the bench- and pilot-scale systems (b & c, respectively).....	88
Figure 3.10: XRD patterns of samples prepared with varying Ba:Ti:OH ratios using TiBALD. The patterns of the materials produced at ratios of 1:1:0 and 1:1:4 have been scaled for clarity. Tick marks indicate the expected peak positions for BaTiO ₃ , BaCO ₃ and anatase phase TiO ₂	91
Figure 3.11: XRD pattern of the sample prepared using the 1:1:10 ratio using a titania sol as opposed to TiBALD. Tick marks indicate the expected peak positions for BaTiO ₃ , BaCO ₃ and anatase phase TiO ₂	92
Figure 3.12: Comparison of the XRD patterns (a) and infrared spectra (b) of barium titanate obtained at a Ba:Ti:OH of 1:1:10 before and after washing with 1 M acetic acid. * indicates the sharp band at 1456 cm ⁻¹ indicative of the carbonate species, which is removed after washing.	94
Figure 3.13: The Ba ²⁺ :Ti, Sr ²⁺ :Ti and total M ²⁺ :Ti ratios of the bench-scale Ba _(1-x) Sr _x TiO ₃ samples determined by ICP-MS against x. Dashed lines indicate the targeted values.	96
Figure 3.14: XRD patterns of bench-scale Ba _(1-x) Sr _x TiO ₃ samples with tick marks corresponding to BaTiO ₃ (bottom) and SrTiO ₃ (top) (a) and the	

equivalent Raman spectra (b), and the effect of Sr content on crystallite size and cubic lattice parameter, a , as a function of Sr:M ²⁺ ratio (c).	98
Figure 3.15: TEM images of bench-scale Ba _(1-x) Sr _x TiO ₃ samples at x values of 0, 0.2, 0.4, 0.5, 0.6, 0.8 and 1 (a – g, respectively), and a composite of the corresponding electron diffraction patterns (h). Insets show high resolution images.....	100
Figure 3.16: The M ²⁺ :Ti ratios of the pilot-scale Ba _(1-x) Sr _x TiO ₃ samples determined by ICP-MS against x . Dashed lines indicate the targeted values. 101	101
Figure 3.17: XRD patterns of pilot-scale Ba _(1-x) Sr _x TiO ₃ samples with tick marks corresponding to cubic BaTiO ₃ (bottom) and SrTiO ₃ (top) (a) and the equivalent Raman spectra (b), and the effect of Sr content on crystallite size and cubic lattice parameter, a , as a function of Sr/Ti ratio (c).	104
Figure 3.18: TEM images of pilot-scale Ba _(1-x) Sr _x TiO ₃ samples at x values of 0, 0.5, and 1 (a – c, respectively), and a composite of the corresponding electron diffraction patterns (d). Insets show high resolution images.....	105
Figure 4.1: A simplified schematic of the counter-current continuous flow reactor for the synthesis of metal sulphide nanomaterials with Method A and B labels indicating the difference in entry of the thiourea precursor into the reactor.	113
Figure 4.2: The refined XRD pattern (a) and TEM images (b, c) of ZnS prepared by Method A. Reitveld refinement was performed with both cubic ($F43m$, $a = 5.3656 \text{ \AA}$) and hexagonal ($P6_3mc$, $a = 3.7846 \text{ \AA}$, $c = 6.2089 \text{ \AA}$) phases.....	118
Figure 4.3: The XRD patterns (a) and calculated crystallite diameters and phase percentages from Reitveld refinements (b) of the ZnS nanoparticles obtained by Method B.	120
Figure 4.4: TEM images of ZnS nanoparticles obtained by Method B at the indicated synthesis temperatures. Insets show reconstructed images highlighting crystal planes of the cubic sphalerite (Sph) and hexagonal wurtzite (W) phases of ZnS.	121
Figure 4.5: Fluorescence spectra of ZnS samples prepared by Method A and Method B at the temperatures shown with an excitation wavelength of 370 nm (top) and 290 nm (bottom).....	125
Figure 4.6: The refined XRD pattern (a) and TEM images (b, c) of CdS prepared by Method A. Reitveld refinement was performed with both cubic ($F43m$, $a = 5.8365 \text{ \AA}$) and hexagonal ($P6_3mc$, $a = 4.1361 \text{ \AA}$, $c = 6.7222 \text{ \AA}$) phases.....	127
Figure 4.7: Proposed formation of the observed tetrapod morphology of CdS (red indicates the initial core, followed by growth of the hexagonal phase arms (green)).	128

Figure 4.8: The XRD patterns (a), crystallite diameters and phase percentages calculated from Reitveld refinements (b) of the CdS nanoparticles obtained by Method B.	130
Figure 4.9: TEM images of CdS nanoparticles obtained by Method B at the indicated synthesis temperatures. Insets show reconstructed images highlighting crystal planes of the cubic hawleyite (H) and hexagonal greenockite (G) phases of CdS.	131
Figure 4.10: The XRD pattern of the product obtained from the attempted synthesis of PbS by Method A at 400 °C. The product consists of both PbS (galena) and PbSO ₄	132
Figure 4.11: XRD patterns of PbS samples prepared by Method B at 250 °C and 300 °C. The main product is galena with only minor lead carbonate impurities.	133
Figure 4.12: TEM images of cuboidal PbS nanoparticles obtained by Method B at 250 °C and 300 °C. Insets show reconstructed images highlighting crystal planes of the cubic galena PbS.	134
Figure 4.13: XRD pattern (a) and TEM images (b & c) of the product obtained from the attempted synthesis of CuS by Method A.	135
Figure 4.14: The XRD pattern of copper thiocyanate obtained from the attempted synthesis of CuS by Method B at 250 °C.	137
Figure 4.15: The XRD pattern of the CuS obtained by Method B at 300 °C (a), tick marks indicate the major reflections of covellite, and TEM images showing the hexagonal platelet morphology (b-d).	139
Figure 4.16: HRTEM images of a single layered hexagonal nanoplatelet with the covellite structure overlaid viewed along the c-axis (left), and an edge on view of stacked platelets compared to 4 stacked ‘tetrahedron bilayers’ (two unit cells in the c-direction) of the covellite structure viewed along the (110) axis (right) – image courtesy of Dr Peter Dunne.	139
Figure 4.17: XRD patterns of the products obtained from the synthesis of iron sulphide by Method B at 250 °C, 300 °C and 350 °C. * indicates peaks arising from the sample holder.	140
Figure 4.18: XRD patterns of the stable iron sulphide products obtained by synthesis at 400 °C by Method A and Method B.	141
Figure 4.19: TEM images of pyrrhotite nanoplates and nanoparticles obtained by Method A and Method B at 400 °C.	142
Figure 4.20: XRD pattern of a typical product obtained from a synthesis of Bi ₂ S ₃ under normal conditions, identified as Bi ₂ O ₂ SO ₄	143
Figure 4.21: The XRD pattern (a), and TEM images (b - d), of the Bi ₂ S ₃ self-assembled nanorods obtained by Method B with modified flow-rates.	145

Figure 4.22: The various thiomolybdate species give rise to coloured solutions obtained by the attempted standard Method B synthesis of MoS ₂ (top), and the resulting UV-Vis spectra of the solutions (bottom).....	147
Figure 4.23: Reactor for the production of MoS ₃ by acidification of <i>in-situ</i> generated thiomolybdates (a), and the XRD pattern (b) and HRTEM images (c-f) of the amorphous product (inset shows a possible structure as proposed by Hibble & Wood (Hibble and Wood 2003)).	151
Figure 4.24: The final reactor design for the production of MoS ₂ by further hydrothermal treatment of MoS ₃ (a), and the XRD pattern (b) and HRTEM images (c-f) of the crystalline MoS ₂ product.....	152
Figure 4.25: A simplified representation of the suggested mechanism of Method A and Method B based on the LaMer model (LaMer and Dinegar 1950) highlighting the influence of increasing temperature on critical nucleus radius (Kumar and Nann 2006), and various metal sulphide nanostructures.	157
Figure 5.1: The structure of lithium iron phosphate viewed along the Li-ion channels, with the small spheres representing Li-ions aligning in the channels.	164
Figure 5.2: Simple schematic of the continuous hydro- and solvothermal reactor designed and used at Nottingham for the continuous flow production of lithium iron phosphate.	176
Figure 5.3: Pictures illustrating the preparation of the coin cells in Korea using LFP from the Nottingham counter-current reactor for electrochemical characterisation.	179
Figure 5.4: SEM images and XRD patterns of the products from batch hydrothermal reactions at 180 °C with no additive.	182
Figure 5.5: SEM images and XRD patterns of the products from batch hydrothermal reactions at 180 °C with ascorbic acid additive.	185
Figure 5.6: SEM images and XRD patterns of the products from batch hydrothermal reactions at 180 °C with citric acid additive.	188
Figure 5.7: Possible citric acid growth directing mechanisms in batch hydrothermal LFP synthesis, acting as either a capping and therefore directing agent (discussed further in the 400 °C reactions with citric acid in Section 5.3.1.2) (top), or as a chelating agent controlling assembly, as in the hydrothermal reaction with citric acid at 180 °C (bottom).....	189
Figure 5.8: SEM images and XRD patterns of the products from batch hydrothermal reactions at 400 °C with no additive.	192
Figure 5.9: SEM images and XRD patterns of the products from batch hydrothermal reactions at 400 °C with ascorbic acid additive.	194

Figure 5.10: SEM images and XRD patterns of the products from batch hydrothermal reactions at 400 °C with citric acid additive.	197
Figure 5.11: Summary of the possible growth and morphological evolution processes of LFP formation in supercritical water using citric acid as an additive. (Top right simulated schematics are of LFP particles obtained after hydrothermal reactions for 52 and 120 hours respectively, demonstrating truncated edges and faces due to etching (Lu, Chen et al. 2011)).	198
Figure 5.12: SEM images and XRD patterns of the products from batch solvothermal reactions at 180 °C with no additive.	201
Figure 5.13: Ethylene glycol appears to promote growth and therefore elongation of particles into the c-axis, producing particles with short b-axis lengths which may be beneficial for lithium ion transfer kinetics.	201
Figure 5.14: SEM images and XRD patterns of the products from batch solvothermal reactions at 180 °C with ascorbic acid additive.	203
Figure 5.15: SEM images and XRD patterns of the products from batch solvothermal reactions at 180 °C with citric acid additive.	205
Figure 5.16: SEM images and XRD patterns of the products from batch solvothermal reactions at 400 °C with no additive.	207
Figure 5.17: SEM images and XRD patterns of the products from batch solvothermal reactions at 400 °C with ascorbic acid additive.	210
Figure 5.18: SEM images and XRD patterns of the products from batch solvothermal reactions at 400 °C with citric acid additive.	211
Figure 5.19: TEM images and XRD patterns of lithium iron phosphate synthesised under continuous-flow hydrothermal conditions with and without additives at 400 °C and a residence time of ~5 seconds.	217
Figure 5.20: TEM images and XRD patterns of lithium iron phosphate synthesised under continuous-flow hydrothermal conditions with and without additives at 400 °C and a residence time of ~15 seconds.	222
Figure 5.21: TEM images and XRD patterns of lithium iron phosphate synthesised under continuous-flow solvothermal conditions with and without additives at 400 °C and a residence time of ~5 seconds.	225
Figure 5.22: TEM images and XRD patterns of lithium iron phosphate synthesised under continuous-flow solvothermal conditions with and without additives at 400 °C and a residence time of ~15 seconds.	227
Figure 5.23: Comparison of bench- and pilot-scale lithium iron phosphate produced with ascorbic acid as an additive at 400 °C and a residence time of ~5 s.	229

Figure 5.24: A schematic of a Li-ion battery indicating relative locations of each component and the direction of current flow and Li-ion transfer upon charging and discharging (top, (Lee, Yanilmaz et al. 2014)), an illustration of coin cell components and their order of assembly, with the uppermost working electrode replaced by Li-foil for laboratory tests and in the tests presented in this chapter to create a half-cell, with electrolyte also added (bottom left, (Burns, Krause et al. 2011)) and prepared coin cells used for the electrochemical testing in this chapter (bottom right). 231

Figure 5.25: The battery cycling performance of the pilot scale and laboratory scale lithium iron phosphate samples at 0.1C (open symbol; charge, closed symbol; discharge). 233

Figure 5.26: Highlighted region at 62° in the XRD patterns of the hydrothermally prepared LiFePO₄ powders studied by electrochemical characterisation, displaying increased splitting with increased reaction/residence time indicating better ordering and enhanced crystallinity. 236

Figure 5.27: The cycling performance of the pilot scale and laboratory scale lithium iron phosphate samples at a range of currents (open symbol; charge, closed symbol; discharge). 238

Figure 6.1: A computer generated image of the SHYMAN facility design ... 254

List of Key Abbreviations

CFD – Computational Fluid Dynamics

CFHS – Continuous Flow Hydrothermal Synthesis

CFSS - Continuous Flow Solvothermal Synthesis

CFHSS – Continuous Flow Hydrothermal & Solvothermal Synthesis

EU FP7 – European Union Seventh Framework Programme

IR – Infra-Red Spectroscopy

LFP – Lithium Iron Phosphate

LIB – Lithium-ion Battery

scH₂O/scW – Supercritical Water

scWHS - Supercritical Water Hydrothermal Synthesis

SEM – Scanning Electron Microscope/Microscopy

SHYMAN – Sustainable Hydrothermal Manufacturing of Nanomaterials

TEM – Transmission Electron Microscope/Microscopy

UoN – University of Nottingham

UV-Vis – Ultraviolet-Visible Spectroscopy

XRD – X-ray Diffraction

1. Introduction & Background

This chapter seeks to introduce the topic of nanomaterials and nanotechnology in general, by giving a brief history and more importantly a current definition of ‘nano’, coupled with an explanation of the unique properties of nanomaterials and their exploitation and potential in advanced technologies. The traditional synthetic methods towards the production of nanomaterials will be introduced, with particular focus on hydrothermal synthesis and supercritical water. The chemistry utilised in this PhD project is underpinned by continuous flow hydrothermal and solvothermal synthesis, and hence, the recent developments of this synthesis technology will be introduced and discussed, to demonstrate the importance of the development of a more sustainable, economical and reliable synthesis technology for producing novel and industrially applicable nanomaterials. The SHYMAN project will be introduced, which concerns the scale-up of the reactor technology and the discovery and development of new materials. This chapter will provide context to the research and provide the basis for the motivation behind this PhD project.

1.1. Opening

As the industrial revolution and later the digital revolution promoted the United Kingdom and other advanced global societies towards a higher quality of life, so too does nanotechnology present just as exciting an opportunity to enhance human existence into realms only imagined by previous generations. The potential for nanotechnology to accelerate the rate of change to all aspects of

Chapter 1: Introduction & Background

the way we live and more importantly, survive into the future, is one of the most exciting propositions scientists of our generation can wish to influence.

Perhaps most pressing, certainly if we are to think of overall human interaction and longevity with earth, is the need to limit and counteract the acceleration of climate change due to increased levels of greenhouse gas emissions through industrial, automotive and agricultural activity. In a world where fossil fuel depletion, volatile global relations and population expansion is increasing a country's energy requirements and need for energy independence, the push towards more sustainable, efficient and economical environmental and energy processes is strong. The movement away from fossil fuels has led to the emergence of technologies for renewable energy generation. The generation, capture, utilisation and storage of energy from technologies such as photovoltaic devices, fuel cells, wind and hydroelectric power and batteries are all either underpinned or have proposed benefit from nanotechnology in terms of their function or performance.

Heightened public and consumer awareness of all matters 'green' and sustainable, particularly in a highly commercial age where competition is strong, forces producers, manufacturers and companies to utilise nanotechnology advancements to push their processes and products to be as efficient and environmentally friendly as possible and show green credentials in production, use and disposal. This is an interesting objective to achieve, particularly when consumers are torn between the environmental factors discussed and the insatiable need in a technologically driven society for products, particularly electronics, to be as advanced as possible: lasting longer,

Chapter 1: Introduction & Background

charging faster, completing ever more complex processes and being lighter yet more hardwearing. There is a necessity therefore for novel materials and innovative processing and production methods that can satisfy both objectives. Nanomaterials possess unique characteristics that give them a technical edge in a wide range of applications, and manufacturers must employ methodologies of production that excel environmentally by being inherently safer, sustainable or green.

Away from energy and consumer goods or processes are a number of other concerns. Environmental considerations for instance, such as the limitation, destruction or remediation of pollutants, be that physical material such as packaging or more evasive and potentially more harmful contaminants such as emissions, heavy metal contaminants or by-products and pharmaceuticals in wastewater. Adsorption and catalytic processes for these purposes have and could benefit further from advances to nanotechnology. Further to this, population expansion and extension to human life has dramatically heightened the demands on healthcare, not just in terms of volume but in the variety and complexity of illnesses and conditions needing treatment. Nanotechnology has enabled the development of new drug delivery systems, imaging techniques, cancer therapies and biomedical materials such as bone scaffolds and dental implants. Industrial processes that rely on or use sensors, pigments, inks, precise engineering and highly advanced electronics have all also found innovative ways to improve and economise thanks to nanotechnology.

What is clear is that an array of technologies, materials, sectors, products or processes have already benefited from the advances arising through

Chapter 1: Introduction & Background

nanotechnology, and they have the capability to benefit at a rapid rate into future years if implemented further. All of the ‘technologies’ in nanotechnology have one important aspect in common – there is no benefit, or even technology itself, without the nanoparticles and nanomaterials that give rise to the unique properties which provide the technologies their innovative edge and advantage. As such, it can be said that in order for these great advances to occur and for materials science and applied materials pioneers to further the nanotechnology side, nanomaterial chemists and chemical engineers must come up with ever more innovative, sustainable and economical ways of producing the nanoparticles themselves, together with discovering new materials or routes to those materials, and it is this aspect upon which this thesis is concerned.

Presented herein are a series of materials produced by a technology that aims to provide an environmentally benign synthetic solution for accessing technologically important nanomaterials, a reactor working under continuous flow hydrothermal and solvothermal conditions. The intention is that this technology and these materials now synthesised, with development, can go on to become the innovative materials described as necessary above, enabling the nanotechnological advances vital to the on-going enhancement of society and life.

1.2. Introduction to Nanoparticles and the Nanoscale

The currently accepted definition of the nanoscale, or for a particle to be classified as a nanoparticle, is for the particle to have at least one dimension between one and one hundred nanometres, where a nanometre is described as

Chapter 1: Introduction & Background

one billionth (10^{-9}) of a metre. Whilst both the interest and utilisation of nanoparticles has grown significantly in recent years, it would be wrong to assume that they are a new phenomenon. Quite the opposite in fact – nanoparticles are abundant in nature and their use can be evidenced throughout time, even if the user did not particularly recognise their existence or understand the significance of the contribution made by the nanoparticles themselves in the particular application or effect. The addition or occurrence of nanoparticles to glass or in glazes on pottery and ceramics to produce remarkable colouring or light properties or anti-corrosion properties can be dated as far back as AD400, such as in the Lycurgus Cup (Freestone, Meeks et al. 2007) or in the thirteenth to sixteenth century in Renaissance Mediterranean pottery (Pérez-Arantegui, Molera et al. 2001). Damascus Steel swords, made in the Middle East between AD300 and AD1700, which were renowned for their incredible strength, shatter resistance and sharp cutting edge were later found to be a steel-carbon nanotube nanocomposite, where the orientational alignment of the nanotubes and elongated carbon particles produced the sharp edges (Reibold, Pätzke et al. 2009).

In modern times, we define nanotechnology as the synthesis, manipulation and utilisation of nanomaterials to offer unique properties, which are different to those exhibited by the equivalent bulk scale material. These properties can manifest themselves in and provide benefit to catalytic applications, due to small size and increased surface area to volume ratio effects, or optical and electronic effects, due to quantum confinement phenomena. The surface area of particles increases drastically as the particle size of the material decreases and hence, the smaller the particle, the greater the accessible and exploitable

Chapter 1: Introduction & Background

surface for beneficial processes, as demonstrated in Figure 1.1. The number of atoms at the surface of the particle in relation to those embedded within the particle increases at smaller size. In contrast to bulk solids, nanoparticles can be thought of as mostly surface atoms. This can lead to enhanced catalytic activity or remarkable and useful optical or electronic properties from nanomaterials, relative to bulk materials. These effects can vary drastically with size, and hence, can be controlled for a desired effect or tailored to a desired application.

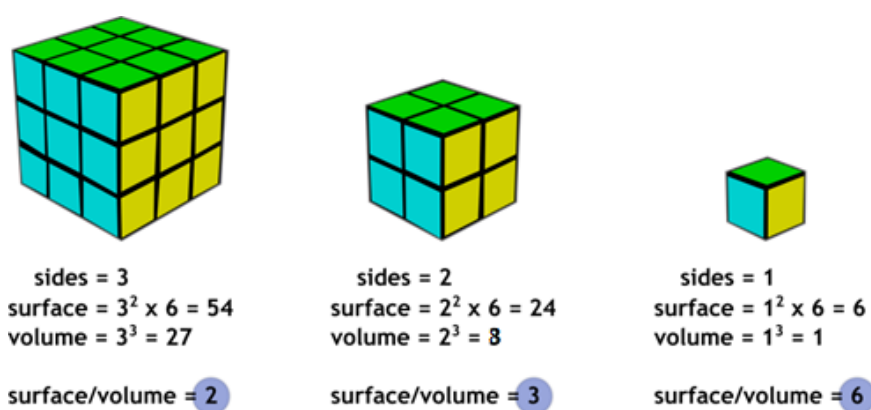


Figure 1.1: Graphic illustrating the increased surface area to volume ratio of smaller (right, nanoscale) material compared to larger (left, bulk) material. Nanoparticles can be viewed as mostly accessible and exploitable surface for novel properties. Image from (Sustainable-nano.com 2013).

In addition to the fundamental properties exhibited by nanomaterials in terms of their chemistry and physics which will be expanded upon in Sections 1.2.1 and 1.2.2, nanomaterials also offer practical benefits with regard to processing. Nanoscale materials often exhibit superior properties, such that the desired effect or greater can be achieved in the target application with lower weight loadings of material than the equivalent bulk material.

Chapter 1: Introduction & Background

Relating this to cost and quality, it can be inferred therefore that producers are required to produce and use reduced quantities of material, thereby reducing processing costs, but still gaining comparable or superior quality. This can be manifested in terms of miniaturisation of components or devices, or superior properties of the product. For example, in the case of ceramics, the bulk materials traditionally require labour intensive and expensive processing steps such as grinding and high temperature reaction and calcination steps, but in comparison, the production of the equivalent nanoscale material is achieved in a more facile way, for instance from solution, with highly crystalline materials being produced without the need for high temperature post processing steps. The small sizes and exploitable surface chemistry of many nanomaterials also means they may be more easily dispersed into water or solvents or mixed into inks and other formulations by way of forming a suspension or dispersion. The capability to form a stable suspension can be highly beneficial in many applications, since the avoidance of agglomeration, clumping or settling can permit easy solution processing and the production of high weight loading composites.

1.2.1. Catalytic Properties

The catalytic properties of nanoparticles are governed by the small particle size dictating an increased surface area compared to bulk materials. Hence nanoparticles display superior catalytic activity – an increased surface area can be viewed as effectively more ‘working surface’ – that is, more accessible and exploitable surface for the catalytic processes of adsorption, reaction and desorption to occur simultaneously. Many nanoparticles also ‘suffer’ from high

Chapter 1: Introduction & Background

proportions of defects, which can induce further enhanced catalytic activity.

Nanoparticles can also act as supports for catalytic reactions or processes.

TiO₂ nanoparticles provide an example of the advantage nanoparticles have in catalytic applications. They have historically received attention due to their ability to act as photocatalysts for a number of applications, from water splitting (Sato and White 1981), to the photochemical degradation of organic and inorganic pollutants (Carp, Huisman et al. 2004, Gaya and Abdullah 2008) in wastewater samples and in self-cleaning surfaces (Parkin and Palgrave 2005), in addition to acting as semiconductor nanocrystals in photovoltaic devices (Bai, Mora-Seró et al. 2014). It has been shown that nanoscale titania outperforms larger particles in terms of photocatalytic activity, attributed to the previously discussed small particle size ensuring high surface areas and specifically, shorter path lengths for electron-hole diffusion to the crystal surface. Additionally, synthetic methods can be developed to promote the adoption of preferred crystalline phases and habits of nanomaterials to enhance the catalytic activity. Photodeposition studies for example, have shown that the rutile-(101) and anatase-(001) surfaces are most active for oxidation reactions while the rutile-(110) and anatase-(101) surfaces are most active for reduction reactions (Batzill 2011).

1.2.2. Optical/Electronic Properties

For optical or electronic effects there must be a transfer of energy for electrons to move from valence to conduction bands, and the energy required to initiate this process or indeed the energy generated or emitted is reliant upon the band gap, that is, the energy gap between the valence and conduction bands or

Chapter 1: Introduction & Background

required energy to transfer electrons between the two. For regular semiconductor crystals, or rather, bulk materials not confined to the nanoscale, this gap is fixed, as the energy levels constituting the electronic configuration are definite due to the continuous, effectively infinite nature of the energy levels. In other words, predictable behaviour can be expected and cannot be manipulated with size or shape of the material, and the energy input to produce a required transition and therefore an output is constant and cannot be manipulated. Upon reaching a critical lower size however, particles do not obey the classical laws of physics, but rather, adhere to quantum physical rules, specifically quantum confinement in the case of optical and electronic transitions. If the size of the particle is smaller than the wavelength of the charge carrier, such as an electron, then quantum confinement occurs. The electron that was once obeying random motion now becomes restricted in its movement, or confined, into discrete energy levels. These discrete energy levels have variability in their band gap comparable with the environment, size and shape of the particle and hence, manipulation of particle size and shape offers manipulation of the band gap energy and optoelectronic effects. This therefore offers the possibility of designing a nanoparticle crystal with exact size and shape, such as ZnS, CdS or PbS quantum dots (Carey, Abdelhady et al. 2015), with tailored optoelectronic properties to offer a precise band gap energy, which, upon excitation with the specific wavelength of light to interact with this tailored band gap, emits energy, such as photoluminescence, in an expected and desired wavelength, i.e. a desired colour. The strong size-dependence on this effect can be demonstrated by cadmium selenide quantum dots, where the emission can range from orange and red at longer wavelengths

Chapter 1: Introduction & Background

for larger particles of 5-6 nm to green and blue at shorter wavelengths for smaller particles of 2-3 nm. Quantum dots thus find use in photovoltaic devices (Chen, Seo et al. 2013), light-emitting diodes (Tan, Zhang et al. 2007) and biological imaging (Wu and Yan 2013). The ease of transmission through the body of nanoparticulates and advanced systems to 'guide' nanomaterials allows for their accumulation in specific target regions, which, under UV irradiation, can fluoresce indicating regions of disease.

A major research theme within this PhD thesis and one that will be discussed in detail is the synthesis of lithium iron phosphate nanoparticles, a lithium intercalation compound with promise in the field of energy storage. In order for lithium ions to 'shuttle' into and out of channels within the iron phosphate and lithium iron phosphate structure, they need to pass readily into and through the full 3-dimensional structure of particles. In a sample of larger particles, the surface area available for this process to occur is reduced, and hence, is sluggish and less efficient, leading to a reduced capacity of the resulting battery cell. With the increase in surface area afforded by smaller particles, lithium ions and electrons can pass into particles more readily due to their greater number/surface area in comparable space to larger particles, and the electron transport can occur throughout the whole diameter of the particle more readily, rather than being confined to the surface. With better ease of transport of the lithium ions, devices can deliver more energy and power, charge quicker and last longer. Other strategies to improve the electrochemical behaviour of particles includes coating of the particles with a conducting layer such as carbon, or doping of the particle structure, both more facile and effective with nanoscale materials compared to bulk equivalents. Finally, the number of

Chapter 1: Introduction & Background

particles and therefore density of active material within a volumetric space also increases with nanoscale particles compared to larger particles, therefore increasing the volumetric density and energy density of the material within the cell, increasing energy capacity. Nanoscale materials therefore offer considerable advantage over micron sized material in this application.

1.3. The Synthesis of Inorganic Nanomaterials

1.3.1. Introduction

The synthesis of inorganic nanomaterials is driven by and focused on the ever increasing array of applications found to benefit from the reduction in size of the primary particles. The properties demonstrated by the nanoparticle or material are highly dependent upon the materials' composition, size, morphology, purity, crystallinity, surface area and surface chemistry to name a few, and these characteristics are in turn determined largely by the synthesis method employed to produce them. The varying synthesis methods all have their associated advantages and disadvantages and each may be the most suitable option depending on the target material or application. Often there is a best case scenario, however, a compromise exists. For instance, the cheapest synthesis method may not produce the optimum material for a given application, so the cost and sustainability of production is weighed against the characteristics and performance of the resulting product. Generally, it is possible to split the methods of nanomaterial production into two categories: top-down approaches and bottom-up approaches. Top-down methods are typically destructive, starting from a bulk material and breaking it down to the

Chapter 1: Introduction & Background

nanoscale. This can be achieved in a number of ways: mechanical milling, anodisation, or lithographic techniques, for example. While top-down methods can be very powerful they are also generally situational and specific. This thesis is concerned with a bottom-up, constructive, synthetic approach; thus, bottom-up synthetic methods, whereby nanomaterials are ‘built up’ by chemical reactions will be discussed in greater detail in the following sections.

Before going into detail on the precise synthetic approaches to nanomaterials, it is useful to understand the factors to be considered in their production. There are many factors to be considered in the synthesis of nanoparticles. The ideal for most purposes is to obtain nanoparticles with controlled sizes and a narrow size distribution. The LaMer model (Figure 1.2) for the growth of monodisperse colloids, developed in the 1950s for colloidal sulphur, offers a simple conceptual framework with which to consider the formation of nanoparticles (LaMer and Dinegar 1950).

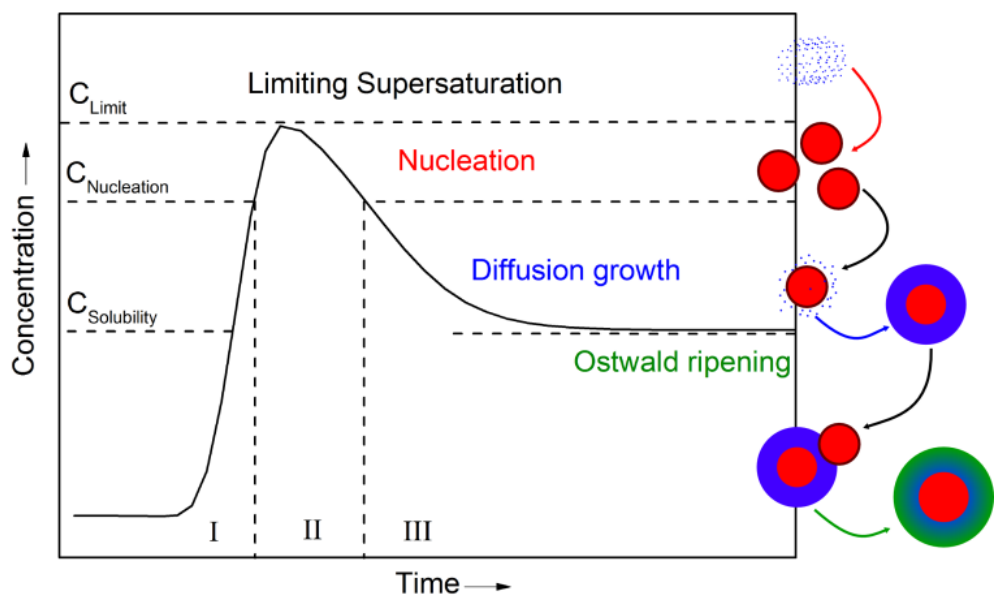


Figure 1.2: The LaMer model of nanoparticle nucleation and growth.

Chapter 1: Introduction & Background

Upon mixing of reagents, or otherwise initiating a reaction (effectively an increase in concentration of the active chemicals by their meeting and interaction or their introduction into an environment designed to stimulate reaction such as elevated temperature, into solvent, or into appropriate chemical parameters), there is a build-up of precursors or the active species (Stage I, Figure 1.2), creating a degree of supersaturation. This creates non-ideal dissolution behaviour of the species, for instance a metal salt or inorganic nanoparticle, and when the level of supersaturation surpasses the critical nucleation threshold ($C_{\text{nucleation}}$), nucleation occurs (Stage II, Figure 1.2), reducing the degree of supersaturation. If the rate of nucleation outstrips the rate of precursor formation or availability, the precursor concentration will drop back below the nucleation threshold, and the production of primary particles will cease. Nanoparticle growth of the existing particles in solution may then proceed by a number of pathways: monomer addition, in which additional precursor units deposit onto the preformed nuclei from solution; Ostwald ripening, whereby energetically disfavoured small nuclei redissolve and deposit onto more thermodynamically favourable larger nuclei; and finally coalescence in which multiple nanoparticles come together and fuse (Stage III, Figure 1.2).

This framework allows us to consider methods by which both size and size distribution may be controlled, as the chemistry and formation of the nanoparticles are governed by key processes occurring within solution dictated by reaction (chemical and experimental) parameters. Synthetic approaches must therefore consider precursor availability or ‘activation’, that is, in what form does one prepare the reagents so that reaction occurs only when desired,

Chapter 1: Introduction & Background

and how is their activation or reaction controlled from the initial nucleation period. The availability of reagents during the reaction affects whether and when nucleation or growth processes occur, and indeed, with considered design, these processes can be separated and manipulated to access desirable and interesting phenomena such as controlled growth and shape control or novel ordering and layering of materials. Given the complexities and range of reaction parameters involved it is easy to understand how varied chemical approaches to materials synthesis can be, and also easy to imagine how each can offer a certain niche. Regardless, it is clear that whilst complex, a carefully designed system with a controlled environment can afford access to an array of innovative materials with varied potential applications.

1.3.2. Solid State Reactions

Solid-state approaches typically take the form of high temperature ceramic methods (Rao 1993). This method mixes simple metal oxide or carbonate precursors and then these are reacted using high temperatures (700-1000 °C) in air or other gases, typically over the course of hours. The premise is that the target material, the ceramic, is stable at the high temperatures employed in the reaction, so any intermediates are converted to products or any contaminant species are unstable at the high temperature and are decomposed leaving the pure product. The precursors are generally cheap and the technology is scalable, however, the process prohibits chemical flexibility and the products are generally large in size (microns), with poor size distribution and particle morphology control, so for applications where controllable size and shape of material is vital, alternative synthesis methods must be employed. BaTiO₃ for

Chapter 1: Introduction & Background

example is widely used in electronic components and devices, and the progressive miniaturisation of devices means that solid state reactions producing larger particles are now becoming unsuitable. Given the high temperatures involved, solid-state ceramic methods are generally energy intensive, and so additionally struggle to be categorised as a sustainable or 'green' synthetic method.

1.3.3. Vapour Phase Reactions

Physical/thermochemical synthetic techniques, such as physical vapour deposition and chemical vapour deposition (Choy 2003, Tjong and Chen 2004, Helmersson, Lattemann et al. 2006) and other vapour phase methods such as spray pyrolysis have long been favoured in the industrial production of nanomaterials, as they are typically cheap and relatively easy to run; however they can suffer from high capital costs and the frequent need for toxic precursors. Salt solutions or organometallic compounds are mixed with carrier gasses such as N₂ and nebulised to produce droplets, which are then introduced into a furnace at high temperature (~1000 °C), or sprayed onto a heated surface, which induces evaporation of the solvent and reaction of the metal containing precursors to give products which are deposited onto a substrate. This method can be undertaken in a continuous manner, but due to the high temperatures involved is an energy intensive process. These techniques are largely restricted to the production of coatings and films, such as CdS thin films (Ramaiah 1999) and CuInSe₂/CdS heterojunction diodes (Strifler and Bates 1992).

1.3.4. Solution Phase Reactions

1.3.4.1. Sol-Gel

Sol-gel methods involving the controlled hydrolysis of metal salts or alkoxides, followed by thermal treatment of the resulting gels, have been used extensively for many years in the synthesis of metal oxide nanoparticles (Cushing, Kolesnichenko et al. 2004). Precursors form colloidal solutions which over time develop into a gel of solid nanoparticles dispersed in a liquid phase. Low temperatures of reaction and a highly controllable environment in terms of concentration, pH, reaction time and rate of reagent or precursor addition allow for a more controlled growth of nanoparticles than the harsher solid-state methods. Sol-gel methods typically yield highly homogenous samples with size and size distribution control, however, products generally suffer low crystallinity and purity and require further post-synthesis heating steps (Hakuta, Onai et al. 1998), both an additional time and cost consideration, and the thermal treatment step may cause unwanted sintering which reduces the quality of the controlled size nanoparticle sample. The controlled nature of the growth generally necessitates low concentrations and prolonged reaction times, restricting the scale-up potential of the synthesis route in an industrial context (Tighe, Quesada Cabrera et al. 2013). Regardless, due to the ease of the technique in terms of the lack of specialist equipment and the low cost coupled with the degree of control, sol-gel techniques are a popular route to nanomaterials. LiFePO₄ (Hsu, Tsay et al. 2004, Hu, Doeff et al. 2004, Gao, Li et al. 2014), ZnS (Senthilkumaar and Selvi 2008), doped TiO₂ (Devi, Kottam et

Chapter 1: Introduction & Background

al. 2010) and BaTiO₃ (Takashi, Naoto et al. 1994) have all been accessed through sol-gel routes.

1.3.4.2. Co-Precipitation

In co-precipitation techniques, aqueous metal salts are mixed or added dropwise to a base which acts as a precipitating agent and the product is a co-precipitated powder which drops out of solution. Similarly with sol-gel techniques, the ease of the process and lack of specialist equipment find this method favour in the production of nanomaterials. The particle size, shape and composition of the product is usually dictated by the type of precursor used, the reaction temperature and the pH of the solution, with some cases displaying poor size distribution. Washing, drying and calcination of the resultant powder leads to the nanomaterial product. LiFePO₄/graphene composites (Ding, Jiang et al. 2010) and BaTiO₃ (Lu, Quilitz et al. 2007) have both been prepared from co-precipitation methods.

1.3.4.3. Hot Injection

Hot-injection routes are highly popular for quantum dot synthesis. They offer excellent control over the size, shape, composition and surface chemistry of nanomaterials through the injection of precursors into hot, high boiling point solvents, together with the presence of chelating agents such as oleylamine, oleic acid and trioctylphosphine oxide for growth limitation, morphological control and surface modification. Nucleation and growth can be carefully controlled. It is possible for instance to inject precursor to produce initial nuclei, and upon injecting new precursor at a reduced reaction temperature,

Chapter 1: Introduction & Background

new material is deposited onto the existing nuclei to promote growth, often into hierarchical structures rather than forming further nuclei. For this fine control of the process however, the reagents, solvents and growth and shape directing agents used are typically expensive, and the purification steps of the resulting materials can be highly labour and time intensive, involving multiple steps. As such, the scale-up potential is limited. To date, however, the applications where particles such as quantum dots find use require only small quantities of the material for function, thus, the fine control to produce tailored materials far outweighs any scale considerations for hot-injection methods. PbS quantum dots for photovoltaic devices (Zhao, Osedach et al. 2010), AgInS₂ (with ZnS shell added post-synthesis) photoluminescent particles (Shenghua, Yu et al. 2015) and 1.5-2.2 nm diameter CdSe quantum dots (Čapek, Lambert et al. 2009) are all examples of the hot-injection route.

1.3.4.4. Hydrothermal & Solvothermal Synthesis of Nanomaterials

Hydrothermal and solvothermal methods allow a high degree of flexibility in experimental design, using relatively low cost, environmentally benign and widely available precursors, with strong control over reaction parameters to achieve products with controllable characteristics and typically high crystallinity, usually without the need for post-synthesis steps. Since this method forms the basis for the chemistry of the continuous flow reactor used in this work, it is explained in much greater detail, firstly in batch reactions in this section, and then in continuous flow systems in Section 1.4.

Hydrothermal and solvothermal synthesis techniques, whereby precursor solutions are heated in a sealed vessel such as an autoclave or high pressure

Chapter 1: Introduction & Background

continuous system at temperatures above the boiling point of the solvent and therefore elevated pressure, allow an enormous degree of freedom in terms of the available chemistry (Byrappa and Yoshimura 2008). The choice of temperature, solvent, reaction time, pH, reagents and additives invites the design of elegant reaction systems. The moderate temperatures at which these reactions take place also permit the synthesis of metastable phases which may not be accessible by other means (Modeshia and Walton 2010). While these conditions are relatively mild when compared to ceramic methods it is often the case that the products obtained are highly (nano-) crystalline in nature, without the need for further heating steps. This is particularly the case when the reaction medium is supercritical water, that is, water above its critical temperature ($T_c = 374\text{ }^\circ\text{C}$) and critical pressure ($P_c = 22.1\text{ MPa}$). Water below this temperature is described as subcritical. Batch hydrothermal and solvothermal syntheses, however, tend to require long reaction times. Typically Teflon lined autoclaves are used which are limited in temperature to subcritical conditions, and hence longer reaction times. Reactors to withstand supercritical conditions are typically bespoke and custom made, and are therefore, more expensive.

In conventional hydrothermal and solvothermal reactions, like most batch processes, such as sol-gel and co-precipitation, precursor formation occurs over a long time period due to, for example, slow heating rates. As a result of this the precursor concentration is often maintained above the critical nucleation threshold for extended periods and nucleation occurs continuously and concurrently with growth. This gives rise to broad particle size distributions. If

Chapter 1: Introduction & Background

sufficiently long reaction times are employed then particle size will focus, narrowing the size distribution, but increasing the size.

As with all batch processes, hydrothermal and solvothermal methods are not easily scalable. Scaling these reactions usually produces similar, but larger vessels, which given the elevated temperatures and pressures involved, carry their associated risks. As industrial demand for nanomaterials increases the need for scalable, cost effective and flexible methods of hydrothermal and solvothermal production becomes ever more pressing. Translating the benefits of hydrothermal and solvothermal chemistry particularly in supercritical fluids, from a batch to continuous manner, affords the unique opportunity this environment provides for the production of tailored materials at industrially and commercially viable scales. Hydrothermal methods are particularly attractive, as they are often referred to as a green and sustainable technology, purely for the fact that they occur in water.

Section 1.4 will introduce the various continuous-flow hydrothermal and solvothermal reactor developments and designs previously and currently employed to produce nanomaterials. Due to the continuous manner of flow chemistry, naturally reactions that occur in batch over the course of minutes and hours have to be completed within seconds to minutes, due to the practical logistics in terms of space and equipment, cost and scale-up potential. Supercritical water can aid in this reduction of reaction time, and underpins all aspects of both the beneficial properties of the process compared to batch, and the materials arising from it. Supercritical water is therefore introduced in more detail in Section 1.3.4.4.1.

Chapter 1: Introduction & Background

1.3.4.4.1. Supercritical Water (ScW)

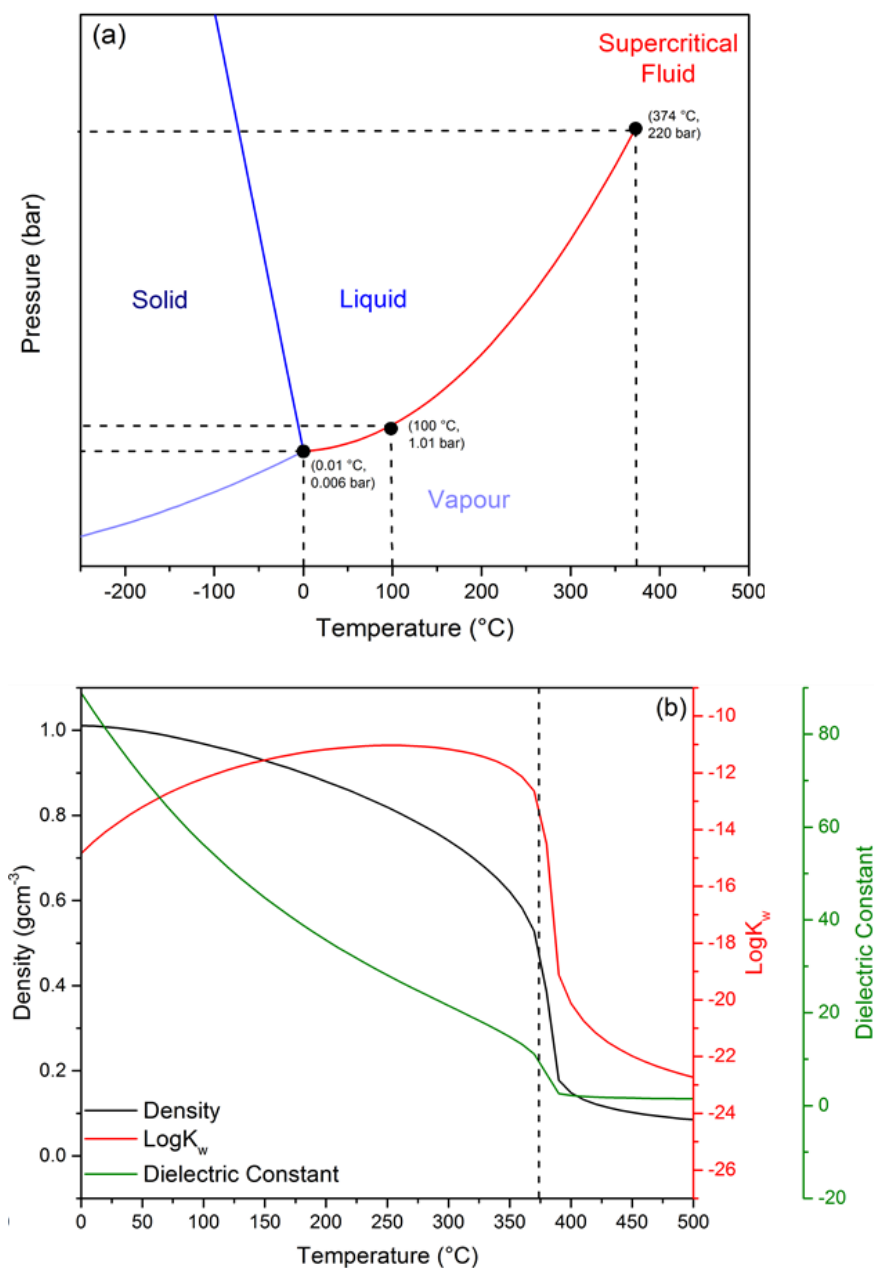


Figure 1.3: A simplified representation of the phase diagram of water (a) and selected isobaric properties (b).

Hydrothermal reactions (or solvothermal if the solvent is not water) can occur at a range of temperatures, where the water can be described as sub- or supercritical. Subcritical water describes any water beneath the critical point (critical temperature, $T_c = 374$ °C, critical pressure, $P_c = 22.1$ MPa). Water under

Chapter 1: Introduction & Background

ambient conditions is a polar molecule, making the dissolution of ionic salts a facile process. As water is heated in a pressurised environment the polarity changes, due to the breakdown of the hydrogen bonds between water molecules, and approaching and above the critical point of water, this effect is exacerbated and a drastic decrease in dielectric constant and increase in the water dissociation constant K_w (Figure 1.3) leads to higher breakdown of water molecules to H^+ and OH^- ions (Adschiri, Kanazawa et al. 1992, Lester, Blood et al. 2006). At these elevated temperatures and pressures, supercritical water is non-polar and thus ionic and polar species such as inorganic salts lose solubility. It is possible to exploit this phenomenon, by having high solubility of inorganic salts at lower temperatures, and at the elevated temperature and pressure, performing chemistry accompanied by a rapid change in solubility, such that inorganic material formed under these conditions is predisposed to precipitate out of the reaction medium, allowing the formation of materials as nanoparticles. This phenomenon forms the basis behind nanoparticle synthesis in supercritical water; however, subcritical water can also be used as a reaction medium, dependant on the material, composition, crystal habit, surface chemistry, size and morphology of nanomaterial desired. Supercritical water exhibits unique behaviour, having characteristics of both liquid and gaseous states, whilst being described as neither. The decreased dielectric constant and increased dissociation constant is coupled with a decrease in density and surface tension, allowing supercritical water to act as a solvent and diffuse as a gas. Coupled with the mentioned 'swing' in solubility of inorganic salts around the supercritical point, the decrease in density is also an interesting property to exploit, particularly for those working in pressurised continuous flow reactors,

Chapter 1: Introduction & Background

to direct flow and product transfer, as will become evident when discussing reactor design and configuration. Whilst supercritical water or alcohol or other super-heated solvent is a proven medium to undertake synthesis of nanomaterials in batch autoclave reactions, for example in the synthesis of LiFePO_4 (Ellis, Kan et al. 2007, Koltypin, Aurbach et al. 2007, Yang, Wu et al. 2009, Rangappa, Sone et al. 2010, Rangappa, Sone et al. 2010, Lu, Chen et al. 2011, Nan, Lu et al. 2011, Pei, Yao et al. 2012, Zhu, Fiore et al. 2013, Chen, Xu et al. 2014, Ghafarian-Zahmatkesh, Javanbakht et al. 2015), batch methods have their associated and previously discussed drawbacks. To become commercially viable at industrial scales, the exploitation of supercritical water or solvent for synthesising nanomaterials is ideally performed under continuous flow conditions. It is also important to note that whilst the early continuous flow work exploited supercritical water to act as both reaction solvent and reactant (OH^- ions for hydrolysis and dehydration to metal oxides), it is also possible to undergo alternative chemistry depending on the reagents used for synthesis. Supercritical water can act as the solvent, but by introducing sulphur containing reagents, for example thiourea, and controlling the reaction conditions, metal sulphides can be produced through the active HS^- species, or by including a phosphate containing reagent, metal phosphates can be produced. Supercritical water therefore offers a versatile and innovative medium in which to synthesise nanomaterials in a continuous fashion.

1.4. Continuous-Flow Hydrothermal & Solvothermal Synthesis

Over the past twenty years continuous-flow hydrothermal and solvothermal synthesis (CFHSS) methods have been investigated as a highly promising one-step process for the production of inorganic nanomaterials. They have the potential to provide a wide variety of nanoparticles cheaply and effectively at the scales required to supply the increasing industrial demand. All continuous flow systems used by researchers in the field operate on the premise of using pumps to drive reactants through a heated, pressurised pipework reactor system, with the differences between groups arising from the reactor design crucially around the mixing point of the metal salts with the heated or superheated water. It is accepted that whilst many operating parameters affect the production and post-synthesis processes such as growth of the nanomaterials, the immediate environment around the mixing and reaction point determines the resultant physical and chemical properties of the produced nanomaterials.

1.4.1. Principles and Reactor Design

In 1992 Prof. Tadafumi Adschiri *et al.* were the first to exploit the properties of near- and supercritical water (Figure 1.3) to facilitate the rapid continuous production of a variety of metal oxides in what has become known as supercritical water hydrothermal synthesis (scWHS) and which is more generally known as CFHS (Adschiri, Kanazawa *et al.* 1992). Here a reagent stream, typically an inorganic metal salt, is brought into contact with a separate

Chapter 1: Introduction & Background

stream of water preheated to a near-critical or supercritical state. The high concentration of OH⁻ species in the preheated water stream leads to the immediate hydrolysis (1.1) and dehydration (1.2) of the metal salt to generate the metal oxide which immediately precipitates as nanoparticles due to supersaturation of the solution, according to the equations:



These metal oxide nanoparticles are then carried further downstream through an additional heating zone to promote growth. This process essentially replicates the hot injection procedure in a continuous-flow system and the basic principle now informs the majority of continuous-flow hydrothermal techniques. Early work on scWHS reactors utilised simple T-piece mixing points. These were generally favoured due to being readily available off-the-shelf parts and offering a simple method of rapidly heating up the precursor stream compared to batch processes. A typical reactor configuration used by Adschiri *et al.* is shown in Figure 1.4.

The initial T-piece mixers used in the field were prone to issues such as poor process and product reliability, reproducibility and control. Indeed, concurrent work in the Clean Technology research Group at Nottingham in continuous flow systems with a vertically aligned Swagelok® T-piece mixer were all hindered by poor product and process reliability and reproducibility, limiting the scale-up potential of the process. A schematic of the reactor used for this work is shown in Figure 1.5.

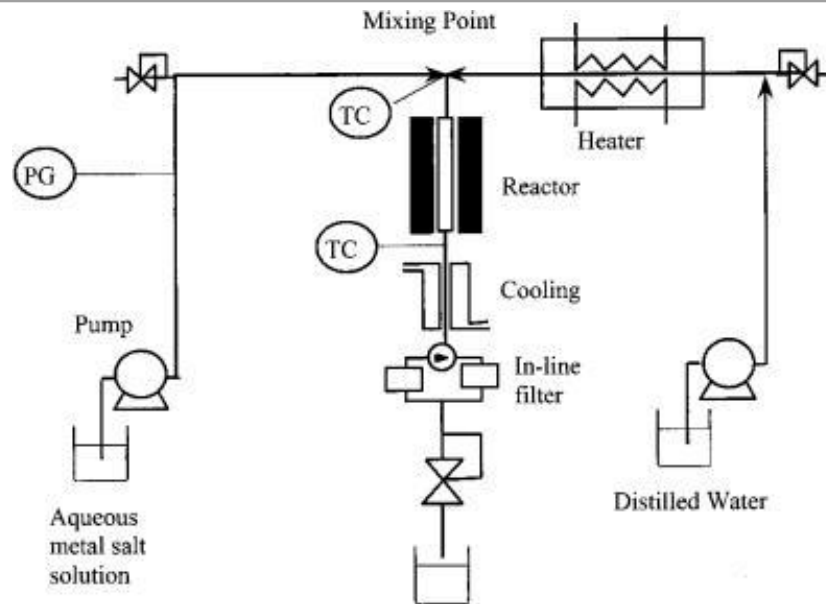


Figure 1.4: Schematic diagram of the reactor configuration typically used by Adschiri *et al.* for the continuous hydrothermal synthesis of nanoparticles (Adschiri, Kanazawa *et al.* 1992).

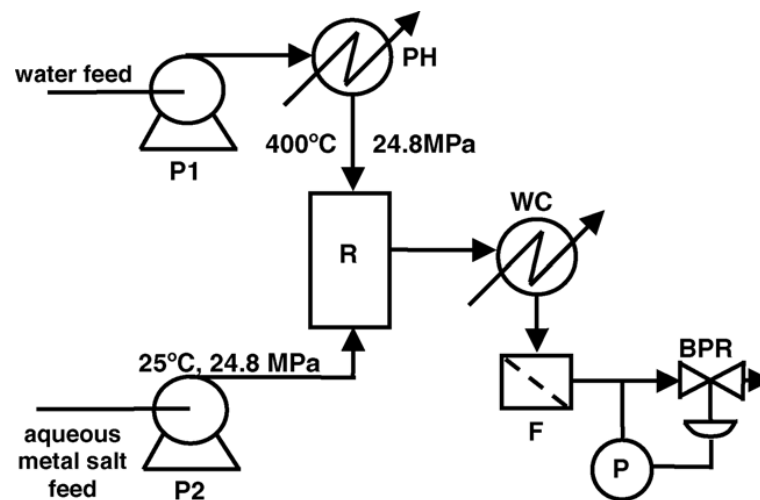


Figure 1.5: Schematic of the Nottingham reactor configuration for nanomaterials synthesis using a T-piece mixer (Lester, Blood *et al.* 2006).

‘R’ in Figure 1.5 represents the T-piece reactor mixer. In this case, supercritical water was fed into the side arm of the T-piece, and the aqueous metal salt solution was fed into the top arm of the T-piece. The two fluids would meet, mix and then pass out the bottom arm of the T-piece mixer. The main issue

Chapter 1: Introduction & Background

within this reactor system was the accumulation of produced nanomaterial within the reactor and two inlets, which caused gradual build up, narrowing of pipework and led to eventual blockages. Blockages in a system such as this require process downtime, as the equipment has to be taken apart, investigated, cleaned (in some instances, dense ceramics form which have to be drilled out) and rebuilt before the process can continue, which is a labour and time intensive process. The accumulation of material and blockages would also lead to poor process control, since the distribution of particle residence time in the reactor is uncertain, with material potentially undergoing additional heating and then gradually breaking free from the pipework and passing into the product solution. Attempts to alleviate these problems by physical or chemical means such as increased flow rates or lower concentration of reagents proved unsuccessful, and indicated that the design of the reactor piece was pivotal to the process reliability.

The mixing efficiency within the reactors was therefore studied in a collaboration between chemists and chemical engineers at Nottingham, with a view to design a new reactor that was capable of larger scale production. Two techniques were used to model the mixing of the flows in the T-piece reactor, namely Light Absorption Imaging (LAI) and Computational Fluid Dynamics (CFD) simulations. The first, LAI, performed by Blood *et al.* (Blood, Denyer *et al.* 2004) was used as a ‘real-life’ case, using a pseudo-reactor, whereby methanol and sugar water, with densities of 0.79 gcm^{-3} and 1.178 gcm^{-3} respectively, were used as analogues for low-density supercritical water and the higher density cold stream. This was a powerful visualisation technique, since visualisation of the mixing regimes and fluid properties inside pressurised

Chapter 1: Introduction & Background

continuous flow reactors is impossible besides highly complex synchrotron radiation techniques. The experimental results were confirmed by the CFD simulations. They suggested that the Reynolds numbers (Re) for both reactant inlet streams were extremely low, 148 for the ScW and 20 for the metal salt, and therefore highly laminar in nature. However, despite the observed Reynolds numbers indicating laminar flow, highly turbulent macro-mixing was actually observed when the two fluids met. Since the Reynolds numbers were low, this macro-mixing could not be due to turbulent flows. It was found however that the significantly different fluid densities of the pseudo-supercritical water stream and the pseudo-metal salt stream produced strong buoyancy forces and turbulent mixing when the two fluids met. Whilst the turbulent macro-mixing is favourable for nanomaterials synthesis in terms of the rapid heating and mixing of the reagent streams, the investigation showed that the T-piece mixer was not the most appropriate of environments for this unusual fluid behaviour, or rather, that it did not make the most benefit of the unique fluid phenomena observed. The T-piece mixer did not provide uniform mixing and suffered from undesirable premixing of the two streams. Blockages could be attributed to a) inlet mixing, whereby the density differences of the two fluids causes mixing within the inlet streams of the two fluids, causing crystallisation of material before reaching the reaction point, b) stagnant zones, non-uniform mixing may cause stagnant zones where material becomes isolated from the net flow, potentially leading to growth of material and build-up of material, and c) flow partitioning, whereby the two flows effectively split into two distinct zones with minimal mixing due to the different densities (Blood, Denyer et al. 2004). These effects can be observed in Figure 1.6.

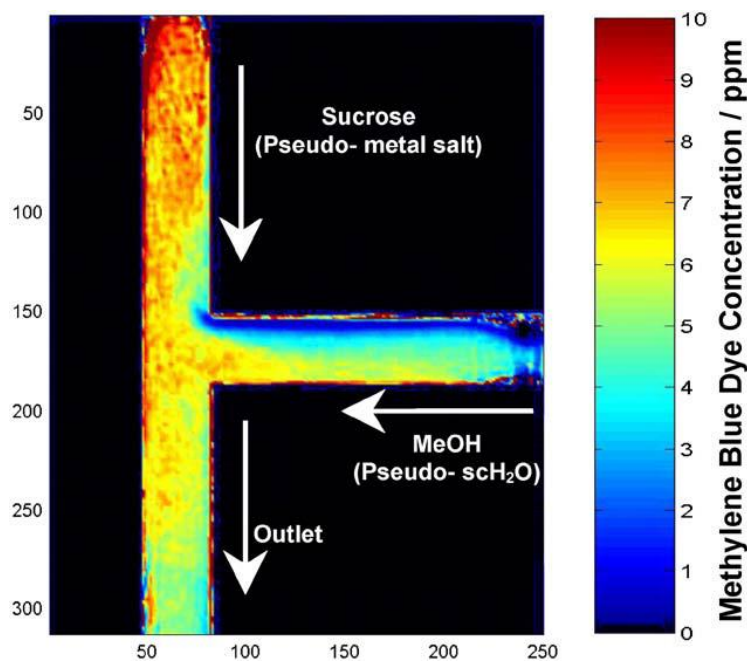


Figure 1.6: Steady state concentration map from the pseudofluid models showing the mixing regime in a T-piece mixer acting as a pseudoreactor (Blood, Denyer et al. 2004).

Since it was identified that the controlling factor within the reactor was the density difference between the two fluids, that impacted not only the mixing point of the two fluids but how the fluids behaved from inlet stream through the mixing point and into the outlet of the reactor, it was clear that exploiting this density difference was the key to achieving exceptional mixing of the two fluids and providing an ideal environment in which to produce nanoparticles in a reliable, reproducible and controllable way free from blockages.

Through these studies, design criteria were identified for an ideal scWHS reactor. The reactor must provide:

- Instant, uniform and complete mixing of the reagent streams to yield a high number of small nuclei, thereby decreasing particle size.

Chapter 1: Introduction & Background

- Short average residence times and narrow residence time distributions in order to prevent growth and maintain small size and narrow size distributions, respectively.
- Minimal heating of the precursor stream prior to mixing to avoid premature nucleation, unwanted reactions, and blockage of the tubing prior to the reactor.
- Immediate and rapid heating of the metal salt solution upon contact with the superheated fluid to induce supersaturation combined with the instant, uniform and complete mixing.
- Strong downstream flow to prevent particle settling and accumulation within the reactor.

The application of these criteria led to the development of the pipe-in-pipe counter-current mixing reactor now used in the laboratory scale synthesis in Nottingham (Lester, Blood et al. 2006) and in this PhD project. A supercritical water stream is achieved by pumping water through a preheater unit before passing downwards through a central inner tube to a mixing point where it meets a room temperature reagent stream flowing upwards in an outer-tube and counter-current to the heated water stream, demonstrated in Figure 1.7. This vertical tube-in-tube arrangement exploits the lower density of the supercritical stream by promoting rapid and symmetrical mixing followed by immediate passage upwards of the product stream out of the reaction point and into the cooling system, while the physical arrangement prevents undesirable mixing or heating of the reagent stream that could lead to blockages. A schematic of this reactor and pseudo-fluid modelling highlighting the efficient mixing dynamics are shown in Figure 1.8. The laboratory scale reactor and pilot system

Chapter 1: Introduction & Background

geometries, scaled by 30 times from the laboratory scale, together with materials synthesised in recent years, are described in Section 1.4.3.

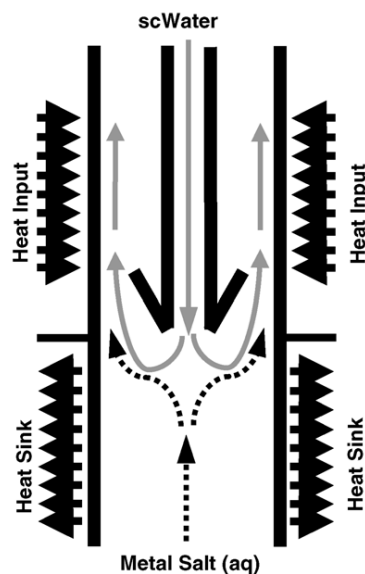


Figure 1.7: The patented pipe-in-pipe counter-current continuous hydrothermal and solvothermal reactor designed at The University of Nottingham.

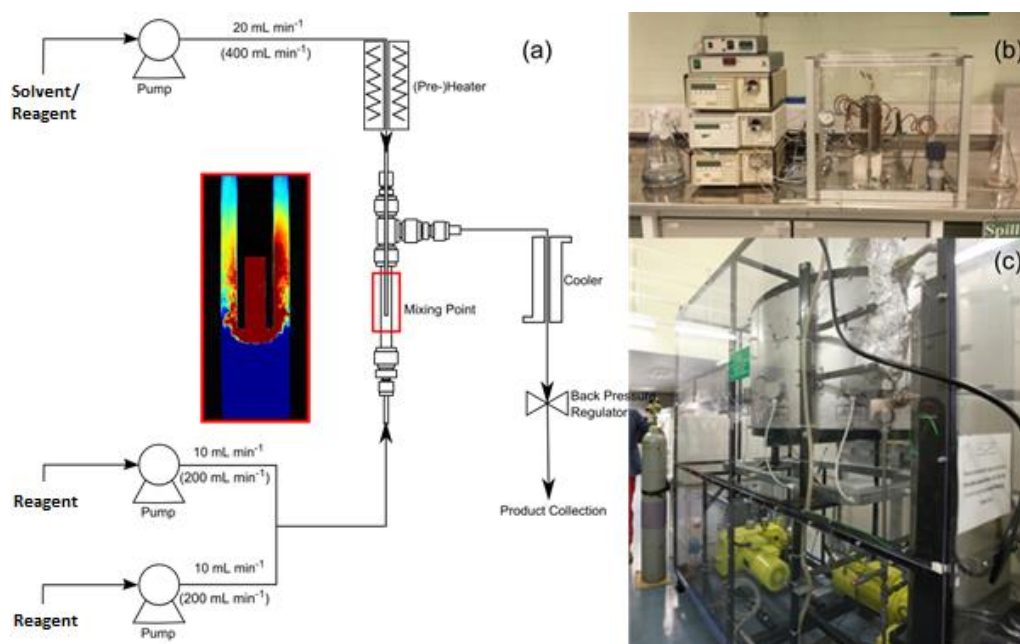


Figure 1.8: The Nottingham counter-current reactor schematic with inset showing the mixing dynamics (a), and the actual system at laboratory scale (b), and pilot scale (c).

Chapter 1: Introduction & Background

Since the developmental work away from T-piece mixers by Lester *et al.*, other groups have also presented reactor designs and have been producing nanomaterials. Prof. Jawwad Darr and his research group based at University College London have been actively involved in reactor design and nanoparticles synthesis in supercritical water by CFHS since 2007. Initially, they used the counter-current reactor set-up designed by Lester *et al.* shown in Figure 1.7. Darr *et al.* later developed a high throughput system for producing metal oxides, named the High-throughput Continuous Hydrothermal (HitCH) synthesis system. At lab scale with total flow rates up to 40 ml/min, the research group demonstrated the production of 66 $Ce_xZr_yY_zO_{2-\delta}$ samples in a short time frame (~12 hours). This was combined with high throughput X-ray diffraction using the beamline at I11 Diamond Light Source in Oxford to obtain rapid characterisation (Weng, Cockcroft *et al.* 2009). Furthermore, the group have automated the process; using a robot, the system produced, cleaned and printed samples of nanoparticles. Named RAMSI (Rapid Automated Materials Synthesis Instrument), the equipment was used to produce europium-doped yttrium oxide, $Y_2O_3:Eu^{3+}$ phosphors. Currently, only this material has been reportedly synthesised using RAMSI, with focus remaining on the production of material via the conventional continuous flow route.

In 2013, Gruar, Tighe and Darr published a paper, based on observing jetting effects in the counter-current design (Tighe, Gruar *et al.* 2012), presenting a new patented reactor configuration named the confined jet reactor/mixer (CJM) (Gruar, Tighe *et al.* 2013) for the production of nanomaterials. Their argument was that in a counter-current reactor, when the flow of supercritical water is greater than the flow of metal salt, a ‘jetting’ of the supercritical water

Chapter 1: Introduction & Background

penetrating far down into the metal salt flow occurs, causing an initial increase in temperature in the most penetrated region, with subsequent gradual heating as the two fluids mix further and travel upwards towards the reaction point and towards the outlet of the mixer. They argue that this limits the scale up potential of the process and could lead to poor control of products. As opposed to using the counter-current arrangement designed by Lester *et al.*, this new arrangement essentially turned the reactor piece upside down and had the two fluids (supercritical water and metal salt solution) flowing in the same direction, shown in Figure 1.9. The authors argue that this arrangement causes more instantaneous heating and mixing of the metal salt solution upon contact with the supercritical water. The CJM has been scaled up from laboratory scale (total flow rates up to 40 ml/min to produce 1-10 g/h) to pilot scale (total flow rates up to 800 ml/min, >1 kg/h) (which equates to a 400x increase in scale in terms of particle production) (Gruar *et al.*, 2013, Tighe *et al.*, 2013).

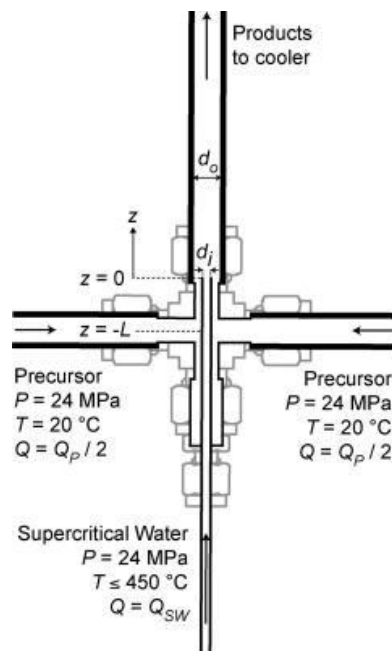


Figure 1.9: Diagram demonstrating the orientation of the co-current Confined Jet Reactor designed by Darr *et al.* at UCL (Gruar, Tighe *et al.* 2013).

Chapter 1: Introduction & Background

Prof. Jaehoon Kim, previously of the Korea Institute of Science and Technology (KIST) and now at Sungkyunkwan University (SKKU), Suwon, South Korea, and Prof. Youn-Woo Lee of Seoul National University (SNU), have together worked on CFHS reactors and reaction media. After also identifying the common problems associated with typical continuous flow reactors working with supercritical water, rather than optimise reactor design only, they opted to investigate alternative solvents such as supercritical alcohols. In many examples, they synthesise nanoparticles in supercritical methanol, crediting the ability of methanol to act as a surface modifier in addition to being compatible with many other surface modifiers to prevent particle growth and agglomeration which can lead to blockages in traditional CFHS, thus providing an alternative method for nanomaterial synthesis that alleviates the typical problems with T-piece mixers. The reactor used for the early work emulates traditional continuous flow reactors using a T-piece mixing point, and is shown in Figure 1.10. The preheated water or methanol enters the T-piece through the top arm and meets the room temperature metal salt solution that enters through the side arm. The mixed feeds then flow into a cylindrical reactor vessel, with internal volume of 14.58 cm^3 , which holds the reaction solution at elevated temperature, increasing the residence time of the reaction to allow for particle growth or for improved conversion to products.

From 2011-2013, S. A Hong and Prof. Kim presented research into the synthesis of lithium iron phosphate nanoparticles in supercritical water using continuous flow (Hong, Kim et al. 2011, Hong, Kim et al. 2012, Hong, Kim et al. 2013). This will be discussed in detail in Chapter 5. However, this work also led to the development and presentation of a number of different reactor

Chapter 1: Introduction & Background

geometries and mixing regimes and investigated the mixing patterns inside T-piece reactors with three different geometries (Hong, Kim et al. 2013). T-piece mixers with the incoming flows at 90°, 50° and a swirling effect tee mixer were studied and how these geometries affected the properties of synthesised LiFePO₄ particles; the three different T-piece geometries are shown from the Computational Fluid Dynamics (CFD) images in Figure 1.11. The 90° Tee is an off-the-shelf part from Swagelok, whilst the 50° and swirling tees are both custom made by the research group. The study also examined the effect of different temperatures, flow rates and concentrations on the structure and properties of the product; however, based on mixing regime alone, the results indicated that the swirling tee mixer provided the most ideal conditions for LiFePO₄ synthesis. Use of the swirling tee at high flow rates resulted in smaller-sized particles, beneficial for lithium ion transfer kinetics, which displayed higher discharge capacities upon battery cycling. When the flow rate decreased, particle size increased. Even though similarly sized particles in the range 400–900 nm were produced using the three mixing tees at the low flow rate, a smaller amount of impurities was present in the particles produced by the swirling tee when compared with those from the 90° and 50° tees, attributed to more efficient and complete mixing of the reagent streams with the supercritical water. As a result, a higher discharge capacity was observed with samples produced with the swirling tee.

This research demonstrated the effect the mixing regime between metal salt precursor and supercritical water can have on the chemistry invoked and the mechanism of formation of materials, and how this can lead to products with varying characteristics in terms of purity, composition, crystallinity, size and

Chapter 1: Introduction & Background

size distribution, and how this translates into their performance in application based testing.

It is therefore vital if one is to tailor or control a reaction to have a thorough understanding of all aspects of a reaction set-up, from understanding the behaviour of the chosen solvent, to implications of reactor design and geometry on the mixing and heating and flow of reagent and solvent streams, in addition to the chemistry this will induce and the products that are likely to form.

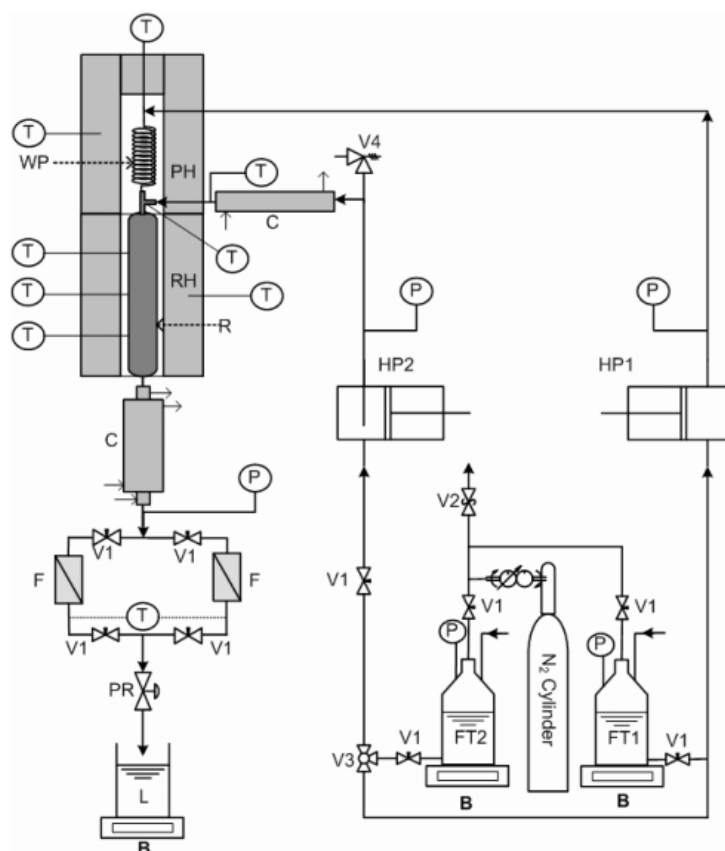


Figure 1.10: A schematic diagram of the continuous flow reactor system used by Kim *et al.* for the synthesis of metal oxide nanoparticles in supercritical water or methanol. R: supercritical reactor; RH: reactor heater; (Kim, Park *et al.* 2008).

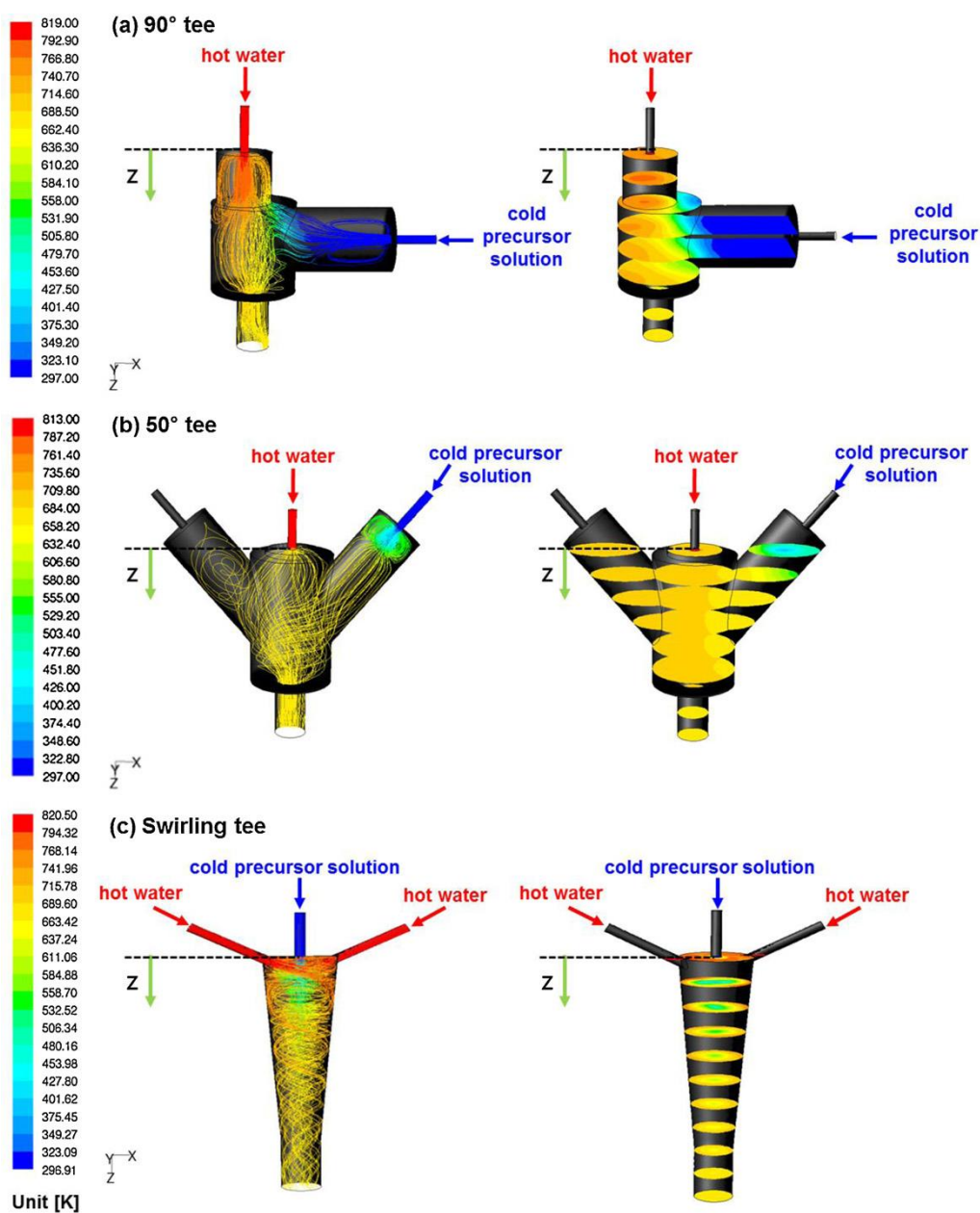


Figure 1.11: CFD simulations of the three tee reactors (90°, 50° and swirling tee) investigated at the Korea Institute of Science and Technology for the synthesis of LiFePO_4 nanoparticles (Hong, Kim et al. 2013).

Chapter 1: Introduction & Background

1.4.2. Nanomaterials Produced by CFHS

In the first work (Adschiri, Kanazawa et al. 1992), Adschiri *et al.* used metal nitrates, sulphates and chlorides with supercritical water as both solvent and reagent to produce the corresponding metal oxides, including AlOOH, Fe₂O₃, Fe₃O₄, Co₃O₄, NiO, ZrO₂ and TiO₂. Flow rates of the metal salt solutions were between 3-5 mL/min at 0.001 - 0.1 M, and hence, throughput of nanomaterial (dry product after isolation and drying steps) was between 0.1 – 10 g/h depending on material and reaction parameters. This breakthrough work demonstrated the potential of supercritical water and continuous flow reactors to produce a variety of ultrafine or nanoparticulate and highly crystalline nanomaterial. Later work demonstrated further material production, including BaTiO₃ (Atashfaraz, Shariaty-Niassar et al. 2007), ZnO (Ohara, Mousavand et al. 2008), MgFe₂O₄ (Sasaki, Ohara et al. 2010) ITO (indium tin oxide) (Lu, Minami et al. 2013) and CoAl₂O₄ (Lu, Minami et al. 2013).

Using the initial reactor design emulating the Nottingham reactor, Darr *et al.* synthesised Co₃O₄, NiO and mixed Ni-Co systems (Boldrin, Hebb et al. 2007), magnesium substituted hydroxyapatite (Chaudhry, Goodall et al. 2008), doped ceria-zirconia solid solutions (Weng, Perston et al. 2009), TiO₂ (Zhang, Brown et al. 2009), bismuth molybdates (Gruar, Tighe et al. 2010), Zn-Ce oxides (Kellici, Gong et al. 2010), sodium titanate nanosheets (Zhang, Goodall et al. 2010), In₂O₃ (Elouali, Bloor et al. 2011) and Eu:Y₂O₃ (Gruar, Tighe et al. 2012). Using the later confined jet reactor the group have been successful in producing a range of materials at both lab and pilot scales, including Fe₃O₄ (Lübke, Makwana et al. 2015), ZnO and In₂O₃ (Naik, Gruar et al. 2015), VO₂

Chapter 1: Introduction & Background

(Powell, Marchand et al. 2015), Co_3O_4 (Denis, Tighe et al. 2015), TiO_2 and Sn-doped TiO_2 (Lübke, Johnson et al. 2015, Makwana, Tighe et al. 2016) and LiFePO_4/C and V-doped LiFePO_4/C (Johnson, Lübke et al. 2016).

In addition to LiFePO_4 , Kim *et al.* have also used alcohols to synthesise CeO_2 (Kim, Park et al. 2008), LiCoO_2 in water (Shin, Koo et al. 2009), ZnO (Veriansyah, Kim et al. 2010) and the metal nanoparticles Ni, Cu and Ag (Choi, Veriansyah et al. 2010).

1.4.3. The Nottingham Counter-Current Reactor

The counter-current reactor used in this work (Figure 1.8) is comprised of a preheater section which feeds supercritical water downwards through an inner tube into a vertically aligned outer tube through which room temperature reagent streams flow. The supercritical water and reagent streams mix thoroughly at the outlet of the inner tube before immediately passing through a heat exchanger to cool down. The product stream exits through a back pressure regulator which maintains pressure within the system. Both the bench- and pilot-scale reactors are constructed from stainless steel 316 Swagelok[®] components. The mixing point of the bench-scale system employs an outer tube of 3/8" diameter, with a wall thickness of 0.065", and an inner tube of 1/8" diameter at the mixing point. The heater consists of 6 m of 1/8" tubing coiled around an aluminium cylinder heated by Watlow[®] cartridge heaters. The water and reagent streams are delivered into the high pressure system via Gilson[®] 305 HPLC pumps. Pressure is maintained using a Pressuretech[®] manual back pressure regulator.

Chapter 1: Introduction & Background

The pilot-scale system operates on the same principle. The reactor section uses a 1 ½” outer tube (wall thickness ¼”) and an inner tube of ½” diameter with a wall thickness of 0.083”. The heater in this case is a custom built Watlow® system with an output of 9×4.3 kW. The water and reagent streams are pumped by Milton Roy® Milroyal B and Cat Pumps® model 5CP pumps capable of pumping at a flow-rate of 500 mL min^{-1} and a pressure of 24 MPa. Pressure in the pilot-scale reactor is maintained with an automatic Tescom® BPR.

As mentioned the scWHS method was initially developed for the production of fine metal oxide nanoparticles and much of the work in the field has remained focussed on these materials. Since the development of the continuous flow counter-current system, various nanomaterials have been successfully developed within Promethean Particles (a spin out company in Nottingham based around the reactor technology) and within the Lester group at The University of Nottingham (Dunne, Munn et al. 2015). Metal oxide materials developed include yttrium aluminium garnet (Cabanas, Li et al. 2007), Eu:ZrO_2 (Hobbs, Briddon et al. 2009), Co_3O_4 (Lester, Aksomaityte et al. 2012), BaTiO_3 (Dunne, Starkey et al. 2016) and doped TiO_2 (Dunne, Starkey et al.). The group have expanded the technology out to other classes of materials, with Gimeno-Fabra and Munn *et al.* producing metal organic frameworks (Gimeno-Fabra, Munn et al. 2012, Munn, Dunne et al. 2015), Aksomaityte producing silver nanoparticles (Aksomaityte, Poliakoff et al. 2013), Lester and Tang producing hydroxyapatite, an artificial bone substitute based around a phosphate (Lester, Tang et al. 2013), layered double hydroxides (Wang, Tang et al. 2013), and

Chapter 1: Introduction & Background

Dunne, Starkey and Munn producing metal sulphide materials (Dunne, Starkey et al. 2014, Dunne, Munn et al. 2015).

1.4.4. The SHYMAN Project

The SHYMAN Project started in May 2012 with funding from the European Union Seventh Framework Programme for a four year project based around the Sustainable Hydrothermal Manufacturing of Nanomaterials. The project is an inter-disciplinary venture between 18 industrial and academic partners, based around the production and application of materials synthesised via CFHS and scale-up of the process, but also encompassing an array of issues associated with CFHS manufacture, with a number of key objectives:

- The design, build, commission and utilisation of a full-scale nanomaterial production facility, capable of producing nanomaterial at ~2000 T per year scale within industrially and commercially viable limits and parameters. At the time of designing, a Korean company, Hanwha Chemical Corp., already had a facility producing LiFePO_4 at > 200 T/year, which would have made the SHYMAN facility the world's largest capacity facility for CFHS. However, Hanwha recently announced plans for a 30,000 T/year facility, only to scrap these plans and temporarily close down their existing facility citing issues selling the product due to patent regulations in China. With this development, the SHYMAN facility will therefore become not only the world's largest, but the only facility for the continuous flow hydrothermal and solvothermal production of nanomaterials
- Reactor modelling and optimisation through experiment, CFD and pseudo-fluid modelling, to assess reactor geometries, flow rates and scale-effects

Chapter 1: Introduction & Background

- Life cycle assessment analysis to determine the energy costs of the process compared to other existing nanomaterial synthesis technologies, encompassing chemical factors such as the effect of precursor type, concentration, flow, and process factors, such as waste disposal and heat and precursor recycling
- The production of materials which have not been previously accessed by CFHS or the Nottingham counter current reactor – taking either existing batch reactions or materials traditionally produced and confined to batch production and translating them for the first time into a continuous manner, or improving existing continuous flow routes to materials. The aim is to expand the library of materials accessible via this synthetic route by exploiting innovative chemical pathways and reactor configurations and forms the basis of this PhD project.

1.5. Target Materials of this PhD Project

A number of key target materials have been identified based on previous work in the field of continuous-flow hydrothermal synthesis, developments made in earlier University of Nottingham work, and anticipation of industrial and technological trends, to focus on in this PhD project. Among these target materials are metal oxides, building on the original remit of the continuous-flow hydrothermal technology, metal sulphides, expanding the technology out into a new class of materials never before accessed by continuous-flow hydrothermal methods, and lithium iron phosphate, anticipated to be the next generation battery material. The targets are listed below:

Chapter 1: Introduction & Background

- Transition metal doped titania: proven performance as a photocatalyst in fields such as self-cleaning glass, water treatment and antibacterial coatings
- Barium titanate and barium strontium titanate: widely used ceramics for electronic applications with emerging potential in high density data storage
- Zinc, cadmium and lead sulphide: the quintessential quantum dot materials with applications in LEDs, biomedical imaging and photovoltaic devices
- Copper, iron and bismuth sulphides – expanding to a ‘general’ route for metal sulphide nanoparticle synthesis
- Molybdenum sulphide: exceptionally stable high temperature lubricant which also serves as a catalyst in the oil industry and is being investigated for use as a battery anode material - topical and future trend material
- Lithium iron phosphate: generally accepted as the next generation cathode material for the development of cheaper, safer and longer lasting batteries, with applications in electronics such as power tools and long-life laptops, and electric vehicles such as e-bikes, busses and short range cars

Subsequent chapters in this thesis will deal with each of these materials in turn. In many of these cases the standard Nottingham reactor was insufficient to generate the desired materials and modifications were made. These changes to reactor design will be highlighted where necessary.

The objectives, goals and criteria for success for this thesis and PhD project are now defined in Section 1.6.

1.6. Aims of this PhD Project

It has been explained in this chapter the unique and exciting properties nanomaterials possess that are already making them applicable and beneficial to numerous advanced technologies and that they hold a major key to success of developments in technologies in the future. It is also clear that to meet this rise in popularity and interest, development of sustainable and industrially and commercially viable synthesis techniques for the production of the nanomaterials is paramount to the widespread utilisation of nanomaterials. Continuous flow hydrothermal and solvothermal synthesis has the opportunity to become one of these enabling technologies, if it can demonstrate that it can successfully produce an array of materials within numerous materials classes of industrial importance and interest, whilst being economical, at scale. This PhD project concerns the synthesis of materials via this synthetic route, expanding early metal oxide work but venturing out into other classes of materials to expand the library of materials accessible via this synthetic route. All the materials chosen are either currently industrially applicable, or are forecast to be vital in emerging technologies. The materials have either been previously confined to batch-wise production by other researchers, thereby becoming the world's first continuous flow production of the material, or have been produced by continuous flow methods before, thereby providing innovative chemical and reactor configuration solutions to translate these reactions into an improved continuous manner. Any materials that are particularly industrially applicable and that lend themselves to industrial scale-up by their reaction characteristics

Chapter 1: Introduction & Background

will also be trialled at pilot scale with further scale-up and commercial production after this PhD project is completed in mind.

The subsequent chapters will now address three materials classes in turn; metal oxides, metal sulphides and metal phosphates, and present the materials developed in each class. The materials presented in this thesis all have the Nottingham counter-current reactor and CFHS as a common theme, hence this has been introduced in detail in Chapter 1. Due to the differing nature of the materials presented in this thesis, individual, more specific introductions and experimental sections are provided in each relevant chapter and section. This is coupled with a presentation of the results, and discussion relevant to that specific material, class of materials, and what information this can provide to the Nottingham counter-current reactor and field of CFHS as a whole. As such, each chapter can be viewed as packets of work, with CFHS and the Nottingham reactor as central themes, with each chapter yielding information about the specific materials, but providing information, ideas and conclusions to the thesis topic as a whole.

2. Materials Characterisation Techniques

This chapter will introduce the main characterisation techniques used to identify, characterise and analyse the structural properties of the materials developed in Chapters 3, 4 and 5. For each technique, the main principles and operating considerations will be introduced, together with the most useful information which can be extracted from the technique in terms of characterisation of a sample. This chapter will mainly deal with the structural characterisation techniques used in this thesis, with specific descriptions of application testing techniques described in the relevant chapter.

2.1. X-Ray Diffraction (XRD)

X-Ray Diffraction provides information on the crystal structure, particle size and composition within a solid sample. X-rays of known wavelength, λ , are fired at the sample (Figure 2.1), which in this case is dry nanoparticulate powder, and these X-rays are scattered by the electrons of the atoms in the solid and ‘collected’ by a detector. Amorphous solids in which there is no long-range ordering of the atoms result in incoherent scattering; however crystalline solids, where the atoms are arranged in periodic units with long-range order, can result in constructive interference of the scattered X-rays. The periodic arrangement of matter within a crystalline solid allows a fundamental building block, the unit cell, to be defined as the smallest repeating unit which can represent the entire crystal structure. Miller planes can be defined on the basis of this unit cell as planes extending throughout the crystal. Due to the periodicity of the structure any given set of Miller planes will have identical

Chapter 2: Structural Characterisation Techniques

electron densities and a fixed spacing between planes. For constructive interference of scattered X-rays to occur Bragg's Law must be satisfied:

$$n\lambda = 2d\sin\theta$$

where: n is an integer (if n is a whole number then a scattered ray is detected by the detector),

λ is the wavelength of the X-rays,

d is the spacing between diffracting crystal planes of the material, and

θ is the incident angle of the X-ray to the sample.

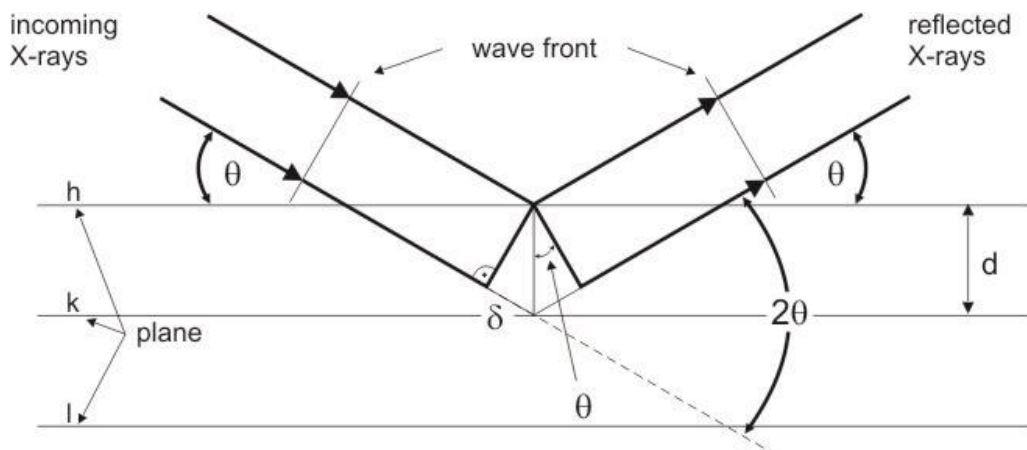


Figure 2.1: A schematic demonstrating the principles and key values associated with XRD. Image from http://physik2.uni-goettingen.de/research/2_hofs/methods/XRD

In the case of powder X-ray diffraction the sample volume exposed to X-rays contains a great number of particles in random orientations relative to the incident X-ray beam (ideally, assuming no preferred orientation effects). Thus all sets of Miller planes are exposed such that diffraction will occur from all sets of planes, i.e. all d -spacings. As diffraction only occurs when Bragg's Law is satisfied scanning across θ (and 2θ) permits the collection of diffracted X-rays corresponding to different d -spacings. The diffraction pattern obtained for

Chapter 2: Structural Characterisation Techniques

each crystalline solid is unique, since the placement and spacing of the atoms within a repeating crystal plane and lattice and the spacing between planes is specific to the material. This dictates that each crystal structure will give peaks of different intensity at different 2θ angles, thus a diffraction pattern can act as a 'fingerprint' for a given substance.

In addition to this fingerprinting powder diffraction patterns may also yield information on the size and shape of particles within the sample. An ideal crystal is, effectively an infinite repeating pattern of atoms in a specific arrangement. Impinging X-rays are only diffracted according to the Bragg equation and complete destructive interference occurs at any angles which do not precisely satisfy the equation. Thus an X-ray diffraction pattern from a perfect crystal would consist of infinitely sharp peaks at each Bragg angle. In reality there will always be some amount of peak broadening due to instrumental factors; however it is also the case that in reality few materials are perfectly crystalline. Nanomaterials in particular are typically so small in at least one dimension that there are, effectively, not enough Miller planes across the particle to cause complete destructive interference at angles near the Bragg angle. The lack of complete destructive interference results in further broadening of the diffraction peaks. The breadth of a diffraction peak can be related to the length of the crystal normal to the diffracting plane according to the Scherrer equation:

$$D = \frac{K \lambda}{\beta \cos\theta}$$

Chapter 2: Structural Characterisation Techniques

where D = crystallite size, K = the Scherrer constant (assuming spherical nanoparticles), λ = the wavelength of the X-rays used for analysis, β = the full-width of the peak at half the maximum value (FWHM), and θ = the Bragg angle.

The crystallite size thus calculated is the crystalline domain size (the region which is an ordered crystalline solid), and so may be different to actual overall particle size, due to amorphous content, agglomeration, or twinning, thus, this must be combined with additional techniques, such as transmission electron microscopy for a more accurate understanding of crystallite and particle size. X-ray diffraction can therefore aid in determining the composition, purity, crystallinity, phase and crystallite size of a material (or nanomaterial) product.

Powder X-ray diffraction patterns in this work were recorded using a Bruker D8-Advance diffractometer with Cu K_{α} radiation ($\lambda = 1.5418 \text{ \AA}$). A 2θ range of 5 to 70° was scanned with a step size of $0.04^{\circ} 2\theta$ and a collection time of 6 s/step. The patterns were assessed using the EVA software package, which enables comparison to known reference patterns. Additionally, crystallite diameters were calculated using the Scherrer equation from line broadening determined with the program Xfit (Cheary and Coelho 1996).

2.2. Scanning Electron Microscopy (SEM)

Once information has been yielded from XRD such that one can confirm the structural formation of the desired product from a reaction (in terms of composition, crystallinity, phase), further characterisation is informative, such as the assessment of particle size, morphology, size distribution, crystallite

Chapter 2: Structural Characterisation Techniques

nature and topography. This can be done by microscopy imaging. SEM (Figure 2.2) uses electrons to probe the surface of particles, generating a 3-dimensional image of particles within a sample. Typical optical microscopes use light to form an image, however, the use of electrons in SEM enables higher magnifications (100 – 100,000 times) due to the shorter wavelength of electrons than light, and a large depth of field, allowing the imaging of a large area of sample concurrently to assess homogeneity throughout the sample.

The electrons are generated by an electron gun, which become focussed by a series of apertures and lenses and travel down the apparatus to reach the sample and the beam is rastered across the surface. Upon reaching the sample, the electron beam interacts with the sample in numerous ways, generating secondary electrons and backscattered electrons, and both can be detected using the detectors in Figure 2.2. The two different types of electrons offer the opportunity to probe different characteristics of the sample. Secondary electrons are electrons expelled by the sample due to interaction of the sample with the electrons from the beam. These electrons are lower in energy than backscattered electrons and are generated from the surface of the particles. They can therefore be used to study the topography of materials and offer the greatest resolution for imaging. Backscattered electrons arise from electrons that penetrate deeper into the sample, and interact through collisions with the nuclei of the atoms within the sample. These collisions cause the electrons from the beam to be directly scattered back, with higher atomic number atoms (larger) causing more electrons to be scattered back. Thus the intensity of signal from higher atomic number atoms will be stronger, or brighter, generating a method of studying sample composition based on contrast.

Chapter 2: Structural Characterisation Techniques

The electron intensity from secondary or backscattered electrons is converted to a light intensity which forms an image which can be digitally viewed. Importantly, in contrast to TEM which will be explained shortly, SEM uses electrons which are either emitted from the surface of the sample, or primary beam electrons scattered back from the sample, to form an image.

Samples are dry powders that are placed onto sticky carbon tape supported on an aluminium stub. Only a small quantity (mg) of material is required for analysis. Prior to imaging, the sample can be coated with a metal such as gold or platinum, which improves the conductivity of the sample and improves the flow of electrons over the surface of the sample, improving the images that can be obtained. The sample stub is then placed into a holder within the sample chamber, and the system is evacuated to produce a vacuum.

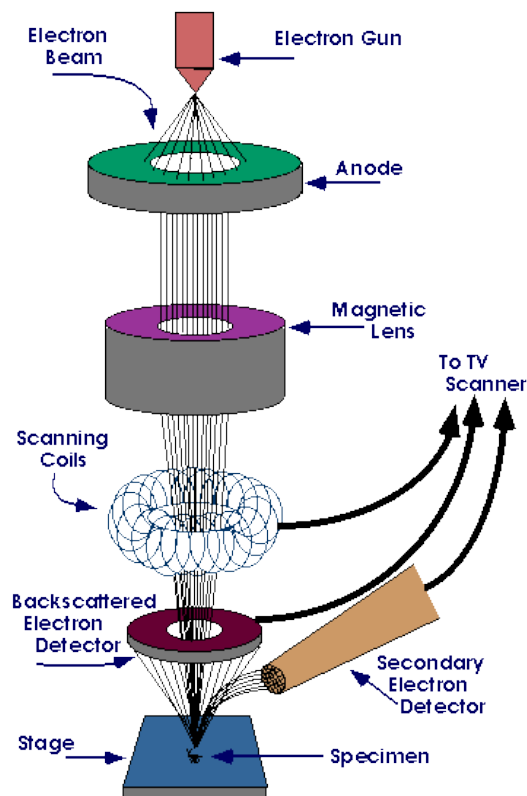


Figure 2.2: Diagram of a scanning electron microscope

Chapter 2: Structural Characterisation Techniques

The many features that can be investigated by SEM, coupled with the ease of sample preparation, rapid and reliable data acquisition, viewing and analysis, the high level of magnification and quality of imaging, and the non-destructive nature of the technique (samples are unchanged due to electron bombardment and can be imaged repeatedly), makes SEM a powerful tool. It has been utilised in this work for the characterisation of lithium iron phosphate, in terms of the particles size and size distribution, morphology, homogeneity, crystallinity and crystalline nature in Chapter 5. Scanning electron microscope images were obtained by depositing the powders onto a sticky carbon grid and coating the materials with platinum, and using a FEI/Philips XL30 FEG-ESEM at 20 kV.

2.3. Transmission Electron Microscopy (TEM)

As mentioned, SEM uses electrons which are scattered back from the sample. TEM (Figure 2.3) is another microscopy imaging technique that operates on the principle of the electrons passing through the sample material. The transmitted electrons generate a projection on a screen located underneath the sample, with differences in the image contrast arising from the density of the material that the electrons have passed through. Thus, a particle's size and morphology can be determined based on the contrast difference of the electrons that have passed through it, which generates an 'image' of the particles on the screen which can be digitally viewed. In addition to imaging the size and morphology of particles, the internal structure of materials may be probed, for instance hollow structures, due to the density differences this creates and therefore the corresponding contrast on the viewing screen.

Chapter 2: Structural Characterisation Techniques

The resolution of the SEM used in this work results in a lower size limitation of ~ 100 nm for clear imaging of particles. TEM, whereby the image is obtained by the focussed beam transmitted through the sample rather than rastered across the surface, benefits from increased magnification and (almost) atomic resolution, with particle sizes < 5 nm able to be imaged. Whilst TEM can provide detailed imaging of small nanoparticles, only a small section of sample can be imaged, and as such, may not be an accurate representation of the sample as a whole. It should therefore be used in conjunction with other characterisation techniques, to add to the information on a material and offer another perspective with which to compare results. For example, powder X-ray diffraction provides structural and size information relating to the average particle within the bulk sample, while TEM allows the characterisation of individual particles. Regardless, the strong magnification and resolution offered makes TEM a powerful imaging tool and characterisation technique.

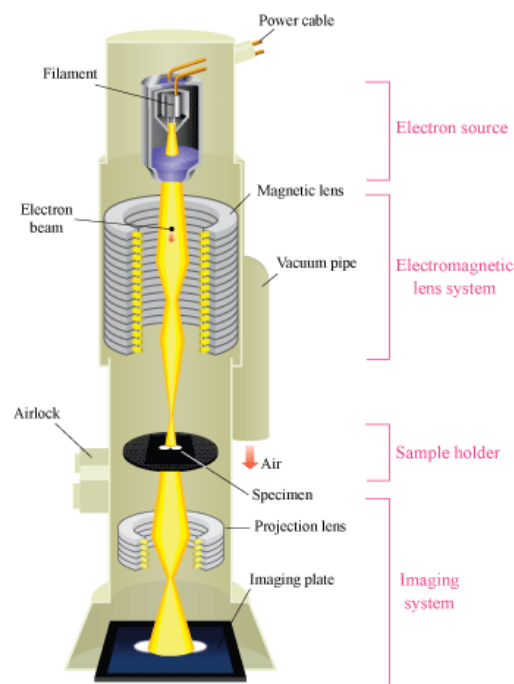


Figure 2.3: Diagram of a transmission electron microscope

Chapter 2: Structural Characterisation Techniques

In addition to its capacity for imaging, electron interaction with a sample during TEM (or SEM) analysis can also produce X-rays, and these X-rays can be detected and measured to identify constituent elements within a sample, in a process called Energy Dispersive X-Ray Spectroscopy. EDX can target one element specifically, demonstrating where throughout the scanned region (whether that is a single particle or a collection of particles/whole sample) an element is present.

Samples, or nanoparticles in this work, are typically suspended in acetone and sonicated to disperse the samples in the solvent. They are then deposited dropwise onto holey carbon films mounted on copper grids, before being left to air dry. This leaves nanoparticles deposited on the grids which are ready to be imaged. In this work, particularly in the characterisation of metal sulphides in Chapter 4, TEM images were recorded using a JEOL 2100F microscope operating at 200 keV equipped with a Gatan Orius camera. An Oxford Instruments INCA X-ray Microanalysis System was used to undertake EDX analysis of the doped titania samples in Chapter 3.

2.4. Inductively Coupled Plasma Mass Spectrometry (ICP-MS)

ICP-MS is principally used to determine elemental compositions of samples, in terms of identifying elements and assessing their relative occurrence within a sample – thus providing sample stoichiometry. It is used within this work in Chapter 3 to accurately determine the Ba:Sr:Ti ratio that exists within the barium strontium titanate nanocrystals. The technique combines an inductively coupled plasma with a mass spectrometer. Samples are digested in acid to

completely dissolve and separate all constituents and are then introduced to the system where they are nebulised to an aerosol. They are then introduced to the ICP torch, where the elements are desolvated and converted into gaseous atoms and then onto ions. These ions are separated by the mass spectrometer by their mass-to-charge ratio, which can determine the composition of the ions present and their relative concentration compared to the other ions present in the sample. This technique is vital in Chapter 3, since accurately determining the Ba:Sr:Ti ratio is pivotal in understanding how precursor preparation and the conditions within the counter-current reactor dictate the stoichiometry of the final products, which in itself is vital for the properties exploited in applications. Compositional analysis to assess the actual Ba:Sr:Ti ratio compared to the target ratio in this work was performed by ICP-MS using a ELAN DRC-e instrument (Perkin Elmer, Waltham, USA), in a ISO class 6 1000 clean room. Samples were digested by heating in closed PTFE vessels using concentrated HCl prior to measurement. These analyses were performed by Dr Liam Morrison in the Earth and Ocean Science Department at the National University of Ireland, Galway (NUIG).

2.5. Ultraviolet-Visible Light (UV-Vis) and Fluorescence Spectroscopy

UV-Vis Spectroscopy is an absorption spectroscopy technique which uses ultraviolet and visible light to promote electronic transitions from ground to excited states within the molecules of a sample. When the ultraviolet or visible wavelength light has energy matching the energy of an electronic transition within the sample molecules, absorbance occurs and the energy is used to

Chapter 2: Structural Characterisation Techniques

promote an electronic transition. A sweep of wavelengths of light from ultraviolet to visible is used to irradiate the sample, and an optical spectrometer records the wavelengths at which absorption occurs together with the intensity of absorption at each wavelength. A graph of absorbance vs. wavelength can therefore be constructed. Since the absorbance wavelengths correspond to the energy required for electronic transitions, the nature of the electronic transitions occurring within the molecule can be elucidated and this gives information about the structure and bonding of the sample being measured, making possible the determination of the functional groups present within a molecule. For instance, in Chapter 4, UV-Vis spectroscopy is used to determine the degree of oxygen substitution by sulphur, since $\text{MoO}_3\text{S}^{2-}$, $\text{MoO}_2\text{S}_2^{2-}$, MoOS_3^{2-} and MoS_4^{2-} all possess different bonding and electronic energy states, and therefore absorb light of different wavelengths across the UV-Vis range. Measuring a sample across the full UV-Vis wavelength range allows identification of the electronic transitions present, and can therefore be attributed to a specific compound, yielding information as to the reaction product that has been achieved. In addition to sample identification, characteristics such as the band gaps of semiconductor nanocrystals can be calculated. By irradiating nanoparticles that possess fixed energy levels due to quantum confinement, electronic transitions observed in the UV spectra can be ascribed to known energy levels, such as the band gap of the materials. By probing this energy with UV-Vis spectroscopy, the differences in band gaps of different materials (for instance, different transition metal doped titania's in Chapter 3) can be measured, since the utilisation of a wider wavelength of light can be an indicator as to how suited that material is to catalytic applications

Chapter 2: Structural Characterisation Techniques

compared to the other samples. UV-Visible spectroscopy spectra in this thesis were recorded with a Varian Cary 300 Bio UV-Vis system.

Fluorescence spectroscopy is related to UV-Vis, in that electronic transitions are measured, however this is an emission spectroscopy technique, since it measures the emitted energy upon electronic transitions from excited to ground state energy levels. In the fluorescence measurements undertaken in Chapter 4 of this thesis, metal sulphide particles are excited by UV radiation in the 250 to 400 nm wavelength range and absorb photons. The energy gained from this absorption causes excitation and causes an excited electronic state (as in UV-Vis). Electrons can move into vacant energy levels and the system wishes to return to its more stable ground state. A number of possible processes can occur to dissipate this energy, such as quenching, intersystem crossing and internal conversion. Energy is dissipated in these processes and upon return of the electron to the original energy level, a photon is emitted with lower energy than the initial irradiation. Since some form of 'work' has occurred, the emission photons are at lower energy and therefore longer wavelength than the excitation photons, meaning the photons are emitted in the visible wavelength range (400-700 nm), giving rise to the colours observed by quantum dot materials, in a process named fluorescence. The wavelength of the emitted photon can be used to assess the nature of the sample. In the fluorescence tests in Chapter 4, ZnS materials were investigated with a Flexstation II fluorimeter.

2.6. Infra-Red and Raman Spectroscopy

Infra-Red (IR) Spectroscopy is an absorption spectroscopy technique which uses infra-red radiation to probe the chemical environment of constituents

Chapter 2: Structural Characterisation Techniques

present within an absorbing sample, by nature of the characteristic absorption of light from bonds present within the molecules of a sample. In a covalent compound bonds between atoms vibrate at frequencies which are dependent upon the mass of the atoms, the strength of the bonds and their chemical environment. These vibrational frequencies typically lie within the infrared region of the electromagnetic spectrum. Molecules thus absorb specific frequencies of infrared light dependent upon their structure and bonding, and when the energy of the radiation matches the resonant frequency of a particular bond, absorption occurs and the bond or functional group resonates/vibrates. By scanning across a large range of frequencies and measuring absorbance at each a spectrum of absorbance at each wavelength can be obtained. This spectrum will contain absorption bands corresponding to all infrared active vibrations within the frequency range studied, and much like XRD this spectrum can act as a fingerprint, or may give a strong indication of the components and environment within an unknown sample based on known vibrational frequencies of common functional groups. Infrared spectra for the investigation of the carbonate species in Chapter 3 were recorded using a Bruker Tensor 27 FTIR ATR spectrometer at a resolution of 4 cm^{-1} .

Raman Spectroscopy can be described as similar to IR spectroscopy in that the technique offers identification of the functional groups and bonding within a material by the interaction of certain frequencies of light at the corresponding energy of the vibrational energy levels. In the case of Raman spectroscopy a sample is irradiated with a monochromatic laser beam typically in the visible range. The majority of light is scattered back without interaction with the sample, known as elastic scattering or Rayleigh scattering, and is therefore at

Chapter 2: Structural Characterisation Techniques

the same frequency as the source. However, a small portion undergoes the mentioned interaction with vibrational energy levels of the molecule, and is therefore shifted in energy from the laser frequency. Plotting the intensity of the shifted light against the frequency provides a Raman spectrum, where regions of intensity indicate interaction at that frequency, and can be attributed to a particular vibration. Through identifying the molecular vibrations within a sample the nature of the constituents and type of bonding present within molecules offers sample identification and characterisation. Raman spectroscopy has been used in this work in Chapter 3 to assess the cubic/tetragonal nature of the barium strontium titanate nanopowders. The cubic or tetragonal structures lead to different vibrational energy levels, and therefore, interaction with different frequencies of light. Therefore by analysing a range of frequencies, it can be determined whether the barium strontium titanate powders have the cubic or tetragonal structure. Raman spectra were collected by Dr Alan Ryder and Yannick Casamayou-Boucau in the School of Chemistry at NUIG using a Raman WORKSTATION™ Analyzer with PhAT imaging probe (Kaiser Optical Systems, Inc.).

2.7. Surface Area Analysis

The specific surface area of a sample can be accurately determined by the controlled physical adsorption of a non-reactive gas such as nitrogen onto all accessible surface of a sample. The sample to be analysed is thoroughly degassed and held under vacuum at low temperatures (77 K for nitrogen adsorption). Known quantities of gas are then introduced to the system and the pressure is allowed to equilibrate. When the inert gas is in contact with a

Chapter 2: Structural Characterisation Techniques

surface it will adsorb through weak interactions, forming first a monolayer, with subsequent dosing and adsorption building further layers by effectively condensing the gas within the pores of the solid. The quantity adsorbed can be calculated on the basis of the known quantities of gas added to the system and the measured pressure after adsorption and equilibration. With a known (or assumed) size or cross sectional area of the adsorbent gas molecule (typically dinitrogen) the surface area can thus be calculated on the basis of monolayer coverage. Information of pore size volume and shape can be attained by analysis of the adsorption up to saturation (all pores filled) and the subsequent desorption. The most widely used method to determine surface area is that of Brunauer-Emmett-Tellet (BET), while the Barrett-Joyner-Halenda (BJH) method provides information regarding pore size distribution.

3. Metal Oxide Nanoparticles

As discussed in Chapter 1, CFHS and the Nottingham counter-current reactor have typically produced metal oxide materials, using supercritical water as both reagent and anti-solvent to form and precipitate metal oxide nanoparticles. At the time of starting this PhD project, there existed interest within the group at Nottingham, in the wider field of CFHS and in industrial applications for the production of transition metal doped titania nanoparticles for an array of applications, and hence, it became a focus of study for this PhD project (Section 3.1). Synthesising the materials would offer insight into the ability of the reactor to produce truly doped nanoparticles, as opposed to mixtures of the respective metal oxides, an area of interest to demonstrate more fine control of particle composition than simply particle production. Concurrently, learning and understanding more about titania formation and the control of composition using different metal ions aided in the development of barium titanate and later barium strontium titanate nanopowders (Section 3.2), an industrially relevant material for electronic components and devices. The synthesis and characterisation of these materials, information learnt about the reactor and CFHS, and selected application testing and pilot scale trials, is presented in this chapter.

Work in this chapter has been adapted and expanded from two publications; one focussed on the doped titania nanocrystals and their photocatalytic activity and the other on the production of barium strontium titanate nanopowders at both laboratory and pilot scales. These can be found through the chapter footer.

3.1. Titania and Transition Metal Doped Titania

3.1.1. Introduction

Titanium dioxide (TiO_2) has been extensively studied for its photocatalytic properties (Fujishima, Zhang et al. 2008). The photoactivity of TiO_2 is one of its most attractive properties for technological applications (Diebold 2003). The formation of electron-hole pairs due to electronic transitions initiated by the absorption of photons from irradiation by light and the resulting chemical or electron transfer reactions between TiO_2 and absorbed molecules forms the basis behind TiO_2 application in photodevices across a range of industries and sectors, and is used in some well-developed applications, for example, in water splitting (Sato and White 1981), the photochemical degradation of organic and inorganic pollutants (Carp, Huisman et al. 2004, Gaya and Abdullah 2008) and self-cleaning surfaces (Parkin and Palgrave 2005), in addition to acting as semiconductor nanocrystals in photovoltaic devices (Bai, Mora-Seró et al. 2014). TiO_2 has received particular attention in remediation processes, such as wastewater treatment, through the photochemical oxidation and reduction and therefore degradation of organic and inorganic pollutants (Carp, Huisman et al. 2004, Gaya and Abdullah 2008).

The three commonly encountered polymorphs of titania are anatase, rutile and brookite, each consisting of TiO_6 octahedra but with different vertex-, edge- and face-sharing arrangements. Of these polymorphs, anatase (Figure 3.1) is widely accepted as the most active in photochemical processes (Luttrell, Halpegamage et al. 2014).

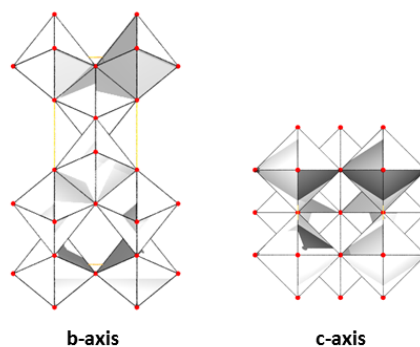


Figure 3.1: The structure of anatase viewed along the b- and c-axes.

The inherent activity of anatase may be further enhanced by various means. Synthesising titania at the nanoscale results in materials with very high surface areas, shorter path-lengths for electron/hole diffusion to the crystal surface, as well as offering the capacity to control the crystallite habit, and consequently higher activity (Ong, Tan et al. 2014). Controlling the crystallite habit can favour the resulting particle for preferential reactions. For example, Ohno et al. (Ohno, Sarukawa et al. 2002) showed differences in the deposition of Pt and PbO_2 onto anatase and rutile titania faces by the photocatalytic reduction and oxidation of different crystal faces, respectively. The photodeposition studies concluded that the rutile-(101) and anatase-(001) surfaces were most active for oxidation reactions while the rutile-(110) and anatase-(101) surfaces were most active for reduction reactions (Batzill 2011). Therefore, one can tailor crystal design to achieve a desired reactivity. A further strategy to improve the photocatalytic behaviour of anatase is the manipulation of its electronic properties through the incorporation of dopant ions. The substitution of Ti^{4+} for alternative metal ions, typically of the transition metals or f-block elements, has been shown to introduce sub-bands to the electronic structure of anatase with the overall effect of lowering the band-gap energy, and thus enhancing

Chapter 3: Metal Oxide Nanoparticles

photocatalytic efficiency (Devi, Kottam et al. 2010, Fonseca de Lima, Harunsani et al. 2015).

Due to the wide band-gap of TiO₂ at ~ 3-3.2 eV, it is only active under ultraviolet and near-ultraviolet irradiation, and so significant efforts are taken to modify the structure with dopants to effectively lower the band gap energy and increase the wavelength range of absorbance, to enable photocatalytic activity into the visible light range. For applications, absorbance across a wider range of wavelengths is generally favoured, and materials that can utilise visible light as opposed to being confined to UV irradiation have an advantage. Doping of titania with low levels ($\leq 5\%$) of cobalt or nickel, for example, has previously been shown to improve the photochemical properties and photocatalytic performance (Choi, Park et al. 2010, Khurana, Pandey et al. 2015). The incorporation of dopant ions may have the additional effect of disrupting the crystal structure inducing disorder which can also increase photocatalytic performance.

The increasing demand for clean catalysis to mitigate environmental damage, particularly by organic contaminants, puts titania based photocatalysts in high demand. Doped anatase nanoparticles have been produced by a wide variety of methods (Chen and Mao 2007), from simple co-precipitation, to sol-gel type routes (Colmenares, Aramendía et al. 2006, Devi, Kottam et al. 2010), to more involved microwave assisted (Esquivel, Nava et al. 2013) and hydrothermal and solvothermal methods (Castro, Nunes et al. 2009, Fonseca de Lima, Harunsani et al. 2015).

Chapter 3: Metal Oxide Nanoparticles

In this section pure anatase titania as well as 1% cobalt and 1% nickel doped anatase nanoparticles are produced and the materials are characterised to assess the nature of the doping of the TiO₂ nanoparticles. The band gap energy of the three materials is calculated and the particles have been assessed for their photocatalytic activity in the degradation of methylene blue.

3.1.2. Experimental

3.1.2.1. Synthesis

The synthesis of the anatase and doped anatase nanocrystals was performed as shown in Figure 3.2. A solution of titanium bis(ammonium lactato) dihydroxide (TiBALD) (50% in water) with appropriate amounts of metal nitrate salts (Co(NO₃)₂·6H₂O or Ni(NO₃)₂·6H₂O) such that the total metal concentration was 0.05 M was used as the metal precursor stream. A 0.2 M solution of KOH was used as a precipitating agent to ensure the incorporation of the dopant ions. These two solutions were mixed in flow using a T-piece mixer at flow rates of 10 mL min⁻¹ each, before meeting the supercritical water stream in the counter-current reactor which was flowing at 20 mL min⁻¹. The preheated supercritical water stream also contained ~1% H₂O₂ in order to minimise contamination from organic residues from the TiBALD precursor. The temperature of the preheater was set to 400 °C giving a post-mixing temperature of ~ 380 °C, the system pressure was maintained at 25 MPa using the back pressure regulator. Products were collected and washed by centrifugation before drying under air at 70 °C.

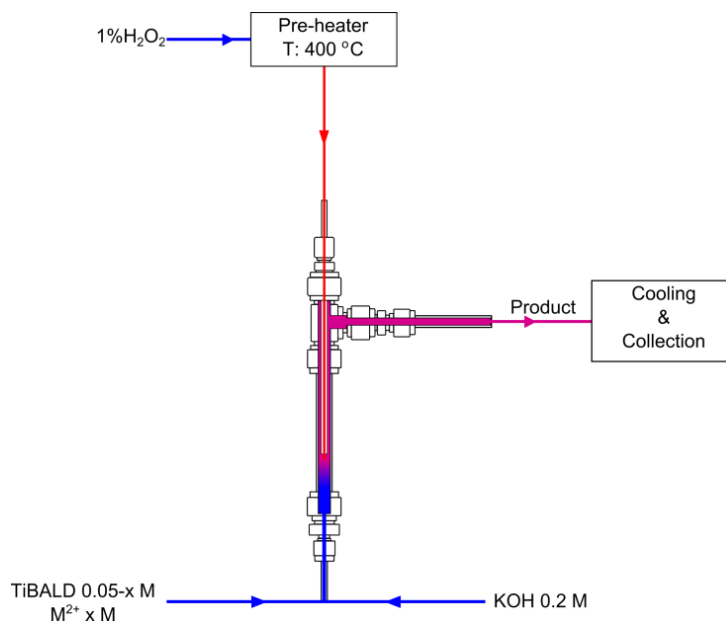


Figure 3.2: Reaction scheme for the production of transition metal doped anatase nanocrystals.

3.1.2.2. Characterisation

Powder X-ray diffraction (XRD) patterns of the products were collected on a Bruker D-8 Advance diffractometer using Cu K α radiation ($\lambda = 1.5418 \text{ \AA}$) over a 2θ range of $20 - 70^\circ$, with a step size of 0.04° at 4s/step. Transmission electron micrographs (TEM) and energy dispersive X-ray analysis (EDX) elemental maps were recorded using a JEOL 2100F microscope operating at 200 keV equipped with a Gatan Orius camera and an Oxford Instruments INCA X-ray Microanalysis System. Nitrogen adsorption isotherms and surface area analyses were performed with a Micromeritics Tristar II 3020 system at 77 K. Diffuse reflectance UV-Visible (UV-Vis) spectroscopy spectra were recorded with a Varian Cary 300 Bio UV-Vis system.

3.1.2.3. Photocatalytic Testing

To assess the catalytic nature of the titania nanomaterials, the photocatalytic activity was investigated in a custom made photoreactor. The degradation of methylene blue is a test recommended by the International Organisation for Standardisation as a measure of the photocatalytic activity of photoactive surfaces in an aqueous medium under artificial UV irradiation (ISO/CD10678). It is utilised here as a tool to assess the applicability of the titania materials synthesised via CFHS towards heterogeneous photocatalytic applications, with the dye acting as a pollutant in an aqueous system. The photoreactor (designed previously in the group) consisted of a 120 cm quartz tube of 1" inner diameter, which was loaded with 500 mL of a 10 ppm methylene blue solution and 0.5 g of the catalyst to be tested. This sample vessel was flanked by two 36 W UVA lamps, to provide the UV light necessary to promote photoactive processes such as electron-hole generation and therefore reactive species generation. Mixing and aeration of the nanoparticles and methylene blue dye (pollutant) were achieved by bubbling compressed air through an inlet at the bottom of the reactor tube at a rate of 0.5 L min⁻¹. After initial irradiation, samples were removed through an outlet port at 15 minute intervals. Solid catalyst was removed from these samples by centrifugation before measuring the absorbance by UV-Vis Spectroscopy at 665 nm (a strong absorbance wavelength of methylene blue), to track its relative concentration and therefore depletion over the course of the reaction. Care was taken to keep the sample in the dark during all manipulations to prevent further photocatalytic processes occurring.

3.1.3. Results & Discussion

3.1.3.1. Synthesis and Characterisation

3.1.3.1.1. X-Ray Diffraction

The powder X-ray diffraction patterns of the pure titania and 1% cobalt and 1% nickel doped samples are shown in Figure 3.3. It is clear from these patterns that only the anatase phase titania is produced as the patterns display peaks matching the expected anatase pattern, with no additional titania or dopant metal oxide phases observed. This is important since it was mentioned that anatase is the most photocatalytically active of the polymorphs of titania, in addition to demonstrating the preference in the counter-current reactor for doping of the titania structure with the transition metal ions as opposed to the formation of both metals metal oxide equivalents. The pattern of the pure anatase sample matches the expected peak positions well. It can also be seen that the inclusion of dopant metals in the reaction system results in the formation of smaller anatase nanocrystals, as evidenced by the increased breadth of the Bragg diffraction peaks.

The crystallite diameter of the pure anatase as calculated using the Scherrer equation is 15 nm, while both the cobalt and nickel doped samples show sizes of ~ 6 nm. The incorporation of the dopant ions into the anatase lattice is also supported by slight shifts in peak positions of the doped materials due to distortions in the anatase lattice structure arising from the substitution of the octahedrally coordinated Ti^{4+} for the larger M^{2+} ions. The a and c lattice parameters vary from $a = 3.794 \text{ \AA}$, $c = 9.525 \text{ \AA}$ for undoped titania, to $a = 3.811$

\AA , $c = 9.638 \text{ \AA}$ for Co-doped titania and $a = 3.778 \text{ \AA}$, $c = 9.407 \text{ \AA}$ for Ni-doped titania.

Whilst this suggests the inclusion of the dopant ions in the lattice it is not conclusive as anatase nanoparticles are known to exhibit a range of unit cell volumes as the crystal size decreases below 10 nm (Ahmad and Bhattacharya 2009). Therefore further characterisation was necessary to assess whether the titania nanoparticles had been fully and homogeneously doped.

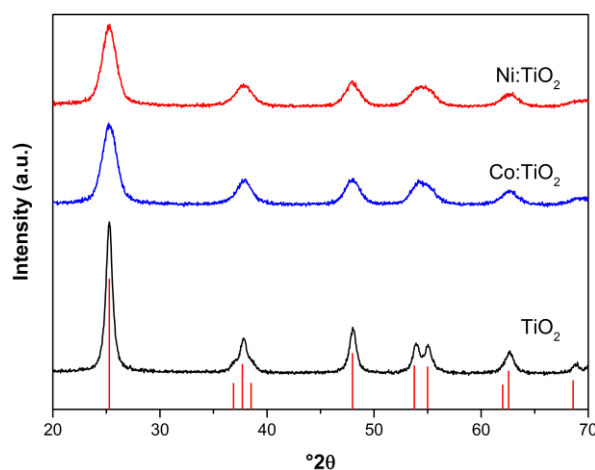


Figure 3.3: Powder X-ray diffraction patterns of the pure and doped anatase nanocrystals, with red lines indicating anatase TiO₂ peak positions.

3.1.3.1.2. TEM Imaging & EDX Analysis

Further support for the inclusion of the cobalt and nickel dopant ions in the crystal lattice of the anatase nanocrystals comes from TEM imaging and EDX elemental mapping, as shown in Figure 3.4. The EDX images (d) show that the dopants are evenly distributed across the sample, rather than in isolated regions or separated on particle surfaces. Ni for example can be identified as present throughout the entirety of the scanned region, indicating homogeneous doping. Not only does this show that nickel has been incorporated into the structure

Chapter 3: Metal Oxide Nanoparticles

throughout the whole sample, but it has done so evenly, since the density of the signal remains constant throughout the image. Additionally, the lattice parameters obtained from the HRTEM images are in close agreement to those obtained by XRD measurements. This is a strong indication that the produced materials are truly doped. The TEM images also demonstrate the small particle size of the three samples, clearly demonstrating the smaller particle size of the nickel and cobalt doped particles.

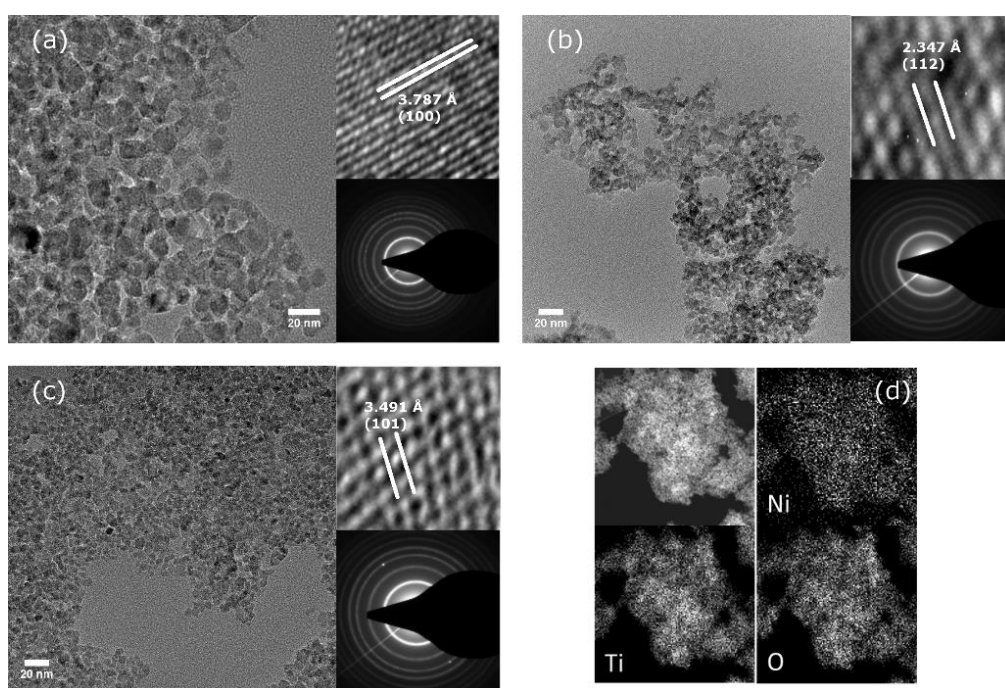


Figure 3.4: TEM images of undoped anatase (a), 1% cobalt doped anatase (b), 1% nickel doped anatase (c), and representative elemental mapping images of a nickel doped anatase sample showing the uniform distribution of the dopant ions (d). Insets show the corresponding HRTEM images and electron diffraction patterns.

3.1.3.1.3. Surface Area Analysis

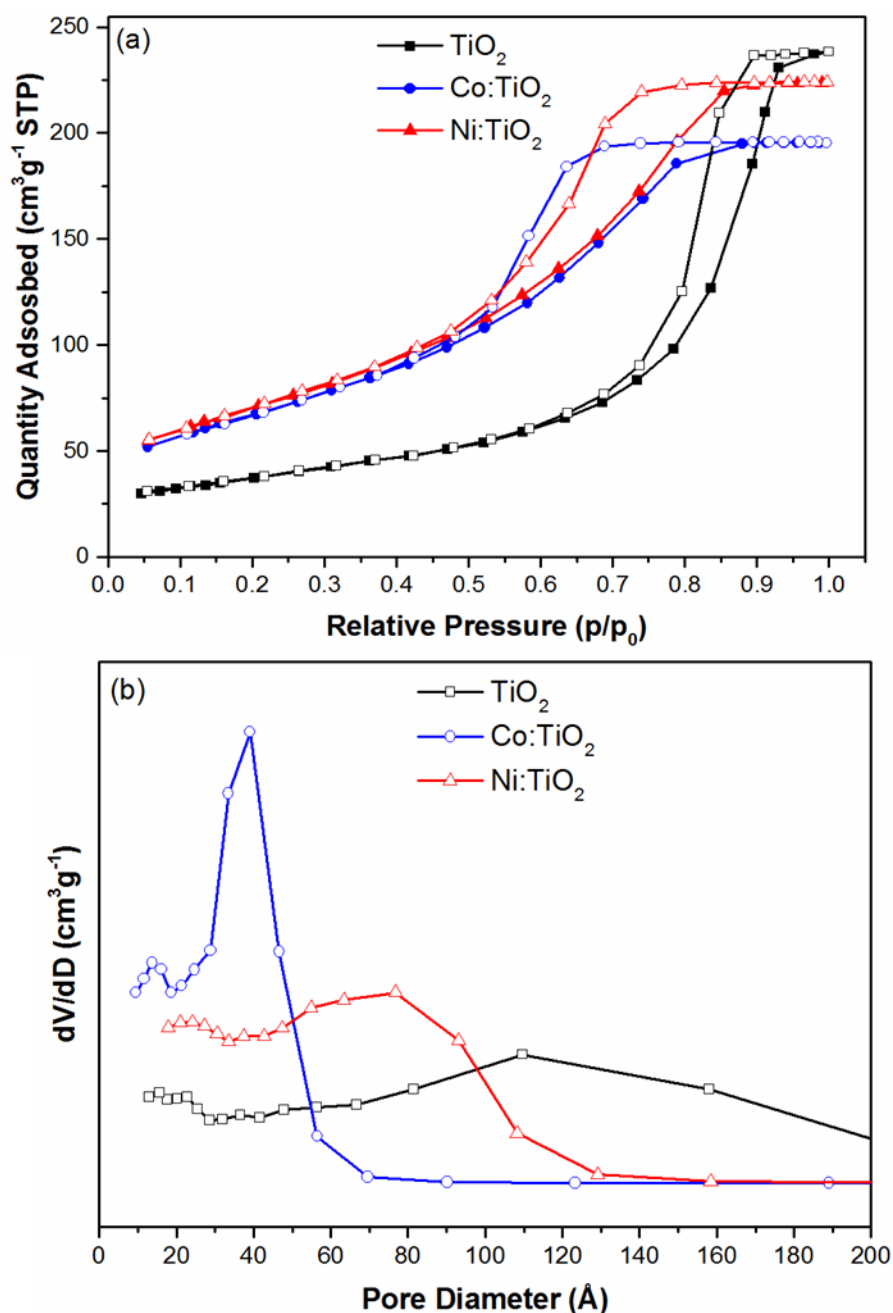


Figure 3.5: Nitrogen adsorption-desorption isotherms (a), and pore size distributions obtained by the BJH method (b) of the pure and doped anatase nanocrystals.

As mentioned in Chapter 1 the high surface area of nanoparticles due to their small size and high ratio of surface to core atoms leads to increased catalytic performance. To investigate the porosity and surface area of the pure and doped titania samples, the nitrogen adsorption-desorption isotherms and BET

surface areas of the three samples were measured and are shown in Figure 3.5. All three samples show typical Type IV isotherms with H2 type hysteresis loops indicative of mesoporous aggregates (Sing, Everett et al. 1985). The calculated BET surface area of the undoped anatase is $128 \text{ m}^2 \text{ g}^{-1}$ while the smaller doped nanoparticles both show surface areas of $\sim 230 - 250 \text{ m}^2 \text{ g}^{-1}$, consistent with the smaller particle sizes calculated from the XRD and observed by TEM. The pore size distributions of the samples were assessed by the BJH method (Barrett, Joyner et al. 1951). The larger undoped anatase nanoparticles exhibit a very broad pore size distribution centred around 11 nm. The cobalt doped anatase shows a relatively sharp distribution around a pore diameter of 4 nm, while the nickel doped sample lies between the two, with a relatively broad pore size distribution centred between 7 and 8 nm.

3.1.3.1.4. UV-Vis Spectroscopy & Tauc Plot

To assess the effect the dopant metal ions have on the absorbance and band gap of the three materials, and to therefore begin to assess their potential for photocatalytic applications, the diffuse reflectance UV-Vis spectra of the samples were measured and are shown in Figure 3.6 (a). The absorbance profile of the undoped titania is as expected, showing a sharp decrease in absorbance immediately below 400 nm, corresponding to the anatase band-edge, followed by a tail off in absorbance with increasing wavelength (Tang, Prasad et al. 1994). The 1% cobalt doped sample shows a similar profile to the undoped anatase at low wavelengths; however it also exhibits additional absorbances across the 400 nm to 700 nm range, due to the d-d electron transitions of the cobalt ions (Choudhury and Choudhury 2012). Similarly the

1% nickel doped sample shows gentler tail-off in absorbance up to 540 nm and an additional absorbance at 720 nm arising from the characteristic ${}^3A_{2g} \rightarrow {}^3T_{1g}$ transition of octahedrally coordinated Ni(II) (Rossman, Shannon et al. 1981, Cui, Wang et al. 2011). This shows that the two doped samples are capable of absorbing higher wavelength or lower energy radiation and undergoing electronic transitions across a wider wavelength range than the undoped titania.

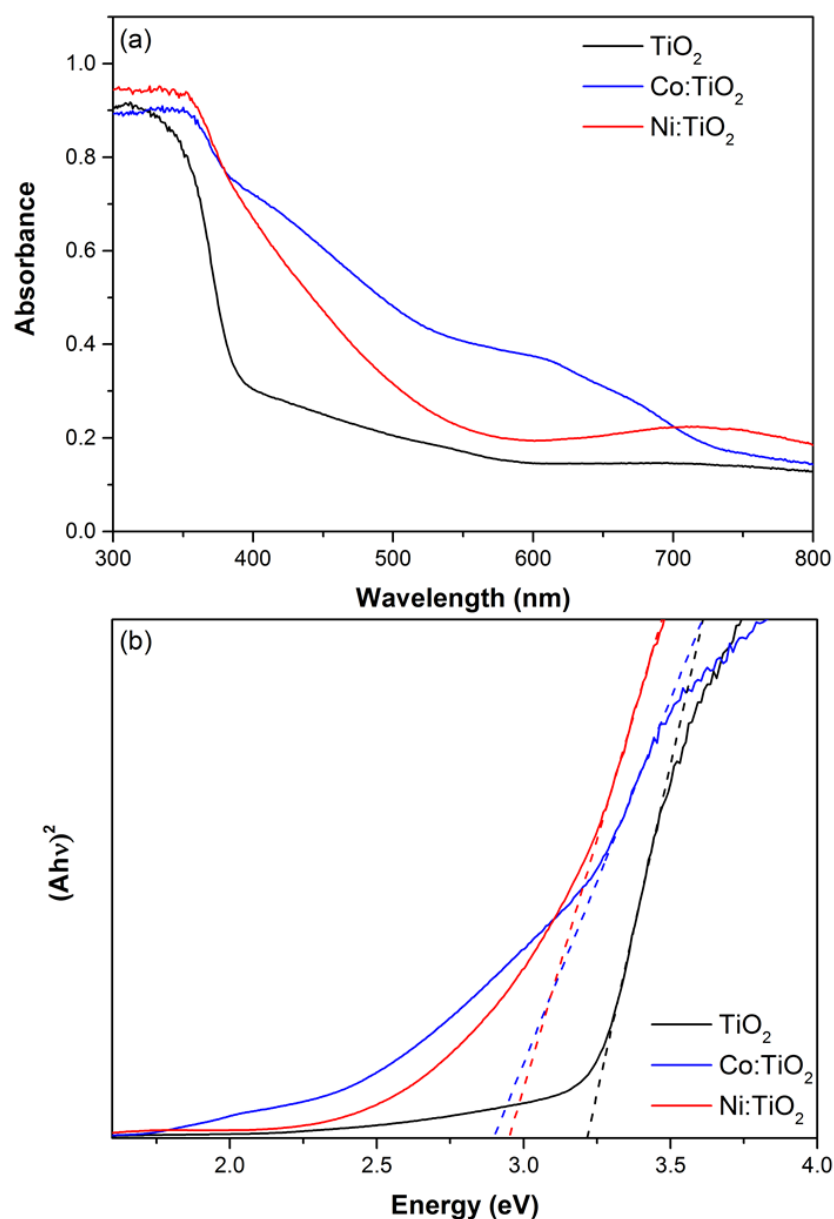


Figure 3.6: Diffuse reflectance UV-Vis spectra (a) and corresponding Tauc plot (b) of the TiO₂, 1% Co:TiO₂ and 1% Ni:TiO₂ photocatalyst nanoparticles.

Chapter 3: Metal Oxide Nanoparticles

Using the UV-Vis data the band-gaps of the materials were determined from a Tauc plot, as shown in Figure 3.6 (b). The Tauc relationship (Tauc 1968) is governed by the equation:

$$(\varepsilon h\nu) = C(h\nu - E_g)^n$$

where ε is the molar absorption coefficient, $h\nu$ describes the photon energy, C is a constant, E_g is the band gap, and $n = 1/2, 2, 3/2$ and 3 for direct allowed, indirect allowed, direct forbidden and indirect forbidden transitions, respectively.

The Tauc plot then comes from a linearisation of this equation:

$$(\varepsilon h\nu)^{1/n} = C^{\frac{1}{n}}(h\nu - E_g) = C'(h\nu - E_g)$$

Thus, we can plot $(\varepsilon h\nu)^{1/n}$ vs $h\nu$, and for one of the values of n there should be a linear range which can be extrapolated to the x-axis (photon energy), to give an energy for the onset of absorption, or more specifically the band gap energy of the material. ε , the absorption coefficient, from the Beer-Lambert Law, is related to the absorbance, by the equation $A = \varepsilon c l$, where c = concentration and l = path length of the radiation. Since the titania and doped titania samples were solid powders, c and l are fixed and constant, and thus, the measured absorbance, A , from the UV-Vis data is directly proportional to ε , the absorption coefficient. A can therefore be used in place of ε in the equation. Therefore, for the Tauc plot, we can plot $(Ah\nu)^2$ vs $h\nu$ to find the band gap of the materials.

Chapter 3: Metal Oxide Nanoparticles

Figure 3.6 (b) shows the undoped anatase nanocrystals possess the expected band-gap of 3.22 eV, while the cobalt and nickel samples have band-gaps of 2.89 eV and 2.95 eV, respectively. This is consistent with doping of the anatase lattice, since doping effectively leads to the alteration of the energy states by insertion of sub-bands of allowed energy states within the titania band structure, where bands previously did not exist, therefore leading to a reduced band-gap which requires lower energy to promote an electron into. A summary of all the physical properties of the pure and doped anatase nanocrystals discussed in Section 3.1.3.1 is given in Table 3.1.

Table 3.1: Summary of the physical properties of transition metal doped anatase nanocrystals

Sample	Size (nm)	Lattice parameter			Surface Area (m ² g ⁻¹)	Band Gap (eV)
		<i>a</i> (Å)	<i>c</i> (Å)	Volume (Å ³)		
TiO ₂	14.8	3.794	9.525	137.09	128	3.22
Co:TiO ₂	5.9	3.811	9.538	138.50	232	2.89
Ni:TiO ₂	6.2	3.778	9.407	134.25	246	2.95

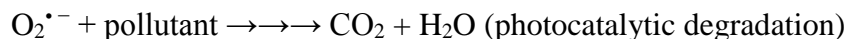
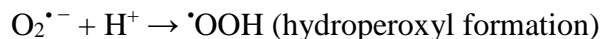
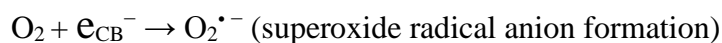
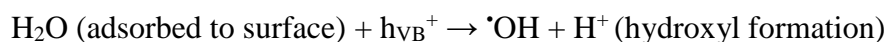
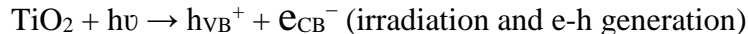
3.1.3.2. Photocatalytic Activity

3.1.3.2.1. Introduction

Upon irradiation by light that has energy greater than the band gap energy of the photoactive material, an electron is excited from the valence band of the energy levels to the conduction band, generating a negatively charged electron in the conduction band, and a positively charged hole in the valence band. The promoted electron and hole can recombine immediately, effectively returning to the original ground state without undergoing further reaction. This is an extremely facile and rapid process that almost 90% of electron-hole pairs undergo (Serpone, Lawless et al. 1995) and leads to low quantum efficiency of the titania (Choi, Termin et al. 1994, Serpone 1997). In this case, no catalytic or photocatalytic activity occurs. Alternatively, the electron and hole can effectively become 'trapped', that is, existing as Ti^{3+} and $O^{\cdot-}$ (Tachikawa, Fujitsuka et al. 2007), preventing recombination and allowing further processes to occur. Doping (defects and impurities) can effectively facilitate this process, by providing additional energy levels allowing increased stabilisation of the excited states and reducing the likelihood of recombination. It was mentioned in Chapter 1 that nanoparticles can be thought of as exploitable surface, and for photocatalytic activity, migration of the generated charge carriers (electrons and holes) to the surface of the material or nanoparticle initiates redox reactions with pollutants adsorbed onto the surface (Curri, Comparelli et al. 2003). It is generally accepted that the photocatalytic activity of titania is dependent upon the generation and reaction of the hydroxyl anion, $OH^{\cdot-}$ (Diebold 2003, Fujishima, Zhang et al. 2008, Pelaez, Nolan et al. 2012),

Chapter 3: Metal Oxide Nanoparticles

however, for balance and to ensure no physical change of the catalyst occurs, the production of the superoxide anion O_2^- facilitates its mechanism. Oxidation of water at the surface of the catalyst by the positive holes generates powerful oxidant OH^\bullet species. These can go on to oxidise adsorbed pollutants causing their decomposition. Coupled with this, reduction of molecular oxygen adsorbed onto the surface leads to the O_2^- superoxide species, which in itself can aid in the oxidation of pollutants or through reaction with protons, can form OOH radicals which offer additional oxidative powers. These processes combined encompass the utilisation of light by titania nanoparticles to generate electron-hole pairs which can migrate to the surface of the particles and undergo redox reactions for the breakdown of pollutants, and can be summarised by the following equations (Pelaez, Nolan et al. 2012):



3.1.3.2.2. Photocatalytic Testing

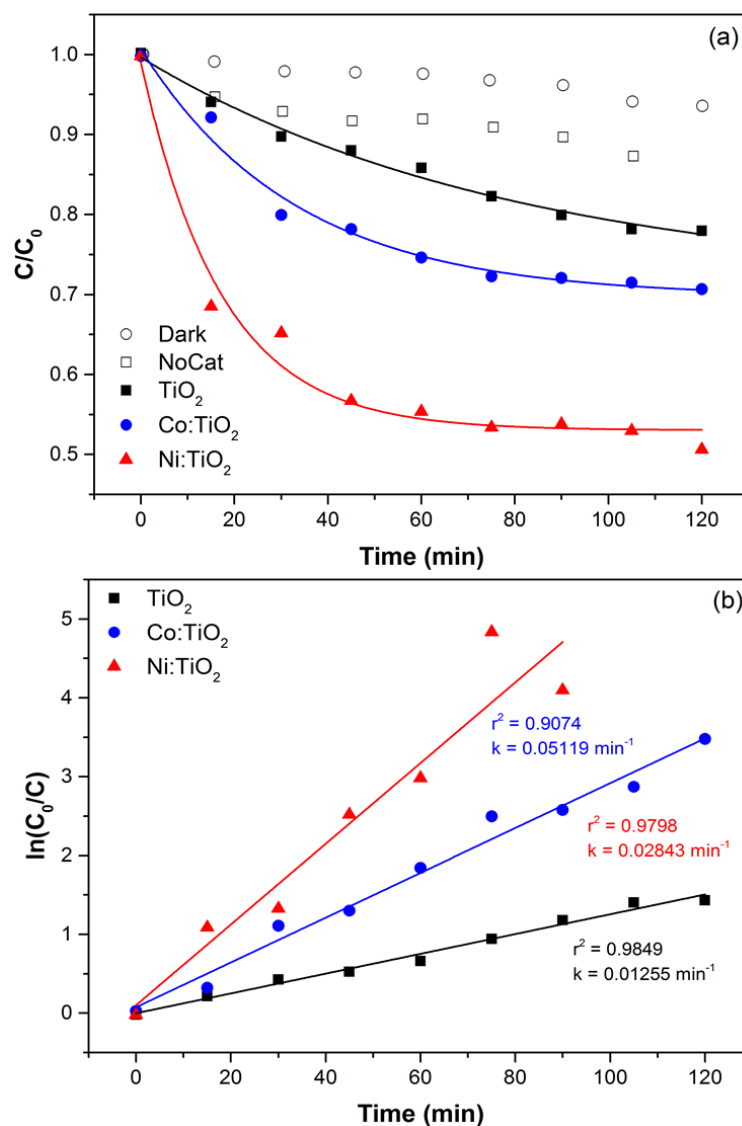


Figure 3.7: Results of photocatalytic testing on the degradation of methylene blue under UVA irradiation in the presence of photocatalysts (a), and plot determining the first-order photodegradation rates (b).

The results of the photocatalytic degradation of methylene blue in the presence of the pure and doped anatase over the course of two hours are shown in Figure 3.7 (a). This graph uses the UV-Vis data to compare the concentration of methylene blue in the samples removed from the outlet port after irradiation of different time periods (C), against the starting concentration of 10 ppm (C_0), to

Chapter 3: Metal Oxide Nanoparticles

give a progressive depletion of methylene blue concentration against time (C/C_0 vs. time), as indicated by the sloping curves in Figure 3.7 (a). Blank tests were carried out under UV irradiation with no catalyst (only the methylene blue solution), to gain a baseline reading for the degradation of methylene blue under UV irradiation and to therefore better assess the effect of the presence of the nanoparticles, and blank tests in the presence of the undoped anatase sample without illumination, to assess the baseline effect of the presence of the nanoparticles through processes such as adsorption of the dye onto the particle surfaces.

As expected the test carried out in the dark shows minimal removal of the methylene blue, with the slight decrease in concentration attributable to the gradual adsorption of the dye onto the nanoparticle surface, which is removed during the centrifugation step, prior to UV-Vis measurement. With no UV light, electron-hole pair generation and hence the generation of active oxidation species does not occur. There is therefore no reaction between the dye molecules adsorbed onto the titania nanoparticles surface with active surface oxidation species. Exposure to UV light in the absence of a catalyst results in a larger decrease in concentration due simply to the photochemical breakdown of methylene blue which is well known (Houas, Lachheb et al. 2001). Exposure of the methylene blue solution to UV light in the presence of each of the three nanoparticle samples, anatase and 1% Co and 1% Ni doped anatase, results in an exponential decrease in concentration, demonstrated by the sloping curves in Figure 3.7 (a). The undoped-TiO₂ showed degradation of the methylene blue dye, with 1% Co:TiO₂ and 1% Ni:TiO₂ demonstrating greater levels of degradation, with 1% Ni:TiO₂ showing the highest photocatalytic activity.

Chapter 3: Metal Oxide Nanoparticles

Whilst these curves demonstrate a trend, it is much more useful to assess the rate of degradation. The oxidation reaction and degradation of the dye are consistent with a first order reaction, based on the concentration of methylene blue, according to the equations:

$$\frac{d[C]}{dt} = k[C]$$

$$\frac{d[C]}{[C]} = -kdt$$

$$\int_{A_0}^A \frac{d[C]}{[C]} = -k \int_{t_0}^t dt$$

$$\ln[C] - \ln[C_0] = -kt$$

$$\ln \frac{[C_0]}{[C]} = kt$$

Plotting $\ln \frac{[C_0]}{[C]}$ against time gives the first-order rate constant k as shown in Figure 3.7 (b). Clearly doping of the anatase nanocrystals leads to an enhancement of photocatalytic activity. The photodegradation of methylene blue using the undoped anatase occurs with a rate constant of 0.01255 min^{-1} , the cobalt doped sample is more than twice as active, with $k = 0.02843 \text{ min}^{-1}$, while the nickel doped anatase shows 4 times the activity of the undoped anatase with a rate constant of 0.05119 min^{-1} . These rates are comparable to those observed by other researchers using doped anatase prepared by more conventional sol-gel and hydrothermal routes (Castro, Nunes et al. 2009, Devi, Kottam et al. 2010).

It is worth noting that both the cobalt and nickel doped samples exhibited similar surface areas ($\sim 240 \text{ m}^2 \text{ g}^{-1}$) and band-gaps (2.89 and 2.95 eV,

Chapter 3: Metal Oxide Nanoparticles

respectively), and thus the significantly higher activity of the nickel doped anatase must be attributed to the presence of nickel as a dopant over cobalt, rather than these other physical factors. Choi *et al.* have previously reported similarly anomalous activities in their studies on a variety of metal ion doped titania photocatalysts, and specifically reported enhanced activity in nickel doped samples, which could not be easily assigned to any obvious physical characteristic (Choi, Park et al. 2010). It was suggested in the case of platinum doped titania that the fraction of rutile played a significant role. While no rutile is observed in this case it may be that slight structural defects or deviations may be responsible for the enhanced activity of the nickel doped samples.

3.1.4. Conclusions

This section has demonstrated the applicability of CFHS and the Nottingham counter-current reactor to produce photocatalytically active anatase titania and 1% cobalt and 1% nickel doped titania nanoparticles. It is important to note the homogenous and thorough nature of the inclusion and doping of the transition metal ions into the titania structure, as opposed to simply forming mixtures of the metal oxides, to demonstrate further compositional control of the resulting particles offered by the reactor and explore the possible advancements that can be made on simply producing single metal, metal oxide nanoparticles. The inclusion of dopant ions in the synthesis is found to result in smaller nanocrystals with higher surface areas and the inclusion of the dopants was confirmed by variations in lattice parameters determined by powder XRD, elemental mapping by TEM and optical characterisation. The doped anatase materials exhibit significantly lower band-gap energies relative to the undoped anatase. The doped anatase nanocrystals were assessed for their photocatalytic activity using a custom made photoreactor. Both doped materials show significantly higher activities than the pure anatase, in the best case with 1% nickel, increasing the catalytic activity through the degradation of methylene blue 4-fold relative to the undoped parent material. Given the scalable nature of the CFHS process, and with an industrial scale facility under construction through the SHYMAN project based on the Nottingham counter-current reactor, this work gives promise to the synthesis of photocatalytically active titania and doped titania nanoparticles with tuneable optoelectronic properties for an array of applications.

3.2. Barium Strontium Titanate ($\text{Ba}_{(1-x)}\text{Sr}_x\text{TiO}_3$)

3.2.1. Introduction

Discovered in the early 1940s as a capacitor material to replace mica, barium titanate (BaTiO_3) has since been the subject of intense and sustained research. Initially it posed an interesting conundrum to the scientific community – a simple ceramic material exhibiting ferroelectric properties previously unheard of in anything but hydrogen-bonded systems. BaTiO_3 adopts the perovskite ABO_3 structure: a network of corner-sharing $[\text{BO}_6]$ octahedra with the 12-coordinate interstitial site occupied by the larger A metal cations, as shown in Figure 3.8 (Mats and Peter 2008, Modeshia and Walton 2010). The ideal archetypal structure, adopted by the closely related SrTiO_3 , is that of a centrosymmetric primitive cubic system. Pure cubic symmetry prohibits ferroelectric behaviour, however below the Curie temperature of 120 °C the titanium atoms of BaTiO_3 are offset from the centre of the $[\text{BO}_6]$ octahedra elongating the c-axis creating a tetragonal phase with a permanent dipole (Kwei, Lawson et al. 1993). This dipole gives rise to the important ferroelectric properties of BaTiO_3 . Its high dielectric constant, low dielectric loss and general ferroelectric properties make BaTiO_3 ideally suited to a vast array of applications (Haertling 1999) including capacitors, RF devices, microwave dielectrics, infrared sensors, and more recently memory devices (Ezhilvalavan and Tseng 2000). Historic applications make use of the commensurate piezoelectric properties arising from the non-centrosymmetric structure, such as microactuators, microphones and sonar devices.

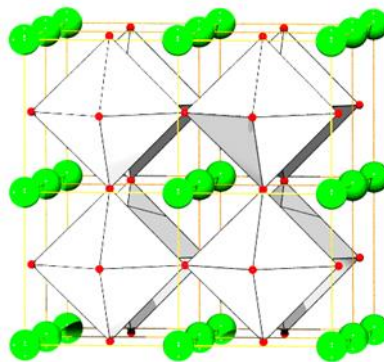


Figure 3.8: The BaTiO₃ perovskite structure, showing in green the Ba²⁺ in the A position.

The flexibility of the perovskite structure is such that a wide range of metal cations may be accommodated, particularly in the A position. With respect to barium titanate this allows significant variation in composition, with barium easily replaced by alternative M²⁺ ions. One of the most common substituents is strontium – a smaller element of group 2. The full phase diagram of Ba_(1-x)Sr_xTiO₃ from x = 0 to x = 1 is known. It has been shown that increasing strontium content stabilises the cubic phase (as mentioned above SrTiO₃ itself adopts the cubic perovskite structure at room temperature). This substitution has the effect of altering the ferroelectric properties of the base BaTiO₃, allowing fine tuning to suit the desired application. CFHS has demonstrated the ability to provide fine control of composition across the full compositional range of a material, such as Ce_{1-x}Zr_xO₂ (x = 0 - 1) (Cabanas, Darr et al. 2000, Weng, Perston et al. 2009, Kellici, Gong et al. 2010). Continuous flow systems therefore present an opportunity, with only simple modifications, to access the full compositional range of materials, and so becomes a powerful tool in the synthesis of BaTiO₃ and the subsequent alteration of the composition with strontium to access the full compositional range of Ba_(1-x)Sr_xTiO₃.

Chapter 3: Metal Oxide Nanoparticles

Conventionally BaTiO₃ and related ceramics have been prepared by traditional ceramic methods: the high temperature sintering of BaCO₃ or BaO and TiO₂ (Feteira, Sinclair et al. 2004); however due to the high temperatures this yields large particles with poor monodispersity, unsuitable for the increasing miniaturisation required of components and devices using the material. For instance in electronics, devices are becoming ever smaller and as such, materials must adapt to provide the desired property but in a smaller physical space, thus, simply by reducing the particle size of materials towards nanoparticles can provide an advantage.

Hydrothermal and solvothermal methods are increasingly finding favour for the production of BaTiO₃. Barium titanate has been produced in continuous-flow systems under both hydrothermal and solvothermal conditions (Bocquet, Chhor et al. 1999, Reveron, Aymonier et al. 2005, Reverón, Elissalde et al. 2006, Matsui, Noguchi et al. 2008, Hayashi, Noguchi et al. 2010, Hayashi, Noguchi et al. 2010). Hydrothermally this has been achieved from dispersions of TiO₂ or titanium tetrachloride and a variety of barium sources (Matsui, Noguchi et al. 2008, Hayashi, Noguchi et al. 2010, Hayashi, Noguchi et al. 2010). Barium strontium titanate has also been produced under continuous flow solvothermal conditions in an approximation of existing sol-gel routes, though precautions were needed owing to the instability of the alkoxide based precursors in the presence of water (Bocquet, Chhor et al. 1999, Reveron, Aymonier et al. 2005, Reverón, Elissalde et al. 2006). Whilst the full compositional range has been achieved, there still exist issues with the synthesis that limit the scale-up potential by CFHS. This will be discussed further in Section 3.2.3.2.3.

Chapter 3: Metal Oxide Nanoparticles

Briefly, BaCO_3 is a common impurity observed in many reactions and is a waste product in that it prevents the full incorporation of barium into the $\text{Ba}_{(1-x)}\text{Sr}_x\text{TiO}_3$ system. Often precursors such as TiO_2 sols or chlorides are used which are generally incompatible with pumps or the standard reactor pipework respectively and in the case of halides, require expensive halide-resistant equipment, limiting the scale-up potential. When other precursors are used, special precautions are required such as the use of alcohols to prevent unwanted side reactions, again limiting the scale-up potential or ‘green’ credentials of the process. Due to competing factors in the synthesis in terms of product characteristics vs. scale, such as the desire to produce the material and scale-up in an efficient manner but also the need to tailor the particle characteristics by preventing impurities and thus gain complete incorporation of barium for the correct stoichiometry, or the want for controlling particle size or morphology which are achieved by using alternative complex precursors or solvents, a fully hydrothermal continuous flow route towards the full compositional range of $\text{Ba}_{(1-x)}\text{Sr}_x\text{TiO}_3$ has never been demonstrated, at laboratory scale or pilot scales.

This section therefore presents the first continuous flow fully hydrothermal production of $\text{Ba}_{(1-x)}\text{Sr}_x\text{TiO}_3$ nanopowders at both bench- and pilot-scale. This demonstrates application of the Nottingham counter-current reactor to an industrially applicable nanomaterial, at both laboratory and pilot scales, demonstrating firstly the capability to produce at scale, with the SHYMAN facility construction in mind, and also understanding the similarities and differences of the products from the two scales. Application of the reactor to controlling the composition across the full compositional range of another

industrially relevant material is achieved, furthering the CFHS method and offering the Nottingham reactor as a powerful tool for more tailored nanomaterial synthesis.

3.2.2. Experimental

3.2.2.1. Synthesis

The reactions presented herein were performed using the standard arrangement of the Nottingham counter-current reactor described in Section 1.4.3 and shown in Figure 3.9 at both laboratory and pilot scales. The reactions make use of water soluble precursors without the need for special treatment or precautions. A 0.05 M solution of titanium bis(ammonium lactato) dihydroxide (TiBALD) with appropriate amounts of the divalent metal nitrate salts $\text{Ba}(\text{NO}_3)_2$ and/or $\text{Sr}(\text{NO}_3)_2$, to a total M^{2+} concentration of 0.05 M, was used as the metal precursor stream. A solution of NaOH at various concentrations was mixed with this in flow at a T-piece mixer, to act as a precipitating agent to ensure the intimate mixing of the metals by gelation prior to crystallisation on further mixing with the preheated stream of supercritical water. The temperature of the preheater was set to 430 °C giving a post-mixing temperature of ~ 390 °C, recorded using a thermocouple in-situ immediately downstream of the reaction/mixing point. The system pressure was maintained at 25 MPa with the back pressure regulator. Products were collected and washed with water by centrifugation before drying under air at 70 °C. It was found that all products as prepared contained barium/strontium carbonate

Chapter 3: Metal Oxide Nanoparticles

impurities which can be easily removed by an additional washing step with 1 M acetic acid prior to the final drying stage, as discussed shortly.

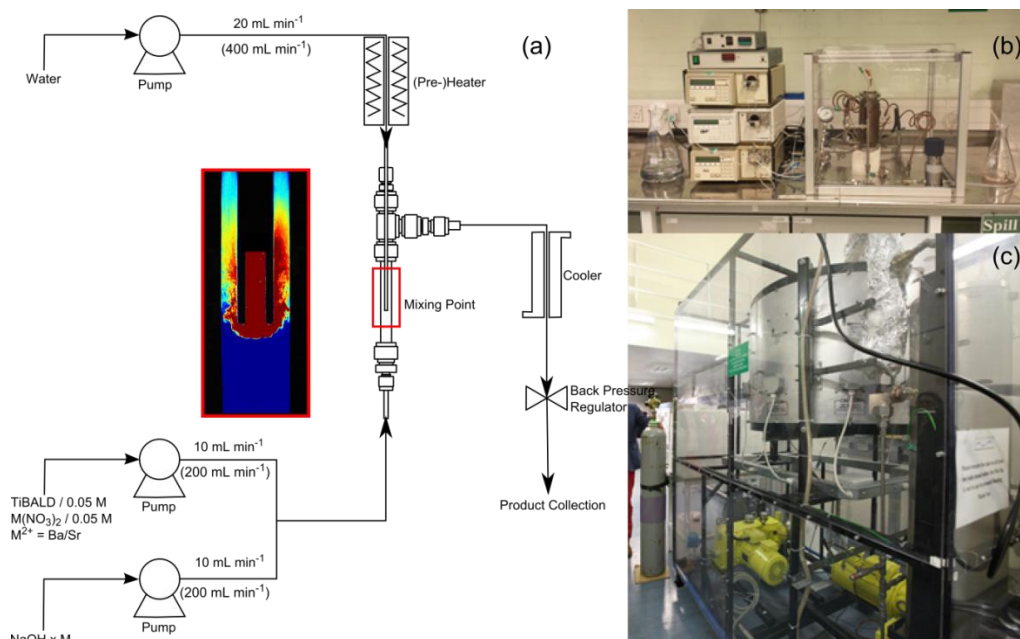


Figure 3.9: A simplified schematic of the reactor used in the production of $\text{Ba}_{1-x}\text{Sr}_x\text{TiO}_3$ with an inset highlighting the counter-current mixing (numbers in brackets indicate flow-rates used at the pilot-scale) (a), and photographs of the bench- and pilot-scale systems (b & c, respectively).

3.2.2.2. Characterisation

Compositional analysis was performed by Inductively Coupled Plasma Mass Spectrometry (ICP-MS; ELAN DRC-e, Perkin Elmer, Waltham, USA) in a class 1000 (ISO class 6) clean room. Samples were digested by heating in closed PTFE vessels using concentrated HCl (ROMIL-SpA™ Super Purity Acid, 32–25%, ROMIL, USA). Powder X-ray diffraction patterns of the products to assess the effect of strontium substitution on the crystal structure were collected on a Bruker D-8 Advance diffractometer using $\text{Cu K}\alpha$ radiation ($\lambda = 1.5418 \text{ \AA}$) over a 2θ range of $10 - 70^\circ$, with a step size of 0.04° at 4s/step.

Chapter 3: Metal Oxide Nanoparticles

Infrared spectra were recorded using a Bruker Tensor 27 FTIR ATR spectrometer at a resolution of 4 cm^{-1} . Raman spectra of the obtained powders were collected using a Raman WORKSTATION™ Analyzer with PhAT imaging probe (Kaiser Optical Systems, Inc.) with 785 nm excitation and a $10\times$ objective. Raman spectra ($200\sim 1896\text{ cm}^{-1}$) at a resolution of $\sim 4\text{ cm}^{-1}$, were collected from a 3×3 grid, and at each point 10×3 second exposures were accumulated. The presented spectra are the average of all 90 exposures (this was done to reduce noise). Samples were prepared for transmission electron microscopy by dispersion and sonication in acetone prior to deposition on a lacey carbon coated copper grid. Transmission electron micrographs and electron diffraction patterns were recorded using a FEI Titan microscope operating at 300 kV.

3.2.3. Results & Discussion

3.2.3.1. Synthesis of BaTiO₃ Nanoparticles

3.2.3.1.1. The Requirement of NaOH for Synthesis

On pumping a solution containing equivalent amounts (0.05 M) of barium nitrate and titanium bis(ammonium lactato) dihydroxide against a supercritical water stream without prior mixing with an additional base stream it was found that only poorly crystalline anatase phase titania nanoparticles ($\sim 2\text{ nm}$ by XRD) were produced. Continuous-flow hydrothermal synthesis typically utilises supercritical water as both reagent and anti-solvent to induce the hydrolysis of metal salts and the rapid nucleation of metal oxides. The synthesis of BaTiO₃ is expected to proceed according to the equation:



Whilst demonstrated in literature, the precise need for additional base in the reaction in addition to the conditions provided by supercritical water has never been confirmed, but was found to be necessary in this work. Initial experiments were therefore performed to assess the effect of the addition of base and to optimise the synthesis of BaTiO₃. On introducing a 0.2 M NaOH stream to give a Ba:Ti:OH ratio of 1:1:4 prior to mixing with the pre-heated water stream a mixture of amorphous hydrous titania (McManus, Cunningham et al. 2012) and barium carbonate was obtained. Increasing the sodium hydroxide concentration to 0.4 M or beyond generated nanocrystalline BaTiO₃. The crystallite sizes were determined to be 15 – 17 nm regardless of any further increase in the sodium hydroxide concentration. In all cases barium carbonate was present as an impurity. The XRD patterns of these products are shown in Figure 3.10. From this it is clear that a minimum OH⁻:Ba²⁺:Ti⁴⁺ ratio of 8:1:1 is required for the successful synthesis of BaTiO₃ nanopowders. All subsequent reactions for the production of Ba_(1-x)Sr_xTiO₃ were thus performed at a M²⁺:Ti:OH ratio of 1:1:10 (*i.e.* the NaOH concentration was fixed at 0.5 M) to ensure complete reaction. Increasing the NaOH concentration further was found to have no additional benefit to the reaction and so to minimise unnecessary chemical use and improve process efficiency 0.5 M was deemed to be adequate.

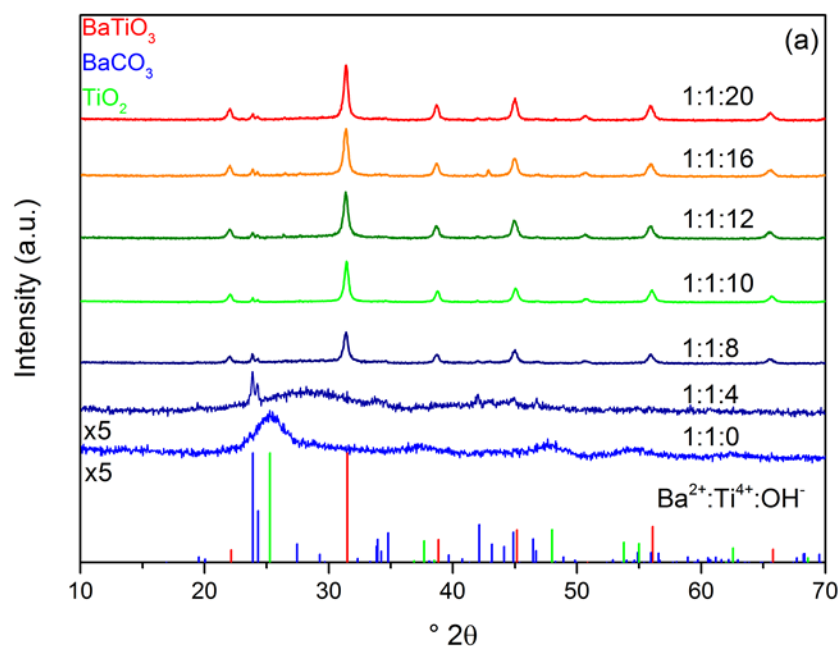


Figure 3.10: XRD patterns of samples prepared with varying Ba:Ti:OH ratios using TiBALD. The patterns of the materials produced at ratios of 1:1:0 and 1:1:4 have been scaled for clarity. Tick marks indicate the expected peak positions for BaTiO₃, BaCO₃ and anatase phase TiO₂.

3.2.3.1.2. Appearance and Removal of BaCO₃ Impurities

As mentioned in the previous sections, BaCO₃ is a common impurity observed by other researchers in the synthesis of BaTiO₃, and was observed here also. Barium carbonate may be produced due to the decomposition of the lactate moieties of the titanium source, since this is the only carbon containing reagent present in reaction. Carbon containing decomposition residues could react with barium ions in solution forming the carbonate species, effectively removing a portion of the available barium species from the reactant solution and preventing full incorporation of all barium substituents into the desired BaTiO₃ product. To investigate this, the reaction was repeated using a titania sol as the titanium source, to remove TiBALD organics from the reaction system. However, this also yielded barium carbonate as an impurity in addition to

unreacted anatase (Figure 3.11). Based on this it was concluded that the carbon must be arising from another source in the reaction, and since no other reagents contained carbon moieties, barium carbonate must be formed due to the reaction of barium with dissolved CO₂ in the water solvent and precursor water under basic conditions. All further reactions therefore continued to use TiBALD as the titanium source, as its solubility makes it easier to handle and causes less wear on the pumps than the titania sol and it permits more complete reaction in the short residence times used here. Steps such as the purging or degassing of precursor and solvent water and reactor pipework prior to synthesis would alleviate CO₂ residues from the reaction and possibly prevent barium carbonate production, however, this laborious and lengthy process would prove unfeasible (and perhaps unnecessary) at larger scales.

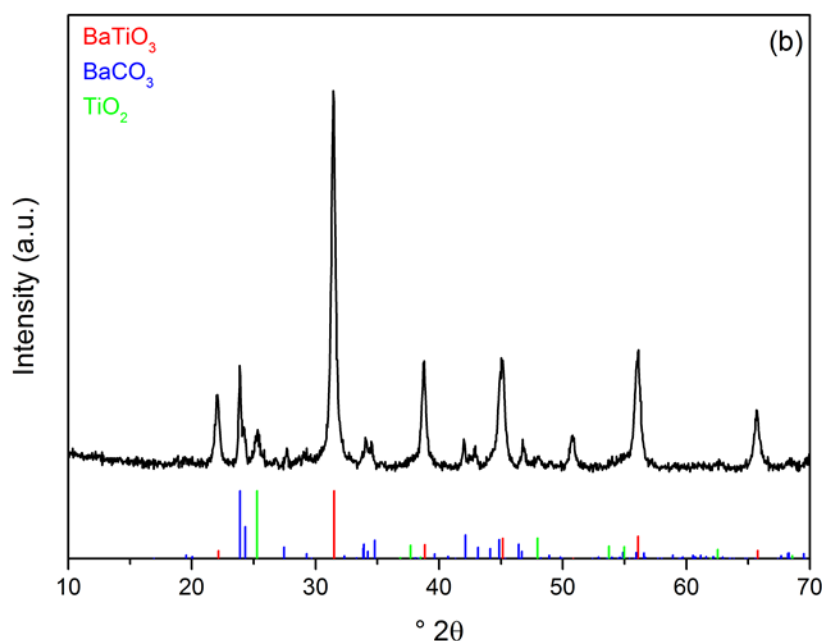


Figure 3.11: XRD pattern of the sample prepared using the 1:1:10 ratio using a titania sol as opposed to TiBALD. Tick marks indicate the expected peak positions for BaTiO₃, BaCO₃ and anatase phase TiO₂.

Chapter 3: Metal Oxide Nanoparticles

For the laboratory scale synthesis here, in order to remove the barium carbonate impurities a washing step was deemed appropriate. Re-suspending the as-obtained powder products in a 1 M solution of acetic acid and briefly shaking before washing by centrifugation proved sufficient to remove the carbonate species without adversely affecting the barium titanate product (verified by XRD, IR and TEM of unwashed and washed products). This washing step could of course be incorporated into the reaction in flow, with acetic acid being pumped into the capping point of the reaction to effectively dissolve and remove the barium carbonate product in the product stream in flow prior to exit of the product solution from the back pressure regulator and reactor system. The XRD patterns of the unwashed and washed samples shown in Figure 3.12 (a) suggest the complete removal of the crystalline barium carbonate impurities. The infrared spectra (Figure 3.12 (b)) support this with washing removing the sharp band at 1456 cm^{-1} due to BaCO_3 (Nakamoto, Fujita et al. 1957), though bands at 1369 and 1631 cm^{-1} arising from COO stretching vibrations remain, attributed to adsorbed CO_2 and carboxylate moieties (Nakamoto, Sarma et al. 1965) on the surface of particles.

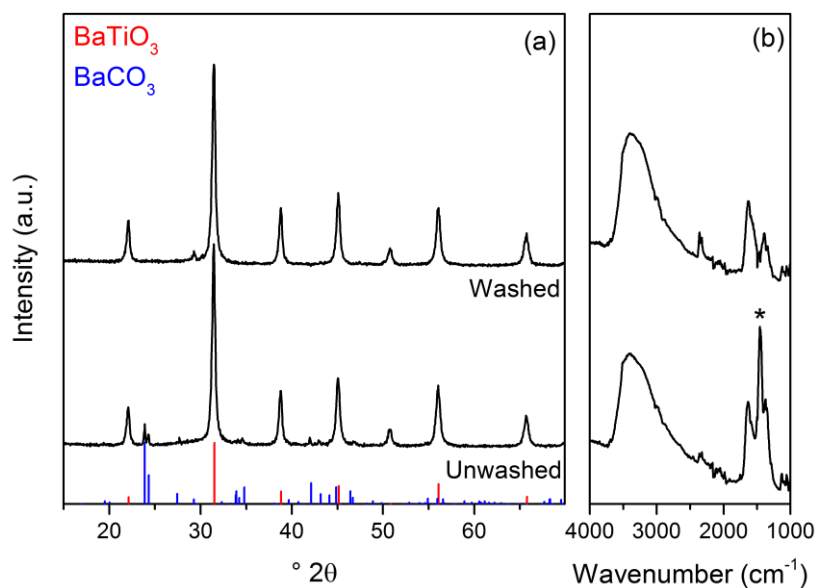


Figure 3.12: Comparison of the XRD patterns (a) and infrared spectra (b) of barium titanate obtained at a Ba:Ti:OH of 1:1:10 before and after washing with 1 M acetic acid. * indicates the sharp band at 1456 cm^{-1} indicative of the carbonate species, which is removed after washing.

3.2.3.2. Synthesis of $\text{Ba}_{(1-x)}\text{Sr}_x\text{TiO}_3$ Nanoparticles

Upon optimisation of BaTiO_3 production in terms of precursor and base ratio to produce BaTiO_3 , and a method for the BaCO_3 impurity removal, expansion to $\text{Ba}_{(1-x)}\text{Sr}_x\text{TiO}_3$ was a logical progression. Selected compositions across the full compositional range of barium titanate to strontium titanate were chosen to give a representation of the ability of the reactor to produce materials of any given composition, and were produced at laboratory and pilot scales.

3.2.3.2.1. Laboratory Scale

Materials with the targeted composition of $\text{Ba}_{(1-x)}\text{Sr}_x\text{TiO}_3$ for the full range $0 \leq x \leq 1$ were synthesised using the method established for BaTiO_3 in Section 3.2.3.1, *i.e.* a 0.05 M mixed metal solution flowing against a sodium hydroxide

Chapter 3: Metal Oxide Nanoparticles

stream to give a M^{2+} :Ti:OH ratio of 1:1:10 before mixing with a supercritical water stream pre-heated to 430 °C at the counter-current mixing point. All products were found to contain carbonate impurities; but, as above these impurities were easily removed with an acetic acid washing step. To evaluate the precise ratio of the constituents in the final products, elemental analysis by ICP-MS was performed (Figure 3.13). This shows that, in all cases, the total M^{2+} :Ti ratio is significantly lower than the precursors were prepared for or that was desired (1:1), varying between 0.8:1 and 0.9:1. Given the presence of MCO_3 species in each of the as-produced materials, which were removed in the washing step, the lower M^{2+} content is to be expected.

It is also worth noting that the strontium is seemingly preferentially incorporated into the perovskite structure over barium, with all mixed $Ba_{(1-x)}Sr_xTiO_3$ samples showing significantly higher Sr:Ba ratios than expected. The preferential incorporation of strontium into the perovskite structure during hydrothermal synthesis of mixed barium strontium titanate nanopowders has been observed previously in low temperature systems (Roeder and Slamovich 1999). It has been suggested that this is a result of the greater thermodynamic stability of the strontium titanate, with barium incorporation increasing over time. While this is certainly a distinct possibility here, it must also be considered that our reaction times are on the order of milliseconds/seconds, rather than hours, which may suggest that where both M^{2+} ions are available barium is more likely to form the carbonate and thus be effectively delayed from incorporation into the perovskite structure. The pure $SrTiO_3$ sample does still show a low Sr:Ti ratio of 0.81:1; the lowest M^{2+} :Ti value observed here.

This indicates that carbonate formation remains a significant issue for the

generation of stoichiometric strontium titanate also. The measured $M^{2+}:\text{Ti}$ ratios are plotted as a function of the target x value in Figure 3.13. While the obtained products are non-stoichiometric, for clarity they will be referred to by the target $\text{Ba}_{(1-x)}\text{Sr}_x\text{TiO}_3$ stoichiometry.

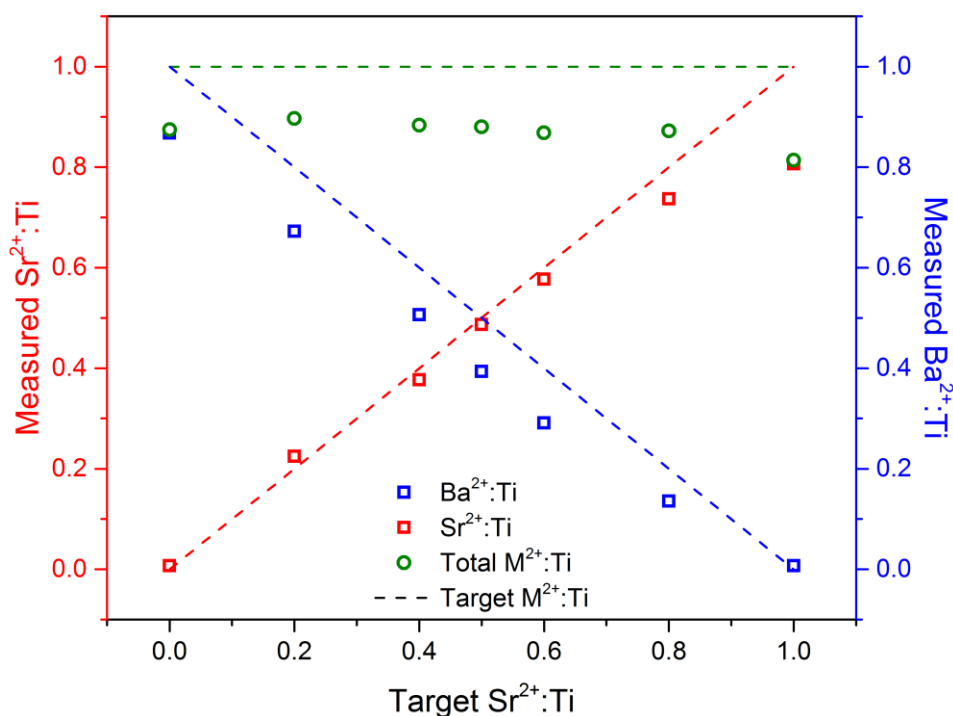


Figure 3.13: The $\text{Ba}^{2+}:\text{Ti}$, $\text{Sr}^{2+}:\text{Ti}$ and total $M^{2+}:\text{Ti}$ ratios of the bench-scale $\text{Ba}_{(1-x)}\text{Sr}_x\text{TiO}_3$ samples determined by ICP-MS against x . Dashed lines indicate the targeted values.

Figure 3.14 (a) shows the powder X-ray diffraction patterns of the washed $\text{Ba}_{(1-x)}\text{Sr}_x\text{TiO}_3$ products obtained at the bench-scale with varying x values. The diffraction patterns show that all products adopt the cubic perovskite structure. Slight deviations from cubic symmetry to the tetragonal phase can be difficult to detect by conventional XRD, particularly with peak broadening in nanocrystalline samples. Raman spectroscopy has been shown to be more sensitive to tetragonal distortions (Clark, Takeuchi et al. 1999, Kim, Jung et al. 2004). The Raman spectra of the $\text{Ba}_{(1-x)}\text{Sr}_x\text{TiO}_3$ products shown in Figure 3.14 (b) exhibit broad features at $\sim 290 \text{ cm}^{-1}$ and 515 cm^{-1} which, though forbidden

in the cubic system, are commonly observed and generally ascribed to local disorder of the B-site Ti atoms (Venkateswaran, Naik et al. 1998, Shiratori, Pithan et al. 2007). The Raman spectrum of the BaTiO₃ sample also exhibits a very weak, sharp peak at 305 cm⁻¹ (which is partly obscured by the filter artefact, but clearly evident in the derivative spectrum) and a stronger band at 715 cm⁻¹ which are assigned to tetragonal BaTiO₃. These features decrease in intensity on increasing the strontium content of the Ba_(1-x)Sr_xTiO₃ to the point where they are no longer discernible at $x \geq 0.8$, as would be expected given the solely cubic structure adopted by SrTiO₃. Increasing the strontium content also causes a decrease in crystallite size, as determined by Scherrer analysis of the broadening of the X-ray diffraction peaks and summarised in Figure 3.14 (c). This shows a steady decline in crystalline domain size from 17.3 nm to 7.9 nm on increasing x from 0 to 1. As expected, increasing the strontium content also causes a shift in Bragg peak positions in the XRD patterns due to contraction of the perovskite lattice resulting from the smaller ionic radius of Sr²⁺ relative to Ba²⁺ (1.44 Å and 1.61 Å, respectively). While the Raman spectra indicate that the samples possess some degree of tetragonality this could not be resolved from the diffraction patterns, and thus only the cubic a lattice parameter was calculated. The crystallite diameters and (cubic) lattice parameters calculated from the XRD patterns are shown in Figure 3.14 (c) plotted against the measured Sr:M²⁺ ratio.

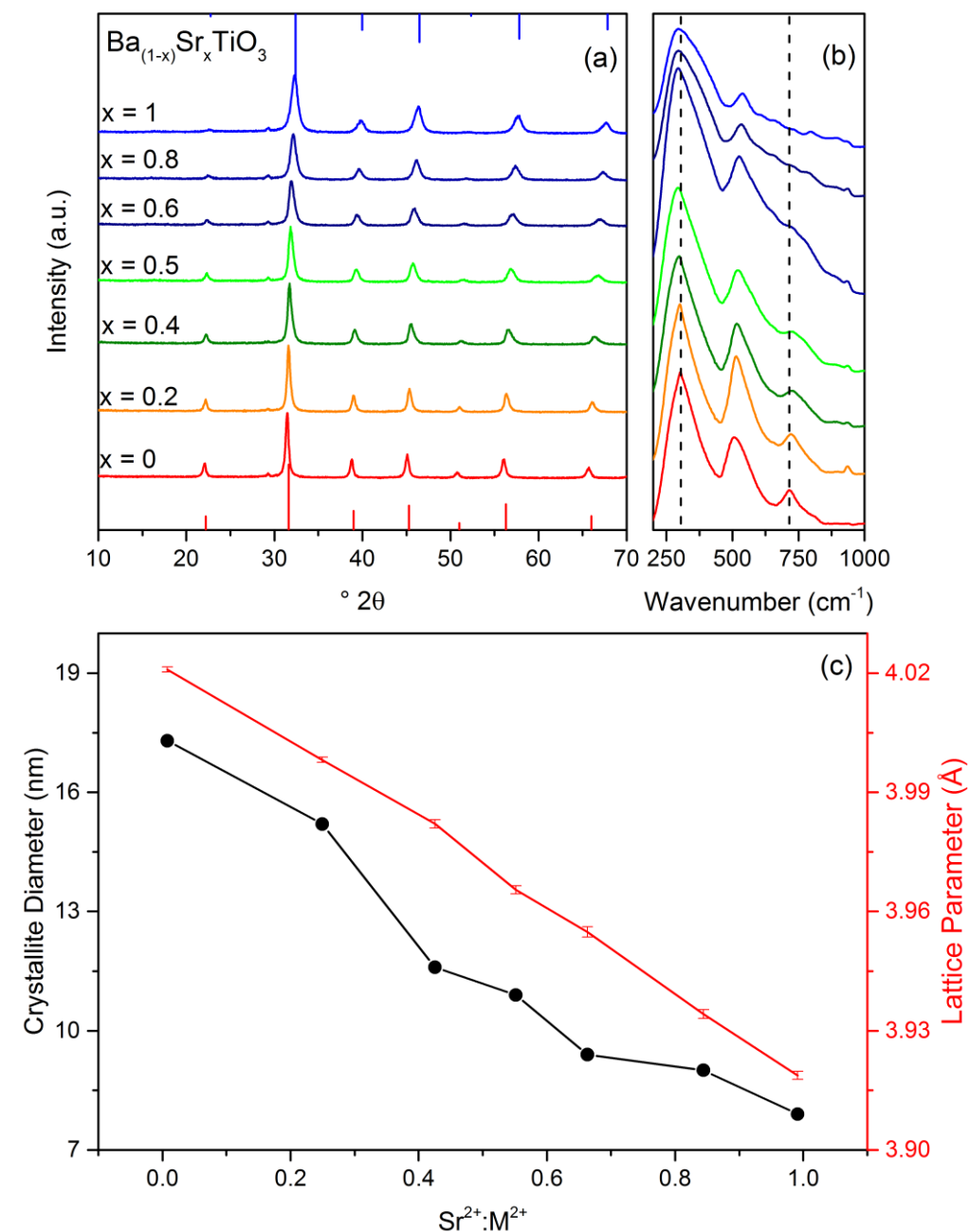


Figure 3.14: XRD patterns of bench-scale $\text{Ba}_{(1-x)}\text{Sr}_x\text{TiO}_3$ samples with tick marks corresponding to BaTiO_3 (bottom) and SrTiO_3 (top) (a) and the equivalent Raman spectra (b), and the effect of Sr content on crystallite size and cubic lattice parameter, a , as a function of $\text{Sr}:\text{M}^{2+}$ ratio (c).

Chapter 3: Metal Oxide Nanoparticles

Transmission electron microscopy images of the seven bench-scale $\text{Ba}_{(1-x)}\text{Sr}_x\text{TiO}_3$ samples are shown in Figure 3.15 (a-g). These images confirm the trends mentioned above; increasing Sr content causes a decrease in both crystallite size and the cubic lattice parameter, a . Electron diffraction patterns (Figure 3.15 (h)) are also consistent with the cubic (or slightly tetragonal) structure observed by X-ray diffraction and show no obvious impurities or additional phases. The properties of all bench-scale $\text{Ba}_{(1-x)}\text{Sr}_x\text{TiO}_3$ samples are summarised in Table 3.2.

The bench scale reactions indicated that whilst gaining specific control of the final product composition would require further work and investigation discussed in Section 3.2.3.2.3, a degree of compositional control and access to products across the whole compositional range was possible with the Nottingham counter-current reactor, and so this warranted selected cases being trailed at pilot scales.

Table 3.2: Properties of bench-scale $\text{Ba}_{(1-x)}\text{Sr}_x\text{TiO}_3$ determined by ICP-MS, Raman spectroscopy and XRD. C and T indicate cubic and tetragonal phases, respectively.

Target x	Sr/Ti	Ba/Ti	M^{2+}/Ti	Sr/M^{2+}	Phase	Crystallite diameter (nm)	Cubic lattice parameter (\AA)
0	0.00	0.87	0.87	0.00	T	17.3	4.02(1)
0.2	0.22	0.67	0.89	0.25	T	15.2	3.99(8)
0.4	0.37	0.51	0.88	0.42	T	11.6	3.98(2)
0.5	0.49	0.39	0.88	0.55	T	10.9	3.96(5)
0.6	0.58	0.29	0.87	0.66	T	9.4	3.95(5)
0.8	0.73	0.14	0.87	0.84	C	9.0	3.93(4)
1.0	0.81	0.00	0.81	0.99	C	7.9	3.91(8)

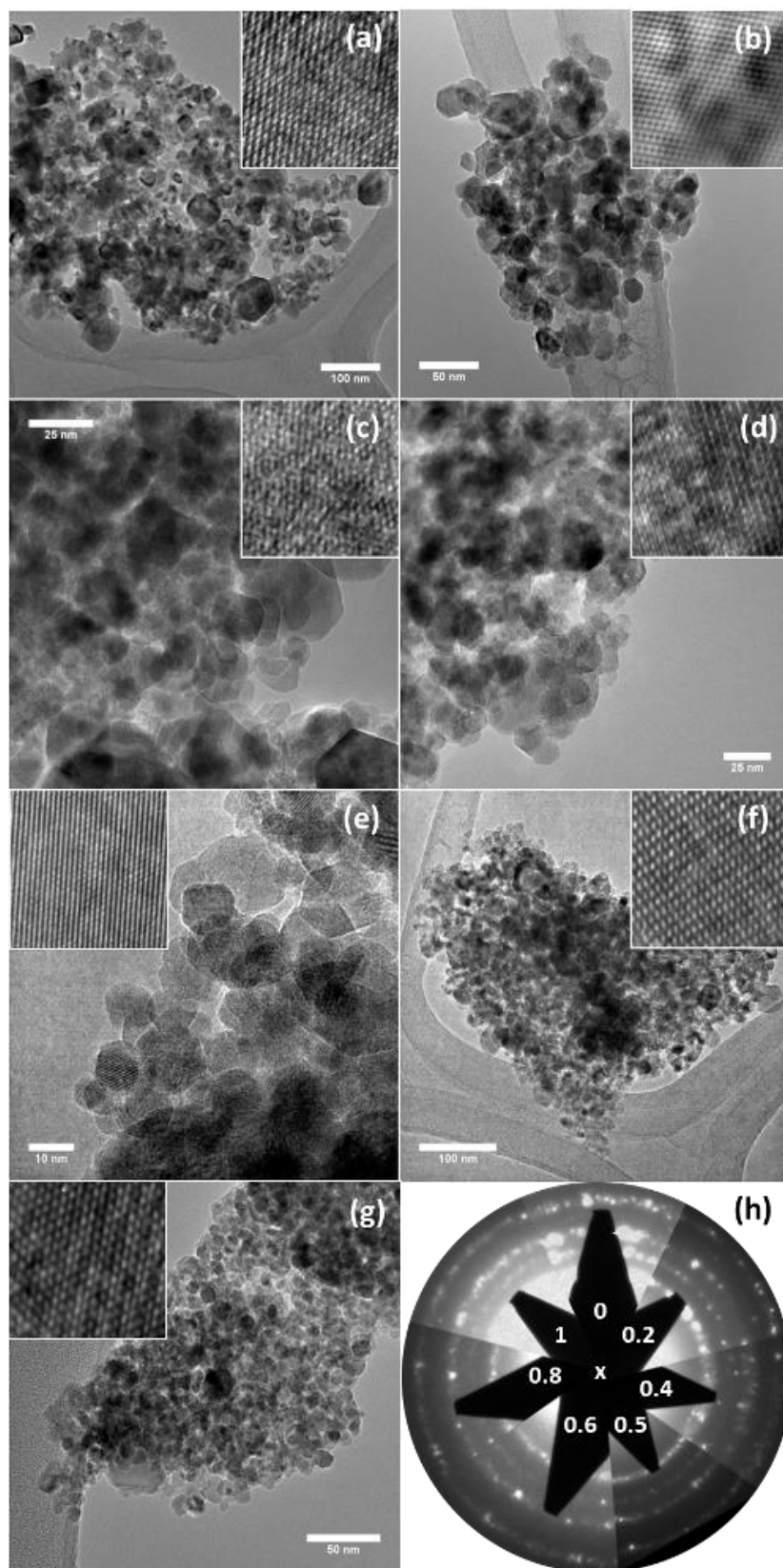


Figure 3.15: TEM images of bench-scale $\text{Ba}_{(1-x)}\text{Sr}_x\text{TiO}_3$ samples at x values of 0, 0.2, 0.4, 0.5, 0.6, 0.8 and 1 (a – g, respectively), and a composite of the corresponding electron diffraction patterns (h). Insets show high resolution images.

3.2.3.2.2. Pilot Scale

Based on the bench-scale syntheses BaTiO_3 , $\text{Ba}_{0.5}\text{Sr}_{0.5}\text{TiO}_3$ and SrTiO_3 were prepared using the pilot-scale counter-current reactor at Promethean Particles as representative samples of the compositional range. These materials were produced using the same synthetic procedure: a mixed aqueous solution of 0.05 M M^{2+} ($\text{M}^{2+} = \text{Ba}/\text{Sr}$) and 0.05 M Ti^{4+} was mixed in-flow with a 0.5 M NaOH solution before meeting a stream of water pre-heated to 430 °C at the counter-current mixing point. In contrast to the bench-scale system which operated at flow rates of 10 mL min⁻¹, 10 mL min⁻¹ and 20 mL min⁻¹ for the metal, base and water streams, respectively, giving a total flow-rate of 40 mL min⁻¹, the pilot-scale reactor operated at a total flow-rate of 800 mL min⁻¹. In the case of BaTiO_3 this gives production rates of ~5 g per hour for the bench-scale system and 80 g per hour at the pilot-scale.

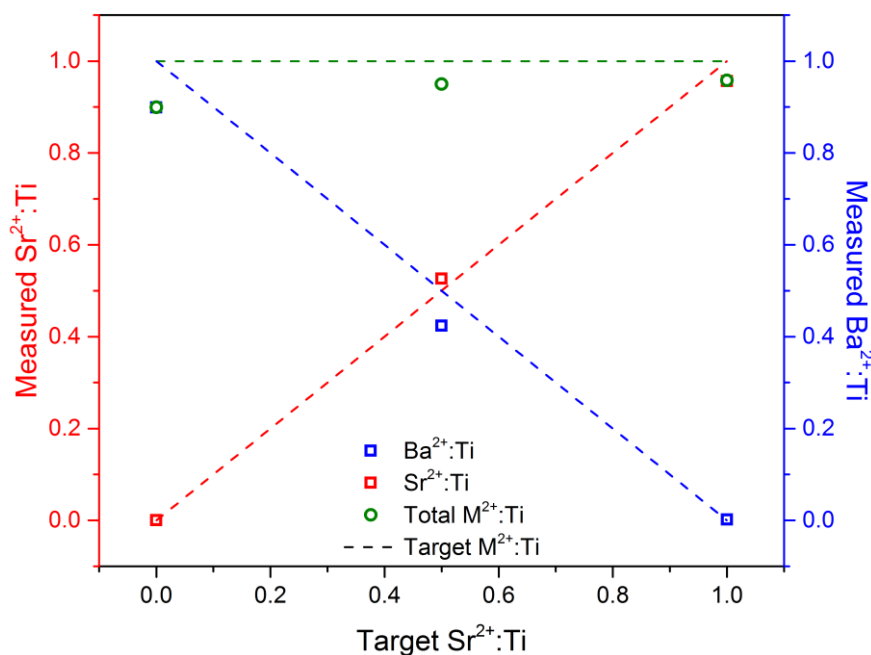


Figure 3.16: The $\text{M}^{2+}:\text{Ti}$ ratios of the pilot-scale $\text{Ba}_{(1-x)}\text{Sr}_x\text{TiO}_3$ samples determined by ICP-MS against x . Dashed lines indicate the targeted values.

Chapter 3: Metal Oxide Nanoparticles

Elemental analysis by ICP-MS of the obtained products, as shown in Figure 3.16, again reveals sub-stoichiometry (1:1 hampered by carbonate production), with the total M^{2+} :Ti ratio increasing from 0.9 to 0.96 on increasing the strontium content. These values are significantly higher than those observed in the bench-scale samples, indicating better incorporation of the metal ions into the titania structure at pilot scale; though the overall behaviour is similar. Strontium ions are seemingly incorporated preferentially over barium, such that the Sr:Ba ratio of the targeted 50:50 product is actually 55:45. The XRD patterns of the three $Ba_{(1-x)}Sr_xTiO_3$ samples prepared at the pilot-scale after washing are shown in Figure 3.17 (a). These pilot-scale samples appear to adopt the cubic perovskite structure; however as with the bench-scale products the Raman spectra (Figure 3.17 (b)) show a clear band at 715 cm^{-1} for both $x = 0$ and $x = 0.5$ due to the tetragonal phase. The band at 305 cm^{-1} is clearly present in the first derivative spectrum for $x = 0$, but it is not as clearly visible for $x = 0.5$. As expected the Raman spectrum of the $x = 1$ cubic $SrTiO_3$ sample does not possess these features. Again, increasing the strontium content causes a decrease in crystallite size and lattice parameter (Figure 3.17 (c)). It should be noted that in these cases the particle sizes are larger than those calculated for the bench-scale materials. The cubic lattice parameter also shows a minor increase ($\sim 0.01\text{ \AA}$) relative to the bench-scale samples in all cases. The properties of the three samples prepared at the pilot-scale are given in Table 3.3. TEM images and electron diffraction patterns of the pilot-scale samples are shown in Figure 3.18.

The pilot-scale reactor has been designed to mimic the bench reactor as closely as possible at the mixing point, with pipe geometries scaled to produce similar

Chapter 3: Metal Oxide Nanoparticles

Reynold's numbers, etc. With that said, it is all but impossible to completely replicate the exact conditions between the bench-scale and pilot-scale. Thus, the differences between the bench-scale and pilot-scale samples are attributed to slight variations inherent in the scale-up process. Factors such as pipe geometry, flow rates, temperature and cooling efficiency will influence the chemistry, mixing dynamics, and residence time (Lester, Aksomaityte et al. 2012), and thus even small deviations between the two systems could lead to different compositions and crystallite sizes. It can be cautiously suggested that the most likely reason for the observed differences between bench- and pilot-scale products is less efficient cooling due to the significantly larger tube diameters and higher flow rates, causing an effective increase in residence time.

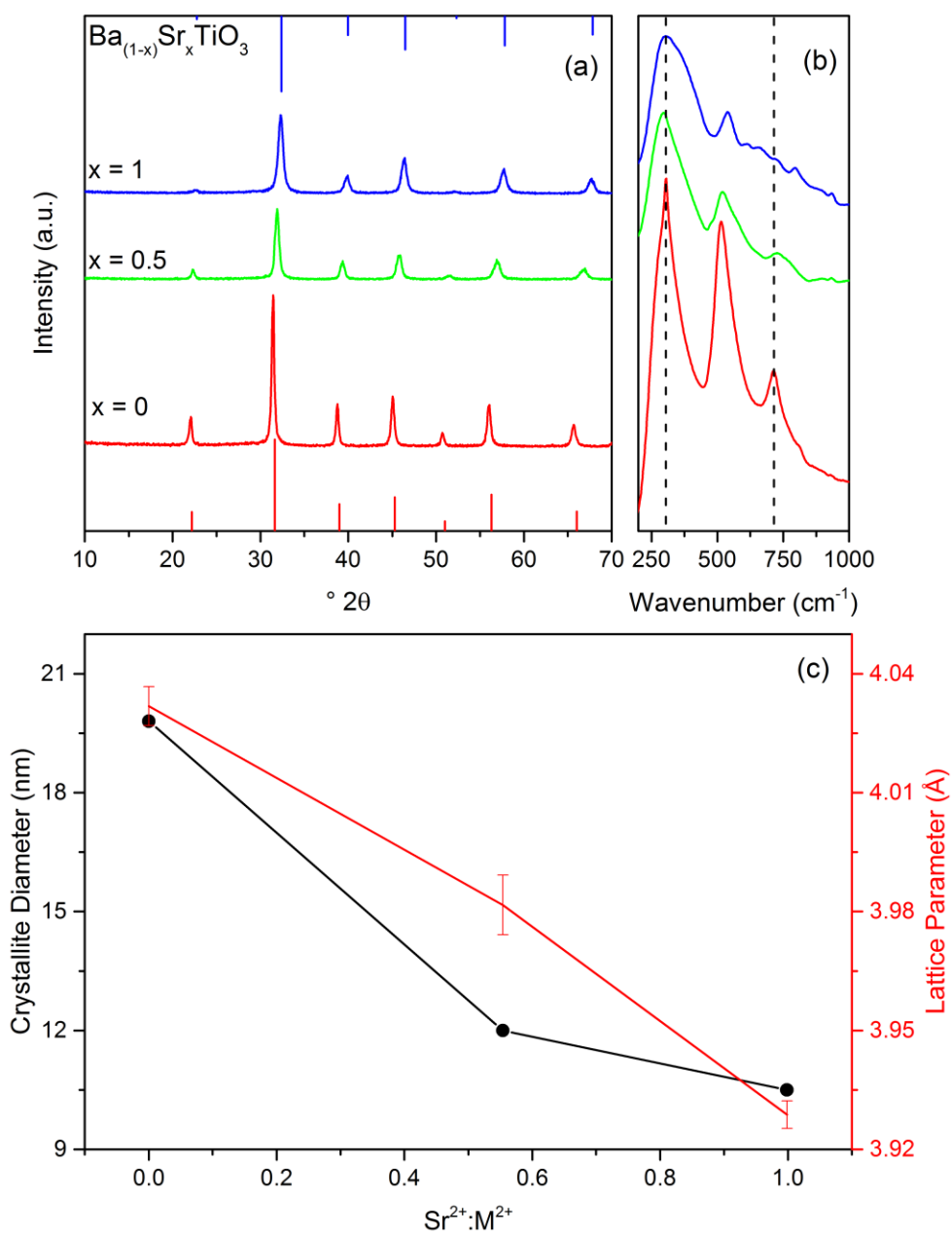


Figure 3.17: XRD patterns of pilot-scale $\text{Ba}_{(1-x)}\text{Sr}_x\text{TiO}_3$ samples with tick marks corresponding to cubic BaTiO_3 (bottom) and SrTiO_3 (top) (a) and the equivalent Raman spectra (b), and the effect of Sr content on crystallite size and cubic lattice parameter, a , as a function of Sr/Ti ratio (c).

Table 3.3: Properties of pilot-scale $\text{Ba}_{(1-x)}\text{Sr}_x\text{TiO}_3$ determined by ICP-MS, Raman spectroscopy and XRD. C and T indicate cubic and tetragonal phases, respectively.

Target x	Sr/Ti	Ba/Ti	M^{2+}/Ti	Sr/M^{2+}	Phase	Crystallite diameter (nm)	Cubic lattice parameter (\AA)
0	0.00	0.90	0.90	0.00	T	19.8	4.03(2)
0.5	0.53	0.42	0.95	0.55	T	12.0	3.98(2)
1.0	0.96	0.00	0.96	0.99	C	10.5	3.92(8)

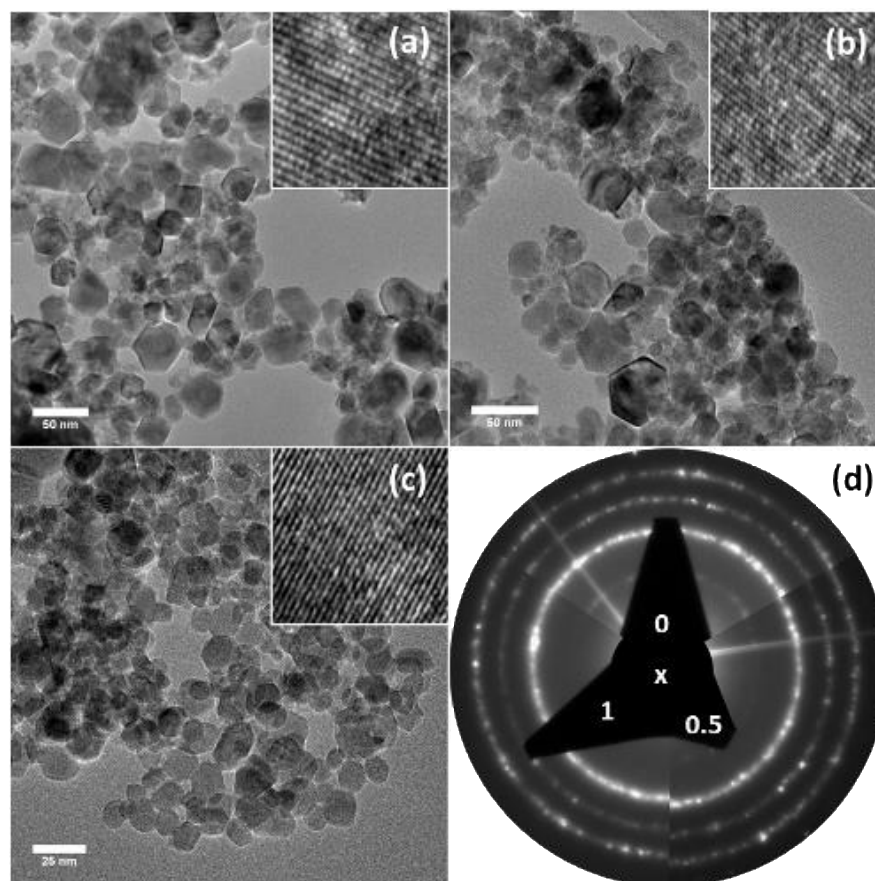


Figure 3.18: TEM images of pilot-scale $\text{Ba}_{(1-x)}\text{Sr}_x\text{TiO}_3$ samples at x values of 0, 0.5, and 1 (a – c, respectively), and a composite of the corresponding electron diffraction patterns (d). Insets show high resolution images.

3.2.3.2.3. Discussion and Outcomes

Prior work by Hayashi *et al.* (Hayashi, Noguchi *et al.* 2010, Hayashi, Noguchi *et al.* 2010) on the continuous-flow synthesis of BaTiO_3 has relied on using either titania sols or titanium tetrachloride as the titanate precursor. These present certain difficulties, as settling of the sol in the reagent container can cause concentration variations when pumped into the reactor, while the sol itself can cause pumping problems due to being particulate in nature and more viscous than water and this enhances wear of pump components. Similarly, while not addressed in these studies, the prolonged use of titanium tetrachloride

Chapter 3: Metal Oxide Nanoparticles

as a precursor would require the use of significantly more expensive halide resistant alloys such as Monel or Inconel to avoid etching and pitting (corrosion) of the reactor by halides at high temperatures. Furthermore these investigations did not consider the stoichiometry of the obtained products, despite also needing an acid washing step to remove carbonate impurities, which would suggest the products were also sub-stoichiometric.

Early work by Bocquet *et al.* (Bocquet, Chhor *et al.* 1999) and subsequent studies by Reverón *et al.* (Reveron, Aymonier *et al.* 2005, Reverón, Elissalde *et al.* 2006) used alkoxide precursors. This approach presents its own issues, such as the significantly higher expenses given the need for organic solvents, and special precautions to prevent unwanted hydrolysis of the unstable precursors such as using anhydrous alcohols for the precursor solutions. It was shown that carbonate impurities may be avoided in the solvothermal synthesis of barium titanate from alkoxide precursors using longer residence times of 2 - 3 minutes (Reveron, Aymonier *et al.* 2005). These carbonate-free products remained sub-stoichiometric, however, which indicates that residual Ba^{2+} ions were retained in solution. When a large excess of Ba:Ti (2:1) was used in this alkoxide system a product with a Ba:Ti ratio of 1.05:1 was obtained with low levels of $BaCO_3$ impurities. This approach could of course be easily adapted to the hydrothermal route developed here, though the preferential inclusion of strontium into the mixed perovskite would affect the stoichiometry of targeted $Ba_{(1-x)}Sr_xTiO_3$ phases. Using consistent reaction conditions and reactors this discrepancy could be accounted for through the establishment of a standard curve of input stoichiometry versus product stoichiometry for a given reactor and reaction system. Reverón *et al.* also reported the continuous synthesis of

Chapter 3: Metal Oxide Nanoparticles

the full $\text{Ba}_{(1-x)}\text{Sr}_x\text{TiO}_3$ solid solution range with stoichiometric control using the alkoxide route and long residence times (Reverón, Elissalde et al. 2006). The importance of this long residence time is consistent with the thorough batch hydrothermal studies performed by Roeder *et al.* (Roeder and Slamovich 1999) and the continuous-flow studies of Matsui *et al.* (Matsui, Noguchi et al. 2008) who showed a significant increase in crystallinity of BaTiO_3 on increasing residence time from 7 ms to 2 s. The results presented herein on moving from bench- to pilot-scale, whereby both particle size and overall $\text{M}^{2+}:\text{Ti}$ ratio increased, also suggest that further increasing the residence time would allow greater control of stoichiometry at the expense of producing larger nanoparticles. The Nottingham bench-scale system is highly adaptable, not just in accessibility to an array of materials, but in its flexible configuration and utilisation, and hence, can be easily modified to increase the residence time and, while the same alterations can be made to the pilot-scale system, it would of course be far more costly and would certainly not be a trivial task. Despite this, the results here suggest that the full range of $\text{Ba}_{(1-x)}\text{Sr}_x\text{TiO}_3$ should be readily accessible through a fully hydrothermal continuous-flow method, and with minor alterations that this approach is scalable to industrially viable levels.

3.2.4. Conclusions

The first fully hydrothermal continuous-flow route to the mixed metal perovskite $\text{Ba}_{(1-x)}\text{Sr}_x\text{TiO}_3$ system has been developed. It was found that, in all cases, MCO_3 species were formed which are believed to be due to dissolved CO_2 present in the water used to prepare the precursor solutions and in the

Chapter 3: Metal Oxide Nanoparticles

reactor. These carbonates can be easily removed by a simple washing step with the possibility of this being undertaken in situ downstream of the reaction point. Carbonate formation however results in a decreased M^{2+} :Ti ratio in the perovskite, which will have an adverse effect on both reproducibility and the important ferroelectric properties of the products. The process thus requires further development. It is suggested that simply increasing the residence time of the counter-current reaction system would be sufficient to promote full incorporation of the M^{2+} ions from solution. The work performed herein shows that the full phase diagram of $Ba_{(1-x)}Sr_xTiO_3$ should be readily accessible by a continuous-flow hydrothermal technique, and more importantly the scalability of the system has been demonstrated by implementing the 5 g h^{-1} bench-scale reaction at 80 g h^{-1} on a pilot-scale system. This fully hydrothermal continuous-flow route thus represents a further step towards a more affordable and environmentally benign large-scale method for the production of barium strontium titanate nanopowders, and demonstrates CFHS and the Nottingham counter-current reactor as a powerful tool for accessing the full compositional range of a family of nanomaterials.

4. Metal Sulphide Nanomaterials

4.1. Introduction

Metal sulphides constitute a diverse and important class of target materials, and the wide range of structures, properties and applications exhibited by metal sulphides make them of interest both scientifically and industrially. Metal sulphides were therefore a logical progression from metal oxides and a key target of the new material programme within the SHYMAN project and of this thesis, and this chapter studies the development of a general continuous flow route towards sulphide based materials.

Metal sulphide nanomaterials such as zinc, cadmium and lead sulphide are among the quintessential quantum dot materials (Wang 2005, Costa-Fernández, Pereiro et al. 2006, Smet, Moreels et al. 2010). A vast library of research is devoted to exploring their size and shape dependent optoelectronic properties, exploiting fluorescent properties for applications in biomedical imaging (Wu and Yan 2013), LEDs (Tan, Zhang et al. 2007) and photovoltaic cells (Plass, Pelet et al. 2002). Covellite phase CuS, for example, was the first naturally occurring mineral found to exhibit superconductivity (Di Benedetto, Borgheresi et al. 2006). It is also investigated for its unusual optical properties (Routzahn, White et al. 2012, Zhao and Burda 2012) and potential use as a battery material (Zhao and Burda 2012). Iron sulphides, which display a wide range of stoichiometries from Fe_3S_4 , to FeS_2 with intermediary phases $\text{Fe}_{(1-x)}\text{S}$ and $\text{Fe}_{(1+x)}\text{S}$ (Rickard and Luther 2007), are commonly studied owing to their importance in biological systems, including iron reducing and magnetotactic

Chapter 4: Metal Sulphide Nanomaterials

bacteria (Faivre and Schüler 2008). They are also under investigation as environmental remediation agents for the removal of heavy metals (Kim, Kim et al. 2011) and as promising candidates for cathode materials in lithium ion batteries (Wu, Song et al. 2011). Other metal sulphides such as Bi_2S_3 are being considered as viable replacements for the toxic telluride-based thermoelectric materials (Zhao, Zhang et al. 2008). The layered metal chalcogenide molybdenum disulphide, MoS_2 , has also come under intense scrutiny in recent years. While it has long been of interest for its catalytic properties (Grange and Vanhaeren 1997) and applications in high temperature lubrication, it is its position as a graphene analogue (Ramakrishna Matte, Gomathi et al. 2010) and member of the so-called inorganic fullerenes (Feldman, Frey et al. 1996, Li, Ge et al. 2004, Blanco, Uzio et al. 2014) and its potential in intercalation chemistry and battery materials (Hu, Chen et al. 2014, Pumera, Sofer et al. 2014, Sun, Zhang et al. 2014) which have driven much of the recent research activity.

The synthesis of metal sulphide nanomaterials has previously been performed in a variety of ways, including hot-injection (Joo, Na et al. 2003, Zhang, Shen et al. 2010), thermolysis of single source precursors (Mandal, Piburn et al. 2011, Shen, Zhang et al. 2011) and hydrothermal and solvothermal routes (Wang, Chen et al. 2006, Ni, Wei et al. 2007, Xia, Chen et al. 2008, Salavati-Niasari, Ghanbari et al. 2009, Cheng, Wang et al. 2010). Microfluidic syntheses have also been investigated for the synthesis of metal chalcogenide based quantum dots by de Mello (Nightingale and de Mello 2010) and Alivisatos (Chan, Mathies et al. 2003). Great strides have been made in the production of few-layer 2-dimensional nanosheets of MoS_2 through vapour deposition techniques and exfoliation from crystalline MoS_2 (Coleman, Lotya

Chapter 4: Metal Sulphide Nanomaterials

et al. 2011, Yin, Yan et al. 2014). Inorganic fullerene-like MoS₂ structures have been synthesised by various methods, including vapour phase reactions (Li, Ge et al. 2004) and post-synthetic annealing of solution processed core-shell precursors (Blanco, Uzio et al. 2014). Nanostructured and hierarchical MoS₂ materials for catalytic and electrochemical applications have also been produced by vapour deposition methods (Wang, Feng et al. 2013) as well as hydrothermal processes, though the hydrothermal routes typically require a post-synthetic annealing step to induce crystallisation (Chen and Fan 2001, Hu, Chen et al. 2014).

Previous work at Nottingham by Dr Selina Tang towards the metal sulphide nanoparticles ZnS and CdS used thiocarbohydrazide as the sulphur source, however, since this reagent possesses relatively high levels of toxicity, this route is limited in scale-up potential. Thiourea was identified as a potentially safer alternative due to reduced toxicity, in addition to being water soluble, readily available and cheap. Examples of metal sulphide nanoparticle production using thiourea were also evident in the literature (Wageh, Shu-Man et al. 2003). It was postulated that thiourea would break down to hydrogen sulphide or hydrosulphide (HS⁻) to provide an active sulphur reactant and source at the mixing or reaction point of the reactor.

Traditionally the Nottingham counter-current reactor can be viewed as a nucleation device – that is, particles nucleate almost instantaneously upon heating and mixing of the metal reagent stream with water or supercritical water, brought on by supersaturation and therefore formation of particles. The particle size is governed by the size of the initial nuclei, which itself is dictated

by the temperature of the reaction and the quantity of precursor available at the nucleation point. Upon formation, the particles are viewed as being produced within extremely small reaction times, with no further growth processes occurring downstream of the reaction point.

This chapter seeks to not only develop a general route towards metal sulphide nanoparticle production using CFHS, but also start to understand the basic principle of developing the reactor further than a nucleation device, capable of inducing growth processes, using metal sulphide synthesis with thiourea as a model. Work in this chapter has been adapted and expanded from two publications; one focussed on the six metal sulphides prepared by the general route using the standard reactor configuration and the other on the production of molybdenum sulphide. These can be found through the chapter footer.

4.2. Experimental

4.2.1. Synthesis

All materials were purchased from Sigma-Aldrich and used as received. $\text{Zn}(\text{NO}_3)_2 \cdot 6\text{H}_2\text{O}$, $\text{Cd}(\text{NO}_3)_2 \cdot 4\text{H}_2\text{O}$, $\text{Pb}(\text{NO}_3)_2$, $\text{Cu}(\text{NO}_3)_2 \cdot 2.5\text{H}_2\text{O}$, $\text{FeSO}_4 \cdot 7\text{H}_2\text{O}$, $\text{Bi}(\text{NO}_3)_3$ and $(\text{NH}_4)_6\text{Mo}_7\text{O}_{24} \cdot 4\text{H}_2\text{O}$ were used as the metal sources. All salts were dissolved in the appropriate amounts of de-ionised water prior to use, with the exception of $\text{Bi}(\text{NO}_3)_3$, which was dissolved in a 5% nitric acid solution to prevent the formation of the insoluble sub-nitrates. In all cases thiourea was used as the sulphur source. All reactions except MoS_2 synthesis were carried out using the vertically aligned counter-current mixing reactor operating in the standard configuration designed by Lester *et al.* (Lester, Blood

Chapter 4: Metal Sulphide Nanomaterials

et al. 2006), shown in Figure 4.1, and described in Section 1.4.3. The synthesis of MoS₂ required reactor modifications and further chemical processes and as such, is described separately later.

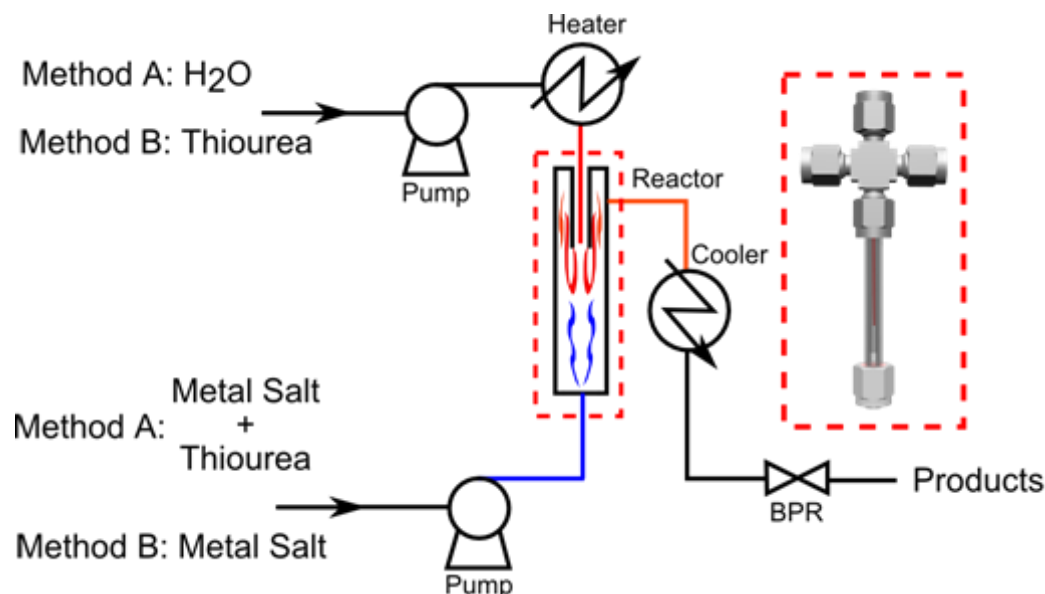


Figure 4.1: A simplified schematic of the counter-current continuous flow reactor for the synthesis of metal sulphide nanomaterials with Method A and B labels indicating the difference in entry of the thiourea precursor into the reactor.

Two methods were developed based around a general route to the continuous flow synthesis of metal sulphide nanomaterials, varying in the point of entry of thiourea to the reactor:

Method A: A solution of metal salt is prepared, typically at 0.05 M. To this is added sufficient thiourea to provide a two-fold excess of sulphur relative to the stoichiometry of the expected product. This mixed metal/thiourea solution is fed upwards as the unheated stream and brought into contact with the heated water stream. Using this method it was found that temperatures of ~ 400 °C are required to break down sufficient thiourea to create the active sulphur source

Chapter 4: Metal Sulphide Nanomaterials

needed to produce significant yields within the short contact time, and as such, lower temperature reactions are not reported.

Method B: Metal salt solutions, typically 0.025 M in de-ionised water, are pumped as the unheated up-flow, while a separate solution of 0.025 M thiourea is pumped through the preheater as the downflow at twice the flow-rate, maintaining the two-fold sulphur excess. Passing the thiourea through the preheater provides a longer residence time for the decomposition to occur, and thus the temperature of the heater may be varied between 250 °C and 400 °C.

Unless otherwise stated the flow rates in both methods were maintained at 20 mL min⁻¹ for the downflow and 10 mL min⁻¹ for the upflow. Products were obtained as aqueous suspensions. Powders were isolated and washed with de-ionised water by repeated centrifugation steps before drying overnight at 70 °C. Further synthesis details of all reactions are provided in Table 4.1.

Chapter 4: Metal Sulphide Nanomaterials

Table 4.1: Details of metal sulphide syntheses performed.

Target	Method	Concentration (mol L ⁻¹)		Flow rate (mL min ⁻¹)		Temperature (°C)			Product
		[M ^{x+}]	[Thiourea]	Preheated	Cold	T _{set}	T ₁	T ₂	
ZnS	A	0.05	0.1	20	10	400	408	300	ZnS
	B	0.025	0.025	20	10	250	245	157	ZnS
	B	0.025	0.025	20	10	300	293	191	ZnS
	B	0.025	0.025	20	10	350	348	246	ZnS
	B	0.025	0.025	20	10	400	393	326	ZnS
CdS	A	0.05	0.1	20	10	400	410	302	CdS
	B	0.025	0.025	20	10	250	245	163	CdS
	B	0.025	0.025	20	10	300	298	194	CdS
	B	0.025	0.025	20	10	350	347	239	CdS
	B	0.025	0.025	20	10	400	392	360	CdS
PbS	A	0.05	0.1	20	10	400	408	300	PbS/PbSO ₄
	B	0.025	0.025	20	10	250	243	155	PbS
	B	0.025	0.025	20	10	300	292	187	PbS
CuS	A	0.025	0.05	20	10	400	385	365	CuS/Cu ₉ S ₅ *
	B	0.025	0.025	20	10	250	243	155	CuSCN
	B	0.025	0.025	20	10	300	295	187	CuS
Fe_(1-x)S	A	0.025	0.05	20	10	400	401	365	Fe _(1-x) S
	B	0.025	0.025	20	10	250	247	158	FeOOH
	B	0.025	0.025	20	10	300	292	192	FeOOH
	B	0.025	0.025	20	10	350	343	236	FeOOH
	B	0.025	0.025	20	10	400	389	340	Fe _(1-x) S
Bi₂S₃	A	0.025	0.075	20	10	400	400	351	Bi ₂ S ₃ / Bi ₂ O ₂ SO ₄
	B	0.025	0.3	5	10	300	263	93	Bi ₂ S ₃ *
	B	0.0125	0.15	5	10	250	227	89	Bi ₂ S ₃

T_{set} = Set temperature of the preheater, T₁ = Temperature of the preheated stream measured immediately after the heater, T₂ = Temperature measured post-mixing, *Caused the rig to block.

4.2.2. Characterisation

Powder X-ray diffraction patterns were recorded using a Bruker D8-Advance diffractometer with Cu K_α radiation ($\lambda = 1.5418 \text{ \AA}$). A 2θ range of 5 to 70° was scanned with a step size of 0.04° 2θ and a collection time of 6 s/step. Crystallite diameters were calculated using the Scherrer equation from line broadening determined with the program Xfit (Cheary and Coehlo 1996). Reitveld refinements were performed (Dr Peter Dunne) on all zinc and

Chapter 4: Metal Sulphide Nanomaterials

cadmium sulphide samples to determine phase composition and crystallite diameters. The GSAS suite within EXPGUI was used for all refinements (Larson and Von Dreele 1994, Toby 2001). Selected materials were examined by full Transmission Electron Microscopy using a JEOL 2100F at an accelerating voltage of 200 kV. Samples were prepared for transmission electron microscopy by resuspending the dried powders in acetone with sonication and then deposited on 300 mesh lacey carbon coated copper grids. The fluorescence spectra of all ZnS samples prepared by both methods A and B were recorded using a Flexstation II fluorimeter from Molecular Devices. Samples were prepared by redispersing the dried powder in water at approx. 0.1% (wt/v) and sonicating for 10 to 15 minutes immediately prior to measurement. For each sample, ~ 200 μ L of material was loaded into a UV-transparent 96-well plate, which was then scanned by the fluorometer. The fluorescence spectra at excitation wavelengths of 370 nm and 290 nm were recorded. These wavelengths were selected after a full sweep of excitation wavelengths between 250 and 400 nm and the corresponding emission spectrum was analysed to find the most intense wavelengths of emission of the ZnS samples – each sample was read ~ 10 times with 2 nm step size at excitation wavelengths of 370 nm and 290 nm). Blank samples of water were also recorded and subtracted from the sample runs to provide a background.

4.3. Results & Discussion

4.3.1. ZnS

4.3.1.1. ZnS - Method A

The XRD pattern of ZnS obtained by Method A is shown in Figure 4.2 (a). Rietveld refinement shows that the product is comprised of a mixture of 58% cubic sphalerite and 42% hexagonal wurtzite phase ZnS, with average crystallite diameters of 12.4 and 22.6 nm respectively. TEM images (Figure 4.2 b & c) show large agglomerates of the primary particles (nanoflowers) with diameters of ~ 200 nm. High magnification imaging reveals these agglomerates to be comprised of smaller nanocrystalline domains, as expected based on the refinement results demonstrating the mixture of phases and sizes. In addition, streaking/striations are visible throughout the surface of the crystallites and agglomerates, indicative of a significant amount of twinning or stacking faults between adjacent particles and within individual particles. This is a commonly observed phenomenon with zinc sulphide materials (Zhang, Gilbert et al. 2003, Zhang, Chen et al. 2006, Zhang and Banfield 2009) due to the closely related cubic and hexagonal phases causing facile coexistence of both phases within a repeating lattice. Furthermore, the flower-like shape of the agglomerates is likely to result from this twinning. Similar morphologies have often been observed in sphalerite-wurtzite systems (Huijuan and Limin 2006, Shi, Chen et al. 2007, Guo, Wang et al. 2011, Cao, Hu et al. 2012, Mahdi, Hassan et al. 2012) with the growth of hexagonal phase petals from a cubic phase core being a common occurrence in mixed cubic/hexagonal phase systems.

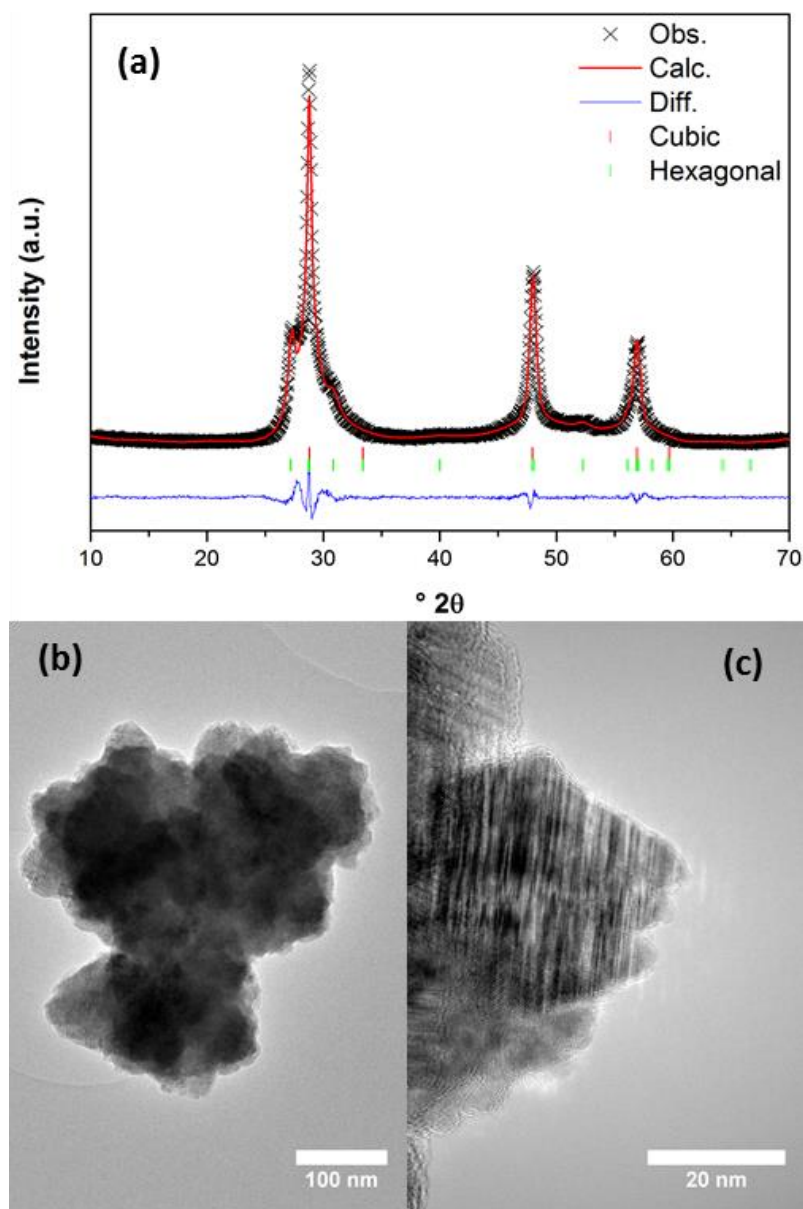


Figure 4.2: The refined XRD pattern (a) and TEM images (b, c) of ZnS prepared by Method A. Reitveld refinement was performed with both cubic ($F43m$, $a = 5.3656 \text{ \AA}$) and hexagonal ($P6_3mc$, $a = 3.7846 \text{ \AA}$, $c = 6.2089 \text{ \AA}$) phases.

4.3.1.2. ZnS – Method B

The XRD patterns of the ZnS obtained by Method B, where the thiourea is preheated, are shown in Figure 4.3 (a). From the XRD patterns it is apparent that increasing the temperature from 250 °C to 400 °C leads to both a general increase in crystallite size (narrowing of peaks) and a transformation from pure

sphalerite to a mixture of the sphalerite and wurtzite phases at higher temperatures, as demonstrated by the emergence of peaks characteristic of the hexagonal wurtzite phase such as at $\sim 27^\circ 2\theta$ at 400 °C. The hexagonal wurtzite phase content increases from 0% at a synthesis temperature of 250 °C to $\sim 22\%$ at temperatures of 300 °C and 350 °C, while the sample prepared at 400 °C contains 34% wurtzite. The calculated crystallite diameters of the cubic sphalerite phase increases with increasing synthesis temperature, from 3.5 nm at 250 °C, to 4.9 nm at 350 °C. The samples prepared at 350 °C and 400 °C both have crystallite diameters close to 10 nm. The calculated diameters of the hexagonal wurtzite phase increases from 6.3 nm to 11.7 nm on increasing the reaction temperature from 300 °C to 350 °C, followed by a decrease in size to 9 nm on further increasing the synthesis temperature to 400 °C, possibly due to increased supersaturation under supercritical conditions. Table 4.2 and Figure 4.3 (b) show the phase composition and crystallite diameters of the four ZnS samples prepared by Method B as calculated from the Reitveld refinements. TEM images of the ZnS obtained by Method B, Figure 4.4, show that the products obtained at temperatures up to 350 °C are comprised of agglomerated nanocrystals. The crystalline domain sizes are consistent with those obtained from analysis of the XRD data. Synthesis at 400 °C affords larger, less agglomerated cuboidal crystallites, again with sizes matching those predicted by XRD analysis. The agreement between the sizes of the crystallites observed by TEM and calculated by XRD suggests that the two phases exist as separate crystallites, rather than as twinned crystals (this is further evidenced by the apparent single crystalline nature of the particles observed by HRTEM).

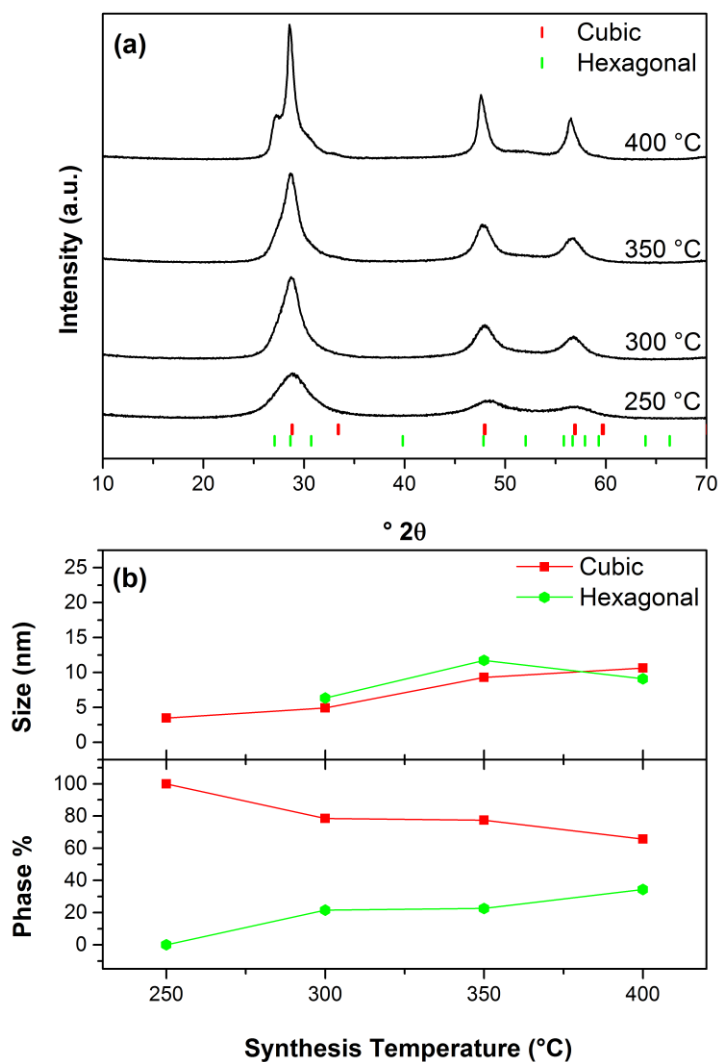


Figure 4.3: The XRD patterns (a) and calculated crystallite diameters and phase percentages from Reitveld refinements (b) of the ZnS nanoparticles obtained by Method B.

Table 4.2: Phase composition and calculated crystallite diameters, D , of cubic sphalerite (Sph) and hexagonal wurtzite (W) phases of ZnS samples prepared by Method B.

T/°C	%Sph	%w	D_{Sph}/nm	D_{w}/nm
250	100	0	3.5	-
300	78.4	21.6	4.9	6.4
350	77.4	22.6	9.3	11.8
400	65.6	34.4	10.6	9.1

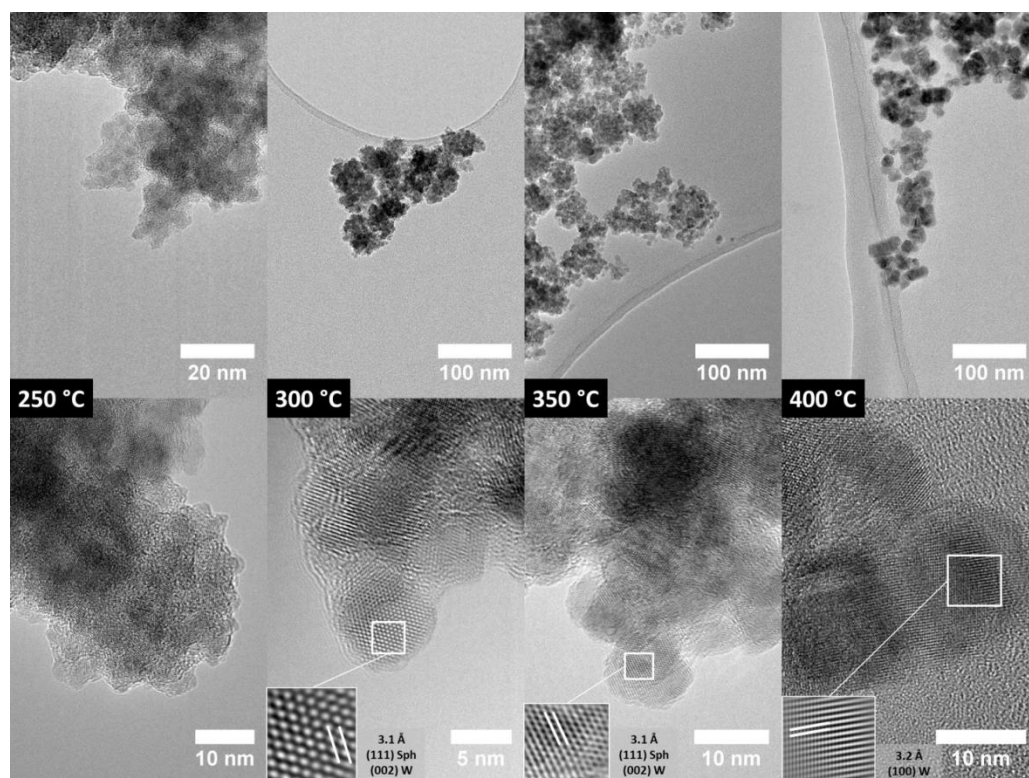


Figure 4.4: TEM images of ZnS nanoparticles obtained by Method B at the indicated synthesis temperatures. Insets show reconstructed images highlighting crystal planes of the cubic sphalerite (Sph) and hexagonal wurtzite (W) phases of ZnS.

4.3.1.3. ZnS - Growth vs. Nucleation Dominated Formation Mechanisms

The large size of the agglomerated particles and the significant twinning observed in the material prepared by Method A, wherein both the zinc nitrate and thiourea are fed against the superheated water stream, suggests a growth dominated formation mechanism. The decomposition of thiourea to an active sulphur source, HS^- , happens concurrently with the formation of the zinc sulphide nanoparticles, leading to a slow, growth dominated process which allows for the intergrowth of the two sphalerite and wurtzite phases. Whilst the cooling of the product stream is usually described as instantaneous, in reality there is a temperature gradient over the course of a few seconds where the

Chapter 4: Metal Sulphide Nanomaterials

reaction solution, or the solution now containing product and unreacted precursor, holds residual heat from the reaction. We can thus imagine that unreacted thiourea which is present in excess can continue to decompose to HS^- , undergoing further reaction with unreacted precursor and promote growth processes to occur. In contrast, Method B, where the thiourea is first completely broken down by being fed separately through the preheater, promotes a nucleation driven process due to the immediate availability of HS^- upon meeting the metal source at the mixing point forcing the rapid nucleation and precipitation of very small ZnS nanoparticles. These processes are described in greater detail in Section 4.4.

It has previously been suggested by other researchers that the formation of ZnS nanoparticles and the crystal structure they adopt proceeds via the aggregation of molecular clusters with the nature of the clusters determining the phase of the product formed (Luther III, Theberge et al. 1999). Smaller $\text{Zn}_3\text{S}_3(\text{H}_2\text{O})_6$ and $\text{Zn}_4\text{S}_6(\text{H}_2\text{O})_4^{4-}$ clusters which favour sphalerite formation are formed at lower S/Zn ratios, while the larger $\text{Zn}_6\text{S}_6(\text{H}_2\text{O})_9$ clusters formed at higher S/Zn ratios promote wurtzite formation. In Method B, the thiourea is passed through the preheater and is therefore broken down in varying degrees depending on the temperature of the preheater. At the lowest synthesis temperature of 250 °C, the breakdown of thiourea to HS^- is incomplete, leading to a lower S/Zn ratio. We can therefore postulate that this leads to the formation of smaller intermediate clusters which favours sphalerite formation. In combination with the lower temperature the formation of the kinetically favoured sphalerite phase is thus promoted. Elevation of the reaction temperature leads to a more complete breakdown of the thiourea increasing the S/Zn ratio, and producing

larger intermediate clusters which, combined with the enhanced stability of the wurtzite phase at higher temperatures permits its nucleation.

4.3.1.4. Fluorescence of ZnS Nanomaterials

ZnS materials express properties allowing them to become functional in applications such as biomedical imaging probes (Gao, Cui et al. 2004, Michalet, Pinaud et al. 2005), exploiting their photostability, brightness and size-dependent photoluminescence (Scholes and Rumbles 2006). Cadmium based fluorescent materials are losing favour, due to the toxicity of cadmium, which limits their biomedical or household electronic application. Cadmium cannot be metabolised by the human body (Choi and Frangioni 2010) and as such limits its biological use. ZnS however, consisting of two biologically necessary constituents of the human body (Yu, Kwon et al. 2013), are finding application, particularly when doped with Mn^{2+} (Sooklal, Cullum et al. 1996, Suyver, Wuister et al. 2001, Goudarzi, Aval et al. 2009), for fluorescence applications. This therefore warranted fluorescence testing to investigate the potential of the ZnS nanoparticles produced by CFHS in the counter-current reactor towards these applications.

At an excitation wavelength of 370 nm all samples show the typical self-activated blue luminescence band of ZnS centred around 440 nm (Figure 4.5, top). This is a well-known transition arising from luminescence from self-activated centres due to sulphur lattice vacancies (Becker and Bard 1983, Sooklal, Cullum et al. 1996). These sulphur vacancies produce localised donor sites which upon irradiation are ionised and populate the conduction band, thus

Chapter 4: Metal Sulphide Nanomaterials

creating charge carriers which undergo internal processes before returning to the ground state and emitting a lower energy photon.

The sample prepared by Method A also shows a strong emission at 590 nm. This was found to be coupled with an excitation band at 290 nm (Figure 4.5, bottom) and excitation at this wavelength gives high intensity orange fluorescence at 590 nm. Fluorescence bands in this region are commonly observed in Mn²⁺ doped ZnS, attributed to the ⁴T₁ → ⁶A₁ transition in the 3d shell of Mn²⁺ (Bhargava, Gallagher et al. 1994, Goudarzi, Aval et al. 2009); however all our samples were prepared from identical sources and no evidence for the presence of manganese has been found in any sample. Similar emissions have previously been reported for ZnS nanobelts and attributed to Mn²⁺ contamination (Denzler, Olschweski et al. 1998, Zhu, Bando et al. 2003), however these authors also reported EDX and TEM results which suggested their product was highly pure. Other zinc sulphide nanoparticles/clusters showed orange luminescence at 590 nm and this was also attributed to low levels of manganese contamination, thus behaving as a dopant, from the zinc precursor (Becker and Bard 1983). That there is no trace of this orange luminescence in the samples prepared by Method B using the same zinc precursor (only 440 nm) indicates that this may be a result of the significant twinning observed in the Method A sample. The twinning and intergrowth of the sphalerite and wurtzite phases is likely to induce a variety of defects, from the observable stacking faults to more subtle point defects. It is also possible that surface elemental sulphur species may be generated in this system, which has been implicated as a likely source of similar fluorescent bands in ZnS

nanobelts (Ye, Fang et al. 2004). It may be postulated that it is these defects which are the source of this fluorescence band.

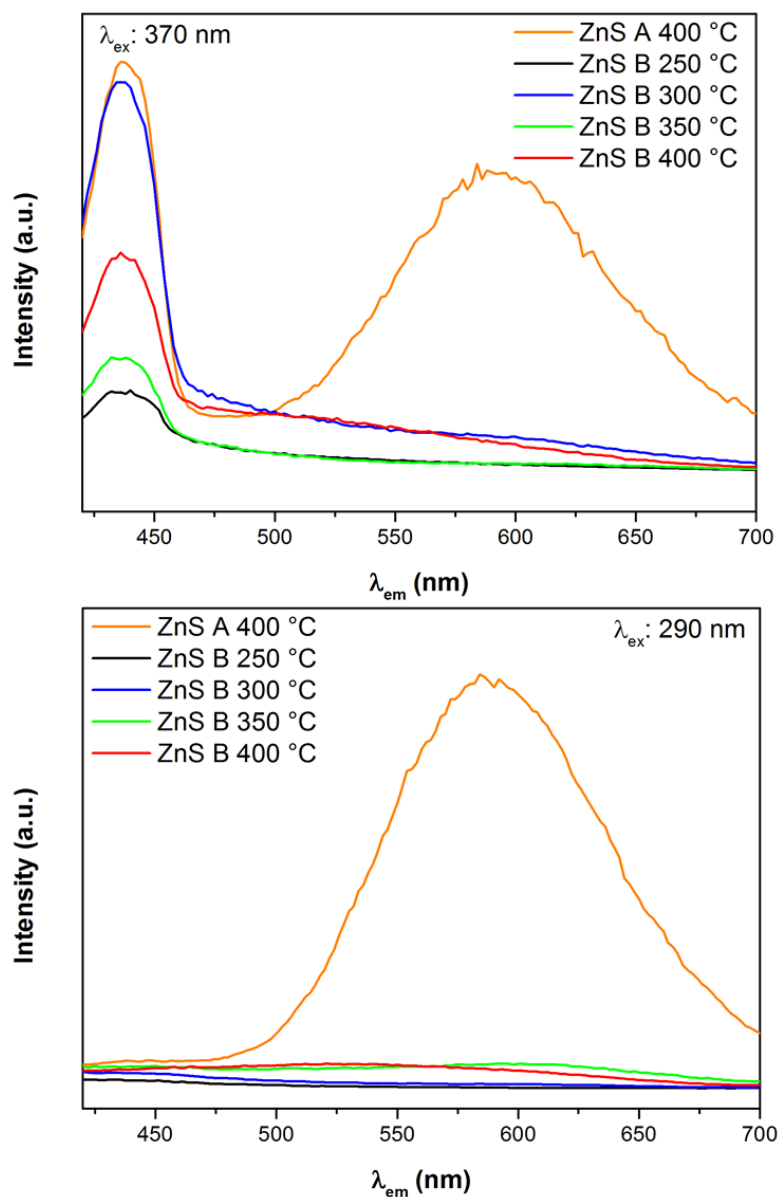


Figure 4.5: Fluorescence spectra of ZnS samples prepared by Method A and Method B at the temperatures shown with an excitation wavelength of 370 nm (top) and 290 nm (bottom).

4.3.2. CdS

4.3.2.1. CdS – Method A

The synthesis of cadmium sulphide by Method A results in a mixture of 11% cubic hawleyite and 89% hexagonal greenockite phase CdS, as shown by the XRD pattern in Figure 4.6 (a). The TEM images of this product, Figure 4.6 (b & c), reveal a mixture of rod, tetrapod and multipodal morphologies. Several clearly defined tetrapodal nanoparticles are also observed with 40 nm diameter cores and 100 nm long arms. These morphologies are well-established in regards to cadmium sulphide and selenide nanomaterials (Manna, Scher et al. 2000, Chen, Xie et al. 2002, Talapin, Nelson et al. 2007) and arise from the same cubic/hexagonal intergrowth phenomenon discussed in relation to the ZnS sphalerite-wurtzite system. The cubic and hexagonal phases of CdS are closely related, with the c-face of the hexagonal phase being related to the (111) plane of the cubic phase by a simple rotation operation. It has been shown, both computationally and experimentally through *in-situ* transmission electron microscopy, that spherical cadmium selenide nanoparticles undergo a thermally induced surface rearrangement to the hexagonal phase. The transformation gives a similar (if stunted) tetrapodal morphology (Fan, Yalcin et al. 2013) to that seen here. It may be suggested that this product is formed by the initial nucleation of the kinetically favoured cubic phased nanoparticles (formed from metal salt reacting with small quantities of the active sulphur species that has broken down at the reaction point), which at the elevated temperatures employed here undergo a surface rearrangement to give hexagonal phase capping on the (111) faces of the cubic core. This may result

in a tetrahedral or multifaceted arrangement. Further deposition of material which is formed immediately after the reaction point and continues to form whilst the reactant solution is held at elevated temperature then causes growth of the hexagonal phase arms leading to the morphologies observed here (Kudera, Carbone et al. 2007). This phenomenon is summarised in Figure 4.7. The rod-like structures likely arise from the direct growth of nucleated hexagonal phase nanoparticles.

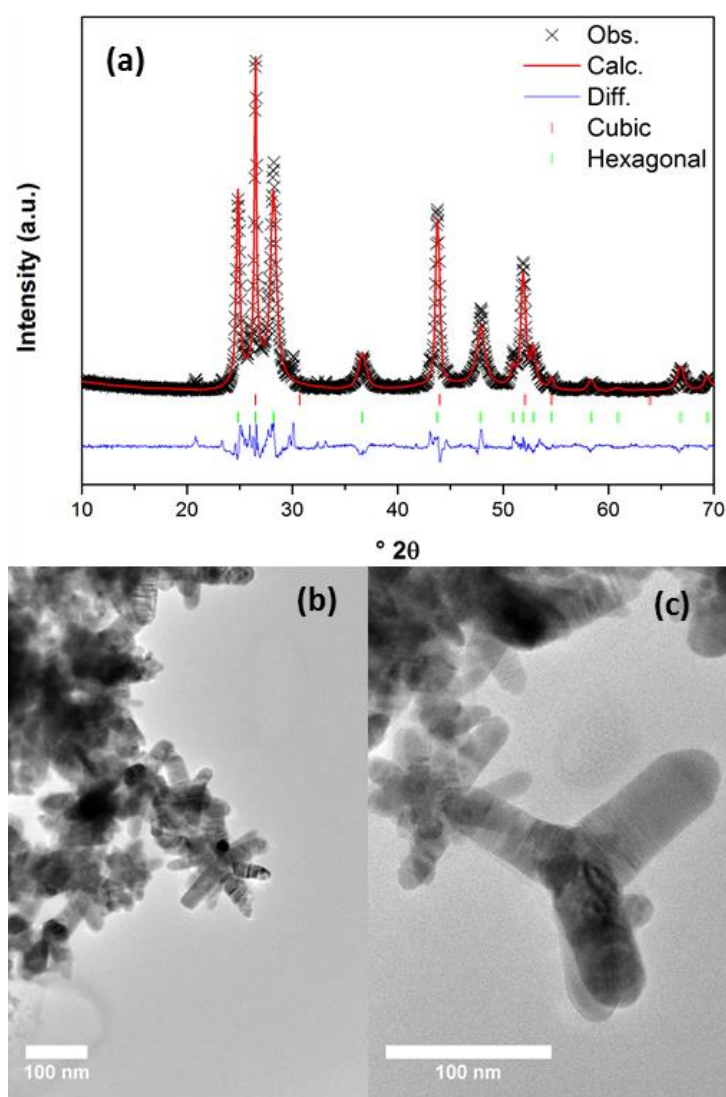


Figure 4.6: The refined XRD pattern (a) and TEM images (b, c) of CdS prepared by Method A. Reitveld refinement was performed with both cubic ($F43m$, $a = 5.8365 \text{ \AA}$) and hexagonal ($P6_3mc$, $a = 4.1361 \text{ \AA}$, $c = 6.7222 \text{ \AA}$) phases.

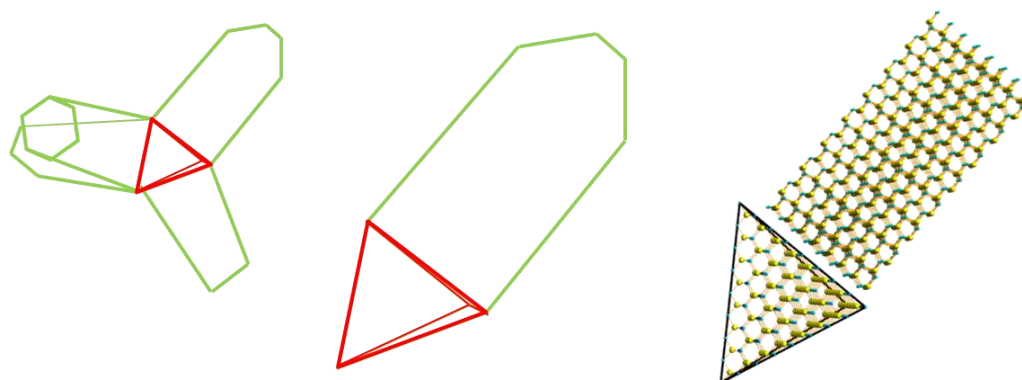


Figure 4.7: Proposed formation of the observed tetrapod morphology of CdS (red indicates the initial core, followed by growth of the hexagonal phase arms (green)).

4.3.2.2. CdS – Method B

As with zinc sulphide, the synthesis of cadmium sulphide by Method B results in the formation of very small nanoparticles. The XRD patterns, refined compositions and crystallite diameters are shown in Figure 4.8 and Table 4.3. At synthesis temperatures of 250 °C the sample consists of 72% cubic hawleyite and 28% hexagonal greenockite phases. The hexagonal phase content increases to 35% at 300 °C, while those samples prepared at 350 °C and 400 °C are comprised of a close to 50:50 mix of the two phases. The calculated crystallite diameters of both phases are ~ 7.3 nm and ~ 8.5 nm when prepared at 250 °C and 300 °C, respectively. Increasing the temperature to 350 °C increases the size of the cubic and hexagonal phase crystallites to 13.6 nm and 16.3 nm. Similar sizes are obtained for the 400 °C sample.

The TEM images of the obtained products, Figure 4.9, show that, aside from the sample prepared at 250 °C, the cadmium sulphide is generally less agglomerated than the zinc sulphide produced by the same method. The crystallite sizes of the nanoparticles observed by TEM are in agreement with

Chapter 4: Metal Sulphide Nanomaterials

those calculated from the XRD patterns. HRTEM images of the products obtained at reaction temperatures of 250 °C and 300 °C show that the nanocrystals, with calculated sizes of less than 10 nm, exhibit some stacking faults and twinning. The extremely small sizes and consequent high surface energies of these nanoparticles may promote the thermal transformation to the more stable hexagonal phase CdS. In the case of the 250 °C sample this may be further exacerbated by the high degree of agglomeration which would give a greater number of particle-particle interfaces at which stacking faults may develop. Interestingly a number of the roughly spherical particles in the 300 °C sample were seen to have undergone a surface rearrangement to yield stunted tetrapodal morphologies. This further confirms the proposed mechanism of formation of the tetrapods synthesised by Method A. The products obtained at 350 °C which showed a 50:50 mixture of the cubic and hexagonal phases and larger sizes was found to be comprised largely of unagglomerated single phase nanocrystals. This may indicate that the increase in size brought about by the higher synthesis temperatures is sufficient to stabilise the cubic phase against the thermal transformation to the hexagonal phase, such that each phase nucleates and crystallises separately, as was the case with the ZnS samples. The sample prepared at 400 °C consists of larger, apparently elongated particles. Individual crystallites are observed with sizes in agreement with calculated crystallite diameters; however many of the particles appear to be the result of the fusion of individual crystallites with twinning and stacking faults at the interfaces. The generation of these stacking faults is consistent with particle growth through oriented attachment processes, wherein the hexagonal

phase may propagate throughout the conjoined crystal from the point of contact (Huang and Banfield 2005).

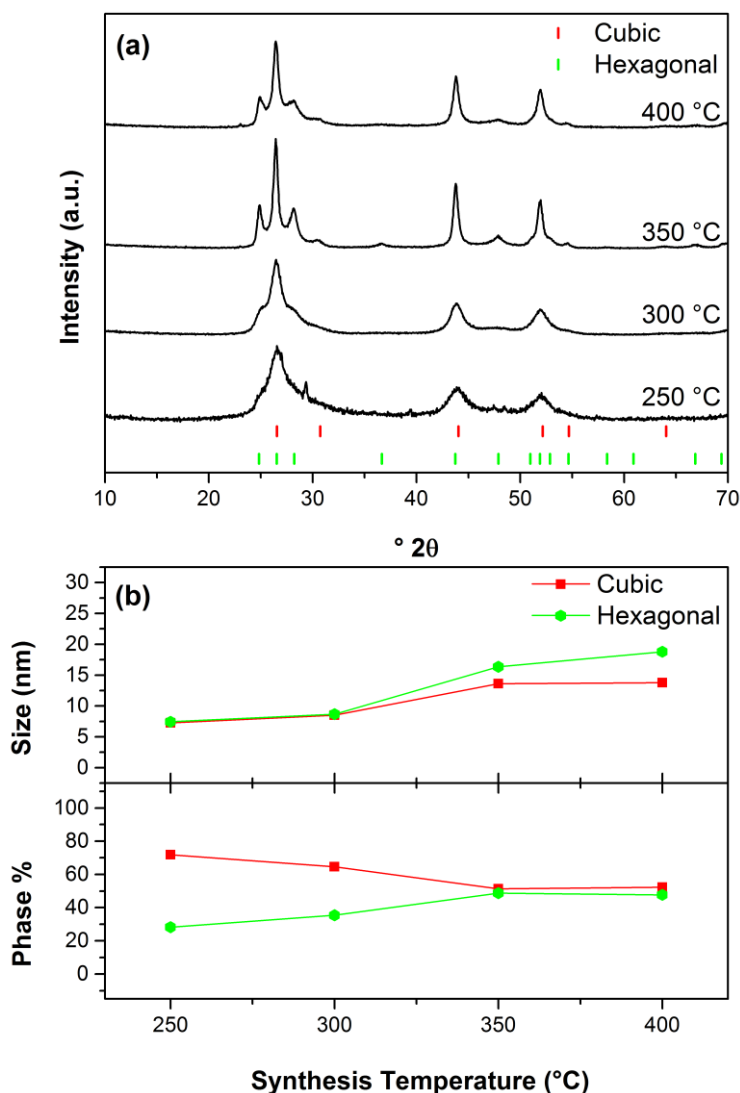


Figure 4.8: The XRD patterns (a), crystallite diameters and phase percentages calculated from Reitveld refinements (b) of the CdS nanoparticles obtained by Method B.

Table 4.3: Phase composition and calculated crystallite diameters, D , of cubic hawleyite (H) and hexagonal greenockite (G) phases of CdS samples prepared by Method B.

T/°C	% _H	% _G	D_H /nm	D_G /nm
250	71.7	28.3	7.2	7.4
300	64.6	35.4	8.5	8.7
350	51.2	48.8	13.6	16.3
400	52.3	47.7	13.8	18.8

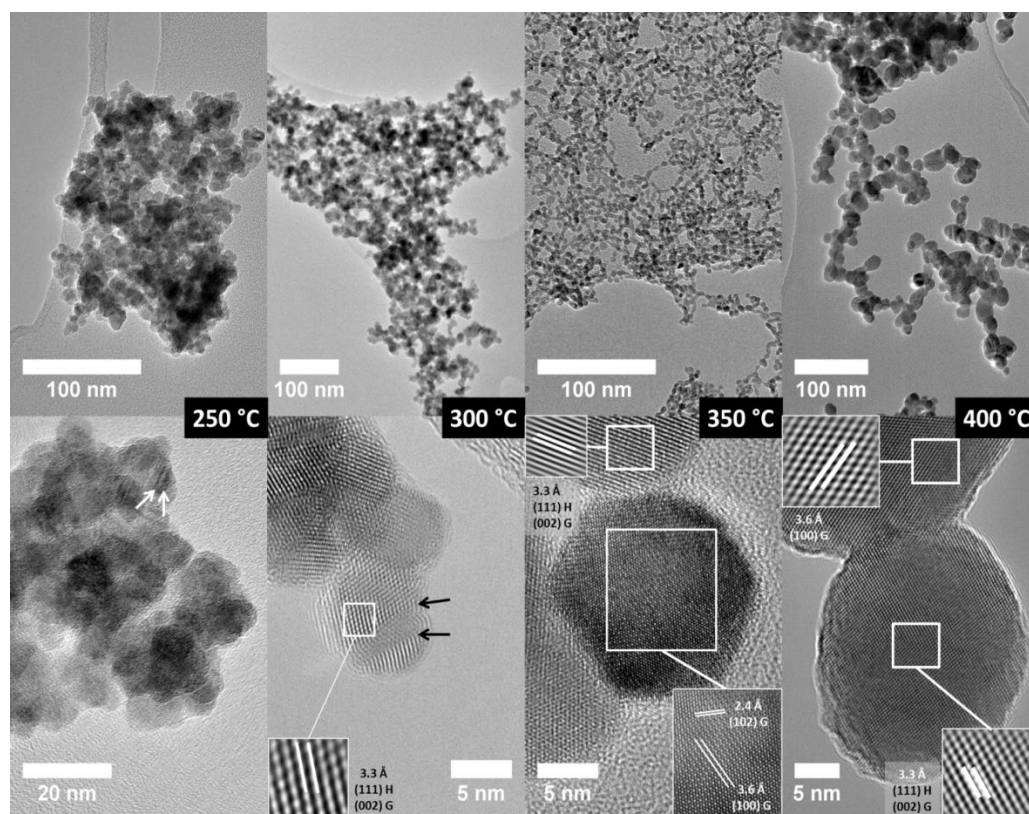


Figure 4.9: TEM images of CdS nanoparticles obtained by Method B at the indicated synthesis temperatures. Insets show reconstructed images highlighting crystal planes of the cubic hawleyite (H) and hexagonal greenockite (G) phases of CdS.

4.3.3. PbS

Efforts to synthesise lead sulphide by Method A and Method B at high temperatures (400 °C by A, 350 °C and 400 °C by B) typically resulted in white/grey powders being obtained. These were identified as containing lead sulphate as a major phase, as shown in Figure 4.10 for the Method A sample. This can be attributed to the presence of nitrate from the lead nitrate precursor in conjunction with the high temperatures required to break down the thiourea in the short contact time by Method A (< 5s). The resulting highly oxidising environment causes the formation of lead sulphate, which forms readily in the presence of oxygen. This a common problem in the synthesis of lead sulphide

nanomaterials (Koupanou, Ahualli et al. 2010). Despite this issue the poor solubility of most other lead salts (and the difficulty this poses for pumping solutions through the reactor due to pump blockages and wear) means that lead nitrate remains the most suitable precursor for lead sulphide synthesis.

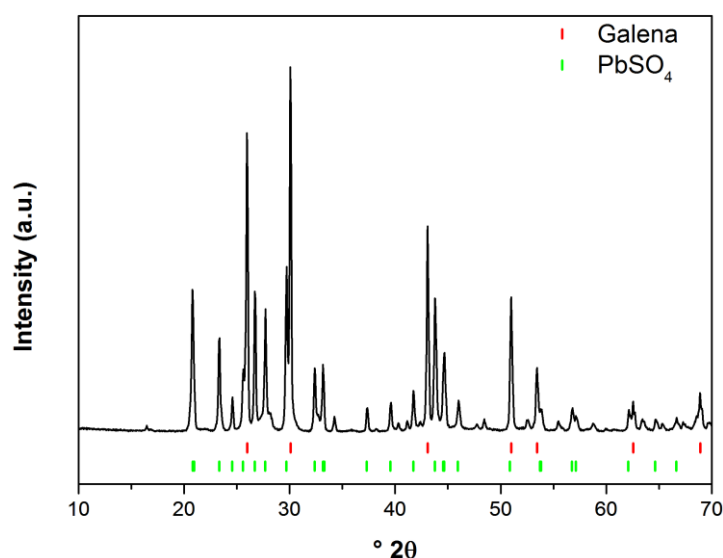


Figure 4.10: The XRD pattern of the product obtained from the attempted synthesis of PbS by Method A at 400 °C. The product consists of both PbS (galena) and PbSO₄.

Lowering the temperature of reaction was necessary to prevent the oxidising environment, and Method B, wherein the thiourea is decomposed in the preheated stream prior to contact with the metal source, permits the use of significantly lower reaction temperatures. This allowed the formation of lead sulphide without lead sulphate contamination. It was found however that even under ambient conditions the pure lead sulphide formed by Method B at lower temperatures oxidised over time (post-synthesis on the bench) and had to be quickly removed from the acidic supernatant to prevent its transformation to lead sulphate. The XRD patterns of the lead sulphide nanoparticles obtained by Method B at reaction temperatures of 250 °C and 300 °C are shown in Figure 4.11. In both cases lead carbonate is present as a minor impurity phase,

however lead sulphate is not observed. Carbonates have been identified as a relatively common impurity using the Nottingham continuous flow reactor, such as in the synthesis of barium and strontium titanate nanopowders in Chapter 2, where barium and strontium carbonate were both observed as an impurity. This was attributed to dissolved CO₂ being present in the water used in the system, and this could be a contributing factor in the appearance of lead carbonate here. The carbon content of the reactant and product solutions will be exacerbated by the breakdown of thiourea also. The major product of both reactions by Method B however is galena, cubic lead sulphide. Lead sulphide, unlike zinc and cadmium sulphide, does not possess any other polymorphs. Scherrer analysis was sufficient to estimate the crystallite diameters as 15 nm and 27 nm for particles synthesised at 250 °C and 300 °C, respectively.

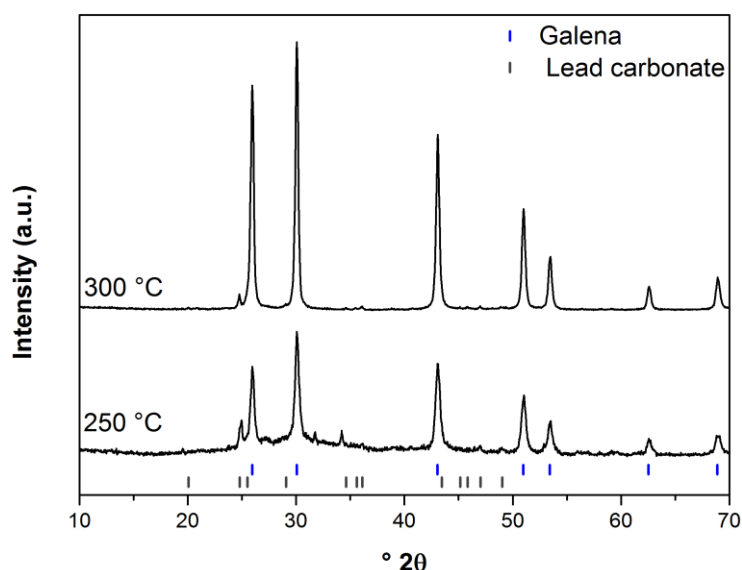


Figure 4.11: XRD patterns of PbS samples prepared by Method B at 250 °C and 300 °C.

The main product is galena with only minor lead carbonate impurities.

The TEM images of both Method B products, Figure 4.12, confirm the crystallite sizes calculated by Scherrer analysis. The obtained lead sulphide

Chapter 4: Metal Sulphide Nanomaterials

nanoparticles are highly crystalline, and generally presented as cuboidal in shape, though a small number of octahedral particles were also observed. Complex hyper-branched lead sulphide nanostructures are common in the literature (Ni, Wang et al. 2004, Zhang, Qiao et al. 2005, Querejeta-Fernández, Hernández-Garrido et al. 2012). These are invariably the result of prolonged or slow reactions, which would promote growth (which Method A effectively emulates). One could imagine that with rig modifications to provide longer reaction and heating time periods, these structures could be accessible by our technology. The extremely small cuboidal nanoparticles obtained here are however consistent with a nucleation dominated process, with temperature dependent size control, as observed for both ZnS and CdS by Method B.

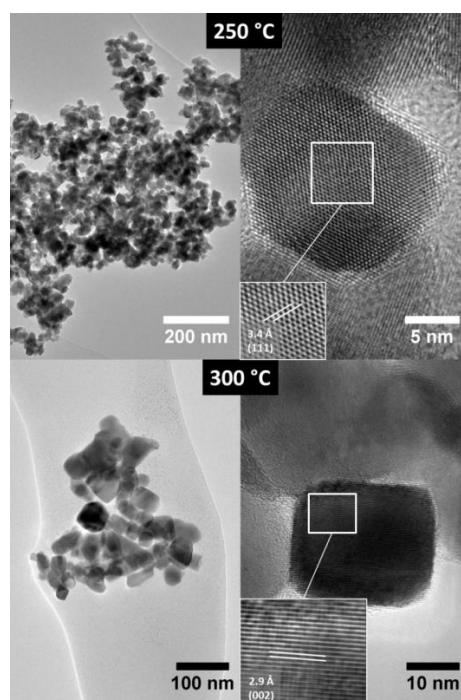


Figure 4.12: TEM images of cuboidal PbS nanoparticles obtained by Method B at 250 °C and 300 °C. Insets show reconstructed images highlighting crystal planes of the cubic galena PbS.

4.3.4. CuS

The synthesis of copper sulphide also proved difficult at the higher temperature required by Method A. The product obtained is a mixture of digenite (Cu_9S_5) and poorly crystalline covellite (CuS). It is likely that covellite is formed initially (from Method B results it is known CuS is the favoured reaction product); however covellite has very low melting and decomposition temperatures, and hence, melting of the formed material causes aggregates to form inside the pipework, which thereby slows passage of the material and causes further melting and decomposition of covellite to digenite, hampering collection efficiencies. Figure 4.13 shows the XRD pattern and TEM images of the attempted synthesis of copper sulphide by Method A. The TEM images indicate particles that are fused together as a result of the melting process.

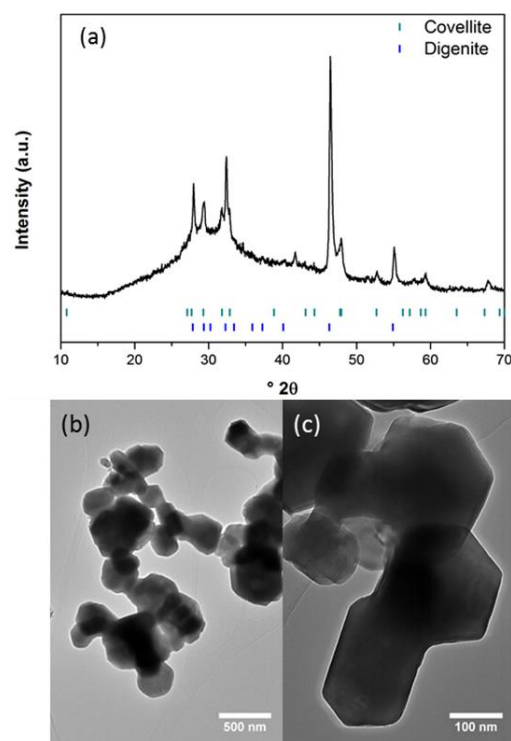


Figure 4.13: XRD pattern (a) and TEM images (b & c) of the product obtained from the attempted synthesis of CuS by Method A.

Chapter 4: Metal Sulphide Nanomaterials

It was therefore necessary to undertake the reaction at lower temperatures, a route offered by Method B. On attempting to synthesise CuS at 250 °C using Method B it was found that a white powder was obtained, identified as copper(I) thiocyanate, CuSCN (Figure 4.14). Thiocyanate complexes were not observed for any other metal sulphide reaction attempted. It is quite likely that at lower temperatures the thiourea undergoes a rearrangement to the tautomeric ammonium thiocyanate (Shaw and Walker 1956) while only a portion decomposes to HS⁻. It was observed in all systems that the reaction at 250 °C generally gave lower yields, which may be a result of this incomplete breakdown to HS⁻. With all other metals studied the presence of thiocyanate is unlikely to interfere significantly with the formation of the sulphides, as many of the metal thiocyanate complexes are soluble, and thus the metal will remain available to react with HS⁻ to give the sulphide, or would remain in solution and be removed on washing. In the case of Cu(II), the formation of Cu(SCN)₂ is immediately followed at elevated temperatures by disproportionation to the insoluble Cu(I) complex CuSCN (Newman 1963). Cuprous thiocyanate will thus be the major product obtained at temperatures sufficient to promote the thiourea/ammonium thiocyanate isomerisation but not enough to completely decompose the thiourea.

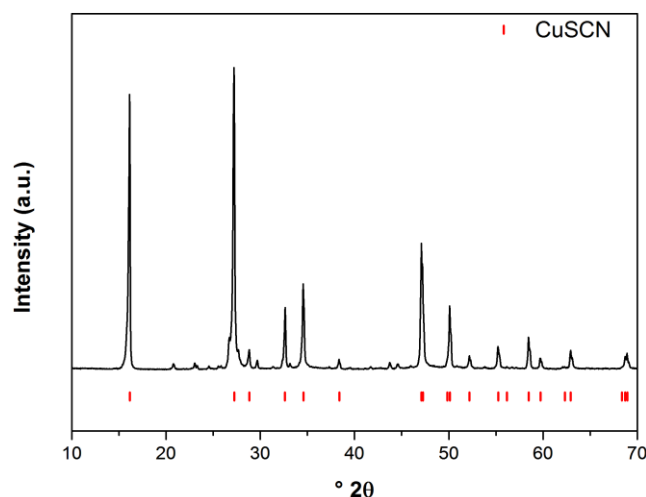


Figure 4.14: The XRD pattern of copper thiocyanate obtained from the attempted synthesis of CuS by Method B at 250 °C.

As a result of the low melting point of covellite giving an upper temperature limit and the formation of CuSCN at lower reaction temperatures, there exists a narrow window in which pure, crystalline covellite phase CuS may be obtained from the Nottingham continuous flow system. In order to achieve this, the synthesis was carried out by Method B, with the preheater temperature at 300 °C to ensure full decomposition of the thiourea to HS^- , while also maintaining low post-mixing temperatures to avoid melting or decomposing the covellite. Using this approach, pure nanocrystalline covellite phase CuS was obtained, and the XRD pattern and TEM images of the product are shown in Figure 4.15.

The highly anisotropic nature of the covellite structure dictates that hexagonal platelet formation is expected, and indeed is quite common, with many copper sulphide nanostructures consisting of self-assembled hexagonal plates (Tang, Chen et al. 2004, Li, Kong et al. 2009, Cheng, Wang et al. 2010). Analysis of the XRD pattern of the covellite material obtained here reveals the product to be entirely pure; however it was noted that the peak intensities did not match those of the standard covellite patterns. The inset in Figure 4.15 shows the

fitted peak areas of the sample normalised relative to the calculated peak areas of a standard pattern simulated from the covellite structure ($P6_3/mmc$, $a = 3.7909$, $c = 16.3764$). This reveals that reflections from the (110) plane are highly overrepresented to expected intensities, indicating a much higher degree of crystallinity in the (110) direction, suggesting a plate-like morphology, as would be expected given the crystal structure. Scherrer analysis gives crystallite diameters of 39.2 nm and 38.3 nm in the (100) and (110) directions, respectively, while the four observed (00l) reflections give an average thickness in the c-direction of 24.4 nm. The smaller size in this direction suggests the formation of planar covellite nanocrystals. Indeed, the TEM images show that the sample is comprised mainly of hexagonal nanoplates, in agreement with the X-ray diffraction results. A number of extremely thin hexagonal sheets were observed, which may potentially be single sheets of the bilayers described above, while the majority of the nanoplates are comprised of stacked layers of these nanosheets (Figure 4.16). Even under nucleation conditions, the highly anisotropic structure of covellite would result in the formation of hexagonal nanostructures. As such it may be suggested that the nucleation mechanism inferred for the previous syntheses carried out by Method B is still in effect in the synthesis of CuS. The relationship of these particle morphologies to the crystal structure of covellite is highlighted in Figure 4.16.

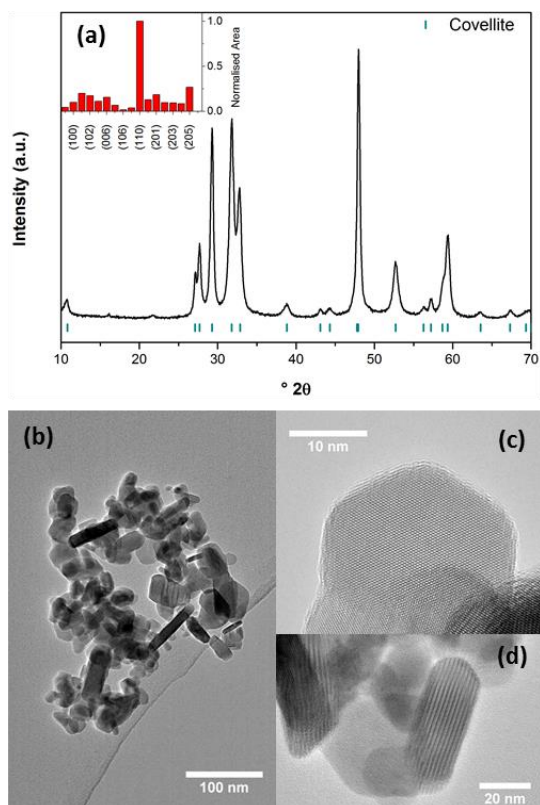


Figure 4.15: The XRD pattern of the CuS obtained by Method B at 300 °C (a), tick marks indicate the major reflections of covellite, and TEM images showing the hexagonal platelet morphology (b-d).

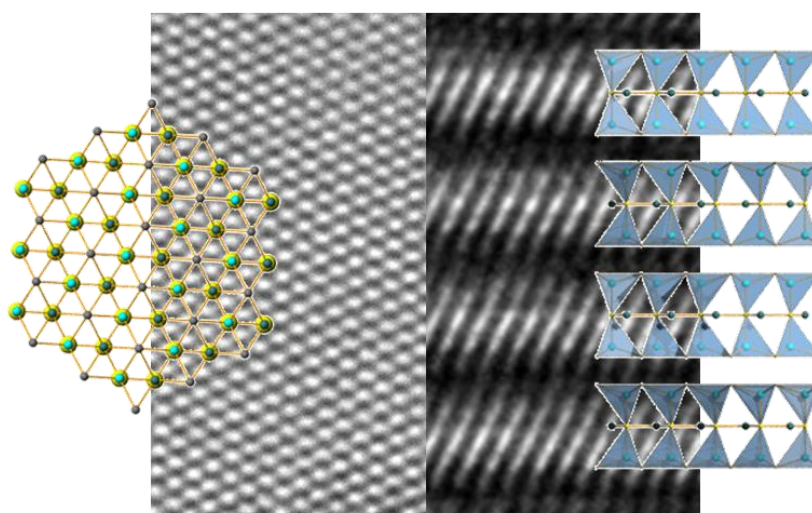


Figure 4.16: HRTEM images of a single layered hexagonal nanoplatelet with the covellite structure overlaid viewed along the c -axis (left), and an edge on view of stacked platelets compared to 4 stacked ‘tetrahedron bilayers’ (two unit cells in the c -direction) of the covellite structure viewed along the (110) axis (right) – image courtesy of Dr Peter Dunne.

4.3.5. $\text{Fe}_{(1-x)}\text{S}$

The synthesis of iron sulphide materials was attempted using both Method A and Method B. All products were initially black (indicative of sulphide formation), however the materials prepared by Method B at temperatures below 400 °C were seen to develop an orange colouration almost immediately, caused by the formation of the oxidation product lepidocrocite, $\gamma\text{-FeOOH}$ (Figure 4.17). It is reasonable to suggest that the lepidocrocite is generated as a result of the inherent instability of pyrrhotite, $\text{Fe}_{(1-x)}\text{S}$, (Miller, Li et al. 2005) compounded by the small particle sizes expected of this synthesis approach based on a nucleation dominated formation.

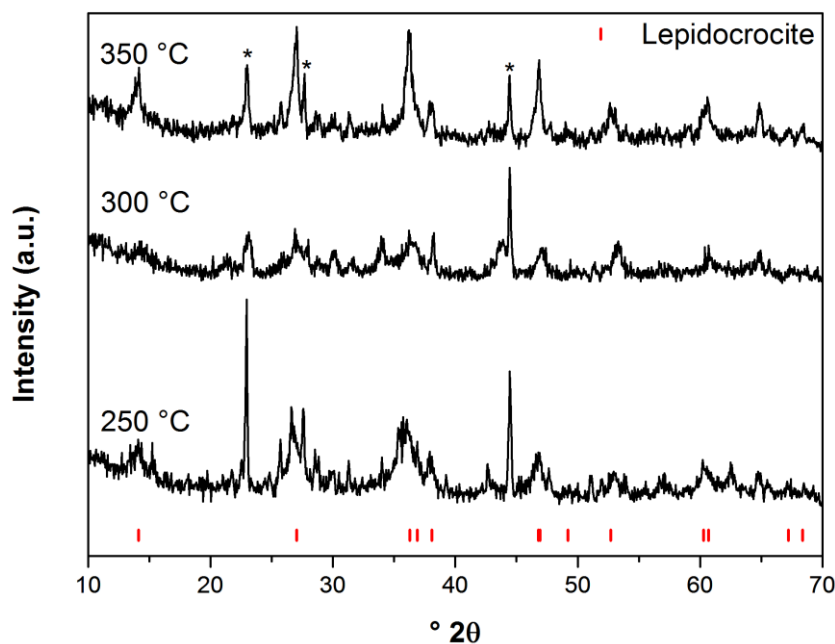


Figure 4.17: XRD patterns of the products obtained from the synthesis of iron sulphide by Method B at 250 °C, 300 °C and 350 °C. * indicates peaks arising from the sample holder.

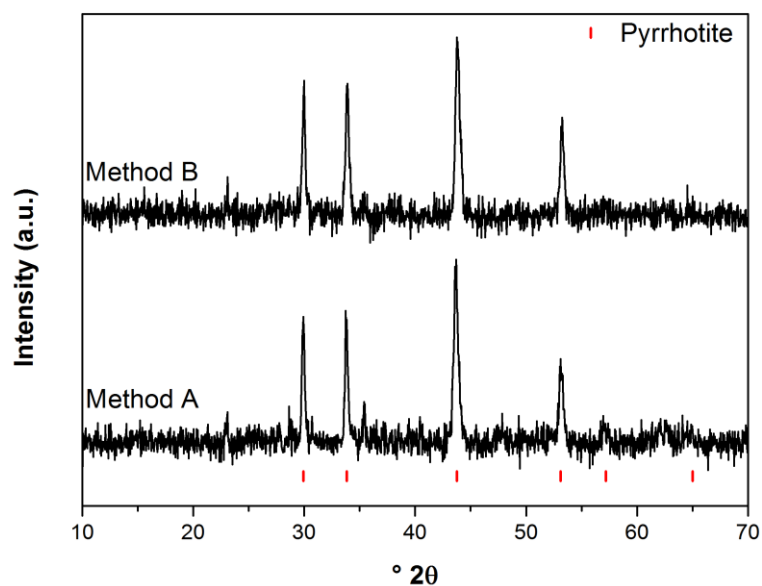


Figure 4.18: XRD patterns of the stable iron sulphide products obtained by synthesis at 400 °C by Method A and Method B.

Samples prepared at the higher temperature of 400 °C by both Method A and B were found to be stable, and the XRD patterns of these stable products are shown in Figure 4.18. The collected patterns are consistent with the pyrrhotite phase, $\text{Fe}_{(1-x)}\text{S}$ ($x = 0 - 0.125$) with the hexagonal NiAs structure. Due to the fluorescence of iron under $\text{Cu K}\alpha$ irradiation used by the standard XRD instrument used in the characterisation of the metal sulphide materials presented here, more detailed analysis of the crystal structure was not feasible. TEM images of both pyrrhotite products are shown in Figure 4.19. The sample prepared by Method A show large, thin hexagonal plates with widths ranging between 0.5 and 1 micron and a typical thickness of only 30 nm. In contrast, Method B leads to the formation of significantly smaller particles. These also possess a hexagonal morphology; however they are far less anisotropic, with the majority of particles having a width of ~ 100 nm and a thickness of 30 nm. These results are consistent with those of Lai and Chen (Lai and Chen 2009) who have shown that pyrrhotite forms large hexagonal plates through the

oriented attachment of smaller hexagonal nuclei. Method A synthesis again dictates a growth dominated process and Method B a nucleation dominated process.

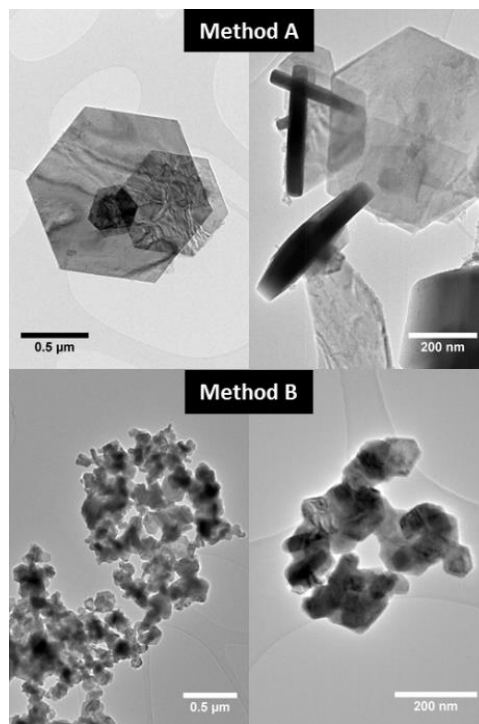


Figure 4.19: TEM images of pyrrhotite nanoplates and nanoparticles obtained by Method A and Method B at 400 °C.

4.3.6. Bi_2S_3

The poor solubility of the bismuth nitrate precursor in water necessitated the addition of dilute nitric acid to the solution to obtain stable solutions suitable for pumping. It was found that all attempts at synthesising Bi_2S_3 by Method A and Method B with the same conditions used for other materials invariably formed the oxidation product $\text{Bi}_2\text{O}_2\text{SO}_4$ (Figure 4.20). This was due to the highly oxidising environment created by the large excess of nitric acid and the high temperatures within the reactor as observed with the lead sulphide synthesis. Based on previous results on the other sulphide materials a minimum

temperature of 400 °C is known to be required to break down sufficient thiourea by Method A, so reducing the temperature using this method was not feasible. It was found however, that even using Method B conditions at 250 °C, $\text{Bi}_2\text{O}_2\text{SO}_4$ was the main product. Therefore even by Method B, which permits reaction at lower temperatures, simply lowering the temperature was not sufficient to generate the sulphide exclusively. Lowering the temperature beyond 250 °C prevents the breakdown of thiourea in the preheater, and so becomes the lower limit for synthesis by Method B.

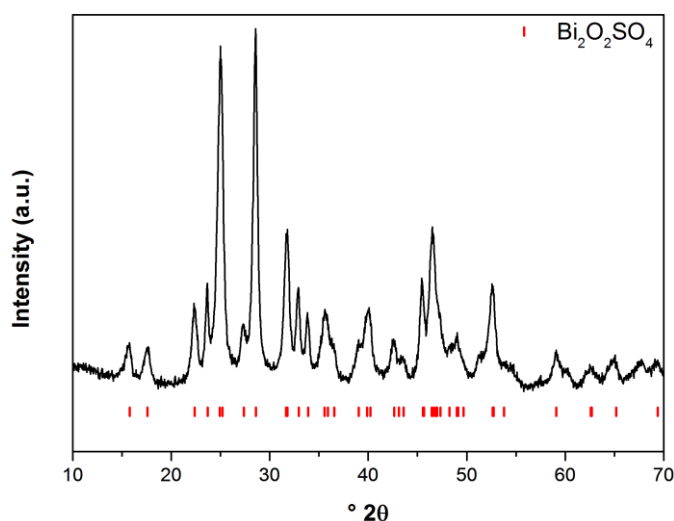


Figure 4.20: XRD pattern of a typical product obtained from a synthesis of Bi_2S_3 under normal conditions, identified as $\text{Bi}_2\text{O}_2\text{SO}_4$.

To mitigate the oxidising potential of the system it was therefore necessary to alter the reaction parameters to maintain low post-mixing temperatures (minimising the temperature of the product solution upon and after Bi_2S_3 formation). This was achieved by varying the flow-rates of the system in Method B operation. The thiourea was flowed at a rate of 5 mL min^{-1} through the preheater, while the metal upflow was pumped at 10 mL min^{-1} (the concentrations were adjusted accordingly to maintain a two-fold excess of thiourea as per Table 4.1 in Experimental Section 4.2). These flow-rates

ensured the thiourea was exposed to sufficient temperature that facilitated the complete breakdown of thiourea to HS^- , while the greater flow of the unheated metal salt dilutes the heat at the reaction point upon mixing with the preheated water to alleviate the oxidising potential of the system upon formation of the target material. These modified conditions allowed pure bismuthinite, Bi_2S_3 , to be obtained. Figure 4.21 shows the XRD pattern and TEM images of the material produced under these modified conditions. The XRD pattern matches that of the expected product, bismuthinite, Bi_2S_3 . Profile fitting using Xfit gave a calculated crystallite diameter of 19.5 nm. High resolution transmission electron microscopy reveals that the product adopts a rod-like morphology, a common morphology observed in bismuthinite nanomaterials (Lu, Han et al. 2007, Phuruangrat, Thongtem et al. 2009, Salavati-Niasari, Ghanbari et al. 2009, Wang, Wang et al. 2010). The nano-rods, with diameters of ~ 20 nm, are seen to self-assemble into larger razor-shell type nanostructures, a number of which appear to have fully closed, to give nanotubular arrangements. These morphologies are indicative of a combined nucleation, growth and oriented attachment mechanism.

This contrasts significantly with the results of previous syntheses by Method B, which demonstrated a nucleation dominated mechanism of particle size control. This discrepancy can be explained by the lower temperatures and flow rates required for bismuth sulphide formation, which lead to slower passage of the product solution and products through the reactor pipework and therefore longer residence times and prolonged heating. The increased residence times promote the growth and self-assembly of these nanostructures from the nanoparticles which may be obtained from the initial nucleation step.

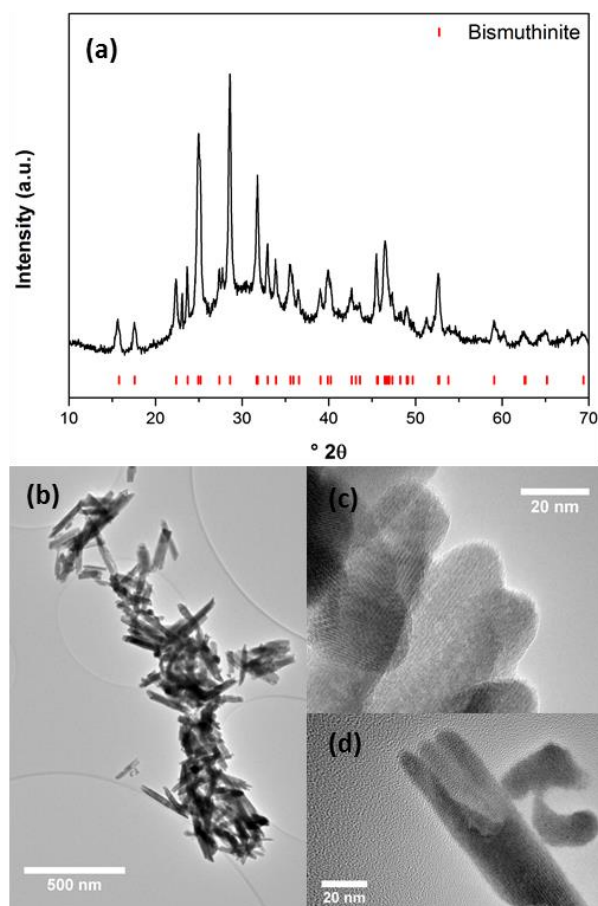


Figure 4.21: The XRD pattern (a), and TEM images (b - d), of the Bi_2S_3 self-assembled nanorods obtained by Method B with modified flow-rates.

The Bi_2S_3 system, due to the intricacies of the formation window in terms of temperature and flow rates required, may prove an informative model to study in future work. Modifying the reactor configuration to allow for the rapid quenching of the reaction and collection of products at short residence times, may offer insight into the initial nucleation step, before other processes such as growth or oriented attachment have occurred. Of course, sequential advancements of the pipework in terms of residence time post-initial-synthesis would allow for the tracking of growth processes after the nucleation period, offering insight into the growth and oriented attachment processes that can be invoked, and eventually controlled downstream of the initial reaction point.

4.3.7. MoS₂

Ammonium molybdate was chosen as the most readily and commonly available, highly soluble molybdenum source for the synthesis of MoS₂. In the initial efforts to produce MoS₂ via Methods A and B it became abundantly clear that the standard reactor design, and simple rapid mixing of two streams that it affords, would not be sufficient to produce the desired product.

Initially, using the standard configuration counter-current continuous flow reactor operating as in Method B, an aqueous stream of ammonium heptamolybdate, at 0.05 M concentration flowing at 10 mL/min, was mixed with an aqueous stream of thiourea, at 0.1 M concentration (maintaining the 2-fold excess of thiourea to the expected MoS₂ product with 2 x the flow rate in the down-flow), which had been flowed through a pre-heater at 20 mL min⁻¹ at temperatures between 250 °C and 400 °C. No solids were obtained from this configuration at any temperature; however the solutions collected at the outlet of the reactor were deep orange to red in colour, indicative of varying and progressive degrees of sulphidation of the molybdate anions (Laurie 2000). The coloured solutions and resulting UV-Vis spectra of the products obtained at various temperatures are shown in Figure 4.22. The UV-Vis spectra show an increasing level of sulphidation with increasing reaction temperature, consistent with the step-wise mechanism:



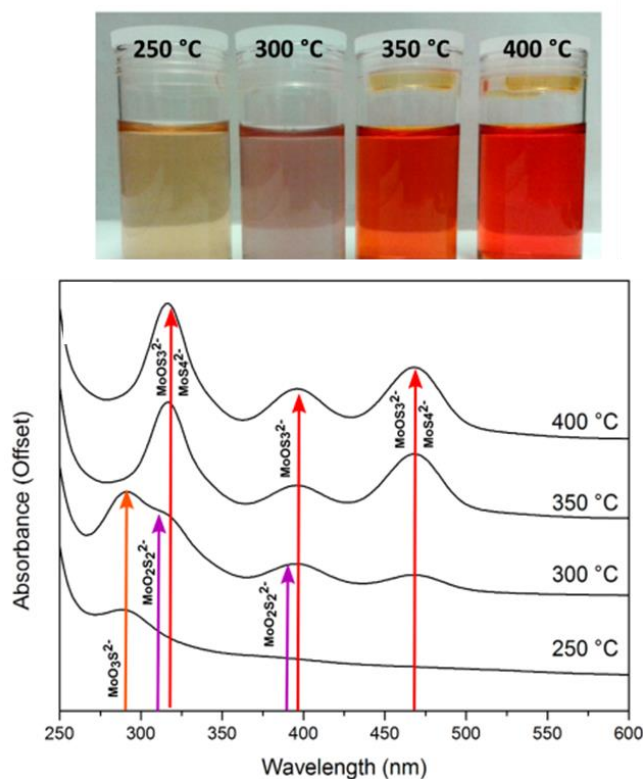


Figure 4.22: The various thiomolybdate species give rise to coloured solutions obtained by the attempted standard Method B synthesis of MoS₂ (top), and the resulting UV-Vis spectra of the solutions (bottom).

It is worth noting that even at the highest pre-heater temperature of 400 °C the absorption maximum at 396 nm due to MoOS₃²⁻ persists – this infers that even under the harshest conditions in terms of elevated temperature, complete sulphidation of the ammonium heptamolybdate precursor could not be completed. This can be ascribed to the much slower rate of reaction for the final sulphidation reaction (reaction 4.4), relative to the preceding steps, which can thus be described as a limiting step towards the synthesis of MoS₂.

In the previously presented metal sulphide nanomaterials in this chapter, the metal salt precursor is a simple nitrate which readily dissociates in the precursor container or at the mixing point allowing the metal ion to be freely

Chapter 4: Metal Sulphide Nanomaterials

available for reaction through an instantaneous nucleation mechanism with the hydrosulphide active species at the reaction point. This leads to the effectively instantaneous nucleation of nanoparticles through the formation of the mentioned clusters or metal-sulphide networks which lead to products, with the reaction conditions then dictating either size controlled nucleation or further growth processes. In contrast, the complex heptamolybdate species, as evidenced by the UV-Vis spectra, requires sequential substitution of the oxygen moieties with sulphur, and this chemistry, certainly within the confines of the standard reactor set-up and short reaction times, appears to be a relatively lengthy process. The substitution process is initiated upon meeting of the room temperature heptamolybdate species with the active sulphur source at elevated temperature, with both increased time and elevated temperature appearing necessary to complete the sulphidation and promote the formation of species able to nucleate towards solid product.

This indicated that the synthesis would not be possible using the single reaction point classical model of the Nottingham counter-current reactor, however, the varying levels of sulphidation indicated that the reaction was beginning to occur, it simply needed an additional ‘push’. It has been shown previously by other researchers that lowering the pH of the reaction solution is an effective method of enhancing the rate of the final sulphidation reaction (Erickson and Helz 2000), forming MoS_4^{2-} from MoOS_3^2 . In addition to speeding up reaction (4.4), acidification is known to precipitate the tetrathiomolybdate anion as amorphous MoS_3 , itself a common precursor to MoS_2 and a species that could be utilised for further reaction in the continuous flow reactor. This chemical solution, through an acidification step, could therefore replace a physical

solution, such as the addition of pipework and increasing of the residence time, to not only complete the sulphidation reaction but precipitate the amorphous MoS_3 species, itself a precursor to MoS_2 , in a single, elegant step. To test this, the addition of small amounts of nitric acid post-synthesis on the bench to the obtained red solutions resulted in the precipitation of a dark brown solid (and gave a colourless supernatant) consistent with MoS_3 formation. It was therefore deemed possible to promote this step with acidification and logical to perform this acidification step in flow and produce MoS_3 in a fast continuous hydrothermal process, with limited modification of the reactor configuration. An additional flow inlet to the reactor, immediately downstream of the initial mixing point, which enters through the existing side arm of the reactor cross-piece, was added to provide an acidic environment. It is important to note that the reaction from MoS_4^{2-} to MoS_3 actually involves the reduction of Mo (VI) to Mo (IV). As demonstrated by the oxidation of lead and bismuth sulphides earlier in this chapter, nitric acid creates too oxidising an environment at the elevated temperatures employed, while the stainless steel construction of the reactor prohibits the use of hydrochloric acid as a reducing acid, since halogenated fluids corrode the pipework. As such, acetic acid was chosen as a non-oxidising acid compatible with the stainless steel reactor.

This resulting reactor arrangement is shown in Figure 4.23, along with the XRD pattern and TEM images of the brown solid obtained. The XRD pattern of the product obtained from this reaction shows only a very broad peak centred at $14^\circ 2\theta$ and diffuse scattering at lower d-spacing indicating a highly amorphous structure. TEM images show the product consists of large micron-sized amorphous chunks. High resolution imaging reveals a highly disordered

structure, seemingly comprised of tangled chain segments, consistent with the structural model of MoS_3 proposed by Hibble *et al.* (Hibble and Wood 2003) on the basis of Reverse Monte Carlo modelling of neutron diffraction data. Some small isolated regions of the sample also exhibited a layered structure close to that expected of MoS_2 , with interplanar spacings of 6.9 Å, suggesting that at the elevated temperatures within the reactor some partial transformation of MoS_3 to MoS_2 has occurred, as has previously been suggested based on *in-situ* EXAFS observations on the decomposition of tetrathiomolybdate to MoS_2 (Walton, Dent *et al.* 1998).

In traditional syntheses of MoS_2 , this is normally achieved by calcination under an inert atmosphere, post-synthesis, however, given the flexibility of the continuous flow process the opportunity to increase the residence time of the reactor such that the MoS_3 would be maintained at sufficient temperatures long enough to decompose to MoS_2 is a possibility. This was achieved by incorporating an additional heating unit between the reactor outlet and the cooling system, affording an additional residence time of ~ 30 s at a set temperature of 250 °C, as shown in Figure 4.24 (a).

The XRD pattern (Figure 4.24 (b)) of the black solid obtained from this reactor configuration reveals it to be crystalline MoS_2 , obtained at near quantitative yields, indicating complete sulphidation of the molybdate precursor, aided by the acidification step, and subsequent precipitation of MoS_3 and conversion to MoS_2 with additional heating. TEM images (Figure 4.24 (c-f)) show the MoS_2 is present as large (1 – 2 μm) masses of tangled nanosheets. HRTEM images

Chapter 4: Metal Sulphide Nanomaterials

taken at the edges of these curled nanosheets show them to be as little as 10 nm in thickness, typically consisting of between 10 and 15 layers of MoS₂.

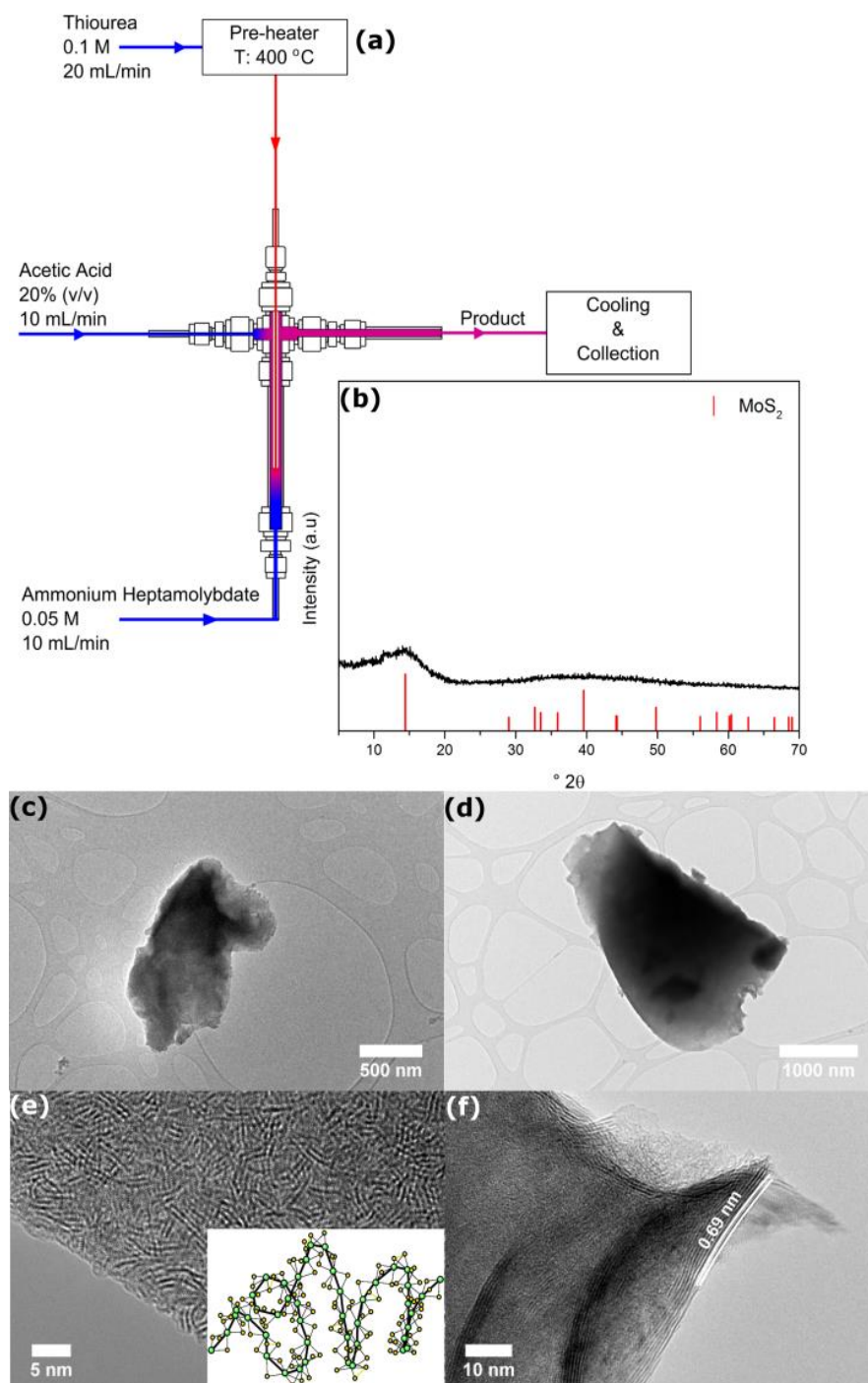


Figure 4.23: Reactor for the production of MoS₃ by acidification of *in-situ* generated thiomolybdates (a), and the XRD pattern (b) and HRTEM images (c-f) of the amorphous product (inset shows a possible structure as proposed by Hibble & Wood (Hibble and Wood 2003)).

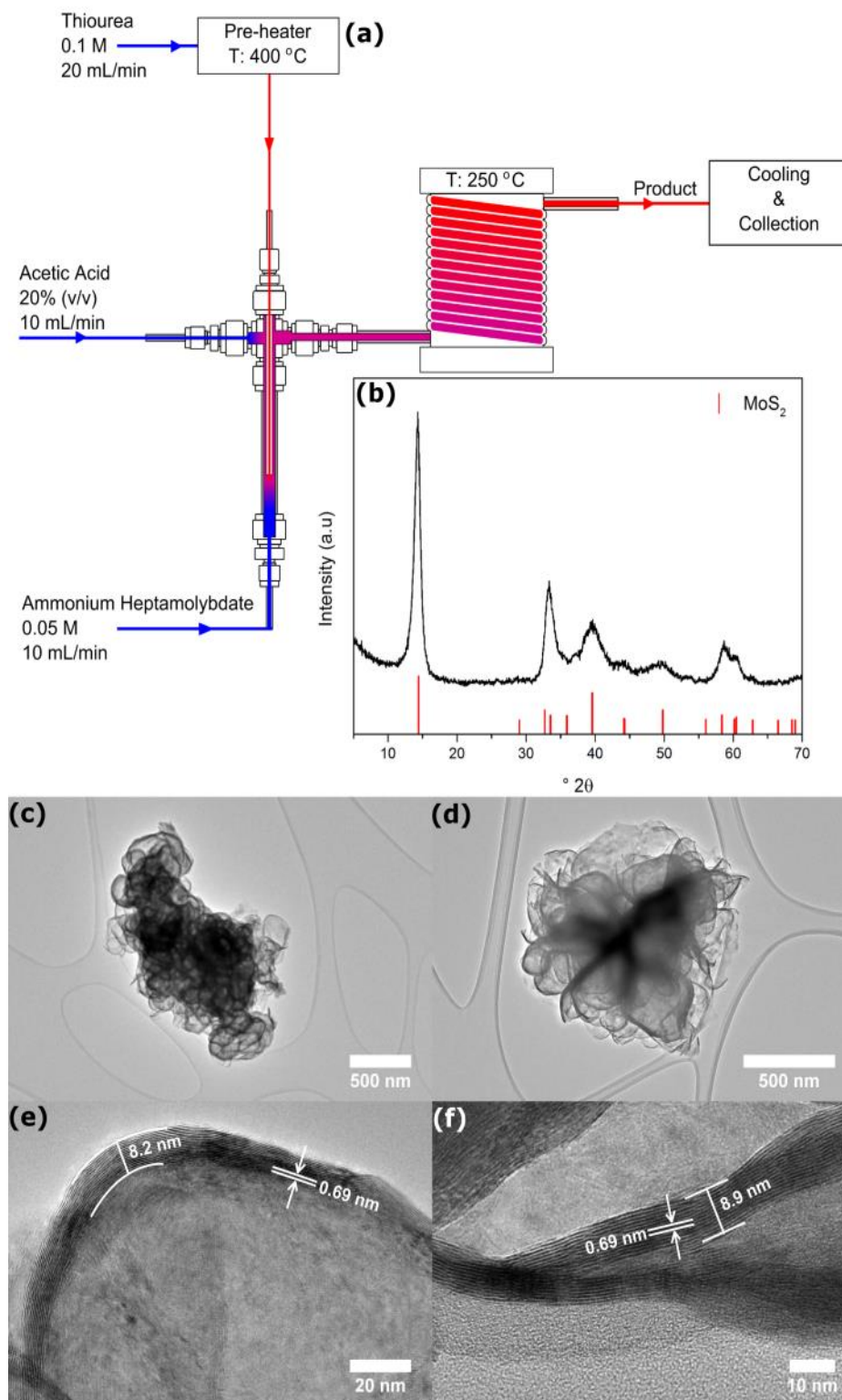


Figure 4.24: The final reactor design for the production of MoS₂ by further hydrothermal treatment of MoS₃ (a), and the XRD pattern (b) and HRTEM images (c-f) of the crystalline MoS₂ product.

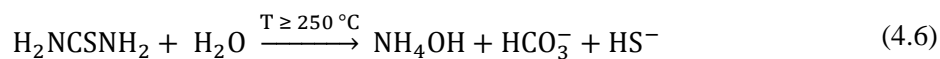
4.4. Mechanisms of Metal Sulphide Synthesis by CFHS

In contrast to the formation of metal oxides, where water plays the role of both solvent and reagent, the formation of the six different metal sulphide nanomaterials by the more general Method A and B routes and the sequential synthesis of MoS₂ are dependent upon the generation of hydrogen sulphide or hydrosulphide. The hydrothermal decomposition of thiourea serves as a convenient method to generate the required HS⁻. By Method A, wherein thiourea is mixed with the metal salt and maintained at room temperature prior to mixing with the preheated water stream, very high temperatures in excess of 400 °C are needed to break down the thiourea within the extremely short contact time. By Method B, in which the thiourea is fed through the preheater, and thus is sustained at temperature for longer, temperatures as low as 250 °C are sufficient to generate significant amounts of HS⁻. At this lowest temperature flow-rates of 10 mL min⁻¹ result in residence times such that the decomposition is not entirely complete. At least some thiourea remains as the tautomeric form, ammonium thiocyanate, as evidenced by the formation of copper thiocyanate, and the generally low yields of other metal sulphide materials under these conditions. This may be overcome by lowering the flow-rate to confer longer residence times as was required for the formation of bismuth sulphide, or by increasing the temperature.

On bringing a mixed solution of thiourea and metal salt into contact with the superheated water stream, as per Method A, thiourea decomposition occurs almost immediately, increasing the hydrogen sulphide concentration; however

Chapter 4: Metal Sulphide Nanomaterials

this is offset by the concurrent precipitation of the metal sulphide, *i.e.*, reactions (4.6) and (4.7) occur at effectively the same time.



This maintains the concentration of metal sulphide precursor at relatively low levels, and subsequently the rate of formation of the sulphide would be relatively low (though the reaction is still complete with residence times of ~ 1 second). This results in a growth dominated mechanism and the formation of metal sulphide nanostructures directed by the underlying crystal structure of the sulphide.

Method B physically and temporally separates the generation of HS⁻ and metal sulphide precipitation. Thiourea breakdown occurs within the preheater, prior to contact with the metal salt. The concentration of hydrogen sulphide at the mixing point is thus maximised, and the excellent mixing dynamics within the counter-current reactor used in this work cause immediate and intimate mixing with the metal stream rapidly increasing the metal sulphide precursor concentration. This drives the nucleation of the metal sulphide, forming nanoparticles. The formed nanoparticles exhibit temperature dependent sizes as may be expected based on classical nucleation theory (Kumar and Nann 2006).

Figure 4.25 represents a simple schematic of the proposed mechanisms of both methods, based on the LaMer model (LaMer and Dinegar 1950), where in this case the x-axis may be considered either as time or position within the reactor.

Chapter 4: Metal Sulphide Nanomaterials

C^* signifies the critical nucleation threshold – the precursor concentration, or degree of supersaturation above which nucleation occurs. When the precursor concentration is below this point particles grow by diffusion, or, at high polydispersion, Ostwald ripening. Method A results in a post-mixing increase in precursor concentration (*i.e.* $[M^{x+}] + [HS^-]$) to a level above the nucleation threshold, but because of the competition between reactions (4.6) and (4.7), the precursor concentration will lie below the critical point, within the growth domain. To obtain small monodisperse nanoparticles a rapid increase in precursor concentration above the nucleation threshold is required. The resultant supersaturation is relieved by the rapid nucleation of a large number of nanoparticles. It is clear that Method B satisfies these requirements, and consequently the products of this route are obtained as generally uniform ultrafine particles.

In contrast to the relatively simple single step processes dominating the CFHS production of most materials to date, the synthesis of MoS_2 involves a more complicated, sequential mechanism, and thus requires chemical and reactor developments to adapt to the intricacies of the target product. Whereas the metal salt precursors for the general route to the six metal sulphide nanomaterials are simple nitrates, allowing the free metal ions to be readily available at the reaction point for reaction with the active hydrosulphide species, the molybdenum precursor ammonium heptamolybdate requires multi-step substitutions of oxygen with sulphur, with the final step requiring additional time and acidification to occur more readily, with acidification providing the additional benefit of promoting the formation of the amorphous MoS_3 phase which acts as a precursor for MoS_2 formation.

Chapter 4: Metal Sulphide Nanomaterials

MoS₂ synthesis therefore utilises the reactor in a different way to the traditional burst nucleation or growth mechanism. By providing excellent and uniform heating and mixing of the molybdenum precursor with the active sulphur species, rapid and sequential substitution of the oxygen moieties is induced in extremely short contact times, with the additional benefit of the flow system having the capability to introduce reagents in flow, in this case acetic acid, immediately after the first period of reaction, to hasten the final sulphidation and promote the formation of the amorphous precursor to MoS₂. Exploiting the flexibility of continuous flow pipework and reactor configurations also allowed for additional heating to be employed to transform this amorphous precursor to the crystalline product, thus, using the reactor as a sequential reaction vessel capable of providing different reaction conditions in quick succession and within relatively short timescales, to access more complicated reaction pathways and products than the traditional ‘one-step’ nucleation products.

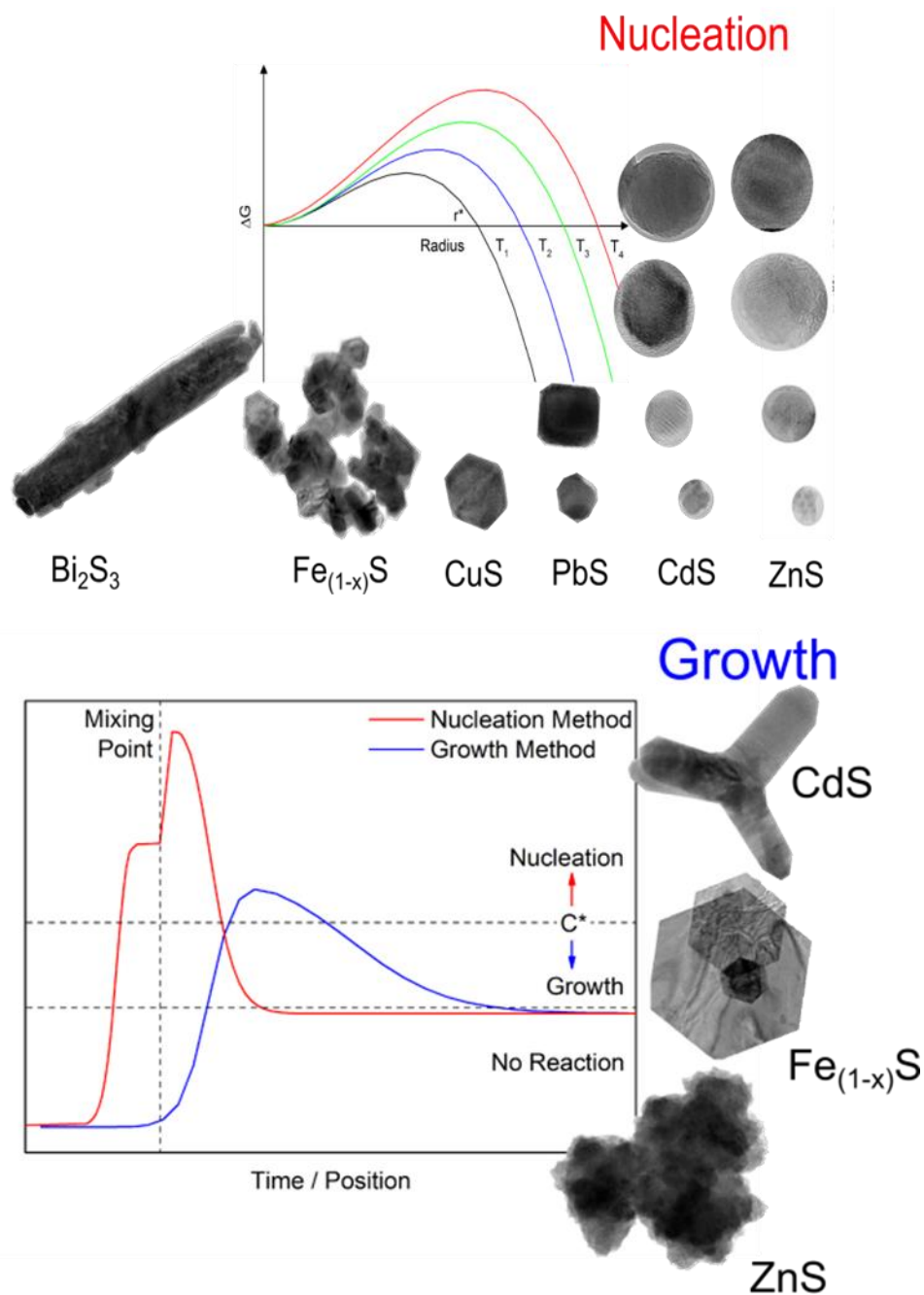


Figure 4.25: A simplified representation of the suggested mechanism of Method A and Method B based on the LaMer model (LaMer and Dinegar 1950) highlighting the influence of increasing temperature on critical nucleus radius (Kumar and Nann 2006), and various metal sulphide nanostructures.

4.5. Conclusions

This chapter has presented the application of continuous flow hydrothermal methods to the synthesis of a wide range of binary metal sulphide nanomaterials, a class of materials never before accessed by CFHS methods. Thiourea has been employed as a sulphur source for the production of ZnS, CdS, PbS, CuS, Fe_(1-x)S, Bi₂S₃ and MoS₂ nanomaterials. Two different methods based around a general route have been developed using a vertical reactor with counter-current mixing which ensures immediate and uniform mixing of reagent streams to produce six of the materials, with MoS₂ requiring reactor modifications. By varying the point of addition of the thiourea sulphur source different nucleation and growth mechanisms may be invoked. On bringing a mixed stream of thiourea and metal salt into contact with a super-heated water stream a growth mechanism is promoted by the concurrent generation of HS⁻ and precipitation of the metal sulphide. ZnS nanoflowers, multipodal CdS nanostructures, and Fe_(1-x)S platelets have been obtained by this method, with the particle shape determined by the underlying crystal structures of the products. By first passing the thiourea through the preheater prior to contact with the metal salt stream the generation of HS⁻ and metal sulphide formation are separated. This results in a nucleation driven process, yielding nanoparticles of ZnS, CdS and PbS, with sizes determined by the chosen reaction temperature. Hexagonal nanoplatelets of CuS and Fe_(1-x)S, and Bi₂S₃ nanorod assemblies have also been obtained.

As the first reported use of continuous flow hydrothermal methods for the production of sulphide nanomaterials this work represents a significant

Chapter 4: Metal Sulphide Nanomaterials

advancement in the scope of continuous hydrothermal synthesis technology. In addition, the hydrothermal approach eliminates the need for the high boiling point solvents that are often used in the synthesis of metal sulphide nanomaterials by more conventional routes. This approach is thus significantly more environmentally friendly, and as a continuous process it is inherently scalable, making it suitable for large-scale industrial production of these materials.

Furthermore, rig configuration modifications and the rapid nature of the CFHS method has allowed various stages of the sequential synthesis of MoS₂ to be observed by isolation of intermediates at different stages of reaction, leading to the first CFHS of MoS₂. The successful synthesis of MoS₂ has demonstrated development of the reactor configuration to a ‘sequential synthesis’ or multi-stage reactor device, by being inherently flexible and versatile, tailored to suit a specific target material and inducing the associated chemistry necessary in order to successfully track the reaction through intermediates and eventually to products. The flexibility of the continuous flow system lends itself to simple but extremely effective modifications allowing complex materials to be accessed and insights into the chemical mechanisms involved to be understood.

Whilst the synthesis of metal sulphide nanoparticles has been demonstrated, further work can be addressed. Increasing the scale of production of the metal sulphide nanomaterials by the methods presented in this chapter would be a desirable process, with the main issue being the excess hydrogen sulphide produced during synthesis, with powerful extraction necessary at larger scales for the removal and then making safe of the excess hydrogen sulphide.

Chapter 4: Metal Sulphide Nanomaterials

In a non-tailored state, that is, the nanoparticles at a given size and morphology with no consideration to surface chemistry or solvent compatibility, they lack targeting to a specific application, and as such, they are currently in a low-volume-low-value state at laboratory scale, with larger scales necessary for a large-volume-low-value state. By tailoring the nanoparticles through advanced chemical processes in a continuous flow manner at laboratory scales, it may be possible to first investigate low-volume-high-value materials, since the materials will be technologically useful, and finally, once optimisation of the materials at laboratory scale has been undertaken, a high-volume-high-value state may be reached with the technology at industrial scales.

A number of characteristics should be targeted to move towards more valuable and tailored products. To truly benefit from the unique optoelectronic properties of metal sulphide nanoparticles, driving the size of the particles down to the quantum dot size range (1-20 nm) would be desirable. The use of surfactants during the synthesis of the nanoparticles may help to effectively cap growing crystals, preventing and terminating growth, whilst maintaining homogeneity in size throughout the sample. The use of surfactants could also be investigated to provide functional surface groups on the nanoparticles, such that the nanoparticles become stable and disperse efficiently into a variety of solvents, dependant on the application. Surfactants can be introduced into the Nottingham counter-current reactor either with the reagents, and are therefore present at the reaction point and point of nucleation and formation of the nanoparticles, thereby being capable of influencing the size, shape and surface chemistry of the nanoparticles, or they can be introduced further downstream, to modify the surface of the particles such that they may be more compatible

Chapter 4: Metal Sulphide Nanomaterials

with a certain solvent system. Finally, advancing towards more developed architectures of nanoparticles may offer new avenues of application; this chapter has demonstrated the power of the continuous flow route to produce particles by a ‘burst nucleation’ method, a subsequent growth method allowing growth into further structures through controlled precursor availability post-initial synthesis, and as a sequential synthesis device capable of rapidly and efficiently modifying reaction conditions in a short period of time and space to promote various changes of materials to yield products – however, these ideas can be developed further. For example, it may be possible to explore the growth of the CdS hexagonal phase arms in future work. Any number of conditions, such as reducing the flow rates to slow the passage of the formed CdS materials through the heated zone, thus lengthening the reaction time, or lengthening the pipework post-synthesis to effectively increase reaction time also, or controlling the availability of sulphur species by varying the concentration or injecting further metal or sulphur precursor after formation, may provide differences in the number of arms and arm length achieved on the cores, thereby providing more tailored CdS materials.

The flexibility of the continuous flow system to enable further reagents to be introduced downstream of the reaction point and additional heating zones to be configured provide a versatile system for metal sulphide synthesis understanding, optimisation and exploitation to move towards tailored materials with higher value. Work must be careful to explore making materials for applications which provide a trade-off between the requirement for heavily optimised materials and the scale that those materials are required.

Chapter 4: Metal Sulphide Nanomaterials

Currently, the applications requiring metal sulphide materials tend to require small quantities of highly tailored materials. Synthetic methods that can provide these tailored materials are therefore at an advantage, even if they are limited in their scale, because the ability to produce superior performance materials outweighs the lack of scale-up potential. Continuous flow methods therefore, certainly those that are more predisposed to be undertaken at larger scales, have to look to improve the level of tailoring of materials they can provide. Of course, with the market for materials such as quantum dots increasing all the time, methods such as CFHS may become both important to meet the supply, and potentially, if developed to produce more tailored materials, extremely lucrative, as the market for the materials becomes a high-volume-high-value sector. However, until that time, if CFHS is to compete with the more bespoke low-volume-high-value technologies, then CFHS methods must attempt to develop from the traditional ‘burst nucleation’ type synthesis of materials, with control over only the approximate size and morphology of particles. Therefore, the information that has been learned in this chapter about the chemical processes occurring during metal sulphide formation, and how these can be controlled to induce preferential nucleation and growth processes to offer more control of particle characteristics, is a valuable development in the quest to move towards improved tailoring of materials.

5. Lithium Iron Phosphate

With the demonstration in Chapter 4 of the application of the Nottingham counter-current reactor to access a class of materials, metal sulphides, never before accessed by CFHS, to further demonstrate the versatility of the system the synthesis of a metal phosphate with high levels of industrial interest and commercial prospects, lithium iron phosphate (LiFePO_4 , LFP), was identified as a key target. This lithium intercalation material already finds application as a cathode material in Li-ion batteries for short range electric vehicles, electronics and grid power storage, in addition to being a promising candidate for use in next generation electric cars. The synthesis of LFP has never been attempted using the counter-current reactor. Hanwha Chemicals Corporation in Korea successfully commercialised CFHS for the production of LFP at industrial scales, with capacity of ~ 1000 T/y (Adschiri, Lee et al. 2011), however, details of the reactor system, mixing geometry or process parameters used is not publicly available. There therefore exists a need for further investigation into the reaction pathway and formation of LFP, and how the process parameters in CFHS control the resulting characteristics of the particles produced.

5.1. Introduction

Lithium iron phosphate (Figure 5.1) has become a promising candidate as a large-scale high performance cathode material in lithium-ion batteries (LIBs), facilitating the development of technologies such as hybrid or electric vehicles (HEVs or EVs) and large scale grid energy storage.

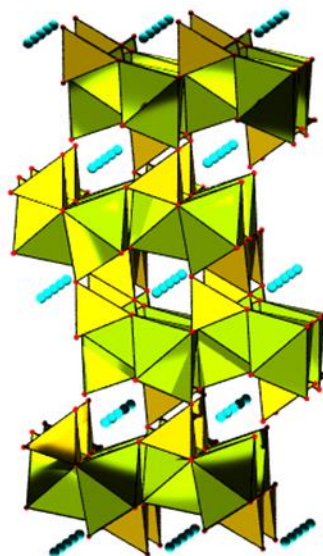


Figure 5.1: The structure of lithium iron phosphate viewed along the Li-ion channels, with the small spheres representing Li-ions aligning in the channels.

This global, increasing demand makes LFP an ideal model case to assess whether CFHS techniques and the Nottingham counter-current reactor are suitable for producing industrial scale levels of lithium-ion battery materials. Consumer thirst for longer lasting, faster charging and more complex personal electronics or vehicles has increased, as has the drive towards electrification in automation to combat fossil fuel depletion and global warming (Whittingham 2004, Etacheri, Marom et al. 2011, Scrosati, Hassoun et al. 2011). Coupled with the necessity to safely and reliably store energy from the plethora of new renewable energy sources and an overall societal push towards greener credentials for economic, social and environmental issues, the discovery and enhancement of new materials for Li-ion batteries and beyond has become a highly interesting, exciting and lucrative pursuit. To be effective in these technologies it is highly desirable for battery materials to be inexpensive and possess inherent safety, whilst displaying high energy and power densities and

Chapter 5: Lithium Iron Phosphate

excellent cyclability (Wang and Sun 2012). To these ends, LFP, proposed by Padhi & Goodenough (Padhi, Nanjundaswamy et al. 1997) is fast-becoming a viable alternative to traditional battery materials and possesses many advantageous features over other battery systems or Li-ion materials such as lead-acid, nickel-metal hydride, LiCoO_2 , LiMn_2O_4 and nickel cobalt manganese oxides. LFP is thermally stable, both to decomposition and to thermal runaway and is therefore inherently safer, LFP has a high theoretical capacity of 170 mAh/g (Etacheri, Marom et al. 2011), strong cyclability, good performance at high current loadings (Kang and Ceder 2009) and thus can deliver high power and is made from readily available and low cost precursors. The utilisation of lithium iron phosphate as a cathode material in lithium ion rechargeable batteries stems from the ability to reversibly intercalate Li-ions into and out of the iron phosphate structure. This allows LFP to act as one half of a battery cell, being a lithium ion ‘sink’, taking Li-ions into the structure, but also readily losing them to the anode, brought about in a battery due to the difference in chemical potential across the electrodes (Whittingham 2004). The resulting chemical energy drives electrical energy in the form of electrons which can flow through an external circuit to do work, thus generating energy. Upon charging and discharging of a battery using LFP as a cathode or more specifically reversible intercalation of Li-ions in the lithium cathode, there is minimal to no distortion to the overall structure of the cathode, since LiFePO_4 and FePO_4 have similar structures, or structures that have to undergo little change to accommodate or lose Li-ions. The Li-ions sit in ‘channels’ in which they can shuttle freely into and out of the structure. This unique feature allows greater stability of LFP cathodes, as other materials undergo expansion and

Chapter 5: Lithium Iron Phosphate

contraction upon intercalation which leads to distortion of the structure and a gradual breakdown of stability, leading to poor cathode performance over extended durations.

Despite these advantages, LFP suffers two key drawbacks: low electronic conductivity ($\sim 10^{-10}$ S/cm) and sluggish Li^+ ion diffusivity ($10^{-14} - 10^{-17}$ cm²/S) (Prosini, Lisi et al. 2002, Wang and Hong 2007), both of which hinder the ability of the material to effectively utilise all active cathode material and maximise lithium transfer, leading to reduced electrochemical capacities and performance. Chemical methods such as doping (Chung, Bloking et al. 2002) or carbon coating (Ravet, Chouinard et al. 2001, Julien, Zaghbi et al. 2006) can alleviate electronic conductivity drawbacks, and manipulation of the particles themselves by driving the size of the particles down to the nanoscale (Yamada, Chung et al. 2001, Delacourt, Poizot et al. 2006, Ellis, Kan et al. 2007) and/or shortening the transport distance for Li^+ ion diffusion (Hsu, Tsay et al. 2004, Chen, Song et al. 2006, Laffont, Delacourt et al. 2006, Fisher, Hart Prieto et al. 2008, Fisher and Islam 2008, Gibot, Casas-Cabanas et al. 2008, Saravanan, Reddy et al. 2009, Nan, Lu et al. 2011) through the manipulation of specific particle face or surface dimensions and preferential surface exposure can aid in more facile and efficient Li-transfer, and thus, increased performance towards the theoretical energy capacity in electrochemical applications.

A wealth of different synthesis techniques are used to prepare LiFePO_4 materials, including co-precipitation, microwave processing, sol-gel, mechanical activation and solid-state methods, (Arnold, Garche et al. 2003, Higuchi, Katayama et al. 2003, Hu, Doeff et al. 2004, Kim, Choi et al. 2007,

Chapter 5: Lithium Iron Phosphate

Koltypin, Aurbach et al. 2007) respectively, and also hydrothermal (Yang, Zavalij et al. 2001, Chen and Whittingham 2006) and solvothermal (Saravanan, Reddy et al. 2009, Yang, Wu et al. 2009, Saravanan, Balaya et al. 2010) production techniques. Whilst in many cases producing high quality LFP, often these suffer the associated problems with batch-wise techniques (certainly when compared to continuous flow techniques), including long synthesis time, low scale and the need for post-processing high temperature sintering to enhance the crystallinity of the obtained materials. Advanced hydrothermal and solvothermal techniques have recently been employed to produce LFP, under batch-wise operation, specifically to offer fine control of reaction conditions such as temperature, reaction time, additive choice and solvent to carefully ‘design’ particles with favourable sizes and morphologies for enhanced electrochemical characteristics (Rangappa, Sone et al. 2010, Rangappa, Sone et al. 2010, Lu, Chen et al. 2011, Nan, Lu et al. 2011, Devaraju and Honma 2012, Pei, Yao et al. 2012, Wang, Sun et al. 2013, Zhu, Fiore et al. 2013). The ideal for Li-ion battery applications are high purity, crystalline LFP nanoparticles, of small size, ideally with short b-axis thicknesses since this is the direction of Li-ion transfer, and with a degree of carbon coating, all to assist in Li-ion transfer into and out of particles, maximising energy capacity and electrochemical characteristics. Due to the current demand and projected increasing global demand, large-scale production of LFP is desirable and continuous hydrothermal and solvothermal methods offers the opportunity to produce LFP at industrial scales.

The first reported synthesis of LiFePO_4 and hence the basis for subsequent work was reported by Yang & Whittingham et al. (Yang, Zavalij et al. 2001),

Chapter 5: Lithium Iron Phosphate

achieved through a batch subcritical water hydrothermal route from LiOH, FeSO₄ and H₃PO₄ precursors. Lee et al. (Lee and Teja 2005) advanced on this work by comparing batch hydrothermal synthesis in both sub- and supercritical water and commencing the discussion on the link between the process parameters and resultant product. It was found that at neutral or slightly basic pH (3:1:1 ratio of Li:Fe:PO₄), lower temperatures (20-290 °C) produced micron-sized amorphous particles of both LiFePO₄ and a reaction intermediate, vivianite, Fe₃(PO₄)₂.8H₂O. Upon increasing temperature above 300 °C, greater quantities of crystalline, uniform, diamond-shaped, submicron LiFePO₄ particles were produced and irregular particles of Fe₃(PO₄)₂.8H₂O were no longer observed.

Efforts then focussed on applying these basic principles of LiFePO₄ formation towards a continuous and scalable scWHS route. Through precise control of process parameters such as temperature, pH, precursor concentration, precursor and water flow rates and residence time, research has focussed on the production of high-quality LiFePO₄ nanoparticles with high levels of purity and the size and morphological control vital for superior electrochemical properties. It is generally accepted that smaller particles allow for more facile Li-ion diffusion into and out of particles, therefore gaining maximum utilisation of all available electrochemically active particle mass, improving energy capacity and electrochemical performance.

Lee, Xu et al. (Xu, Lee et al. 2008) reported advances towards a continuous hydrothermal route to small size LiFePO₄ in sub- and supercritical water. In a direct comparison between the batch and continuous experiments, Xu

Chapter 5: Lithium Iron Phosphate

concluded that smaller nanoparticles of regular shape were obtained in continuous experiments, compared to micron-sized and less regular particles in batch experiments. Having previously developed a continuous supercritical process towards nanoparticles, Aimable et al. (Aimable, Aymes et al. 2009) presented a route towards highly crystalline, nanoparticulate LiFePO_4 with minimal impurities. However, as observed in previous work, the particles displayed a high tendency to agglomerate hindering the electrochemical properties. Similarly to Xu & Lee, Aimable also observed that under subcritical conditions, amorphous $\text{Fe}_3(\text{PO}_4)_2 \cdot 8\text{H}_2\text{O}$ was produced with increasing levels of crystalline LiFePO_4 observed at higher reaction temperatures or after a period of heat treatment. It was also noted that at slower flow rates and hence longer reaction or residence times (12s), pure phase LiFePO_4 was produced due to more effective and efficient mixing of precursors. This is in contrast to higher flow rates and reduced reaction or residence times, where LiFePO_4 was produced but with the intermediate $\text{Fe}_3(\text{PO}_4)_2(\text{OH})_2$ also observed. This observation furthered and confirmed the findings of Lee et al. that $\text{Fe}_3(\text{PO}_4)_2(\text{OH})_2$ must be an intermediate in the formation of LiFePO_4 , even in CFHS conditions. Electrochemical measurements revealed a discharge capacity for the particles of 70 mAh g^{-1} at 0.1 C rate and 90 mAh g^{-1} at 0.01 C rate, compared to the theoretical capacity of 170 mAh g^{-1} . The relatively low discharge capacity was attributed to the rapid and substantial aggregation of primary particles.

Hong et al. reported the effect of the reactor geometry (Hong, Kim et al. 2013) and mixing on the resulting LFP particles (discussed in Chapter 1 Section 1.4.1). T-piece mixers with the incoming flows at 90° , 50° and a swirling effect

Chapter 5: Lithium Iron Phosphate

tee mixer were studied. The 90° Tee is an off-the-shelf part from Swagelok, whilst the 50° and swirling tees are both custom made by the research group. The study also examined the effect of different temperatures, flow rates and concentrations on the structure and properties of the product; however, based on mixing regime alone, the results indicated that the swirling tee mixer provided the most ideal conditions for LiFePO₄ synthesis. Use of the swirling tee at high flow rates resulted in smaller-sized particles, and even though similarly sized particles in the range 400–900 nm were produced using the three mixing tees at low flow rates, a smaller amount of impurities was present in the particles produced by the swirling tee when compared with those from the 90° and 50° tees, attributed to more efficient and complete mixing of the reagent streams with the supercritical water. As a result, a higher discharge capacity was observed with samples produced with the swirling tee. This research demonstrated the effect the mixing regime between precursors and supercritical water can have on the chemistry invoked and the mechanism of formation of materials, and how this can lead to products with varying characteristics in terms of purity, composition, crystallinity, size and size distribution, and how this translates into their performance in application based testing. It also demonstrated the sensitivity of the LFP formation mechanism, and demonstrated the importance of a complete and thorough mixing regime to ensure uniform and prolonged mixing of the metal salt streams and intermediates with the heated water stream.

Most recently, Hong et al. reported (Hong, Kim et al. 2013) the most substantial study to date on the effects of processing parameters on the physicochemical and electrochemical properties of obtained LiFePO₄ particles

Chapter 5: Lithium Iron Phosphate

made by CFHS. It was observed that at subcritical temperatures, similar to the results obtained by Aimable, $\text{Fe}_3(\text{PO}_4)_2 \cdot 8\text{H}_2\text{O}$ formed, together with Fe_2O_3 and Fe_3O_4 . At supercritical temperatures, olivine phase LiFePO_4 formed together with iron oxide impurities. All apparatus, precursor solutions and water were purged with nitrogen for at least one hour to remove the residual dissolved oxygen and to prevent the oxidation of the Fe^{2+} precursor species to Fe^{3+} in the reagent container. It was proposed that the iron oxidation must be occurring during the reaction inside the reaction apparatus. Particles formed under supercritical conditions were also observed to be smaller, less agglomerated and more regular with increased BET surface area compared to subcritical conditions. At increasing water flow rates and hence reduced residence times (11 s), LiFePO_4 XRD peak intensities decreased, and the formation of $\text{Fe}_3(\text{PO}_4)_2 \cdot 8\text{H}_2\text{O}$ dominates. It was therefore concluded that a low water flow rate, or effectively an increase in residence time, aids Li^+ ion incorporation and crystallinity.

It can be concluded that it is vital to carefully control the processing parameters to achieve the desired LiFePO_4 product and that the optimal processing conditions operate in a narrow window. In order to obtain highly crystalline, high-quality LiFePO_4 with minimal Fe^{3+} impurities it is necessary to work at supercritical temperatures and low water flow rates hence/or long residence times. Low temperature or short residence times lead to undesirable products such as $\text{Fe}_3(\text{PO}_4)_2 \cdot 8\text{H}_2\text{O}$, Fe_2O_3 and Fe_3O_4 .

It is obvious that there is a need for a new synthetic methodology towards LiFePO_4 to overcome the drawbacks still evident in the literature. Whilst the

Chapter 5: Lithium Iron Phosphate

current synthetic methodologies produce LiFePO_4 with adequate electrochemical properties, undesirable and laborious steps such as flushing solutions with nitrogen and product characteristics such as impurities, lack of size/morphology control and agglomeration hinder both the electrochemical performance of the particles and the commercial applicability or scale-up potential of these routes. The addition of an organic reducing agent into the reaction may be a more facile and industrially applicable method of eliminating the iron oxide impurities than flushing with nitrogen and simultaneously may aid the formation of crystalline LFP product and direct and control the growth and morphology of the resultant particles. This could alleviate problems observed in current products to produce pure, small particles of LiFePO_4 in the counter-current reactor. Coupling this with investigating the residence time by the addition of heated zones post-initial-synthesis and the development of an online method for optimised carbon coating of particles in the future, an improvement in the electrochemical performance may be achieved.

This chapter reports a series of reactions aiming to understand the formation of LFP by hydrothermal and solvothermal methods, using batch reactions to ultimately inform an optimised continuous flow route using the Nottingham counter-current reactor. One must take care when stating the desire to improve on the existing CFHS routes demonstrated by other researchers using alternative continuous flow reactors, since it has been discussed in this section the intricacies of each reaction that must be considered that are tailored towards the specific reactor set-up and geometry used. Therefore whilst it is an aim to add to the wealth of knowledge in the field on the formation of LFP by CFHS,

optimisation of the reaction using the Nottingham counter-current reactor is the main focus.

5.2. Experimental

5.2.1. Batch Hydrothermal & Solvothermal Synthesis

The batch reactions were undertaken in batch autoclave reactors in the laboratory of Prof. Tadafumi Adschiri at the World Premier Institute, Advanced Institute for Materials Research, Tohoku University, Sendai, Japan. Reactions were carried out in Hastelloy autoclave reactors (AKIKO, Japan) with 5 mL internal volume under autogenous pressure. An organic additive (ascorbic acid/citric acid - 0.05 M) was first dissolved in the total volume of water or ethylene glycol used for the reaction using sonication to minimize oxidation of the $\text{FeSO}_4 \cdot 7\text{H}_2\text{O}$ precursor (0.1 M) upon dissolving this after the ascorbic/citric acid had dissolved. The volume of solvent varies between 4 mL at 180 °C and 2.5 mL at 400 °C to account for the greater expansion of fluid inside the reactor vessel at higher temperatures generating increased pressure. Smaller volumes are required at higher temperatures since the expansion is greater, ensuring pressure is kept within safe operating levels dictated by the pressure limits of the autoclave vessels. Detailed information on the properties of water in terms of its expansion and generated pressure at varying temperatures is available via NIST – the National Institute of Standards and Technology. However, this information is not commonly available for other solvent systems, such as ethylene glycol. For this reason, at both temperatures of 180 °C and 400 °C, 2.5 mL of solvent was used as opposed to 4 mL for 180

Chapter 5: Lithium Iron Phosphate

°C as with water, to account for unexpected behaviour and greater solvent expansion and to ensure pressure stayed within safe pressure limits of the autoclave reactors. The LiOH.H₂O precursor (0.3 M) was added and sonicated to dissolve, finally followed by the H₃PO₄ (85% solution in H₂O) precursor (0.1 M) and the resulting mixture sonicated which produced a thick precursor gel ranging from a thick deep green with water and no additive/ascorbic acid to a thinner lighter green solution with ethylene glycol or citric acid. (This protocol ensures the 3:1:1 ratio of Li:Fe:PO₄ recognised as vital and discussed in the introduction to produce a neutral to slightly basic pH for the precipitation of LiFePO₄). The gel was then loaded into the autoclave which was sealed and introduced to a custom designed furnace set to the required temperature. The furnace was agitated to ensure mixing of the reactant solution inside the autoclave. After the desired reaction time, the autoclave was removed immediately from the furnace and placed into ice water to quench the reaction. Powders were isolated and washed with de-ionised water by repeated centrifugation steps before drying overnight at 70 °C.

5.2.2. Continuous Flow Hydrothermal & Solvothermal Synthesis

All flow reactions were carried out using the counter-current mixing reactor designed by Lester *et al.*, described in Section 1.4.3 and shown in Figure 5.2. For hydrothermal reactions, metal salts were dissolved into water to the required concentration under ambient conditions. For the solvothermal reactions, the metal salts are dissolved with stirring into ethylene glycol at 50 °C, and once dissolved, can then be removed from the heat and exist as stable dissolved solutions. Concentrations of precursors were as follows: Metal salt

Chapter 5: Lithium Iron Phosphate

solution 1: 0.03 M $\text{FeSO}_4 \cdot 7\text{H}_2\text{O}$, zero or 0.015 M ascorbic/citric acid, Metal salt solution 2: 0.09 M $\text{LiOH} \cdot \text{H}_2\text{O}$ and 0.03 M H_3PO_4 (85% solution in H_2O) – conserving the 3:1:1 ratio of Li:Fe:PO₄. Short residence time reactions were undertaken using the standard reactor configuration – longer residence time reactions involved passing the product solution into a 2nd 6 m length heated coil with 1/8” diameter which is wrapped around a cartridge heater set at the desired temperature, before being discharged from the system. Unless otherwise stated the flow rates were maintained at 20 mL min⁻¹ for the downflow and 5 mL min⁻¹ for each pump for the upflow (10 mL min⁻¹ total). Products were obtained as the appropriate solvent suspensions. Powders were isolated and washed with de-ionised water by repeated centrifugation steps (for products in ethylene glycol, diluting the product solution by half with water allowed a reduction in the viscosity of the fluid and allowed the product to be isolated by centrifugation) before drying overnight at 70 °C.

Concentrations of precursors were doubled on the pilot scale reactor due to the larger diameter pipework allowing for increased quantity of product to be produced, which increased product turnover compared to laboratory scale. Doubling of the concentrations was conservative – it is known this could be increased far greater in future work. Concentrations of precursors were as follows: Metal salt solution 1: 0.06 M $\text{FeSO}_4 \cdot 7\text{H}_2\text{O}$, 0.03 M ascorbic acid, Metal salt solution 2: 0.18 M $\text{LiOH} \cdot \text{H}_2\text{O}$ and 0.06 M H_3PO_4 (85% solution in H_2O) – conserving the 3:1:1 ratio of Li:Fe:PO₄. The flow rates of the water and two metal salt streams were 500 mL min⁻¹, 125 mL min⁻¹ and 125 mL min⁻¹ respectively. The pilot scale reactor is currently configured to allow for preheating of the water stream only, with no additional heating post-reaction.

Chapter 5: Lithium Iron Phosphate

Materials were isolated from the product solution as in the laboratory scale reactions.

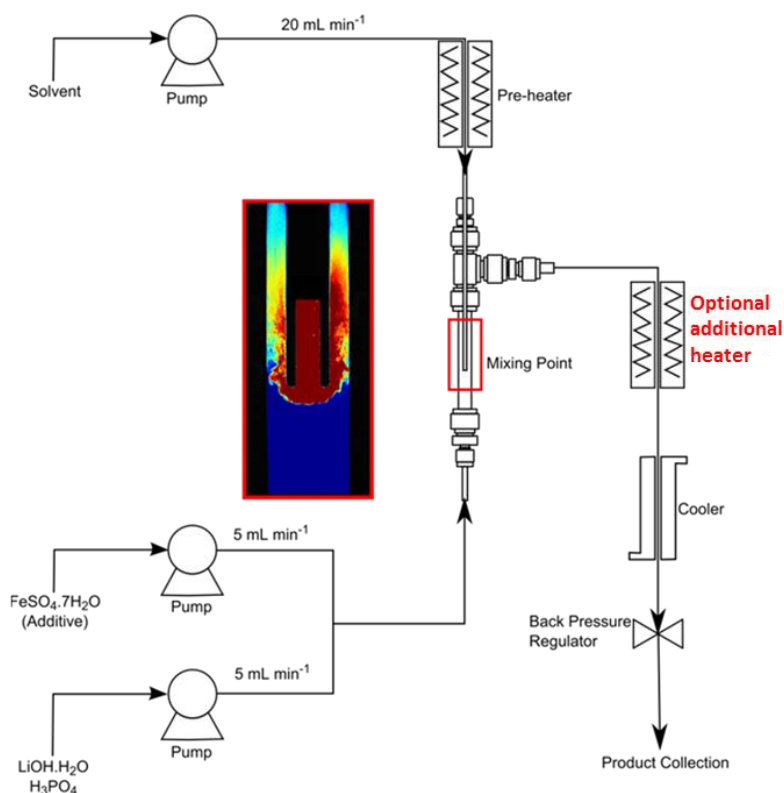


Figure 5.2: Simple schematic of the continuous hydro- and solvothermal reactor designed and used at Nottingham for the continuous flow production of lithium iron phosphate.

5.2.3. Characterisation

Powder X-ray diffraction patterns of the products were collected on a Siemens D-500 diffractometer using Cu K α radiation ($\lambda = 1.5418 \text{ \AA}$) over a 2θ range of $10 - 70^\circ$, with a step size of $0.05^\circ 2\theta$ at 4s/step. Scanning electron microscope images were obtained by depositing the powders onto a sticky carbon grid and coating the materials with platinum, and using a FEI/Philips XL30 FEG-ESEM at 20 kV. Transmission electron micrographs were obtained using a JEOL 2100F at an accelerating voltage of 200 kV. Samples were prepared for transmission electron microscopy by resuspending the dried powders in

acetone with sonication and then deposited on 300 mesh lacey carbon coated copper grids.

5.2.4. Electrochemical Characterisation

A selection of products were tested in Li-ion rechargeable coin cell batteries in the Green Energy Materials & Processes Laboratory at Sungkyunkwan University, Suwon, South Korea, collaborating with Prof. Jaehoon Kim, to assess the applicability of the materials towards lithium ion battery applications. To prepare the material for battery cycle testing, as synthesised selected LFP powders from the counter-current CFHS and CFSS reactions were calcined prior to use as the cathode material (700 °C for five hours under a flow of 5% hydrogen gas in argon). This promotes crystallisation, ordering of the material and the removal of impurities and defects which may be detrimental to electrochemical cycling. The LFP powder constitutes 70% of the cathode slurry mixture, with carbon black (20%) added to increase the electronic conductivity of the electrode, and polyvinylidene fluoride (PVDF) in N-methyl-2-pyrrolidone (NMP) added as a binder to ensure effective mixing of the constituents when homogenised. The mixture is homogenised (4000 rpm, 5 mins) to create a viscous black gel, similar to tar in appearance, which is then deposited onto the cathode current collector (aluminium foil) using a doctor blade to give a uniform layer of cathode slurry at a precise thickness. NMP is used to dissolve the PVDF binder only, and as such after this process needs to be removed. Heating the foil in a vacuum oven at 70 °C overnight allows the NMP to evaporate. Due to the transfer of current from the aluminium foil and the lithium intercalation material, there is a need for strong contact between the

Chapter 5: Lithium Iron Phosphate

two. This is achieved by repeatedly hot-pressing the dry cathode slurry against the foil using heated rollers at 100 °C. Electrodes can then be punched from the foil to precise dimensions, and the cut electrodes are weighed. Knowing the exact dimensions and exact weight of the aluminium foil enables an extremely accurate calculation to be made as to the quantity of active LFP material present on the electrode. This enables the capacity of the LFP in that particular coin cell to be measured from galvanostatic cycling. The electrode is incorporated into a coin cell in an argon filled glovebox. Preparing the coin cell in the absence of oxygen and moisture is vital. The electrolyte LiPF_6 is readily attacked by water forming hydrofluoric acid, which corrodes the coin cell components and can damage the cathode material, leading to reduced electrochemical performance. Firstly, a drop of the electrolyte, LiPF_6 in ethylene carbonate/dimethyl carbonate/ethylmethyl carbonate (EC:DMC:EMC = 1:1:1) solvent is placed on the coin cell casing bottom to ensure contact between the casing and the aluminium foil cathode, which is placed in first as the bottom layer. This is then wetted with 2-3 drops of electrolyte, and a separator, in this case a Celgard 2500 microporous polypropylene membrane is placed on top. This keeps the cathode foil and anode, in this case Li foil, separated, to prevent short circuiting the coin cell. Li foil acts as the source of the lithium ions in the cell. Before the addition of each layer, a drop of electrolyte is added to ensure more facile and efficient transfer of Li-ions and electrons through the cell. A number of components such as spacers and discs are then added to compress the layers and ensure uniform pressure on all components upon crimping the cell together, which is done following pressing the cell top casing onto the stack to complete the layers using a hydraulic

Chapter 5: Lithium Iron Phosphate

crimping machine. The coin cell is then prepared for testing. Figure 5.3 illustrates this process of coin cell preparation for the actual materials and cells used in this testing. Electrochemical measurements were undertaken using a multichannel galvanostatic charge-discharge cyler (WonAtech Corp., Korea, WBCS 2000) at room temperature. The cells were cycled between 2.5 and 4.5 V versus Li^+/Li at 0.1 C for low power application testing, and at various charge rates between 0.1 C and 30 C for potential high power applications.

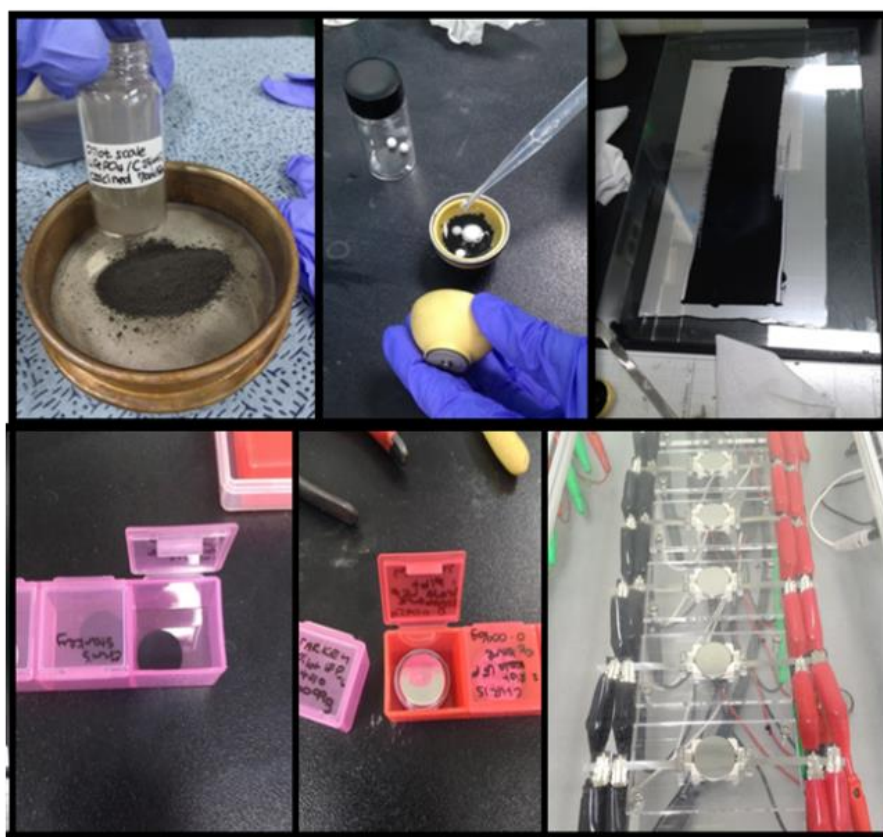


Figure 5.3: Pictures illustrating the preparation of the coin cells in Korea using LFP from the Nottingham counter-current reactor for electrochemical characterisation.

5.3. Results & Discussion

5.3.1. Batch Hydrothermal Synthesis of LFP

5.3.1.1. 180 °C

The conditions employed in the sub-critical batch hydrothermal synthesis of LFP are summarised in Table 5.1, along with the products identified by powder XRD.

Table 5.1: Summary of batch hydrothermal reactions at 180 °C for LFP production

T/°C	V Solvent (mL)	Additive	Reaction Time	Products
180	4	None	1 h	LiFePO ₄ , Fe ₂ PO ₅
180	4	None	6 h	LiFePO ₄
180	4	None	9 h	LiFePO ₄ , Fe ₂ PO ₅
180	4	Ascorbic acid	1 h	LiFePO ₄
180	4	Ascorbic acid	6 h	LiFePO ₄
180	4	Ascorbic acid	9 h	LiFePO ₄
180	4	Citric acid	1 h	LiFePO ₄ , Fe ₂ PO ₅
180	4	Citric acid	6 h	LiFePO ₄ , Fe ₂ PO ₅
180	4	Citric acid	9 h	LiFePO ₄ , Fe ₂ PO ₅

Using no additive (Figure 5.4), the product yielded at short reaction time of one hour consists of large 5-10 µm faceted clumps with submicron sheet material on the surface and in the vicinity, and by XRD is poorly defined LiFePO₄ and Fe₂PO₅. After six hours, pure LiFePO₄ is produced, and the particles are fairly homogeneous in size; ~3 µm in length, 1 µm in width and 0.2 µm thick. The particles are elongated parallelepiped in shape, with an aspect ratio of 3:1 length:width, with high levels of fracturing on the surfaces and edges. These diamond-like particles are explained by Islam et. al. (Fisher and Islam 2008), through TEM analysis of LFP crystal faces by Chen et al. (Chen, Song et al. 2006), who showed the (010) and (100) faces of growing LFP crystals have the

Chapter 5: Lithium Iron Phosphate

lowest attachment energy, which dictates that elongation into the c-axis direction occurs producing thin, elongated parallelepipeds with exposed (010) surfaces. It is believed that Li-ion diffusion, or insertion and de-insertion occurs perpendicular to the c-axis (which is normal to (010)) in the b-axis (010) channels, hence, greater exposure of this surface allows for more facile conduction of Li-ions through these channels, thus improving electrochemical characteristics. The sample from the nine hour reaction consists of extremely elongated needle or shard type rods, which pack together to form large (ca. 50 μm) secondary bunched structures. By XRD this sample is a mix of LiFePO_4 and Fe_2PO_5 . The size of the rods, in terms of width of the main body and the caps/ends, are fairly homogeneous and rhombic in shape, suggesting therefore that these sharp rods are an extension of the parallelepiped structures observed at six hours, with the material depositing through a dissolution-recrystallisation mechanism onto the rhombus shaped exposed (010) face and growing preferentially along the (100) direction.

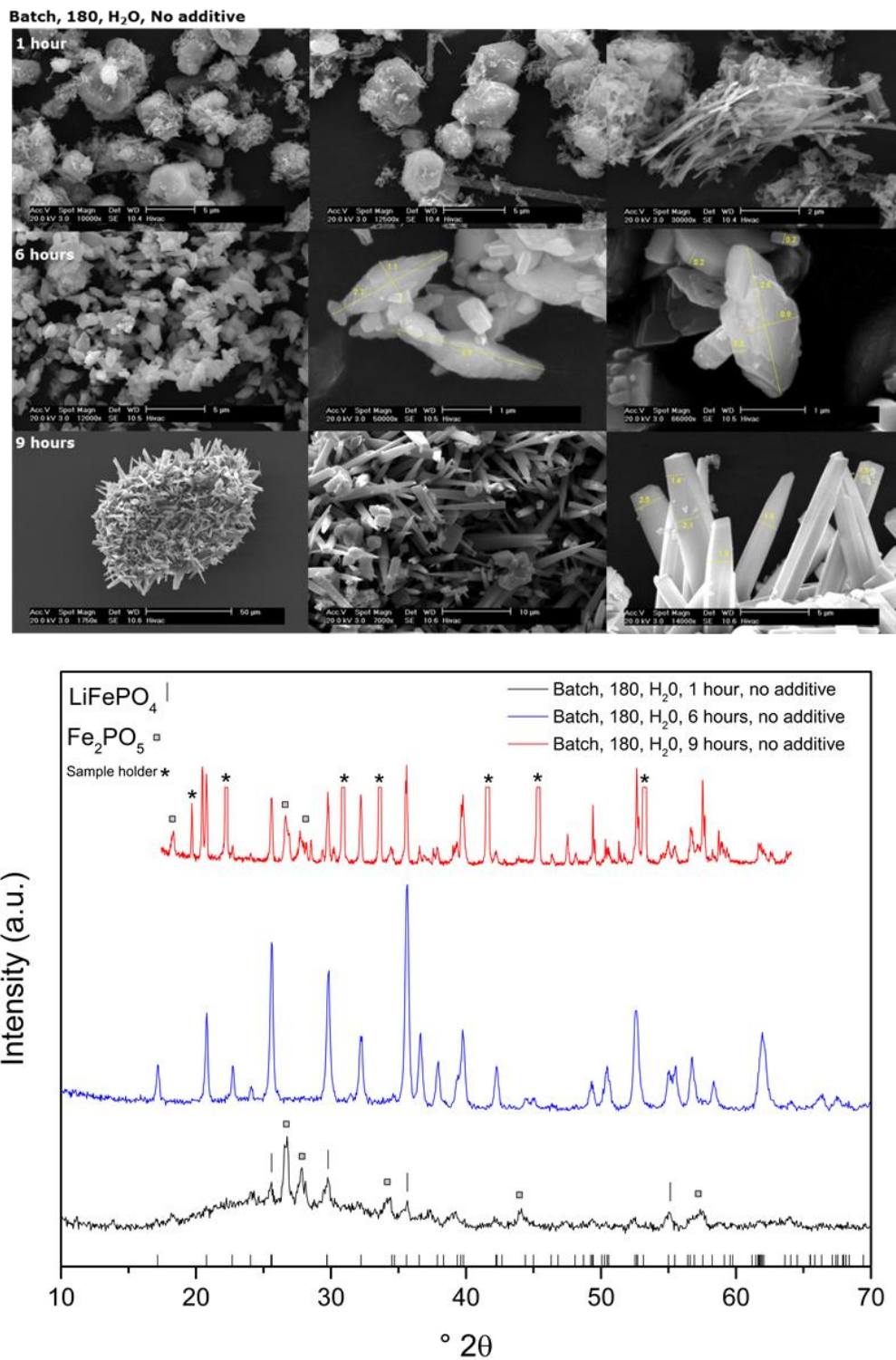


Figure 5.4: SEM images and XRD patterns of the products from batch hydrothermal reactions at 180 °C with no additive.

Chapter 5: Lithium Iron Phosphate

The addition of ascorbic acid to the reaction has a profound effect (Figure 5.5). Firstly, by XRD, the product after one hour is pure LiFePO_4 (there is a slightly increased background between 20-35 °2 θ possibly indicating the presence of small quantities of amorphous product, potentially Fe_2PO_5). This indicates that ascorbic acid is promoting a faster reaction by aiding the formation of intermediates and hastening the subsequent lithiation towards LiFePO_4 . This may be by preventing the oxidation of ferrous ions (Hsu, Tsay et al. 2004). The morphology of particles is again parallelepiped, with the average particle length larger than the no additive product at $\sim 14 \mu\text{m}$, width $\sim 10 \mu\text{m}$, and thickness $\sim 2 \mu\text{m}$. The surfaces of the particles are smooth compared to the fractured and broken surfaces and edges at six hours with no additive, indicating more controlled and uniform growth of particles when under ascorbic acid control. After six hours, the product is well crystalline, pure LiFePO_4 , and there is a clear difference in particle characteristics. The parallelepiped particles are now $\sim 5.5 \mu\text{m}$ in length, $2 \mu\text{m}$ in width and $0.6 \mu\text{m}$ thick, yet their appearance is markedly different – the single crystalline smooth surfaces and edges of one hour have now been replaced with heavily etched surfaces with the particles consisting of smaller crystallites – there is also no undefined material on the surfaces of particles. There appears to be a degree of order and uniformity within particles and throughout the sample, suggesting that these particles are etched versions of the particles at one hour, as opposed to secondary structures formed through oriented attachment of small primary structures, as observed elsewhere (Zhu, Fiore et al. 2013). After nine hours, the sample appears to contain a mixture of some remaining parallelepiped structures, which have ‘fattened’ out, with lengths of $\sim 6 \mu\text{m}$ and thicknesses of

Chapter 5: Lithium Iron Phosphate

~7 μm , and similarly to the no additive examples, rods, roughly 12 μm long and with 4 μm wide rhombus end faces, and by XRD is LiFePO_4 with small quantities of an iron phosphate. The parallelepiped particles appear fairly homogeneous in size in relation to each other, and all express heavily etched and textured surfaces, with visible 'holes' throughout the particle surface and layering towards the edges clearly observable. This may arise through the etching of particle surfaces by ascorbic acid. These rods display the calculated growth morphology proposed by Islam et. al. (Fisher and Islam 2008), terminated by (010), (100) and (101) faces.

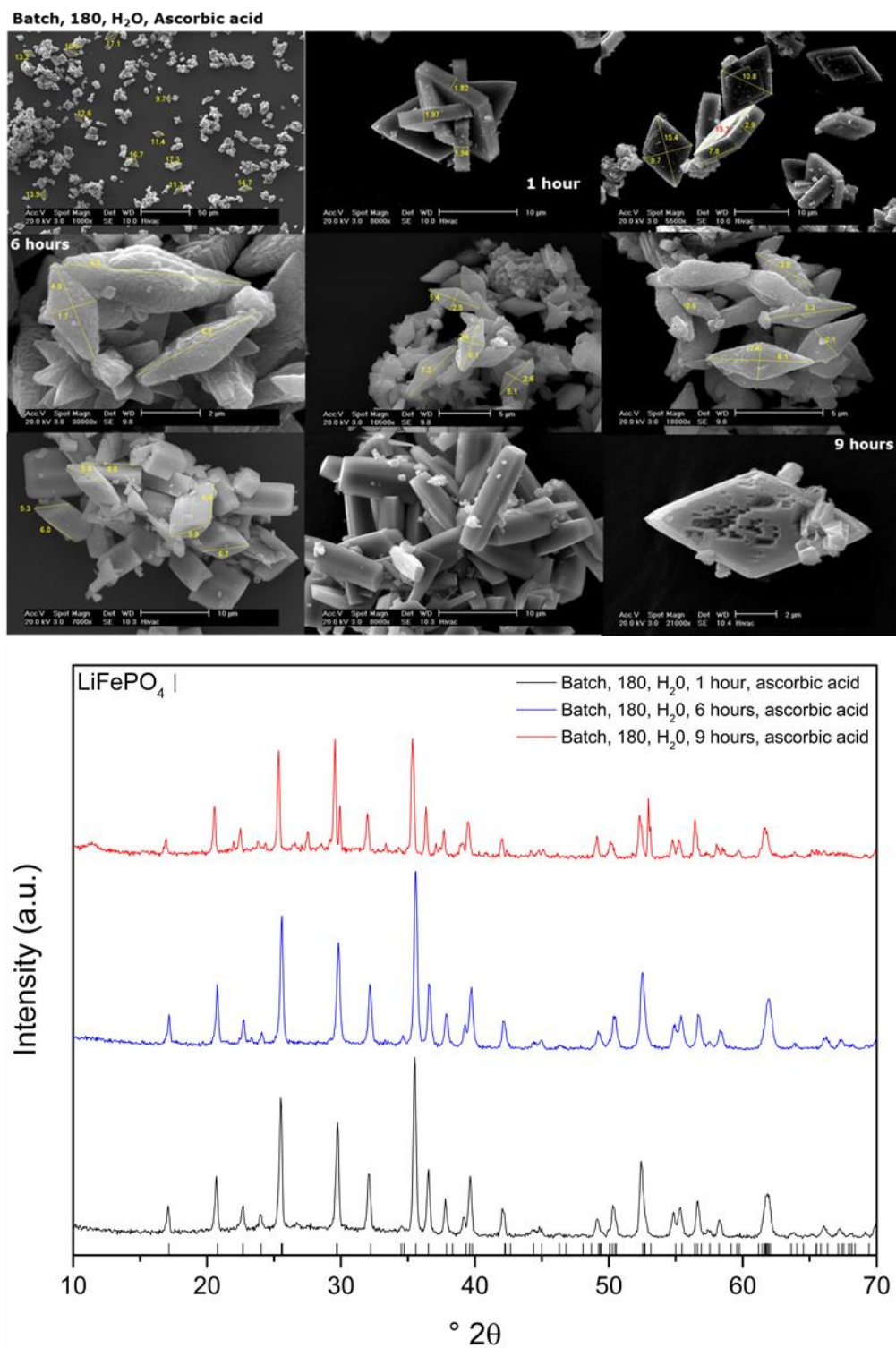


Figure 5.5: SEM images and XRD patterns of the products from batch hydrothermal reactions at 180 °C with ascorbic acid additive.

Chapter 5: Lithium Iron Phosphate

Using citric acid (Figure 5.6) as an additive in the reaction has a marked effect on the morphology and purity of the sample. After one hour, 3 μm desert rose microcrystal type structures are formed, consisting of large, thin (40 nm) wavy sheet structures. The microcrystals are uniform in size and shape throughout the sample, however there does exist other undefined material, perhaps explaining the appearance of both LiFePO_4 and Fe_2PO_5 in the XRD pattern.

It appears that the citric acid is having a pronounced effect on how these particles are bound together, since the high packing density of the particles within the desert rose type microballs suggests the citric acid is binding together the growing sheets. Citric acid has a free carbon chain capable of rotation and strong resonance throughout the structure, allowing the possibility for complexing/chelating, which it does readily. It is also interesting to note (as is observed in the continuous reactions later also) that whilst ascorbic acid produced a pure sample after one hour, it appears citric acid is slowing the process of conversion to LFP down – the intensity of the Fe_2PO_5 XRD peaks at one hour is actually greater than those for LiFePO_4 . After six hours, the intensity of the Fe_2PO_5 peaks has decreased with a comparative increase in intensity of LiFePO_4 peaks. The desert-rose type character of the wavy sheet material has been replaced by large 10 μm balls of highly faceted, tightly packed crystals, varying in length but mostly having thicknesses of ~ 200 nm. Again, there is uniformity in size and shape. The emergence of highly bunched and dense packets of long, thin rods is also observed. These are uniform in the size of the primary and secondary structure, with bunches ~ 3.8 μm in length, 1.8 μm in width at the fanned-out tips, and 1.3 μm wide in the middle. After nine hours, the most noticeable difference concerns the size of the microballs

and packets of rods. There has been severe shrinkage in all dimensions, resulting in balls $\sim 2 \mu\text{m}$ in diameter that are more disc-like in shape as opposed to spherical balls. The appearance has changed to more indistinguishable heavily textured continual material that has etches/protrusions from the surface. The discs appear to consist of large numbers of much smaller crystallites. Similarly, the packets of rods have reduced in size, and become so dense that it is no longer possible to distinguish between individual rods within the bulk of the packet. This densification of the two morphologies could arise from a combination of two factors. The first is a dissolution-recrystallisation mechanism, whereby material is undergoing a constant crystallisation followed by eventual dissolution of LiFePO_4 due to factors such as the decrease of pH of solution due to depletion of OH^- groups as the reaction progresses (Zhu, Fiore et al. 2013) and the elevated temperature. Recrystallisation likely occurs at pre-existing interparticle interfaces. Coupled with this, is the possible enhanced etching effect of citric acid (Lu, Chen et al. 2011), specifically etching of Fe^{2+} and Li^+ , which further enhances the likelihood of dissolution of formed material and forces the particles to adopt more conformationally stable sizes and structures. By XRD, the product is again a mix of LiFePO_4 and Fe_2PO_5 , however, the relative intensity of Fe_2PO_5 is now much reduced. The possible differing capping/chelating actions of citric acid are summarised in Figure 5.7.

Chapter 5: Lithium Iron Phosphate

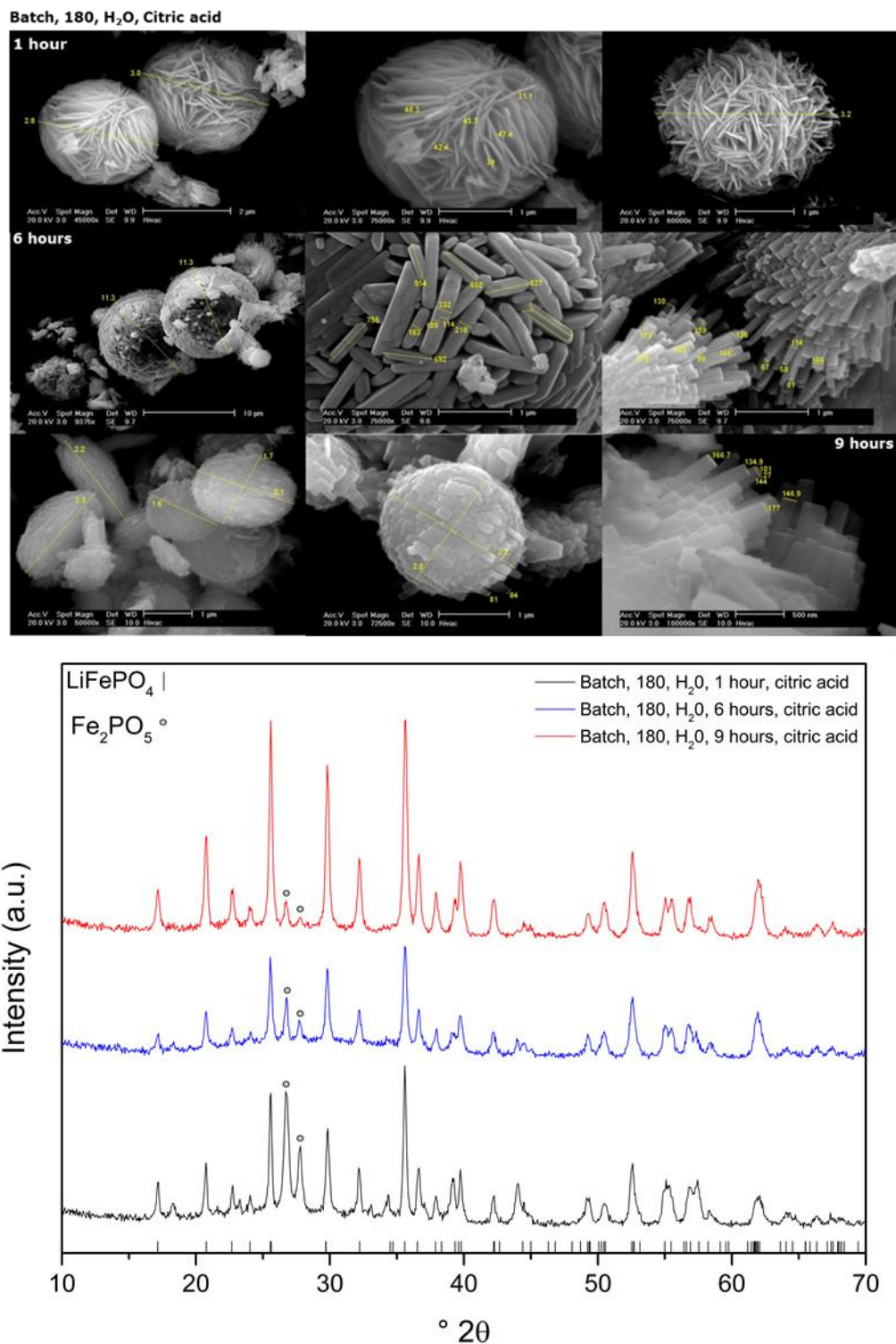


Figure 5.6: SEM images and XRD patterns of the products from batch hydrothermal reactions at 180 °C with citric acid additive.

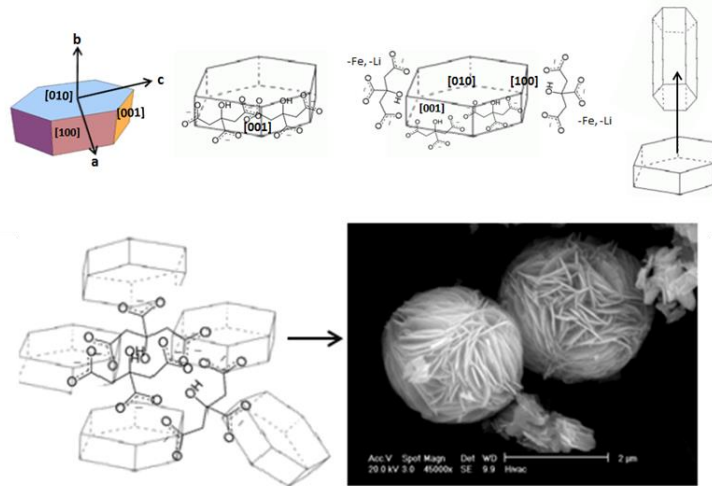


Figure 5.7: Possible citric acid growth directing mechanisms in batch hydrothermal LFP synthesis, acting as either a capping and therefore directing agent (discussed further in the 400 °C reactions with citric acid in Section 5.3.1.2) (top), or as a chelating agent controlling assembly, as in the hydrothermal reaction with citric acid at 180 °C (bottom).

Chapter 5: Lithium Iron Phosphate

5.3.1.2. 400 °C

The conditions employed in the supercritical batch hydrothermal synthesis of LFP are summarised in Table 5.2, along with the products identified by powder XRD.

Table 5.2: Summary of batch hydrothermal reactions at 400 °C for LFP production

T/°C	V Solvent* (mL)	Additive	Reaction Time	Products
400	2.5	None	5 min	LiFePO ₄
400	2.5	None	10 min	LiFePO ₄ , Fe ₂ PO ₅
400	2.5	None	60 min	LiFePO ₄
400	2.5	Ascorbic acid	5 min	LiFePO ₄ , Fe ₂ PO ₅
400	2.5	Ascorbic acid	10 min	LiFePO ₄ , Fe ₂ PO ₅
400	2.5	Ascorbic acid	60 min	LiFePO ₄ , Fe ₃ (PO ₄) ₂
400	2.5	Citric acid	5 min	LiFePO ₄ , Fe ₂ PO ₅
400	2.5	Citric acid	10 min	LiFePO ₄ , Fe ₂ PO ₅
400	2.5	Citric acid	60 min	LiFePO ₄

Under supercritical conditions, the product obtained from a short reaction time of five minutes with no additive (Figure 5.8) is pure LiFePO₄, albeit with a degree of amorphous character to the XRD pattern between 20-35 °2 θ . This is in contrast to the product obtained in identical conditions at subcritical temperatures, which contained high levels of iron phosphate 5-10 μ m clumps and sheet like material (Figure 5.4). Supercritical conditions greatly enhance reaction rates and can rapidly form crystalline materials, and the elevated temperatures appear to have hastened the formation of intermediates and conversion to final products (LFP). Also noticeable is the decrease in size – the roughly defined parallelepipeds are fairly homogeneous in size, with lengths of ~ 600 nm - 1 μ m, widths of 450 nm and thickness of 250 nm.

The fairly loosely defined edges and faces of the particles may arise from the short reaction time and the harsh conditions at supercritical temperatures, with

Chapter 5: Lithium Iron Phosphate

the particles needing more time to form more defined faces and edges. After ten minutes, the sample is highly-crystalline LiFePO_4 , with the loss of amorphous character from the XRD pattern, but the appearance of a small quantity of Fe_2PO_5 . From the SEM images it can be observed that a range of sizes of parallelepipeds are formed, ranging from 1-5 μm in length (5 μm roughly the average), 3 μm in width, and 800 nm thick. After sixty minutes, the appearance of well-formed, disperse, fairly homogeneously sized and shaped tablet/lozenge type parallelepipeds is observed. The particles appear to have smoothed down edges and the surfaces of particles also appear smooth and single crystalline. The particles have an average length of 2 μm , width of 1-1.5 μm , and thickness of 500 nm.

Chapter 5: Lithium Iron Phosphate

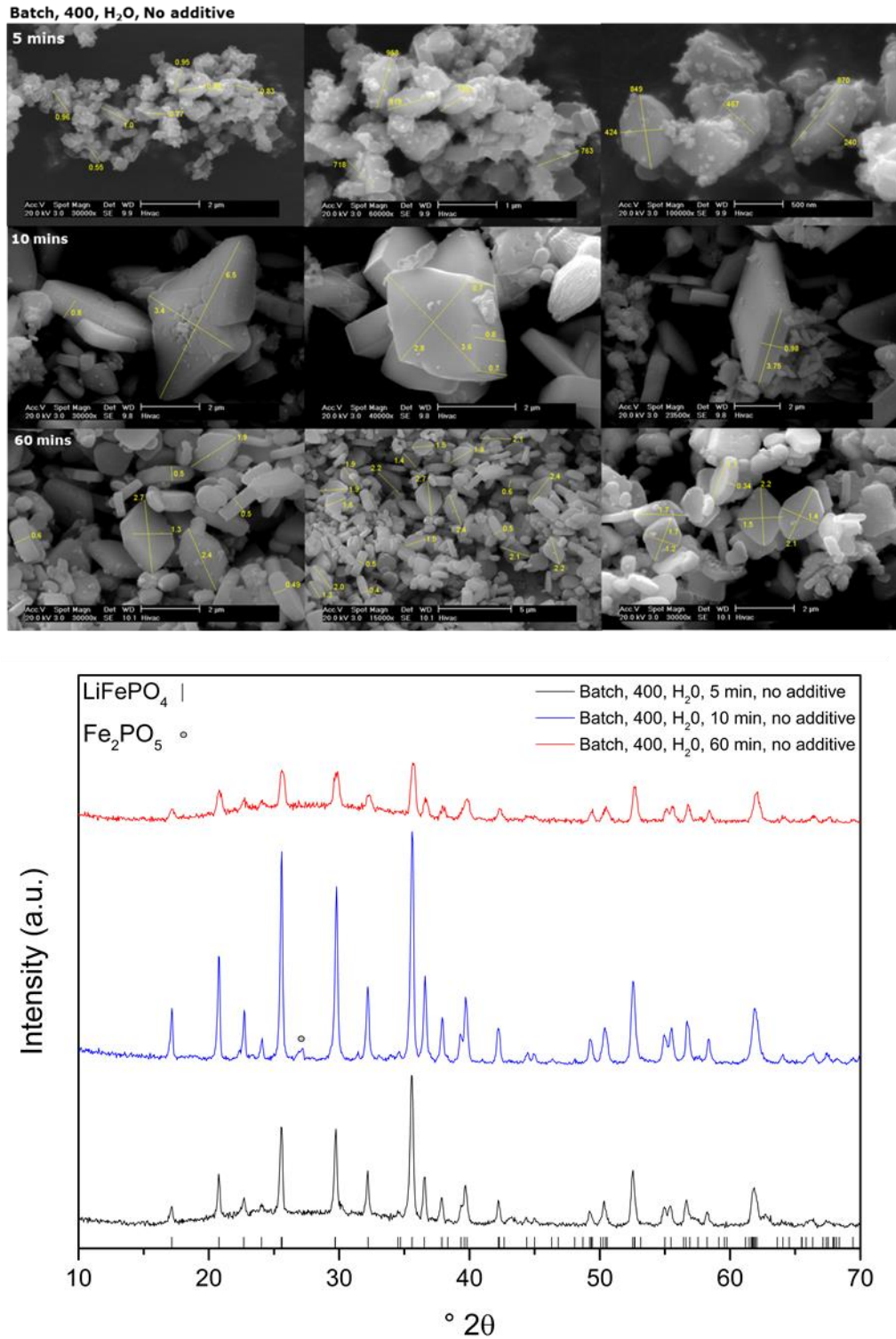


Figure 5.8: SEM images and XRD patterns of the products from batch hydrothermal reactions at 400 °C with no additive.

Chapter 5: Lithium Iron Phosphate

When ascorbic acid was employed as an additive (Figure 5.9), at a reaction time of five minutes, LiFePO_4 is produced, though very low intensity Fe_2PO_5 peaks are also present in the XRD pattern. Again this demonstrates the ability of ascorbic acid to hasten and facilitate the reaction towards LFP. The majority of particles are parallelepipeds with lengths of 5 μm , widths of 3 μm and thickness of 1 μm (similar dimensions to those achieved after ten minutes with no additive). There is a noticeable difference in the characteristics however, as the (010) particle surfaces formed in the presence of ascorbic acid appear to be layered or stacked. They appear more to consist of smaller flakes that have fused together into defined shapes to create the faces of the parallelepipeds. After ten minutes there is again an overall shrinkage and densification of particles, with parallelepipeds $\sim 1.5 \mu\text{m}$ in length, 0.9 μm in width and 350 nm in thickness observable. By XRD, crystalline LFP still dominates, however the relative intensity of Fe_2PO_5 has increased, further enhancing the theory that the reaction evolution is undergoing constant dissolution-recrystallisation. In contrast to the longer residence time reaction without an additive, the particles at sixty minutes are considerably larger than after ten minutes. This could be an effect of the kinetics of reaction – for instance we may have observed particle growth if the slower, no additive reaction, reaction time was increased. However, it certainly appears that the ascorbic acid promotes continual growth through sixty minutes into all dimensions and interestingly into a specific crystal plane/dimension. These thicker parallelepipeds are now $\sim 6 \mu\text{m}$ in length, 4 μm in width, and 2 μm thick. This fattening out of the particles (growth that lengthens the (100) face or onto the (010) surface) is expected from the equilibrium barrel like structure of lithium iron phosphate (Fisher and

Chapter 5: Lithium Iron Phosphate

Islam 2008). There is evidence of severe etching in specific regions on particles, with portal like openings evident on the surfaces of some particles. By XRD, again the product is highly crystalline LiFePO_4 , however certain peaks have slight splits, with the closest match to these extra peaks matching $\text{Fe}_3(\text{PO}_4)_2$, a known intermediate in the formation of LiFePO_4 .

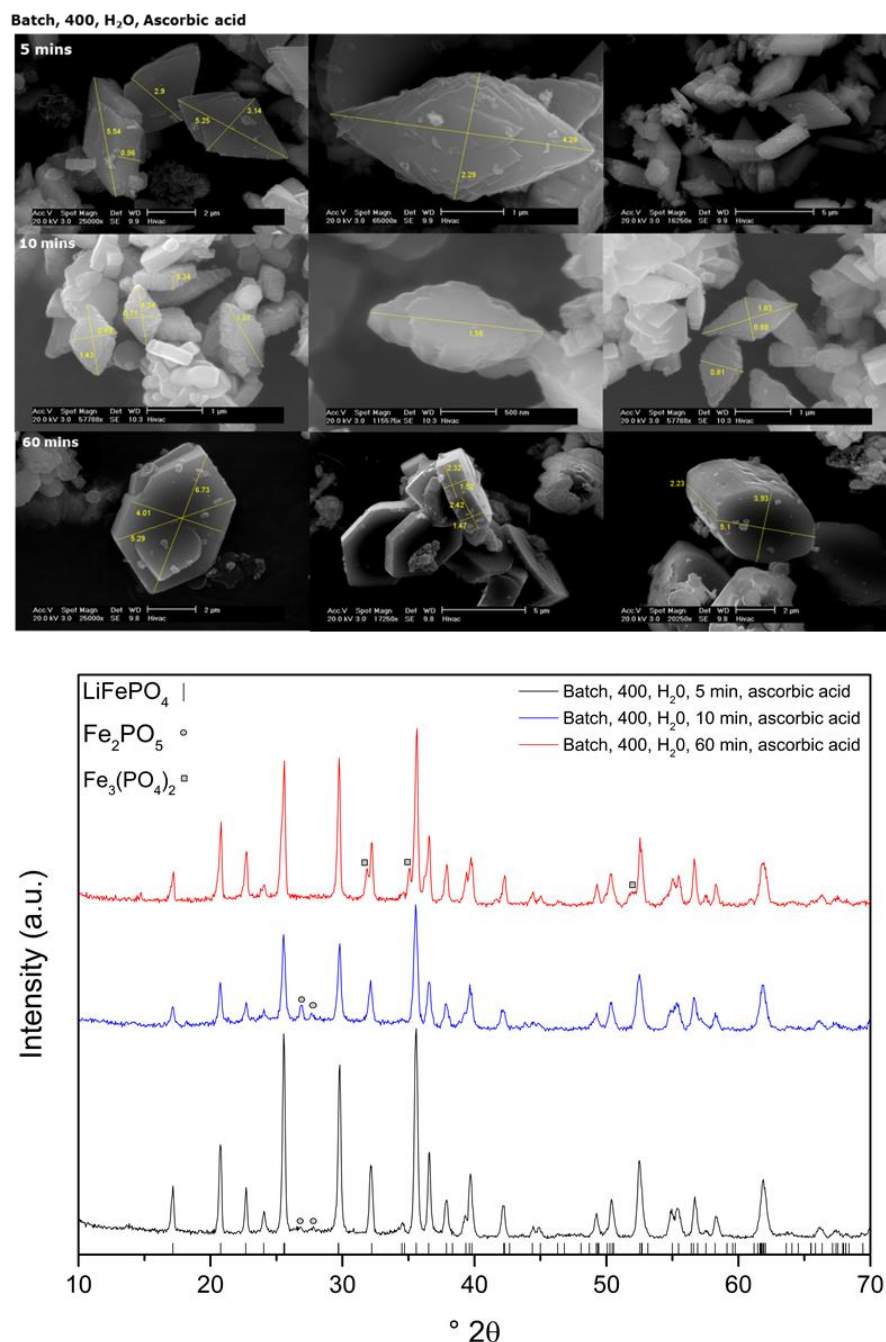


Figure 5.9: SEM images and XRD patterns of the products from batch hydrothermal reactions at 400 °C with ascorbic acid additive.

Chapter 5: Lithium Iron Phosphate

Whilst the general dominant morphology for the LFP particles in this study thus far with no additive or ascorbic acid has been the parallelepiped structures, citric acid appears to have a different effect, as demonstrated by the balls, discs and rods observed at subcritical conditions and under supercritical conditions this effect is drastically exaggerated. With the exception of the length of some rod structures at just over 1 μm , all particles obtained via this route are sub 1 μm in all dimensions (Figure 5.10). At five minutes, all particles are within the 100-500 nm size range. Due to the small size, there is aggregation, yet individual particles remain defined and separate. This sample by XRD is highly crystalline LiFePO_4 and the two strongest peaks for Fe_2PO_5 are present in significant relative intensity – furthering the evidence to suggest citric acid promotes a slower, gradual conversion of intermediates to LFP. After ten minutes, the relative intensities of LiFePO_4 and Fe_2PO_5 remain fairly constant; however the dominant morphology of the sample is now nanorod. The nanorods appear highly crystalline, with well-defined edges, faces and corners, and smooth surfaces, albeit with some portal-type etching as mentioned previously on the surface of some of the nanorods. There is a small portion of material still in the block type morphology of five minutes, however, they have begun to thicken and lengthen out towards the nanorod morphology. The dominant rod-structures are $\sim 1\text{-}1.5 \mu\text{m}$ in length, with 350-550 nm hexagonal end faces. It is clear that citric acid is preferentially forcing material to deposit onto the (010) surface causing elongation into the b-axis. It does this effectively throughout the majority of the sample, with uniformity in size and shape of the formed nanorods. However, due to the presence of shorter rods or elongated block-type particles there is the possibility that the citric acid

Chapter 5: Lithium Iron Phosphate

concentration was slightly too low to effect all the sample equally, or that some particles are undergoing transformation, perhaps through dissolution, reducing in size in certain dimensions through etching to be incorporated into other particles as the reaction progresses. The citric acid may preferentially bind to the high energy surfaces, effectively stabilizing the crystals and capping these faces from growth, ensuring material is deposited or grown onto the lower energy (010) face (Figure 5.7 (top)). After sixty minutes, the sample by XRD is pure, crystalline LiFePO_4 . The exact particle morphology is difficult to assess by SEM, due to the small particle size and excessive truncation, however, all material appears to exist as discrete, singular particles with no fusing or twinning and little aggregation or clumping. All material expresses highly faceted polygonal structures in various forms from cubic to cuboid to perhaps octahedron in severe cases, with evidence of smoothing of corners and edges, as if the particles have become truncated in the harsh conditions and been forced to adopt more conformationally stable structures. These truncated drum or barrel like particles have been observed in very long residence time low temperature reactions, either with citric acid additive (Lu, Chen et al. 2011) or ethylene glycol as solvent (Zhu, Fiore et al. 2013). The size range is within 200-500 nm with good uniformity around the average of 300 nm. These structures may have arisen through the gradual etching and truncation of the hexagonal-prism rod structures observed after ten minutes, forming uniform nanoparticles that may possess beneficial electrochemical performance due to their small size and high surface area for Li-ion transfer. These growth and morphological transformations are summarised in Figure 5.11. It is clear that

Chapter 5: Lithium Iron Phosphate

the combination of supercritical temperatures and citric acid has ensured the particle size has been driven down to the nanoscale.

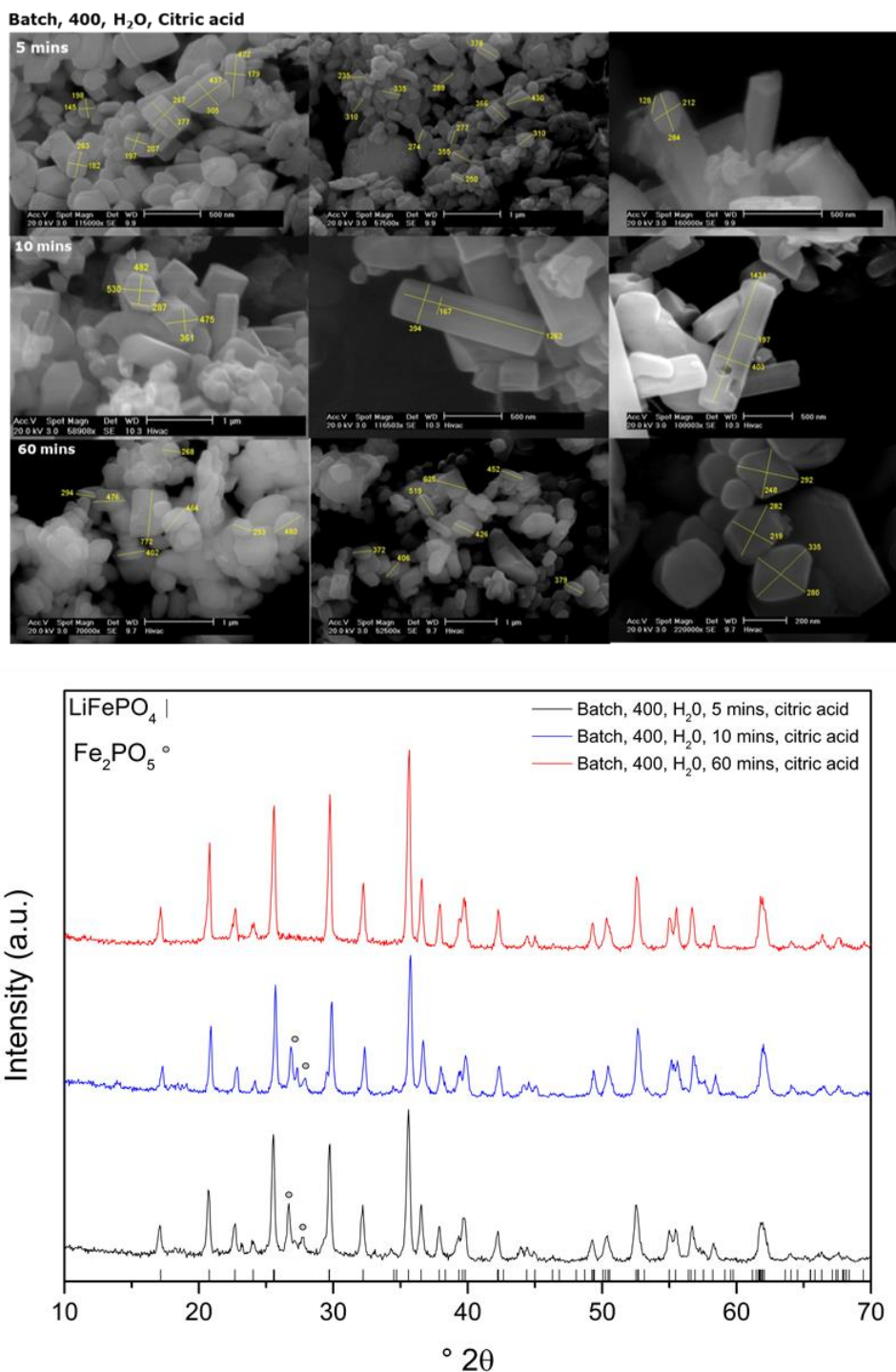


Figure 5.10: SEM images and XRD patterns of the products from batch hydrothermal reactions at 400 °C with citric acid additive.

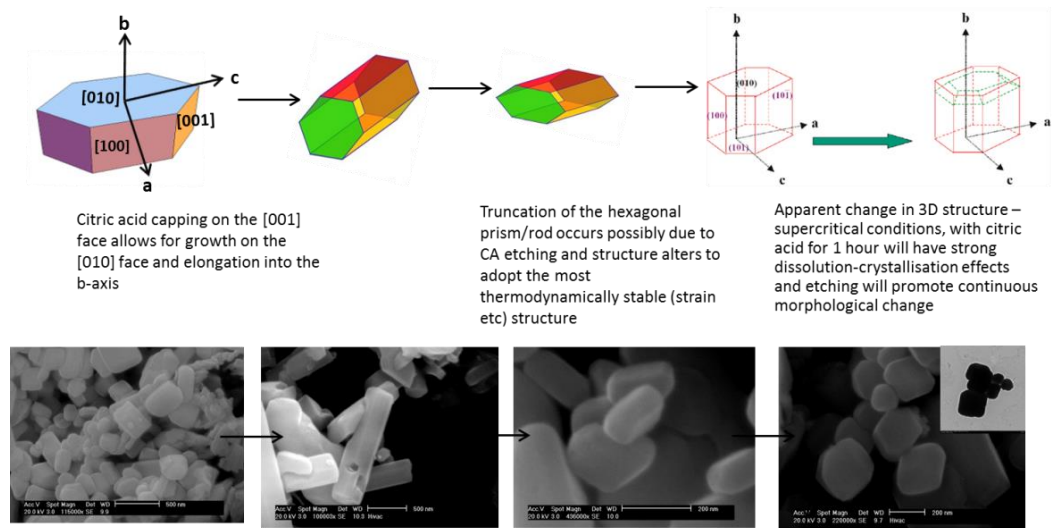


Figure 5.11: Summary of the possible growth and morphological evolution processes of LFP formation in supercritical water using citric acid as an additive. (Top right simulated schematics are of LFP particles obtained after hydrothermal reactions for 52 and 120 hours respectively, demonstrating truncated edges and faces due to etching (Lu, Chen et al. 2011)).

5.3.2. Batch Solvothermal Synthesis

Ethylene glycol has been used previously to synthesise lithium iron phosphate materials since its higher viscosity to water slows the ion diffusion rate and hence can reduce particle size (Nan, Lu et al. 2011) and direct growth processes through capping and oriented attachment. There is also the possibility of carbonaceous material being produced from its breakdown at elevated temperatures and reaction times, to form a degree of carbon coating on formed nanoparticles. All reactions undertaken in water were repeated in ethylene glycol to assess the differences between the two solvents.

5.3.2.1. 180 °C

The conditions and products of the low temperature batch solvothermal syntheses of LFP are summarised in Table 5.3.

Table 5.3: Summary of batch solvothermal reactions at 180 °C for LFP production

T/°C	V Solvent (mL)	Additive	Reaction Time	Products
180	2.5	None	1 h	LiFePO ₄ , Fe ₃ O ₄
180	2.5	None	6 h	LiFePO ₄ , Fe ₃ O ₄ , Fe ₂ PO ₅
180	2.5	None	9 h	LiFePO ₄
180	2.5	Ascorbic acid	1 h	LiFePO ₄
180	2.5	Ascorbic acid	6 h	LiFePO ₄ , Fe ₂ O ₃
180	2.5	Ascorbic acid	9 h	LiFePO ₄
180	2.5	Citric acid	1 h	LiFePO ₄ , Fe ₂ PO ₅
180	2.5	Citric acid	6 h	LiFePO ₄
180	2.5	Citric acid	9 h	LiFePO ₄ , Fe ₂ PO ₅ , Fe ₂ P ₂ O ₇

At 180 °C with no additive (Figure 5.12) for one hour, the product appears to be a mixture of flat elongated plates and more stunted three-dimensional structures, all 100-300 nm in size. The hexagonal plate type structures are elongated into the c-axis, with an extremely thin (immeasurably so by SEM) b-axis with large exposure of the (010) surface, which is preferential for Li-ion

Chapter 5: Lithium Iron Phosphate

transfer kinetics (Hsu, Tsay et al. 2004, Laffont, Delacourt et al. 2006, Fisher, Hart Prieto et al. 2008, Gibot, Casas-Cabanas et al. 2008, Kang and Ceder 2009, Saravanan, Reddy et al. 2009). Interesting to note is that these elongated particles have hexagonal exposed surfaces, whereas the elongated parallelepiped structures from the hydrothermal reactions have rhombus exposed surfaces, indicating differing growth mechanisms or preferential behaviour between the solvents. There is also present a large quantity of undefined material on the surfaces and aggregated around the defined particles. By XRD, the product is poorly defined LiFePO_4 , with an enhanced background and the presence of Fe_3O_4 . After six hours, the product again consists of multiple particle types, however, the defined particles are now extremely thin elongated diamonds/plates with lengths 200-800 nm with more defined edges and faces than after one hour. Their possible growth mechanism is illustrated in Figure 5.13. By XRD, the LiFePO_4 is more defined, however, Fe_3O_4 and now Fe_2PO_5 are also present. After nine hours, the product is pure LiFePO_4 by XRD, indicating that the formation of LFP is a slower reaction in ethylene glycol than water. The two dominant particle types are large flat plates ~500 nm in size and large quantities of small aggregated particles that appear sub-100 nm.

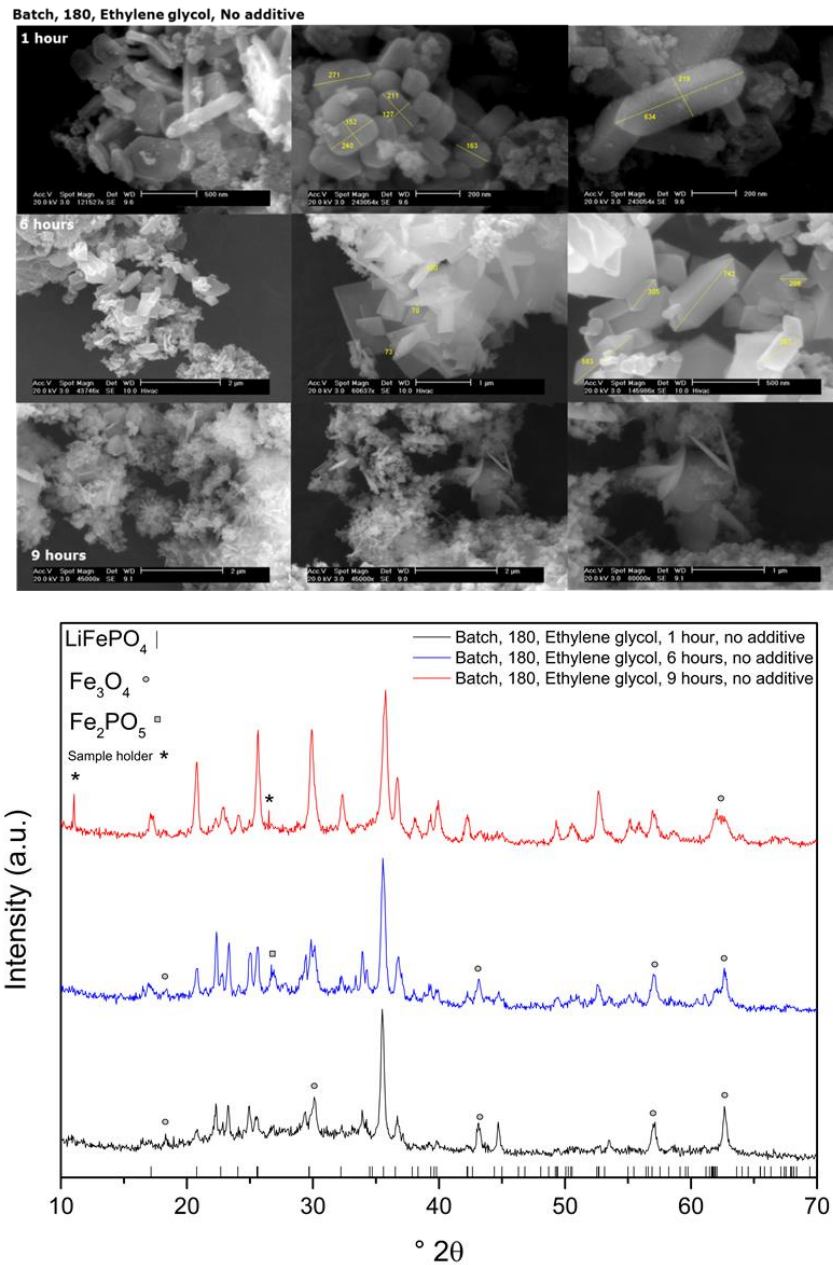


Figure 5.12: SEM images and XRD patterns of the products from batch solvothermal reactions at 180 °C with no additive.

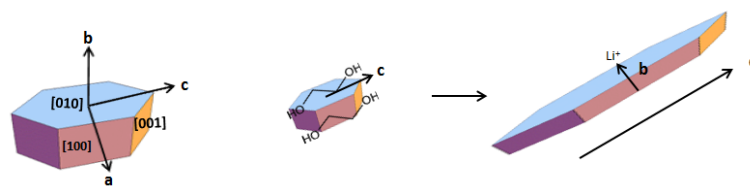


Figure 5.13: Ethylene glycol appears to promote growth and therefore elongation of particles into the c-axis, producing particles with short b-axis lengths which may be beneficial for lithium ion transfer kinetics.

Chapter 5: Lithium Iron Phosphate

The addition of ascorbic acid (Figure 5.14) allows for the formation of 'pure' LiFePO_4 within one hour, at least to the limits of XRD analysis – the XRD pattern displays fairly well-defined LiFePO_4 with broader peaks than would usually be expected, and with an enhanced background between $20\text{-}35^\circ 2\theta$, possibly indicating some amorphous character to the sample or small quantities of intermediate iron phosphate material. The particles consist of sub-micron flakes/plates with rounded edges, with lengths and widths making them almost spherical yet remaining thin, in addition to large quantities of small particles appearing heavily aggregated but individual particles $\sim 100\text{-}250$ nm in size. After six hours, the particles remain largely unchanged, with the only difference being there is relatively less flake/disk type particles and more smaller aggregated $100\text{-}250$ nm particles, perhaps indicating that individual particles crystallise with time and separate from the LFP disks, or these are the Fe_2O_3 that is present in the XRD pattern, which may arise from oxidation of amorphous material. The product obtained after nine hours by XRD is pure LiFePO_4 with the persistence of the enhanced background between $20\text{-}35^\circ 2\theta$. However, the particles are more homogeneous and disperse than the shorter reaction time products. All particles exist as $1\text{-}2$ μm flakes, with varying lengths and widths but all particles remaining thin. This result matches well with literature observations (Nan, Lu et al. 2011), where ethylene glycol was postulated to slow the ion diffusion rate due to the increased viscosity of ethylene glycol over water, and in addition to stunting growth, this also promotes the formation of the most stable face, (010). It appears that the longer reaction time combined with the additive has allowed controlled formation of more uniform and pure LFP particles.

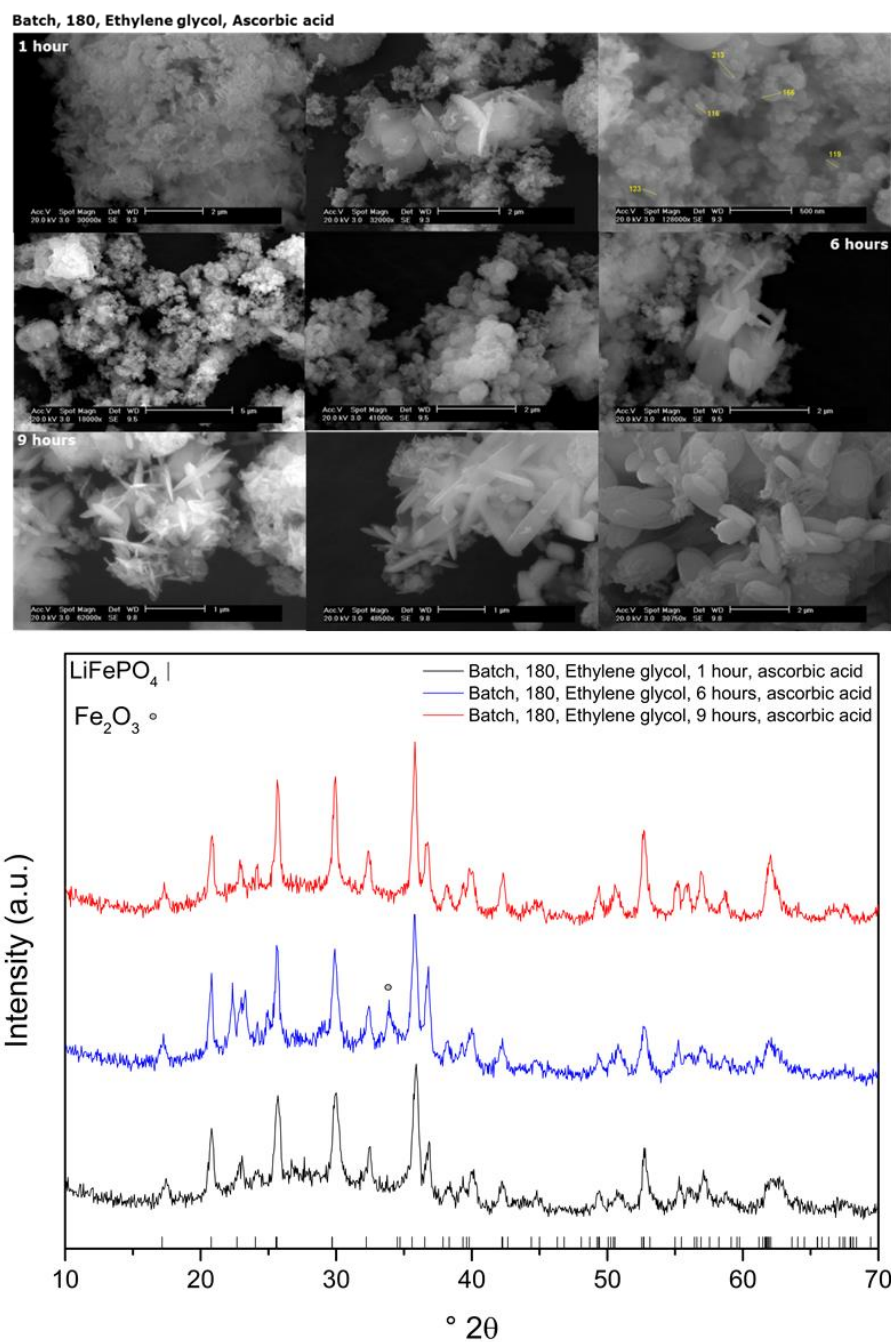


Figure 5.14: SEM images and XRD patterns of the products from batch solvothermal reactions at 180 °C with ascorbic acid additive.

Chapter 5: Lithium Iron Phosphate

The addition of citric acid to the reaction has a marked difference (Figure 5.15). After one hour, vast networks of highly elongated and thin rods are dominant, densely packed together to form webs of rods. The rods themselves appear well defined and separate with clear edges and faces, and are many microns in length and roughly 100-200 nm in width. They appear to be elongated into the b-axis (100) direction, in contrast to the no additive and ascorbic acid examples, which keep this thickness axis suppressed and elongates into the lengthening c-axis, exposing the (010) surface (Pei, Yao et al. 2012). By XRD, the product is poorly crystalline, in contrast to the sharp edges and faces and smooth surfaces of the rods visible in the SEM images. A small number of peaks match to the reference LiFePO_4 pattern, however, there is a greatly enhanced background particularly between $20\text{-}35^\circ 2\theta$, and the presence of a Fe_2PO_5 peak. After six hours, the material appears as large agglomerates, however, structures within the large agglomerates appear to retain a rod structure. The XRD pattern is dominated by the increased background between $20\text{-}35^\circ 2\theta$, with weak LiFePO_4 peaks evident. After nine hours, the XRD pattern starts to portray more LiFePO_4 character, with major peaks being assigned to LFP together with some impurity peaks from Fe_2PO_5 and $\text{Fe}_2\text{P}_2\text{O}_7$. The particles are now thicker rods, almost block-like, up to $5\ \mu\text{m}$ in length and $0.6\ \mu\text{m}$ in width and thickness. As was noted in the hydrothermal examples, whilst ascorbic acid tends to hasten the formation of LFP product, citric acid appears to also slow the reaction in ethylene glycol. It may be a cooperative effect of both additive and solvent that slows the growth rate and conversion to product.

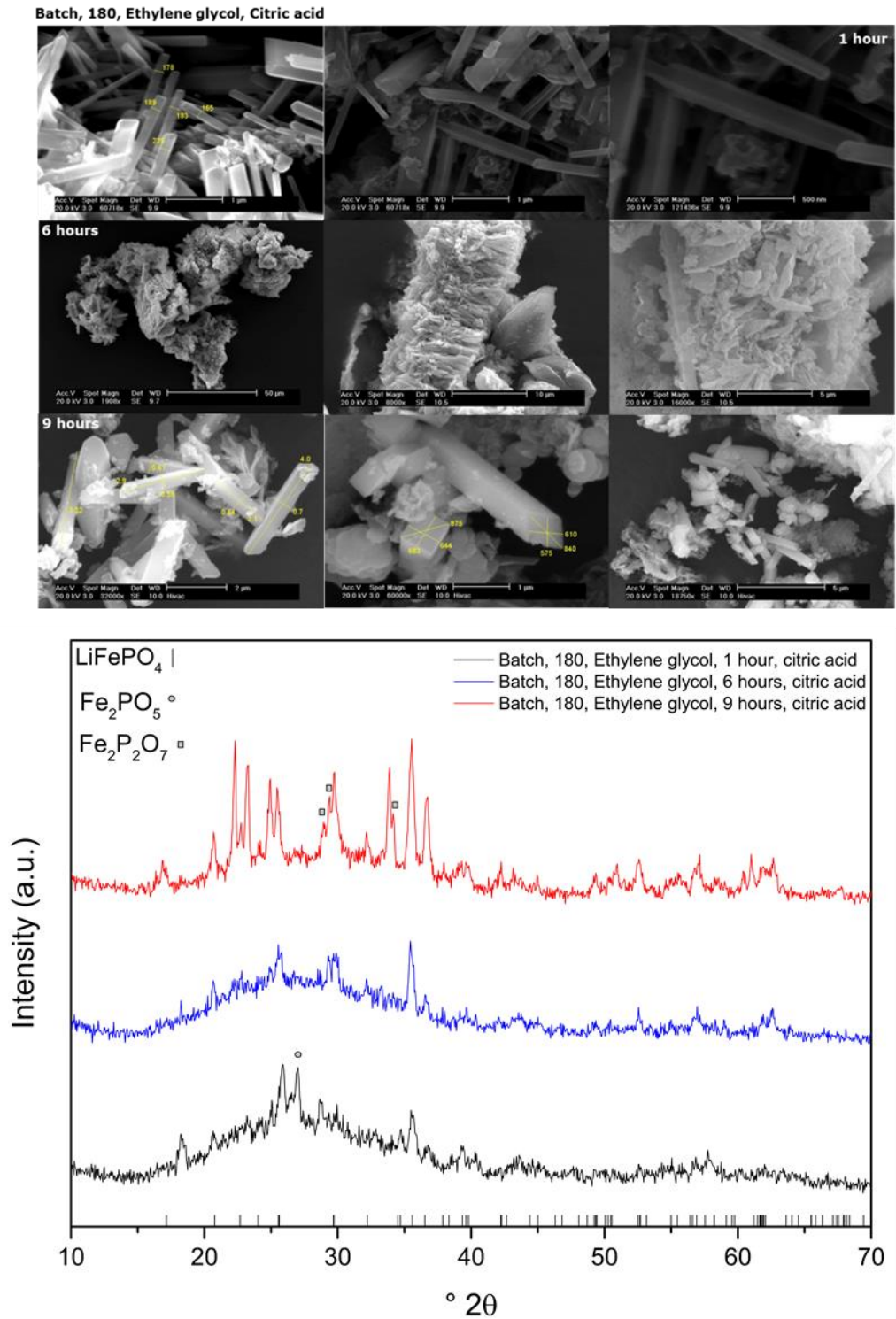


Figure 5.15: SEM images and XRD patterns of the products from batch solvothermal reactions at 180 °C with citric acid additive.

Chapter 5: Lithium Iron Phosphate

5.3.2.2. 400 °C

The conditions and products of the higher temperature batch solvothermal syntheses of LFP are summarised in Table 5.4.

Table 5.4: Summary of batch solvothermal reactions at 400 °C for LFP production.

T/°C	V Solvent (mL)	Additive	Reaction Time	Products
400	2.5	None	5 min	LiFePO ₄ , Fe ₃ O ₄
400	2.5	None	10 min	LiFePO ₄ , Fe ₂ P ₂ O ₇ , LiFeP ₂ O ₇
400	2.5	None	60 min	LiFePO ₄ , Fe ₃ O ₄
400	2.5	Ascorbic acid	5 min	LiFePO ₄
400	2.5	Ascorbic acid	10 min	LiFePO ₄ , Fe ₃ O ₄
400	2.5	Ascorbic acid	60 min	LiFePO ₄ , Fe ₃ O ₄
400	2.5	Citric acid	5 min	LiFePO ₄
400	2.5	Citric acid	10 min	LiFePO ₄ , Fe ₃ O ₄ , FePO ₄
400	2.5	Citric acid	60 min	LiFePO ₄ , Fe ₃ O ₄

At 400 °C with no additive for a reaction time of five minutes, by XRD the product is relatively crystalline LiFePO₄, with some Fe₃O₄ contamination (Figure 5.16). The morphology of the particles is difficult to assess, due to the small size and heavy aggregation, however, it is clear that the particles are below 100 nm in size. After six hours, two sizes of c-axis elongated particles are produced exposing the (010) surface. Particles with 400 nm – 1 µm lengths and 160 nm widths coexist with particles heavily elongated into the c-axis direction with lengths over 1 µm. There also exists a large proportion of other undefined material in the sample. This may explain the mixed nature of the XRD pattern, which consists of LiFePO₄, Fe₂P₂O₇ and LiFeP₂O₇. These particles are similar to those achieved with no additive at 180 °C; however, the particles appear to have been severely restricted growing in width and thickness, leading to heavily elongated flat particles. After sixty minutes, the product is relatively well-crystalline LiFePO₄ with two characteristic Fe₃O₄

Chapter 5: Lithium Iron Phosphate

peaks by XRD, and is more crystalline than any products from the 180 °C solvothermal reactions, indicating the elevated temperature induces better formation of crystalline LFP.

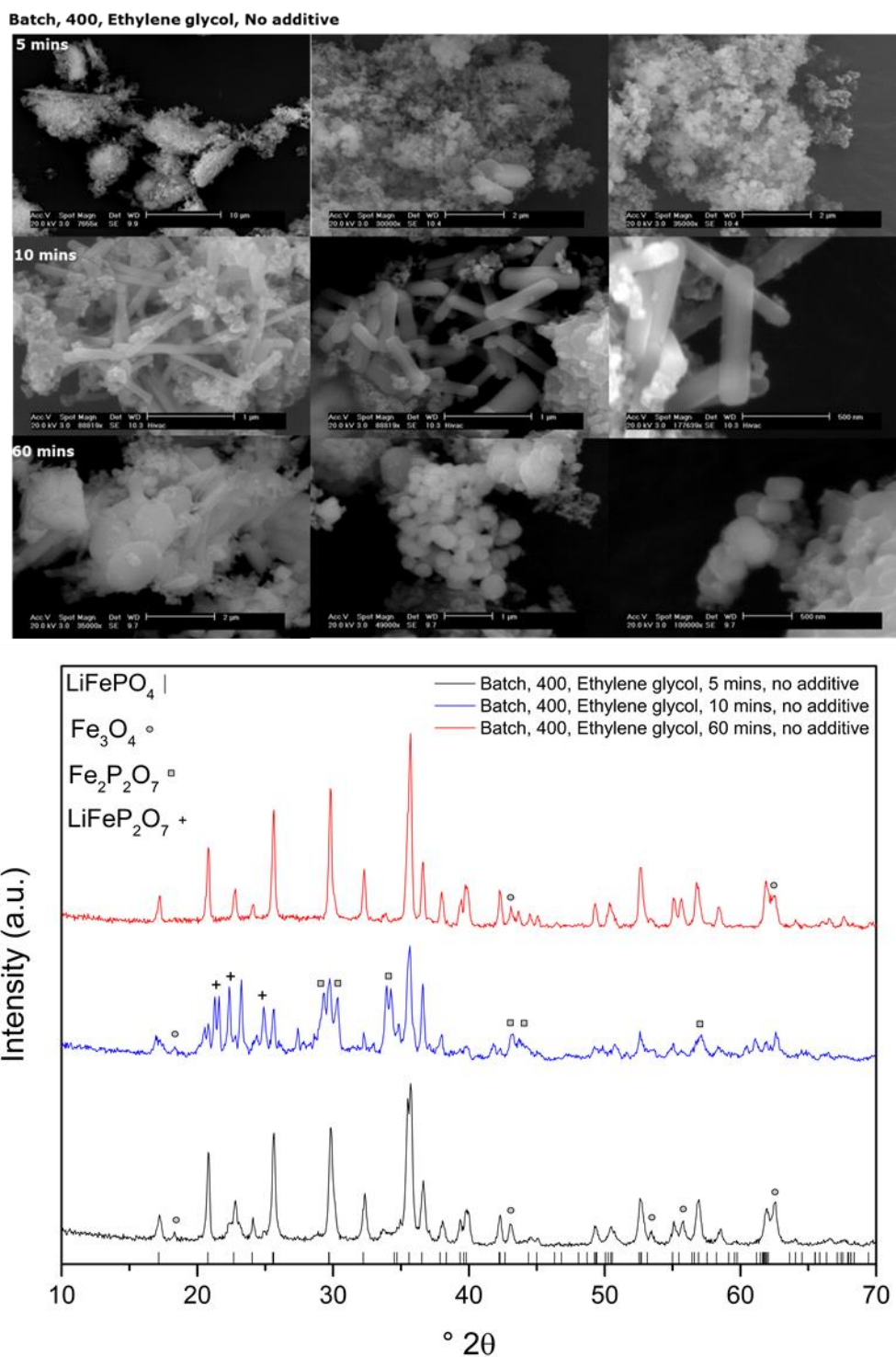


Figure 5.16: SEM images and XRD patterns of the products from batch solvothermal reactions at 400 °C with no additive.

Chapter 5: Lithium Iron Phosphate

Using ascorbic acid as an additive makes no difference to the morphology (Figure 5.17) compared to the same reaction conditions of five minutes without an additive, however, by XRD the product is more crystalline LiFePO_4 and Fe_3O_4 has almost been completely prevented from forming. With ten minutes reaction time, the particles are different to the elongated structures observed with no additive. The particles are uniform in size and shape (undefined 3D shape), with all particles sub 500 nm and most within the 100 – 300 nm range. Relative to the other solvothermal reactions the product is well-crystalline LiFePO_4 , with the persistence of a small quantity of Fe_3O_4 . These particles appear to provide a platform with which to produce uniform, well crystalline LiFePO_4 , since after sixty minutes, well-defined and homogeneous cube/tablet shaped 200 nm particles are produced – suggesting that the high temperatures and thick ethylene glycol solvent are effectively preventing growth of particles. Magnetite persists in the product. Ascorbic acid appears to therefore reduce the preference for growing LFP particles to remain thin and elongate to expose the (010) surface.

When citric acid is employed in the reaction (Figure 5.18), LiFePO_4 is produced after five minutes, but it is clear in the XRD pattern that there is an enhanced background between 20-35 °2 θ , suggesting some amorphous character to the product or residual iron phosphate intermediate is present. Particles are either fattened-out rods with smoothed edges between 500 nm – 1 μm , or spherical nanoparticles ~250 nm in size. The two differing morphologies may indicate the citric acid concentration was too low to act upon all growing particles. After ten minutes, the XRD pattern displays LiFePO_4 , Fe_3O_4 and FePO_4 and three differing morphologies by SEM images.

Chapter 5: Lithium Iron Phosphate

The first are fairly undefined spherical/globular particles sub-200 nm in size, the second are more structured particles that appear cube-like but may in fact be more heavily faceted towards octahedra and are ~100 nm in size. It is most likely these are the LFP particles. The final morphology is large (1 μm) but very thin disks less than 100 nm thick, which is typical of FePO_4 before lithiation. After sixty minutes, it again appears the solvent and additive has provided an effective platform for small uniform LFP particles to be produced. The particles are highly uniform in size and shape, mostly 250 nm but within a 200-400 nm size range. There exists some amorphous character to the XRD pattern and Fe_3O_4 persists, however these are unobservable in the SEM pictures or may arise from the small quantity of other material present. There is visible etching of the particles with the presence of holes throughout the sample on the surfaces of particles, and this has been observed by other researchers when using citric acid for long reaction times (Lu, Chen et al. 2011).

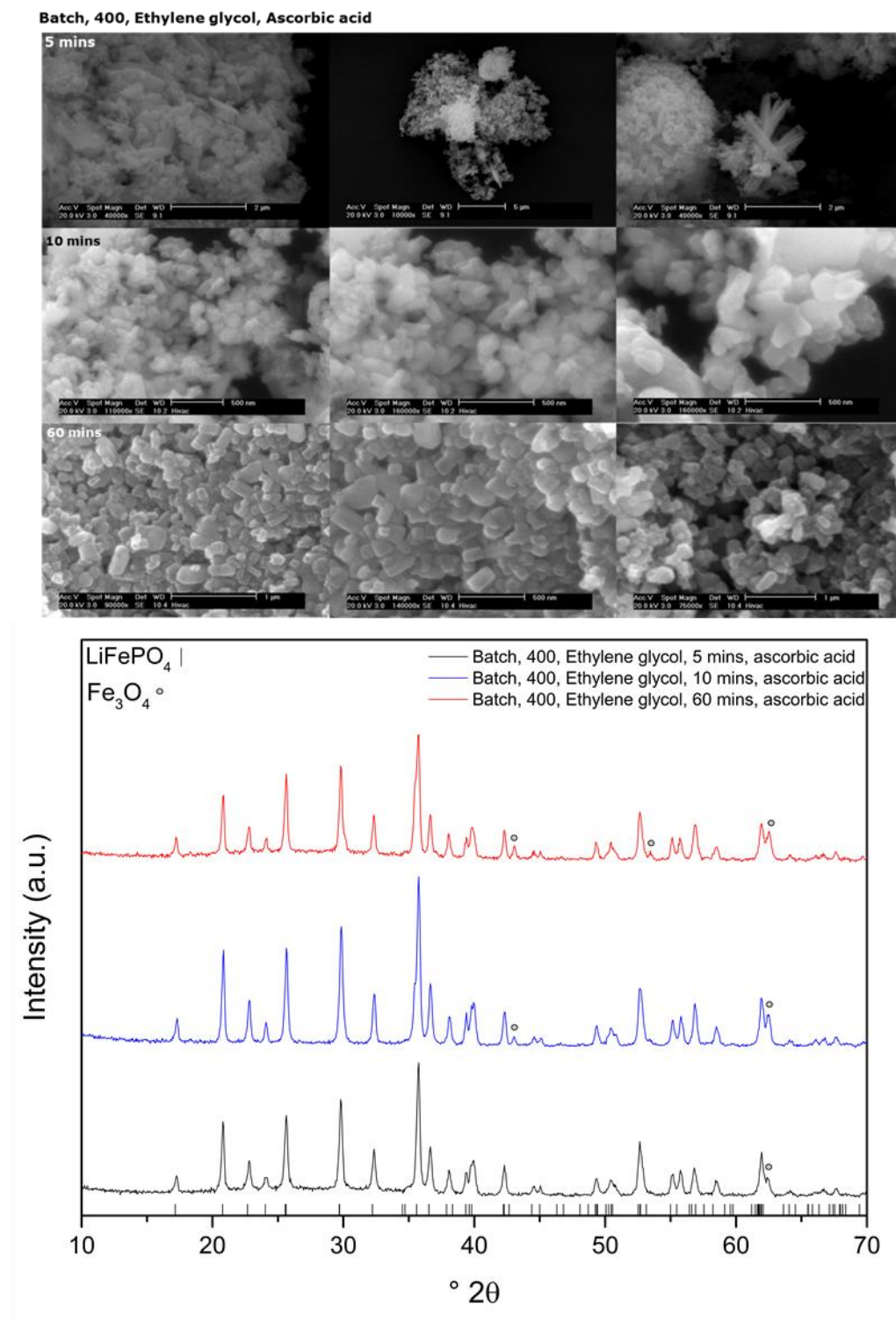


Figure 5.17: SEM images and XRD patterns of the products from batch solvothermal reactions at 400 °C with ascorbic acid additive.

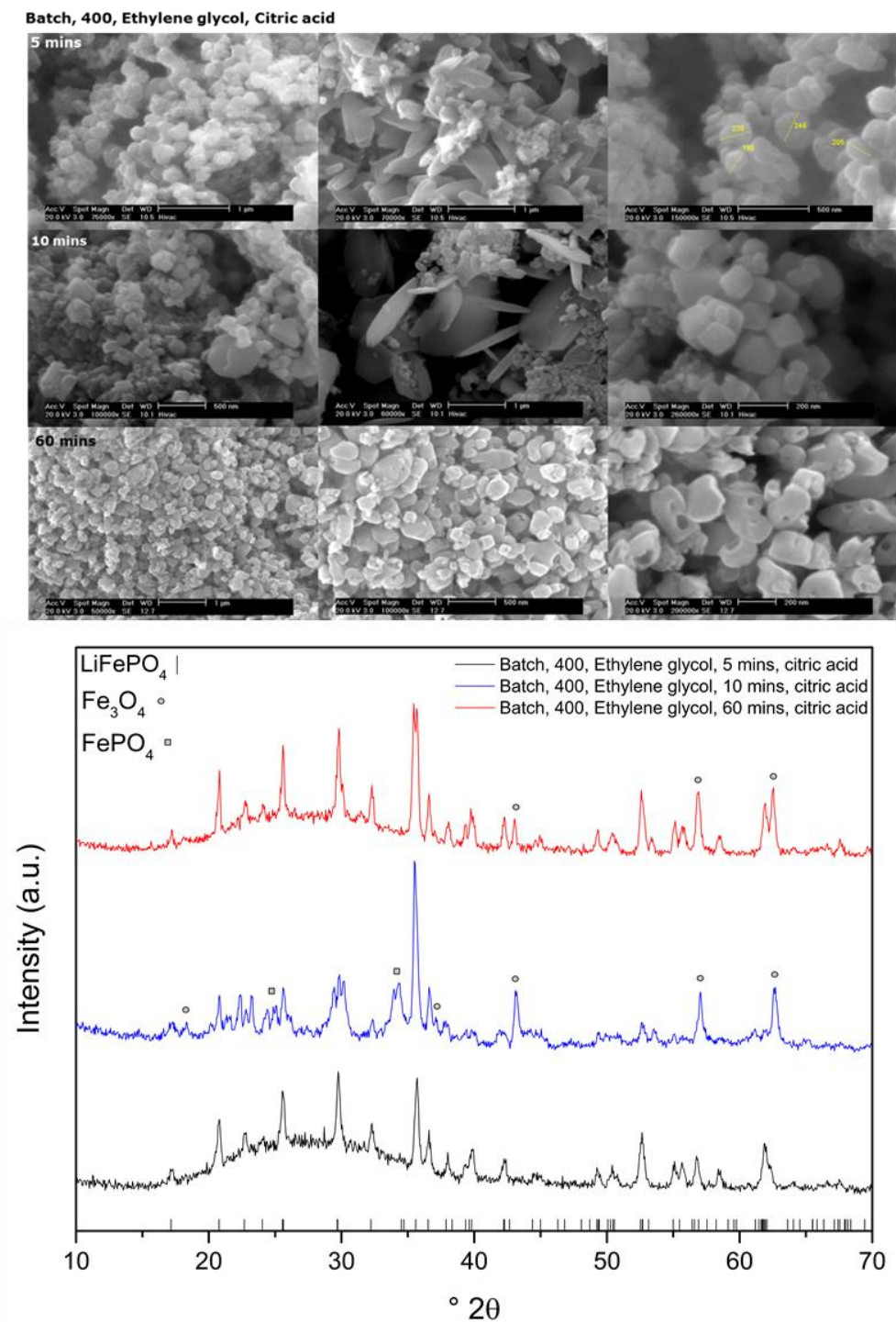


Figure 5.18: SEM images and XRD patterns of the products from batch solvothermal reactions at 400 °C with citric acid additive.

5.3.3. Summary of Batch Reactions

From the batch hydrothermal reactions, it is clear that temperature, reaction time and the presence of additives has a distinct influence on the purity, size and morphology of resulting LiFePO_4 particles. At subcritical temperatures, it appears that an additive such as ascorbic acid can induce a more rapid formation of crystalline product by hastening the formation of intermediate iron phosphate species and facilitating the subsequent lithium intercalation step, in addition to suppressing ferrous oxidation. Citric acid leads to a slower and more controlled growth regime, which may allow for interesting growth and complexing processes to occur. Without an additive, formation of iron phosphate species with varying initial morphologies hinders the formation of uniform LFP particles and prevents fine control of the reaction. The additives may offer the potential in future work to effectively design particles with desirable characteristics, such as surface texturing through etching, morphology through directing or complexing, or the degree to which edges and faces are formed, and tuning the reaction time cooperatively with the additive can control the size and single crystalline nature of the particles.

Supercritical hydrothermal reactions offer the unique conditions in which to induce supersaturation and therefore drive the particle size down, whilst hastening the reaction and improving the conversion. It appears that high temperature induces a higher degree of uniformity upon resulting particles, with homogeneity in size and shape. Whilst the no additive case appears to produce the hexagonal platelets explained by Islam et. al. (Fisher and Islam 2008), the ascorbic acid and citric acid additives clearly offer scope to

Chapter 5: Lithium Iron Phosphate

influence this, by directing growth through capping/complexing to ensure growth onto a specific surface or into a certain axis. Combining the additive effect with long reaction times at elevated temperatures allows for a large influence on the size and morphology of LiFePO_4 nanoparticles, inducing etching and truncation effects, again, highlighting the potential scope for tailored design of these materials in terms of size, morphology, surface texturing, surface area and exposed surface to create materials with desirable characteristics for their electrochemical properties as cathode materials for Li-ion batteries. The effect of ascorbic acid and citric acid on LFP formation has been clearly demonstrated in the batch reactions, where ascorbic acid appears to hasten the reaction and citric acid leads to a slower reaction, and this may be interesting to utilise in the continuous flow reactions, since the ability to hasten lengthy reaction steps in a burst nucleation type reactor may prove invaluable to successfully synthesise complicated materials in short reaction times. Conversely, the ability to perform a slower, more controlled reaction may lead to more effective tailoring of the composition, size and morphology.

The lower temperature solvothermal reactions have demonstrated that whilst not optimised, as evidenced by the non-homogeneous morphology throughout the samples and issues with sample purity, there is scope for size and morphology control using ethylene glycol and additives as directing agents. Without an additive or with ascorbic acid it was demonstrated that the particles can be designed to be extremely thin exposing large proportions of the (010) surface.

Increasing the temperature allowed for effective size control, driving particles to the 200-500 nm range and with excellent homogeneity in size and

Chapter 5: Lithium Iron Phosphate

morphology – it appears that a combination of additive and solvent may require a greater time of reaction than under hydrothermal conditions in order to achieve pure, homogeneous size and morphology particles of LFP. With sufficient reaction time and temperature it was demonstrated that uniform nanoparticles of LFP could be produced using ascorbic acid and citric acid, pointing to the need for longer reaction times and additive control in the continuous process. Finally, the holes evident on a large portion of the long reaction time citric acid particles, which have been observed also by Lu et. al (Lu, Chen et al. 2011) may offer opportunities for further crystal control or design; however, this area has not yet been explored in terms of understanding how it may benefit electrochemical performance.

5.3.4. Continuous-Flow Hydrothermal Synthesis of LFP

Continuous-flow hydrothermal syntheses of LFP were carried out using the reactor set-up shown in Figure 5.2, with and without the optional 2nd heating period. The conditions are summarised in Table 5.5 and Table 5.6. The continuous flow reactions effectively emulate the batch reactions, with obvious differences such as reaction time arising from the nature of the flow system. However, the conditions chosen offer a comparison between the two methods, or rather, an opportunity to use the batch reactions to understand how the effectively identical reactions under continuous flow conditions are operating.

5.3.4.1. 180 °C

Table 5.5: Summary of CFHS reactions at 180 °C for LFP production

Additive	T/ °C	Extra Heating	Reaction Time	Products
None	180	N	< 5 s	Unidentifiable/amorphous
Ascorbic acid	180	N	< 5 s	Amorphous-Fe ₃ (PO ₄) ₂ .8H ₂ O
Citric acid	180	N	< 5 s	No reaction
None	180	Y	15-20 s	Fe ₃ (PO ₄) ₂ .8H ₂ O
Ascorbic acid	180	Y	15-20 s	Fe ₃ (PO ₄) ₂ .8H ₂ O
Citric acid	180	Y	15-20 s	No reaction

Reactions at 180°C yielded undesirable products; in the absence of additives, short residence time (pre-heated water and reactor only) gave a poorly defined unidentifiable product by XRD and with additional heating by incorporation of an additional heating coil to the reaction configuration (longer residence time), vivianite (Fe₃(PO₄)₂.8H₂O) formed. Vivianite has been identified as an intermediate by other researchers (Aimable, Aymes et al. 2009, Hong, Kim et al. 2013). Employing ascorbic acid as an additive allowed more rapid and facile vivianite formation. When citric acid was employed as additive, in both

Chapter 5: Lithium Iron Phosphate

short and longer residence time cases, a slightly yellow, clear, transparent solution was produced, containing no solid product. At the low reaction temperature, the pH of the solution due to the citric acid may have been too acidic to allow for vivianite formation, or the citric acid may have slowed the reaction kinetics (similar to batch results using citric acid). It appears at 180 °C that even with the aid of additives, the reaction would require significantly greater residence time for lithium incorporation at these low temperatures. Even with the additional heating, the residence time increases from ‘instantaneous’ to only 15-20 s. Constructing a reactor configuration to allow for the necessary residence time at low temperature would be unfeasible and not industrially viable and hence, increasing the reaction temperature to 400°C is a preferred solution.

5.3.4.2. 400 °C

Table 5.6: Summary of CFHS reactions at 400 °C for LFP production

Additive	T/ °C	Extra Heating	Reaction Time	Products
None	400	N	< 5 s	LiFePO ₄ , FePO ₄
Ascorbic acid	400	N	< 5 s	LiFePO ₄
Citric acid	400	N	< 5 s	LiFePO ₄
None	400	Y	15-20 s	LiFePO ₄
Ascorbic acid	400	Y	15-20 s	LiFePO ₄
Citric acid	400	Y	15-20 s	LiFePO ₄

TEM images and XRD patterns of products obtained from the continuous-flow hydrothermal synthesis of lithium iron phosphate with a residence time of ~5 seconds are shown in Figure 5.19. At 400 °C and short residence time, a lack of additive caused product collection difficulties. Passage through the reactor tubing and back pressure regulator seal of mixed LFP/FePO₄ micron sized material proved difficult and pressure problems ensued. Without an additive, it

Chapter 5: Lithium Iron Phosphate

appears the lithiation of the produced FePO_4 was too sluggish to be completed successfully throughout the sample. Crystalline LiFePO_4 is formed, however some FePO_4 persists.

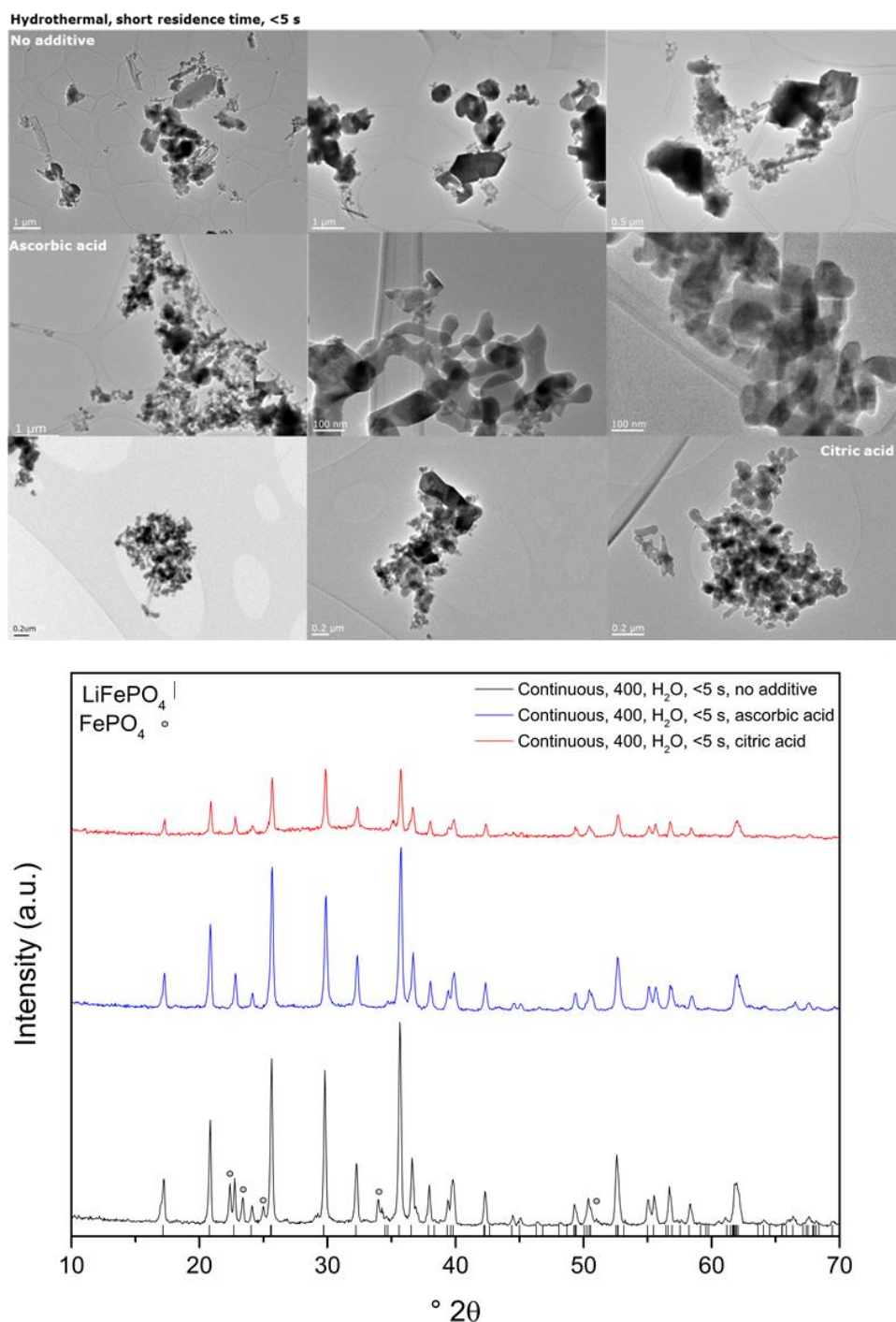


Figure 5.19: TEM images and XRD patterns of lithium iron phosphate synthesised under continuous-flow hydrothermal conditions with and without additives at 400 °C and a residence time of ~5 seconds.

Chapter 5: Lithium Iron Phosphate

The addition of ascorbic acid to the iron precursor solution allows for pure, crystalline LiFePO_4 formation, even at the short residence time (< 5 s). Other examples in the literature with similar reaction conditions and set-up often contain iron phosphate impurities and so it appears the ascorbic acid improves the efficiency of conversion of iron phosphate to phase-pure LFP, as was concluded from the batch hydrothermal and solvothermal reactions also. Iron oxide is another common impurity observed – in this work, at the short residence times, the ascorbic acid is acting as an anti-oxidant preventing the oxidation of precursor Fe^{2+} to Fe^{3+} , either in the precursor vessel or during the reaction which would readily produce Fe_2O_3 or Fe_3O_4 . In other work with longer reaction times (minutes rather than 15 s in the longer reaction time example here), iron oxide is also present. This could be caused through persistence of iron oxide formed at the reaction point in short residence time reactions, or oxidation of iron containing reactants/intermediates or products during the reaction. The addition of ascorbic acid in this work prevents iron oxide formation allowing for more facile and rapid iron phosphate formation and subsequent conversion to LFP. The extremely small reaction times and excellent mixing provided by the counter-current reactor may also favour preferential LFP formation over iron oxide impurities (since Fe_xO_y are not seen in the absence of an additive). Interesting to note is that the product from the ascorbic acid reaction begins to coagulate and settle shortly after exiting the back pressure regulator, and does so completely, leaving a clear supernatant which can be easily decanted off for particle concentration and washing/collection – this reaction is therefore industrially favourable, since complicated or laborious separation techniques are not required. The LiFePO_4

Chapter 5: Lithium Iron Phosphate

particles formed are generally between 100-500 nm in size, and present as interconnected globules with fairly undefined edges and faces.

Using citric acid as an additive leads to products with either low crystallinity as evidenced by XRD, or rather a product with some amorphous character, or products with other unidentifiable peaks (most probably an intermediate iron phosphate). It may be that the product achieved here, a mix between LFP and iron phosphate, or low crystallinity LFP, is an intermediate on the reaction pathway to crystalline LFP. This result agrees with the batch reactions when using citric acid as an additive, which appeared to slow the reaction kinetics down in contrast to ascorbic acid. The particles appear to be smaller than those formed under ascorbic acid influence, with the majority less than 200 nm in size and loosely spherical in shape, with fluffy edges.

Therefore, with only a single heating period/mixing point (the standard reactor configuration) which the pilot scale system is currently operating under, undertaking the reaction using ascorbic acid is the best option. This is the only reaction out of the three scenarios (no additive, ascorbic/citric acid) that produces pure LFP product, and it does so with homogeneity in size and shape of the particles and with beneficial product characteristics for scale-up such as efficient settling post-synthesis.

Adding an extra heating period to the reactor by the attachment of a 6m heating coil placed immediately after the reaction point outlet increases the residence time from less than 5 s to ~15 s, which is a significant increase at 400 °C. The product (Figure 5.20) yielded from this reaction with no additive is pure LiFePO_4 , with particles presenting as a mixture of globular or roughly

Chapter 5: Lithium Iron Phosphate

spherical sub-500 nm particles and smaller, less defined fluffy material, similar to that seen in the citric acid single heater example, which may be an intermediate amorphous precursor phase that is present in insufficient quantities to be detected by XRD. Again with no additive, the reaction is hampered by poor collection efficiencies and pressure fluctuations due to poor passage of product through the reactor set-up. It is clear however that the additional residence time has allowed lithium to be incorporated into the residual iron phosphate, completing the conversion. Allowing the product generated in the presence of ascorbic acid to flow with this increased residence time has a pronounced effect on the particle characteristics. Crystallinity remains high, and the particle size (sub-500 nm) and shape become more uniform and homogeneous throughout the sample, with particles becoming more defined with sharper edges and corners. Particles remain interconnected; however distinct edges between adjacent particles become clearer. Allowing the particles to undergo this additional period of heating may increase the crystallinity of the particles, and increase the ordering of Fe/Li and reduce defects within the crystals, which should be beneficial for the electrochemical characteristics. Again, the particles settle completely over time, leaving clear supernatants. In the case of citric acid the increase in residence time has enabled the complete conversion of iron phosphate or amorphous lithium iron phosphate to crystalline LFP. The particles are again ~500 nm in size, with undefined morphologies and a globular character, with some interconnected regions. It appears therefore that ascorbic acid indeed promotes the rapid and facile formation of crystalline LFP by aiding the formation of, and lithium incorporation into intermediate products, whereas citric acid appears to slow

Chapter 5: Lithium Iron Phosphate

this process down – the exact reason for this is unknown (most probably a chelating effect inducing more gradual formation by ordering and networking of ions before crystallisation) – however, what is clear is that either the use of the organic additives or an additional period of heating is beneficial in providing complete conversion of precursors and producing pure, well-crystalline, sub 500 nm lithium iron phosphate, with beneficial post-synthesis characteristics ideally suited for large-scale production.

The pilot scale facility and SHYMAN full-scale facility will be operating under single reaction point conditions with no additional heating zone, and as such, using ascorbic acid under supercritical conditions with the standard reactor configuration remains the best solution for a hydrothermal reaction. That said, developmental work at smaller scales (until this can be achieved at the large scale) should focus on increasing the residence time of the reaction further, since an increase from 5 s to 15 s has demonstrated enhanced product by improved crystallinity which may be improved further by a longer residence time reaction. There may exist a compromise therefore between what is feasible at industrial scales in terms of reactor configurations and heating periods, and improvements to the product.

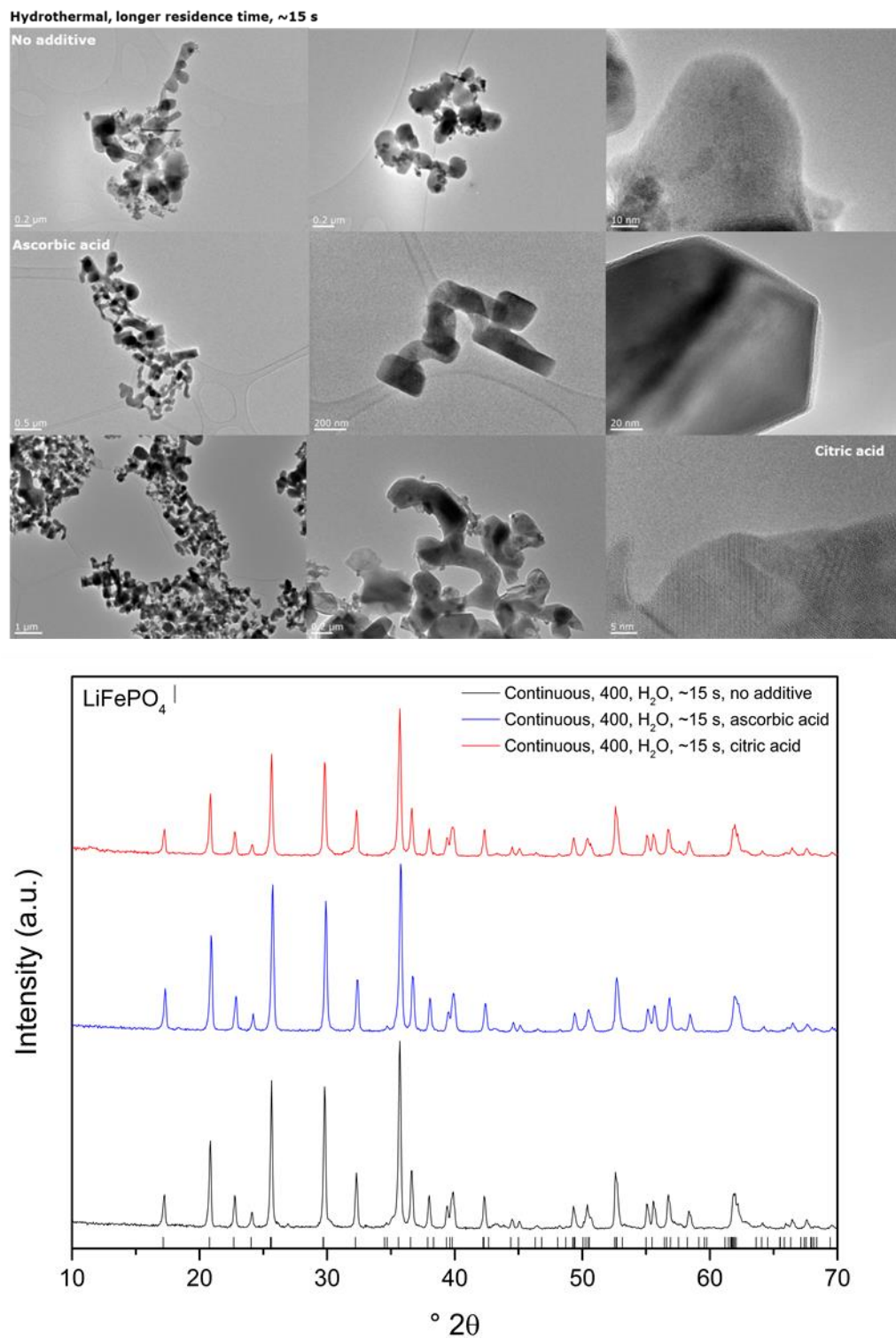


Figure 5.20: TEM images and XRD patterns of lithium iron phosphate synthesised under continuous-flow hydrothermal conditions with and without additives at 400 °C and a residence time of ~15 seconds.

5.3.5. Continuous Flow Solvothermal Synthesis of LFP

Continuous-flow solvothermal syntheses of LFP in ethylene glycol were carried out using the reactor set-up shown in Figure 5.2 with and without the optional 2nd heating period and the conditions are summarised in Table 5.7 and Table 5.8.

5.3.5.1. 180 °C

Table 5.7: Summary of CFSS reactions at 180 °C for LFP production in ethylene glycol

Additive	T/ °C	Extra Heating	Reaction Time	Products
None	180	N	< 5 s	Unidentified/amorphous
Ascorbic acid	180	N	< 5 s	Unidentified/amorphous
Citric acid	180	N	< 5 s	Unidentified/amorphous
None	180	Y	15-20 s	Unidentified/amorphous
Ascorbic acid	180	Y	15-20 s	Unidentified/amorphous
Citric acid	180	Y	15-20 s	Unidentified/amorphous

Reactions in ethylene glycol at 180°C produced amorphous products as light green solutions, unidentifiable by XRD, regardless of the additive conditions or residence time. At these temperatures, the reaction time to produce crystalline LiFePO₄ in ethylene glycol is presumably far greater than can be achieved with the reactor set-up. In addition, ethylene glycol, which is slightly more viscous than water, slows ion diffusion and therefore inhibits reaction rates and growth of particles. This is not a viable route for development of LFP production, and hence, reactions were carried out at 400 °C.

Chapter 5: Lithium Iron Phosphate

5.3.5.2. 400 °C

Table 5.8: Summary of CFSS reactions at 400 °C for LFP production in ethylene glycol

Additive	T/ °C	Extra Heating	Reaction Time	Products
None	400	N	< 5 s	Unidentified/amorphous
Ascorbic acid	400	N	< 5 s	Unidentified/amorphous
Citric acid	400	N	< 5 s	Unidentified/amorphous
None	400	Y	15-20 s	50 nm LiFePO ₄
Ascorbic acid	400	Y	15-20 s	50 nm LiFePO ₄
Citric acid	400	Y	15-20 s	30 nm LiFePO ₄

As can be observed from the XRD patterns in Figure 5.21 the solvothermal products at 400 °C with short residence time are amorphous. In the no additive and ascorbic acid reactions, both product solutions are grey-green in colour and fairly transparent. The product is not easily separated from ethylene glycol, and so, the dilution with equal parts water to reduce the viscosity of solution was required. Upon addition of water, grey-green product visibly begins to coagulate and the products centrifuge to black products. The product solution from the citric acid reaction is light yellow in colour, and is unable to be separated from the ethylene glycol. TEM shows extremely small particle size, and this coupled with citric acid allowing the particles to be stable in solution, prevents them settling upon the addition of water. The grey-green products obtained display excellent uniformity in size and shape, displayed by the TEM images in Figure 5.21. The no additive particles appear to be approximately 10 nm in size and are loosely spherical, and cluster together to form fluffy clusters around 50 nm in size. Particles from the ascorbic acid reaction appear even smaller, perhaps between 5-10 nm, and cluster together more readily and in greater number. Particles formed in the citric acid reaction are extremely small, with particle size below 5 nm. Small particle size, in addition to the uniformity

Chapter 5: Lithium Iron Phosphate

of size and shape throughout the samples for all reactions, make the particles excellent candidates to be intermediates on the pathway towards small-size crystalline LiFePO_4 . They are likely an iron phosphate or lithium iron phosphate amorphous phase, which will go on to crystallise to crystalline LFP.

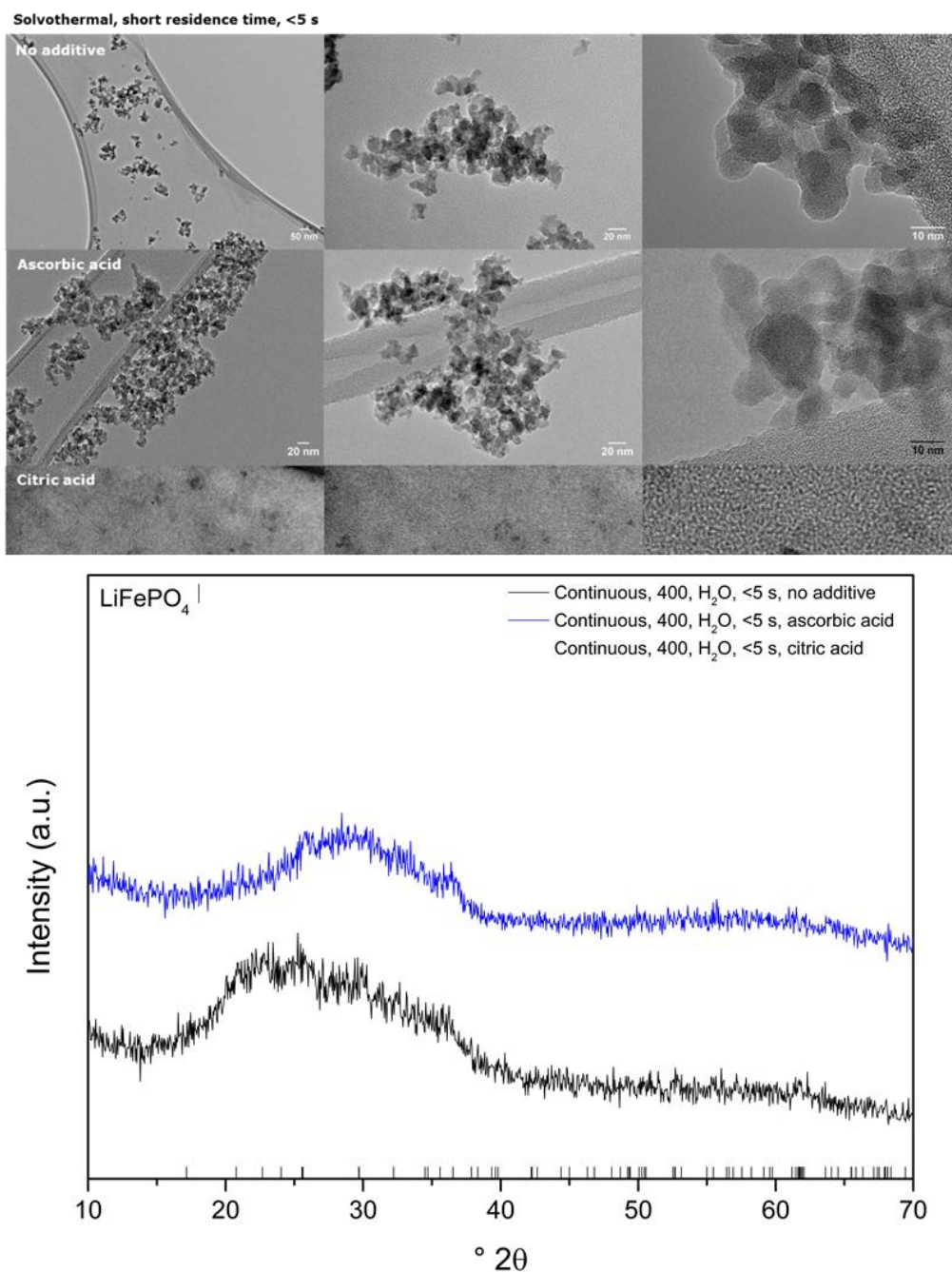


Figure 5.21: TEM images and XRD patterns of lithium iron phosphate synthesised under continuous-flow solvothermal conditions with and without additives at 400 °C and a residence time of ~5 seconds.

Chapter 5: Lithium Iron Phosphate

Upon increasing the residence time of these reactions, the small particle size is maintained, and crystalline LFP is produced in all cases (Figure 5.22). With no additive, roughly 50 nm tablet shaped particles are produced, with lengths roughly twice the width of particles. Uniformity in size and shape is also maintained. The product slurry was grey-green, which after mixing with water, centrifuges to a black product with a light green supernatant. The dry product was a fine black powder. The particles obtained with ascorbic acid are similar in shape, displaying tablet morphology with lengths again greater than width, however, there is less uniformity in size. A large portion of the particles are of similar size range (50 nm), however, larger particles 200-500 nm in length also exist, which may have arisen through rapid growth of particles through the additional heating period, or from non-homogeneous passage of particles through the reactor tubing, with some material becoming sluggish and undergoing an extended heating period compared to the bulk of sample. The product slurry was a red-brown solution, which centrifuges to a black product with red supernatant indicating iron oxide is also formed during the reaction. There is a marked difference with the citric acid sample. As can be observed in the TEM images in Figure 5.22, the particles are exclusively spherical in shape and 30 nm in size. Particles are identical throughout the sample. The broadness of the peaks in the XRD pattern reflects this small particle size. This is the first example of such small particle size for LFP achieved by a continuous flow method. Typically by CFHS, particle sizes are ~100-500 nm. The product slurry was grey-green, which after mixing with water, centrifuges to a black product with a light green supernatant. The dry product was a fine black powder. The black colour is indicative of carbon residue – this would appear to

Chapter 5: Lithium Iron Phosphate

be the citric acid and ethylene glycol breaking down due to the elevated temperature and extended reaction time.

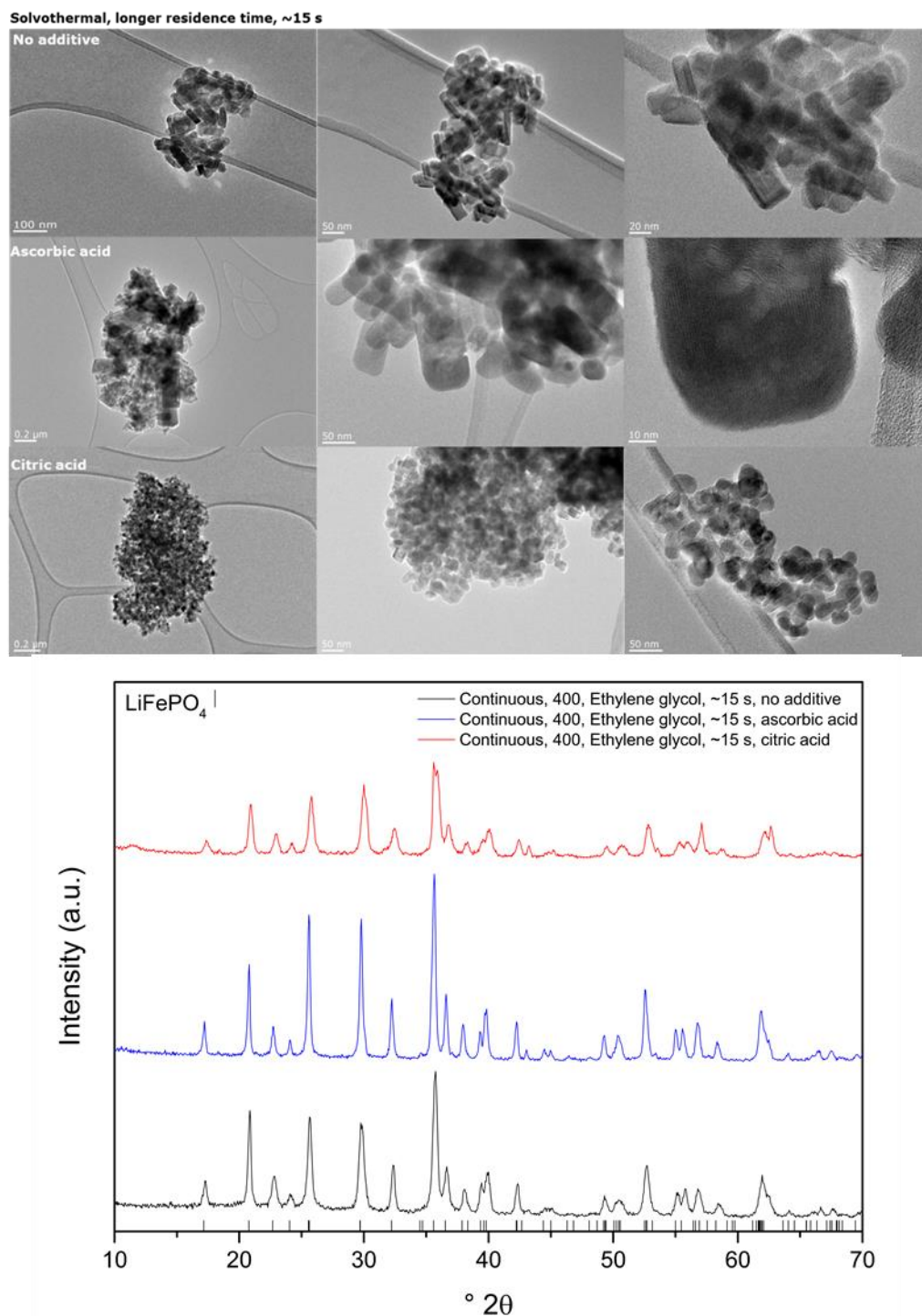


Figure 5.22: TEM images and XRD patterns of lithium iron phosphate synthesised under continuous-flow solvothermal conditions with and without additives at 400 °C and a residence time of ~15 seconds.

5.3.6. Pilot-Scale Hydrothermal Production of LFP

To assess the scale-up potential of this work towards industrial production, a set of conditions were selected to undertake identical reactions at laboratory and pilot scale. The pilot scale set-up has the same counter-current reactor arrangement, with no additional heating period, and since ascorbic acid gives a pure, well crystalline product under short residence time conditions, with efficient settling of material and no residual impurities post-synthesis, this was selected as the ‘best-case’ material. As previously, the short residence time laboratory scale reaction (ca. 0.5 g/hour) with ascorbic acid produced roughly spherical/globular particles ~200 nm in size, with some larger particles up to 500 nm. HR-TEM images displaying lattice fringes demonstrate the high crystallinity and ordering within particles. From the XRD patterns in Figure 5.23, it is observed that pure, well crystalline LiFePO_4 is also produced from the reaction at pilot scale. By TEM, the particles appear similar, perhaps slightly larger at ~300 nm, with more defined edges apparent on particles. Even at the pilot scale (25 x greater scale and twice the concentration), 125 L of grey product slurry settled within reasonable time-scales (overnight), to leave a thick concentrated grey product slurry, and clear supernatant, confirming no residual iron phosphate or any iron oxide was present in the product slurry exiting the back pressure regulator. 125 L of product slurry resulted in ~ 85 g of material, which equated to a production scale of ca. 20 g/hour. The concentration of precursors can be increased at the pilot scale further to increase product turnover in future work. This result confirms that even with very slight differences in particle characteristics the reaction can be successfully scaled for industrial production.

Chapter 5: Lithium Iron Phosphate

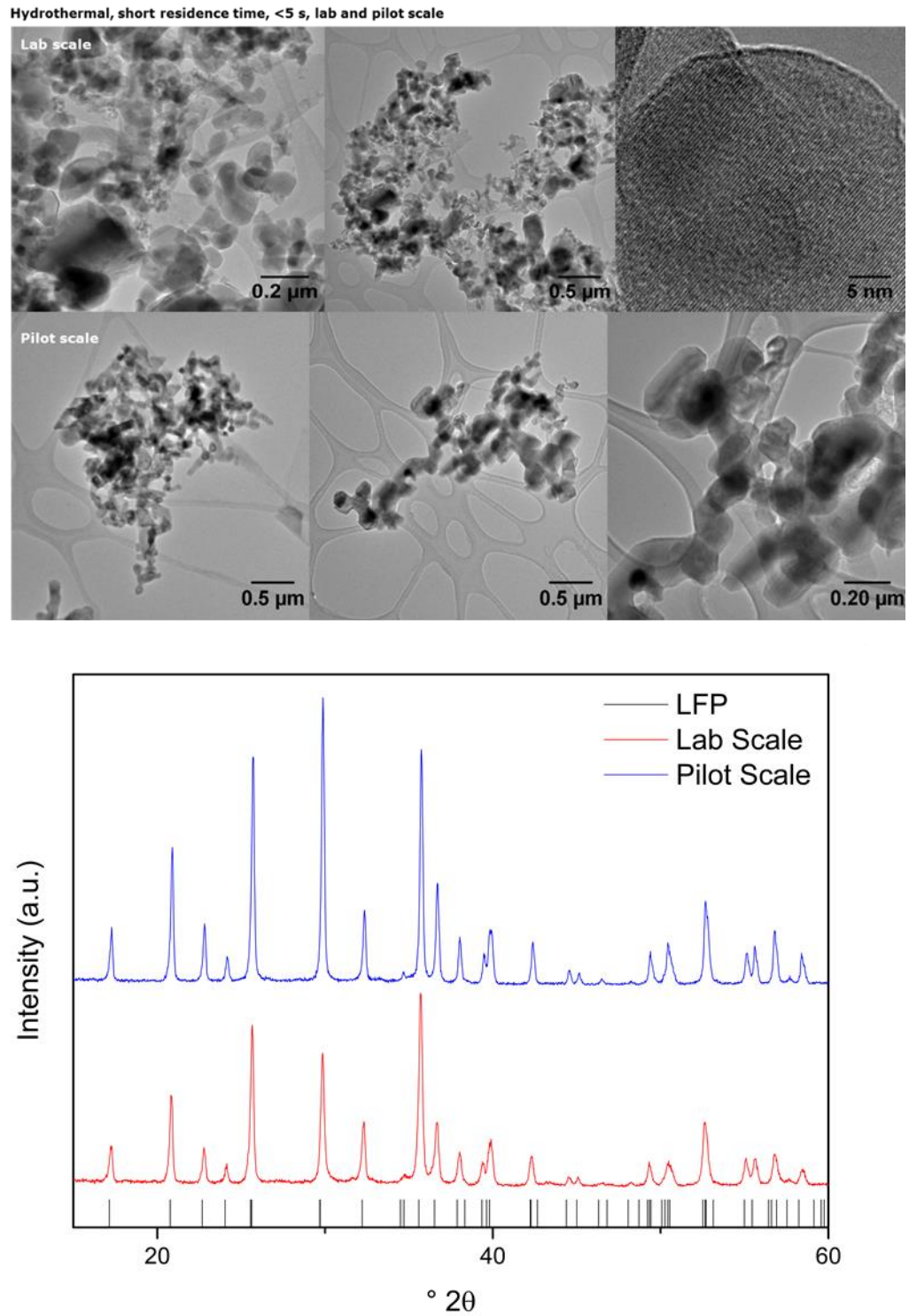


Figure 5.23: Comparison of bench- and pilot-scale lithium iron phosphate produced with ascorbic acid as an additive at 400 °C and a residence time of ~5 s.

5.3.7. Electrochemical Testing of CFHS & CFSS LFP

To begin to evaluate the LFP materials ability to undergo intercalation reactions and act as a Li-ion rechargeable battery cathode, electrochemical testing of the material was undertaken. This involved building an electrochemical cell and subjecting it to galvanostatic charge-discharge cycling. The direction of Li-ion transfer and current flow during cycling, in addition to demonstrating the relative locations of each working component in a battery or coin cell is shown in a schematic of a Li-ion battery in Figure 5.24 (top). Also demonstrated by the illustration in Figure 5.24 (bottom left) are the components and order of assembly of a coin cell, with the uppermost working electrode replaced with Li-foil for the testing undertaken in this chapter to create a half-cell. Figure 5.24 (bottom right) shows the actual constructed coin cells used for the testing in this chapter.

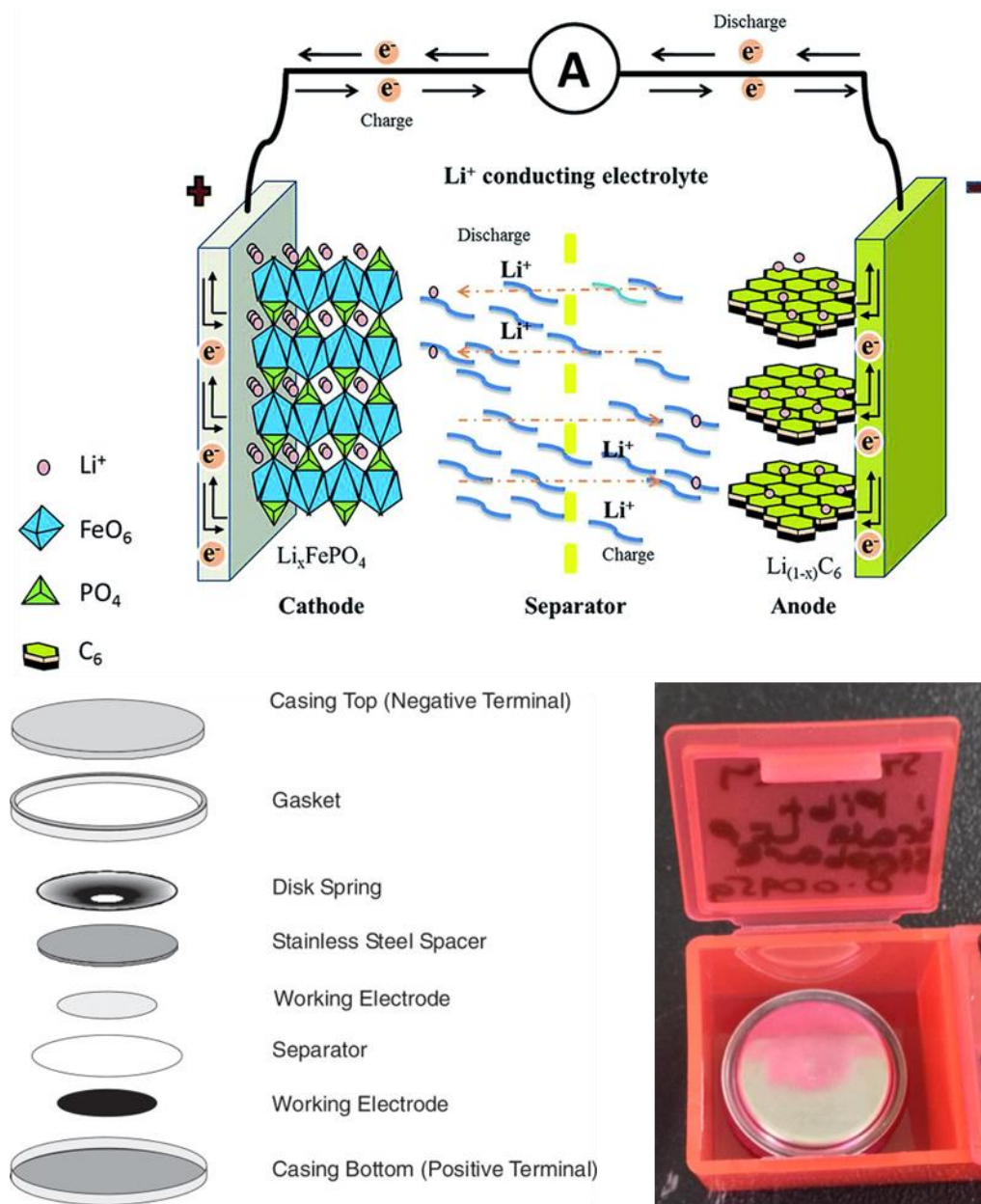


Figure 5.24: A schematic of a Li-ion battery indicating relative locations of each component and the direction of current flow and Li-ion transfer upon charging and discharging (top, (Lee, Yanilmaz et al. 2014)), an illustration of coin cell components and their order of assembly, with the uppermost working electrode replaced by Li-foil for laboratory tests and in the tests presented in this chapter to create a half-cell, with electrolyte also added (bottom left, (Burns, Krause et al. 2011)) and prepared coin cells used for the electrochemical testing in this chapter (bottom right).

5.3.7.1. Electrochemical Testing

Table 5.9: The selected LFP products (and synthesis conditions) that were subject to electrochemical testing. AA = ascorbic acid, CA = citric acid, EG = ethylene glycol.

Sample	Temp (°C)	Extra Heating	Time (s)	Additive	Solvent	Products
Lab 1	400	N	< 5	AA	Water	LiFePO ₄
Pilot	400	N	< 5	AA	Water	LiFePO ₄
Lab 3	400	Y	15 – 20	AA	Water	LiFePO ₄
Lab 4	400	Y	15 – 20	CA	Water	LiFePO ₄
Lab 5	400	Y	15 – 20	CA	EG	LiFePO ₄

Figure 5.25 shows the charge and discharge curves and cycling performance of a selection of the products obtained from the continuous flow hydrothermal and solvothermal reactions. In the first tests, the coin cells were charged at 0.1 C to 4.5 V initially, before being discharged at a 0.1C rate, which corresponds to a 10 hour charge and 10 hour discharge of the cell, to 2.5 V. Li-ion cells generally complete discharge by ~ 3 V. Charging the cells at 0.1 C initially causes slow Li-ion flow from the LFP material to the Li-foil anode. Reducing the cell voltage by discharge then reverses this flow, slowly forcing Li-ions back into the LFP structure. This cycle is repeated over and over again, in this case up to 100 cycles, to assess firstly the capacity of the LFP materials, but also the change in capacity over time, or the cyclability, to assess the effect constant shuttling of lithium ions into and out of the LFP particles has on the structural integrity of the particles, and whether this affects their performance as a cathode material.

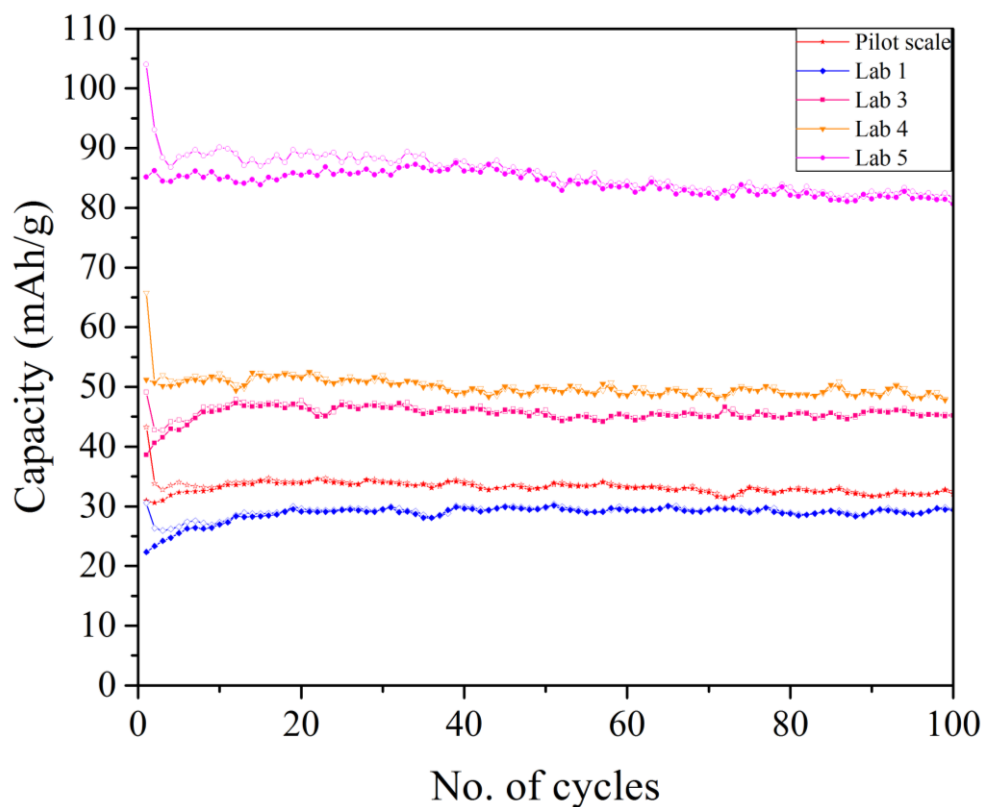


Figure 5.25: The battery cycling performance of the pilot scale and laboratory scale lithium iron phosphate samples at 0.1C (open symbol; charge, closed symbol; discharge).

Bare (non-carbon coated) LiFePO_4 products Lab 1 (hydrothermal, short residence time, ascorbic acid), Pilot scale (hydrothermal, short residence time, ascorbic acid), Lab 3 (hydrothermal, longer residence time, ascorbic acid), Lab 4 (hydrothermal, longer residence time, citric acid) and Lab 5 (solvothormal, longer residence time, citric acid) display discharge capacities of 29, 33, 46, 50 and 85 mAh/g at 0.1 C respectively. Theoretically, a low charge rate of 0.1 C induces the minimal amount of stress on the LFP particles, since the movement of Li-ions is slow and gradual. This also dictates the materials should perform best at this low charge rate, since it is preferential for allowing all active material to be utilised. The relatively low capacities displayed by the hydrothermal products therefore (29, 33, 46, 50 mAh/g) must be attributed to

Chapter 5: Lithium Iron Phosphate

the shorter residence time of reaction (< 5 s & 15 s) compared to other continuous supercritical hydrothermal synthesis literature examples (50-100 mAh/g at LFP residence times of 40 s) (Hong, Kim et al. 2011, Hong, Kim et al. 2013), which dictates certain particle characteristics, discussed in the following text, that are unfavourable for electrochemical performance. The Lab 1 and Pilot scale samples are produced under almost instantaneous conditions, whereby particles are precipitated at the mixing point upon contact with supercritical water, and are immediately displaced from the reaction point and pass into the cooling system. This leads to extremely short residence times for complicated or multi-stage reactions such as in the formation of lithium iron phosphate, and a short time period for further processes such as ordering and crystallisation to occur. In Hong et al.'s work into mixing geometries of the reactor piece (Hong, Kim et al. 2013), the reactor geometry and therefore mixing of the supercritical water and metal salt for the formation of LFP affected the purity of the product, with a swirling type mixer leading to smaller particles and fewer impurities. Fewer impurities were then seen to be influential in increasing the materials capacity in the electrochemical testing. After calcination of the Lab 1 product in this work, iron phosphate is observed together with lithium iron phosphate in the XRD pattern, indicating an amorphous phase exists in the reaction product before calcination, which is not detected in the XRD pattern of the reaction product. This inevitably leads to lower capacity, since this reduces the mass quantity of active LFP material in the final battery. This is not observed in the pilot scale sample, indicating that the pilot scale reactor configuration promotes better conversion to lithium iron phosphate product either through enhanced mixing dynamics and heat transfer

or slightly increased residence time through potentially less efficient cooling due to larger geometry pipework, as was observed in the barium strontium titanate chapter. Upon increasing the residence time of the reaction to approximately 15-20 s at the lab scale, with all other conditions remaining constant, i.e. between Lab 1 and Lab 3, there is a 59% increase in capacity to 46 mAh/g. Similarly with citric acid additive under these longer residence time conditions, the capacity is increased by 73%. The mixing dynamics of the counter-current reactor may be unfavourable towards the production of high quality LiFePO_4 at short residence times, as compared to the swirling mixer for example, however, longer residence times post-synthesis may be able to account for this in the future and increase the capacity of the materials. The capacity increases observed for longer residence time samples are coupled with apparent increases in crystallinity of the longer residence time products, as is observed by sections of the XRD patterns in Figure 5.26 showing better splitting of a characteristic peak at $62^\circ 2\theta$ (Hong, Kim et al. 2011) and TEM images displaying sharper edges and more defined particles at longer residence times. Undertaking the longer residence time reaction with citric acid in ethylene glycol (Lab 5) rather than water increases the capacity of the resulting particles by 70%. This can be attributed to the severely reduced particle size of the particles synthesized in ethylene glycol, due to the higher viscosity coordinating solvent properties of ethylene glycol, and to the ‘in-situ’ nanoparticle-carbon interaction that occurs, as ethylene glycol and citric acid produce partially carbon coated sample upon calcination (estimated ~ 5% by wt. by thermogravimetric analysis). The small particle size allows for better utilisation of the active cathode material and more facile and rapid Li^+ ion

kinetics, and the carbon improves the electronic conductivity between adjacent particles and throughout the cathode.

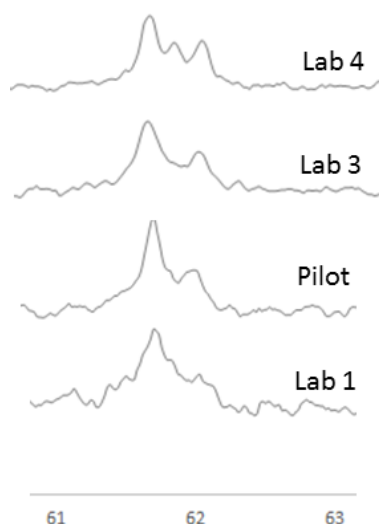


Figure 5.26: Highlighted region at 62° in the XRD patterns of the hydrothermally prepared LiFePO₄ powders studied by electrochemical characterisation, displaying increased splitting with increased reaction/residence time indicating better ordering and enhanced crystallinity.

This work represents the first report of the synthesis of lithium iron phosphate by continuous flow hydrothermal synthesis with the counter-current reactor arrangement, and the first report of the continuous flow solvothermal synthesis, and hence, we must not be discouraged by the capacity of the achieved materials, which if compared to the other reports of LFP synthesised in supercritical water, appear relatively low. This result demonstrates that by utilising the rapid mixing conditions present in the counter-current reactor, together with an organic additive or an extended period of heating, pure samples of LFP can be produced which demonstrate some potential for reversible intercalation for battery applications – it is now a case of adjusting the reaction protocol to discover new ways of providing additional heating to

Chapter 5: Lithium Iron Phosphate

increase residence time and therefore increase the crystallinity of the materials – it is postulated this will improve the capacity of the materials to the literature benchmark. If the residence time can be increased by 100-200% from the 15-20 s to the 40-60 s region, and a similar increase of 60-75% in capacity is achieved due to this, as in the short to longer residence time examples presented here, then we could expect to increase the capacity of the hydrothermal products into the 75-90 mAh/g region – these materials could then be considered for optimisation by carbon coating to improve the capacity further, above 100 mAh/g for commercial applications.

Despite the relatively low capacity at this stage, the cyclability of the materials appears strong, since there is minimal fade (mostly 100% retention, ~5 % loss in Lab 5) of the capacity even over prolonged cycling (> 100 cycles). The capacities of the Pilot scale, Lab 1 and Lab 3 samples increases gradually for the first 10-15 cycles, as the activation of the cell is occurring – interestingly these are the three products synthesized in the presence of ascorbic acid - this is not observed in the Lab 4 or 5 samples, which are synthesised in the presence of citric acid, and these have improved capacity compared to the slower activation products – this may indicate better stability and immediate utilisation of the active material using citric acid.

To assess the applicability of the materials for potential high power applications, the materials were cycled with progressive increases in current from 0.1 C to 30 C (Figure 5.27), at 10 cycles per charge rate, before returning to the original low current rate of 0.1 C to assess the retention of structural integrity. Increasing the current or C-rate effectively decreases the time taken

Chapter 5: Lithium Iron Phosphate

to completely charge and discharge the cell, or move all the Li-ions into and out of the structure. Compared to 0.1 C where a charge and discharge takes 20 hours combined, 1 C takes 1 hour, 5 C takes 12 mins, whilst a single charge and discharge step at 30 C fully lithiates or removes all lithium from particles within 2 mins. At high charge rates a particle must therefore be extremely efficient at inserting/de-inserting lithium into the structure, so all factors such as small particle size, impurity free and highly crystalline materials with no iron on lithium sites, and a beneficial carbon network aid in making this process more efficient.

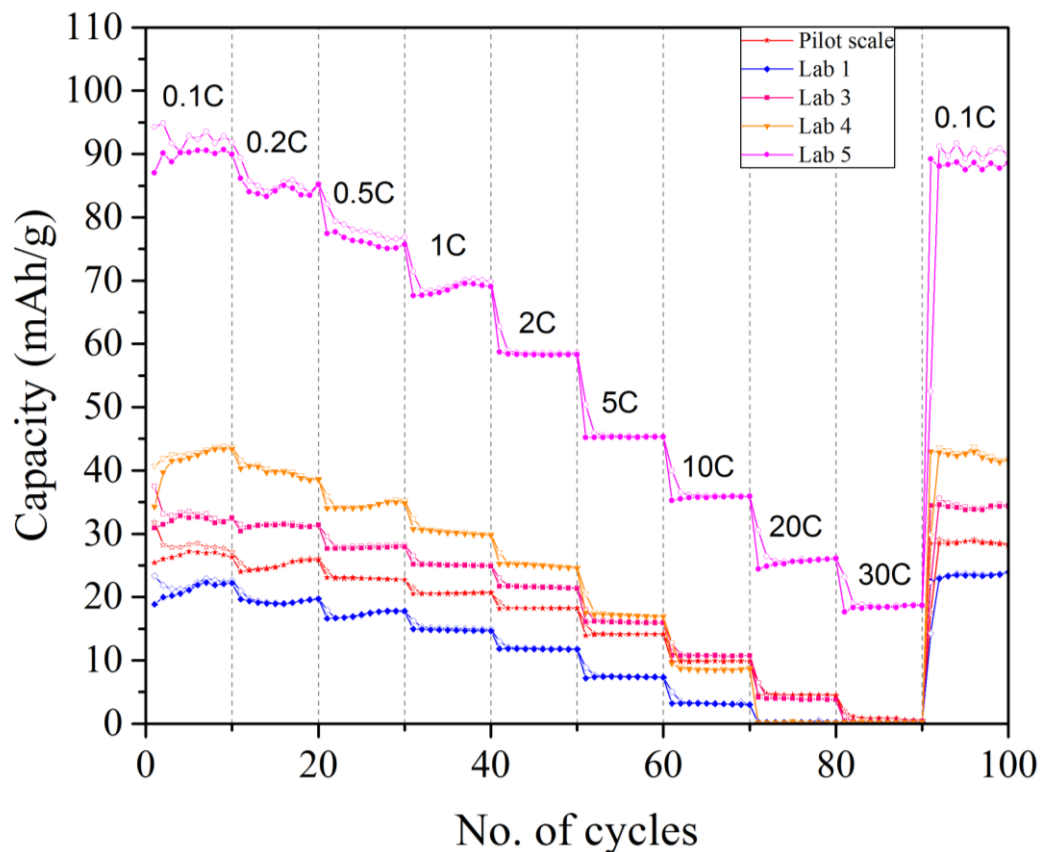


Figure 5.27: The cycling performance of the pilot scale and laboratory scale lithium iron phosphate samples at a range of currents (open symbol; charge, closed symbol; discharge).

Chapter 5: Lithium Iron Phosphate

The same trend can be observed for these high power tests as in the 0.1 C battery tests. The shorter residence time hydrothermal Lab 1 and Pilot scale samples have lower initial capacity and generally lower capacity at subsequent charge rates than the longer residence time hydrothermal samples (Lab 3 and 4). Again, this is attributed to the presence of iron phosphate in the Lab 1 sample, and lower crystallinity of the Lab 1 and Pilot scale products than the Lab 3 and 4 products. Lower crystallinity expresses itself in two ways here – the residence time dictates the degree of lithiation of the material and the level to which a material achieves complete long range ordering towards stoichiometric LiFePO_4 , such that upon battery cycling, maximal Li-ion transfer per mass of material occurs, and secondly and similarly, the level to which the material is ordered such that there are no Fe defects within the structure, or Fe present on Li sites – this is known to effectively block the channel involved in Li-ion transfer – thereby reducing the efficiency of intercalation and lowering the capacity of the material. It can be extrapolated therefore that longer residence time improves lithiation towards defect-free stoichiometric LiFePO_4 , maximising the Li-ion kinetics and improving the capacity. The materials display expected losses in capacity at increasing current rates, and maintain a degree of capacity up to 20/30 C, whereby most of the hydrothermally prepared samples effectively reduce to zero capacity. Upon returning to 0.1 C charge rate, the materials return to effectively 100% of their initial capacity, demonstrating that whilst the materials are unable to cycle effectively at high current rates, they possess excellent structural integrity, which allows them to return to full capacity upon a reduction in current. The solvothermal product Lab 5 displays initial capacity of 90 mAh/g at 0.1 C, and

displays strong capacity retention over subsequent high currents. The material maintains 50% capacity at 5C between cycles 50-60, and holds a capacity of 18 mAh/g at high current rate of 30 C. As with the hydrothermal samples, the material retains 100% capacity upon returning to 0.1 C charge rate. Again, the small size and carbon coating produced in-situ in the synthesis promote better utilisation of the active material, allowing more rapid and facile Li-ion kinetics, even at high current. The high capacity of the Lab 5 sample holds promise of optimisation of this product, to push the capacity towards commercially viable levels.

5.4. Conclusions

A wide range of reaction conditions in batch hydrothermal and solvothermal synthesis such as solvent choice, temperature, reaction time, and organic additive were investigated for their impact on lithium iron phosphate product characteristics such as purity/composition, crystallinity, size and morphology. Under various conditions, it was found that size and shape could be controlled.

The influence of additives on ensuring that phase pure and nanoscale particles are produced and the influence they can have on reaction kinetics was highly beneficial in designing and optimising reactions in the continuous process. The use of ascorbic acid allowed for the exclusive formation of sub-500 nm LiFePO_4 by continuous flow in supercritical water under instantaneous nucleation conditions, and with either ascorbic acid or citric acid at longer residence time of 15-20 s, higher crystallinity LiFePO_4 was produced with enhanced electrochemical properties. In all of these cases, no iron oxide or phosphate impurities were obtained, and the products are easily isolated and

Chapter 5: Lithium Iron Phosphate

processed post-reaction, demonstrated at pilot scale of 20-25 g/h. This production rate was based on a conservative doubling of the precursor concentration – in future work this could be greatly increased to improve reaction efficiency and turnover. No expensive or laborious processes such as flushing of precursor water or solvent water with nitrogen were necessary when using ascorbic acid as an anti-oxidant. Finally, the use of citric acid and a reaction time of 15-20 s in the first continuous solvothermal flow process for LiFePO_4 produced 30 nm particles with a degree of in-situ nanoparticle-carbon interaction, with capacity of 85-90 mAh/g. These LFP particles with such small size may be excellent candidates for use as cathode materials in Li-ion batteries, since the small size leads to large surface area, beneficial for rapid and facile lithium ion diffusivity into and out of particles.

Future work needs to address the relatively low capacity of the continuous flow hydrothermal reaction products, since this is the most directly applicable to the full scale SHYMAN facility. It may be that the counter-current reactor environment of extremely rapid heating and mixing of the metal streams with the supercritical water for instantaneous nucleation may actually hinder pristine LFP formation, and a more gradual reaction is preferential, indicated by the enhanced crystallinity of the longer residence time samples. Indeed this is indicated in the work by Hong et al. (Hong, Kim et al. 2013), where a swirling tee mixer with enhanced mixing dynamics showed LFP particles with fewer impurities and enhanced crystallinity. Since the reactor design and geometry of the counter-current reactor is fixed, modifications to the mixing are not possible, yet, high quality LFP may be accessed by increasing the residence time of the reaction, holding the particles at temperature for longer time

Chapter 5: Lithium Iron Phosphate

periods after the initial synthesis at the mixing point. The results presented in this chapter demonstrated that longer residence time increases the capacity of the materials, and so future work should investigate this further. It may be that holding the particles at temperature for longer improves their crystallinity, in terms of ensuring the full conversion of intermediates to LFP, whilst also improving the ordering of the crystals in terms of situating the metal atoms on their equilibrium locations, such as preventing iron atoms sitting on lithium sites effectively blocking a lithium channel. Research into this area at the laboratory scale may then allow the full-scale facility, when reactor configuration development allows longer residence time at this scale, to produce particles in a hydrothermal manner using the reaction presented for the pilot scale in this chapter with longer residence time, that have improved electrochemical characteristics.

Materials made in the future would also benefit from a degree of in-situ carbon coating within the reactor, to aid in the ease of post-processing such that they are ready to undergo calcination to form a carbon network on the surface of particles and undergo electrochemical characterisation. The carbon coating would also improve the capacity of the materials by improving the conductivity of the particles and improving the connection or conducting pathway between adjacent particles. Usually, LFP powders are mixed with sucrose post-synthesis, which is then calcined to break down to a carbon coating. Sucrose or another similar sugar such as fructose or glucose could be added to the reagent stream to breakdown upon contact with the supercritical water, forming carbonaceous material that would be deposited onto the formed particles surface, thus generating in situ coated particles (Hong, Kim et al. 2012,

Chapter 5: Lithium Iron Phosphate

Johnson, Lübke et al. 2016). These particles could be collected and isolated, ready for calcination without the need for post-processing mixing with sucrose. In this work, it was shown that using an organic additive and ethylene glycol as a solvent, may aid in the formation of a carbon interaction with the particles, by both solvent and additive breakdown at the elevated temperature and reaction time, preparing them for post-synthesis calcination to create a uniform carbon layer on particles, increasing their electronic conductivity and therefore their electrochemical characteristics.

In addition to developing the hydrothermal reaction, the longer residence time solvothermal reactions, particularly when in the presence of citric acid, showed promising electrochemical characterisation results. As previously mentioned the current pilot scale facility and under-construction SHYMAN facility operate using the standard reactor configuration (one mixing/heating point) with no additional heating. This therefore limits the ability to produce these extremely small size LFP nanoparticles at larger scales at present. Whilst requiring longer residence times at present using a secondary heating device downstream of the initial reaction point, this may be altered to a reactor piece with increased length, to hold the particles at temperature for longer before entering the cooling system. This may be sufficient to promote the conversion to small size crystalline LFP particles. Alternatively, mixed water-ethylene glycol systems may be interesting to study, since this may enable a reaction to occur with beneficial characteristics of both solvent systems, to arrive at an ideal scenario where we gain impurity free, settling LFP nanoparticles, that have controlled small size and a degree of in situ carbon coating, all able to occur at short reaction times such that the synthesis can be scaled to industrial

Chapter 5: Lithium Iron Phosphate

levels in the pilot scale and full-scale facility, and the particles displaying improved electrochemical characteristics.

In initial studies in future work leading on from this PhD, the pilot scale sample was retested for electrochemical properties in the 0.1 C cycle test. Powder that was calcined prior to testing as before demonstrated identical capacity. However, powder that was not calcined prior to testing showed a doubling in capacity from 30 mAh/g to 60 mAh/g. It appears the calcination step may have been detrimental to the capacity in the tests presented in this chapter – possibly due to growth of the material/aggregation during the calcination step. Whilst this is only one example, if the other samples, particularly the hydrothermal samples, since they did not have a carbon layer to protect them from aggregation during calcination as the solvothermal particles did, also demonstrate a doubling of capacity when retested with non-calcined powder, then the materials would be expressing capacities comparable to the literature in terms of expected capacity based on reaction conditions. The longer residence time hydrothermal products would be in the region to be expected, and so, this warrants further the development of even longer residence time reaction to further this trend, coupled with the development of in situ carbon coating methods to fully optimise the products and push the capacity into commercially viable limits.

This chapter has demonstrated the application of the counter-current reactor to a material within the phosphate class, in addition to the sulphides already discussed, and to lithium intercalation materials specifically. The knowledge gained about the mechanisms of LFP formation in both water and ethylene

Chapter 5: Lithium Iron Phosphate

glycol, in addition to the use of ethylene glycol as a reaction solvent, through the optimisation of the reaction can be applied to other lithium intercalation materials for battery applications in future work. These could include closely related materials such as mixed iron and manganese systems by simple metal substitution, $\text{LiFe}_{(1-x)}\text{Mn}_x\text{PO}_4$, or topical future trend materials such as lithium nickel manganese cobalt oxides, Li-NMCO.

6. Conclusions, Summary & Future Work

This thesis and the chapters within aimed to demonstrate and have presented innovative chemical engineering and synthetic chemistry advancements within a continuous flow reactor to reliably produce an array of key target materials within the metal oxide, sulphide and phosphate classes, using the counter-current continuous flow hydrothermal and solvothermal reactor developed at The University of Nottingham. With the prior successful demonstration of the technology at larger scales and a European Union funded project to construct an industrial scale facility underway, scalability in terms of the fluid properties and mixing dynamics had been proven, however, demonstration of the versatility of the technique, in terms of the flexibility of the process to access a wide library of materials, was still necessary to further establish the reactor and technology as a viable synthetic tool within the field of nanomaterials production. This would couple the capability of the already demonstrated large scale production with the development of greater control and understanding of the chemistry within the process to overcome and exploit the intricacies of a particular material or material class, showcasing the technology as a flexible and powerful tool for an array of nanomaterials production. This work and the associated publications have achieved this goal. The chapters have demonstrated the successful production of a number of materials spanning different materials classes and in selected cases, scale-up or application based testing.

6.1. Mixed Metal Oxides

Chapter 6: Conclusions, Summary & Future Work

Chapter 3 focussed on traditional metal oxide production; synthesis of transition metal doped anatase nanocrystals which demonstrated photocatalytic activity were presented, in addition to the full compositional range of barium strontium titanate nanopowders at both laboratory and pilot scales. For the anatase nanoparticles, homogenous and thorough incorporation of cobalt and nickel dopants was confirmed by an array of characterisations techniques, as opposed to the formation of a mixture of the respective metal oxides. This is a promising result for the reactor, demonstrating that it is capable of controlling dopant chemistry, an area which can be expanded on in future work to tailor product composition for specific properties required by applications. The inclusion of the dopants lead to a reduction in particle size, an increase in surface area and a lowering of the band-gap energy compared to the undoped anatase nanoparticles. These differences enabled the 1%-Co and 1%-Ni doped anatase nanocrystals to display two- and four- times greater photocatalytic performance, respectively, in the degradation of methylene blue dye compared to the undoped anatase particles. Whilst the dopant metals used and their relative dopant concentration were informed through literature, a more thorough study is warranted in future work, based on the comparable performance achieved by the materials produced using the counter-current reactor to those produced using other methods in the literature, which gives promise for the production of photocatalytically active nanoparticles that are applicable in optoelectronic applications. A systematic study of different metal dopants and dopant concentrations should allow access to a library of materials demonstrating a range of optoelectronic properties suited to varying

Chapter 6: Conclusions, Summary & Future Work

applications, in addition to providing greater understanding of the process of doping of nanocrystals within the reactor.

The production of the full compositional range from barium titanate, barium strontium titanate through to strontium titanate in Chapter 3 is the first reported example of a fully hydrothermal continuous flow route to these materials. Previously in the field, special precautions were required such as the use of alcohols to ensure the stability of the precursors, however, in this work, no special precautions or laborious steps are necessary in the process, therefore improving the scalability of the reaction. In all reactions metal carbonates, specifically BaCO_3 and SrCO_3 , are produced as by-products due to dissolved CO_2 in the water used to dissolve the precursors and as solvent in the reaction. This prevents the full incorporation of the relevant metal constituent into the $\text{Ba}_{(1-x)}\text{Sr}_x\text{TiO}_3$ structure, marginally reducing the experimentally achieved metal:titanium ratio compared to the targeted metal:titanium ratio. Whilst carbonate formation may lead to some degree of difficulty in the reproducibility of metal:titanium ratio in future work, the carbonates can at least be easily removed from the product, by either in-situ washing with acetic acid in-flow, downstream from the reaction point, or offline by washing in acetic acid before centrifugation to isolate the product. In work by other researchers, it has been shown that longer residence times improve the conversion to and crystallinity of BaTiO_3 , and hence, it is suggested that increasing the residence time of the reactions undertaken herein would improve the material towards stoichiometric products. The full compositional range was achieved on the laboratory scale, with selected reactions to provide a representation of the full compositional range undertaken on the pilot scale reactor to assess the scale-up potential of

the reaction. Products achieved on the pilot scale were generally larger in size but showed enhanced incorporation of the relevant metal into the perovskite structure, both attributed to the slight increase in residence time on the pilot scale reactor compared to the laboratory reactor, due to larger pipe geometries and less efficient cooling. This fully hydrothermal continuous-flow route thus represents a further step towards a more affordable and environmentally benign large-scale method for the production of barium strontium titanate nanopowders, and demonstrates CFHS and the Nottingham counter-current reactor as a powerful tool, at both laboratory and pilot scales, for accessing the full compositional range of a family of nanomaterials.

6.2. Metal Sulphides

Chapter 4 presented the first reported production of six metal sulphide nanomaterials by continuous flow hydrothermal methods, via a general route using thiourea as a sulphur source, in addition to presenting the first continuous flow hydrothermal production of MoS_2 , which required reactor modifications to the standard configuration and a sequential synthetic approach. This represented a significant advancement to the continuous flow technique and field, exploring a class of materials never before studied and branching away from the typical use of water as both solvent and reagent to form metal oxides, to the controlled use of the breakdown of thiourea to control the sulphur availability in the form of HS^- , to dictate a nucleation or growth dominated formation mechanism. The differing mechanisms and the understanding gained from their study offer significant scope for future work towards optimised and tailored nanoparticles. This is an important consideration when synthesising

nanomaterials, particularly sulphide and selenide based materials such as quantum dots, since often, as opposed to large scale quantities of non-optimised materials with little value per mass, some applications require only small quantities of heavily tailored nanomaterials which are extremely valuable and lucrative per mass for the producer. Hence when working in this area it is vital to be developing both ‘standard materials’ at large scales, and undertaking work which exploits the flexibility of the system to access new chemistry and being able to understand and then control this leads to higher value products. The sequential nature of the synthesis of MoS₂ offers insight into the modifications that can be made using the reactor set-up dependant on the reaction intricacies of specific products. This demonstrates that in future work one must be aware and prepared to look beyond the classical single reaction point, burst nucleation model in the standard reactor configuration, in order to undergo further complex chemistry and access materials that may require longer residence times, multiple steps or varying stages of reaction conditions in order to undergo the complete reaction pathway and successfully produce the desired product.

6.3. Lithium Iron Phosphate

Chapter 5 explored the synthesis of lithium iron phosphate, a lithium intercalation material which acts as a cathode material in lithium rechargeable batteries, finding application in power tools, e-bikes and buses, with potential application after development in a variety of longer range electric vehicles. Batch hydrothermal and solvothermal synthesis was undertaken, varying a number of reaction parameters to assess their effect on the reaction pathway

Chapter 6: Conclusions, Summary & Future Work

and resulting products, and to gain a deeper understanding about the reaction and the parameters that affect it, to inform and allow understanding of an optimised series of reactions under continuous flow hydrothermal and solvothermal conditions. The batch reactions demonstrated that the solvent, temperature, reaction time and presence of additives dictated the purity, crystallinity, size and morphology of the resulting lithium iron phosphate particles. Under certain conditions, the size of the particles was driven down to the nanoscale, a characteristic beneficial for the diffusion kinetics of lithium ions shuttling into and out of particles during charging and discharging when used in a battery. The translation of these reactions into a continuous manner using the counter-current reactor lead to a deeper understanding of the reaction pathway towards lithium iron phosphate in the reactor, and lead to the successful production of LFP by both hydrothermal and solvothermal synthesis. A reaction undertaken in the standard configuration using ascorbic acid as an additive lead to the production of small size, pure and crystalline LiFePO_4 , at both laboratory and pilot scales. Development of this reaction at laboratory scale by the use of additional heating and therefore residence time appeared to improve the conversion to LFP and the crystallinity of the achieved particles, and this was coupled with an increase in the electrochemical performance. Changing the solvent to ethylene glycol with citric acid as an additive, and using this longer residence time reactor configuration severely reduced the particle size, and lead to particles ranging from 30 nm spheres, which showed greatly enhanced electrochemical performance compared to the hydrothermal samples. This is the first example of such small size particles yielded through continuous flow conditions. Whilst development of the

reaction is needed to improve the electrochemical performance of the materials and methods for this were suggested in the lithium iron phosphate chapter, the work shows promise for the production of lithium battery materials by the Nottingham counter-current reactor, whilst offering further insight into alternate reactor configurations or reaction considerations.

6.4. Closing Remarks

This thesis has demonstrated the ability of the counter-current reactor and continuous flow hydrothermal and solvothermal synthesis as a whole, to be a powerful, flexible and scalable synthesis tool, that, when understood to the point of control, enables synthesis of important, topical and future trend nanomaterials, from simple burst nucleation type models, through to complex materials requiring reactor configuration modifications and chemical innovations to undergo sequential or multiple reaction steps. With an industrial scale facility under construction, and the need for innovative and sustainable nanomaterials and production techniques growing into the future, the demand for increased scales and ever more advanced reactor developments and reaction solutions towards complex products is only going to continue growing, and hence, the future looks promising and potentially lucrative. Demand for materials will be high, yet we must exercise caution when committing ourselves to certain research paths within the continuous flow field, in a scale vs. value of materials trade-off. It is correct that increasing scale will meet products needed in high demand, but tailoring of materials will allow them to be applicable to niche applications, and it is these products which will hold high value from an industrial or commercial context (in terms of holding high

Chapter 6: Conclusions, Summary & Future Work

value per mass). Developments in the field will come therefore in two ways; increasing scale, such as in the SHYMAN Project example, where vast quantities of nanomaterial will be produced, and by designing a process that is economically viable to operate will allow the sale of relatively low-value products in large volumes for profitability. Producing high value products, either by tailoring high volume materials further to increase their performance and therefore value, or by economically producing higher value materials required in much smaller scales for applications, will increase commercial viability. Concurrently, improving the tailoring or control over material properties achieved by reactor configuration developments or innovative chemical strategies within the continuous flow system, such that the end products are more directly suited to an application, in turn making them high value materials but that may only be required on smaller scales, is also a route to commercial and industrial success. This may only require smaller scale reactors optimised to producing only one type of tailored nanoparticle. This therefore necessitates the need to work in both areas to ensure work is both developing on high-volume-low-value materials (since these are necessary in global applications), but also low-volume-high-value products (to maximise profits). Indeed, if one can develop both research streams into one solution, by providing reactor configuration and chemical innovations to allow for advanced tailoring of materials but to do this for a material that is also required on larger scales, whilst maintaining economic viability of the process at that larger scale, then this could be extremely lucrative.

A computer generated image of the design of the full-scale facility, which is based in Nottingham, is shown in Figure 6.1. The build of this is currently

Chapter 6: Conclusions, Summary & Future Work

taking place at the time of writing, with commissioning of the reactor and facility due to take place from April 2016. As stated, it will be the largest and now only large scale commercial facility working under CFHS conditions for the production of nanoparticles in the world, and it is hoped that those materials presented in this PhD thesis that demonstrate both an industrial need and a successful translation to pilot scale will be trialled and produced on this full-scale facility (~ 1000 – 2000 tonnes per year) in the future.



Figure 6.1: A computer generated image of the SHYMAN facility design

7. References

- Adschiri, T., K. Kanazawa and K. Arai (1992). "Rapid and Continuous Hydrothermal Crystallisation of Metal-Oxide Particles in Supercritical Water " Journal of the American Ceramic Society **75**(4): 1019-1022.
- Adschiri, T., Y. W. Lee, M. Goto and S. Takami (2011). "Green materials synthesis with supercritical water." Green Chemistry **13**(6): 1380-1390.
- Ahmad, M. I. and S. S. Bhattacharya (2009). "Size effect on the lattice parameters of nanocrystalline anatase." Applied Physics Letters **95**(19): 191906.
- Aimable, A., D. Aymes, F. Bernard and F. Le Cras (2009). "Characteristics of LiFePO₄ obtained through a one step continuous hydrothermal synthesis process working in supercritical water." Solid State Ionics **180**(11–13): 861-866.
- Aksomaityte, G., M. Poliakoff and E. Lester (2013). "The production and formulation of silver nanoparticles using continuous hydrothermal synthesis." Chemical Engineering Science **85**: 2-10.
- Arnold, G., J. Garche, R. Hemmer, S. Ströbele, C. Vogler and M. Wohlfahrt-Mehrens (2003). "Fine-particle lithium iron phosphate LiFePO₄ synthesized by a new low-cost aqueous precipitation technique." Journal of Power Sources **119–121**: 247-251.
- Atashfaraz, M., M. Shariaty-Niassar, S. Ohara, K. Minami, M. Umetsu, T. Naka and T. Adschiri (2007). "Effect of titanium dioxide solubility on the formation of BaTiO₃ nanoparticles in supercritical water." Fluid Phase Equilibria **257**(2): 233-237.
- Bai, Y., I. Mora-Seró, F. De Angelis, J. Bisquert and P. Wang (2014). "Titanium Dioxide Nanomaterials for Photovoltaic Applications." Chemical Reviews **114**(19): 10095-10130.
- Barrett, E. P., L. G. Joyner and P. P. Halenda (1951). "The Determination of Pore Volume and Area Distributions in Porous Substances. I. Computations from Nitrogen Isotherms." Journal of the American Chemical Society **73**(1): 373-380.
- Batzill, M. (2011). "Fundamental aspects of surface engineering of transition metal oxide photocatalysts." Energy & Environmental Science **4**(9): 3275-3286.
- Becker, W. G. and A. J. Bard (1983). "Photoluminescence and photoinduced oxygen adsorption of colloidal zinc sulfide dispersions." The Journal of Physical Chemistry **87**(24): 4888-4893.
- Bhargava, R. N., D. Gallagher, X. Hong and A. Nurmikko (1994). "Optical properties of manganese-doped nanocrystals of ZnS." Physical Review Letters **72**(3): 416-419.
- Blanco, E., D. Uzio, G. Berhault and P. Afanasiev (2014). "From core-shell MoS_x/ZnS to open fullerene-like MoS₂ nanoparticles." Journal of Materials Chemistry A **2**(10): 3325-3331.
- Blood, P. J., J. P. Denyer, B. J. Azzopardi, M. Poliakoff and E. Lester (2004). "A versatile flow visualisation technique for quantifying mixing in a binary system: application to continuous supercritical water hydrothermal synthesis (SWHS)." Chemical Engineering Science **59**(14): 2853-2861.
- Bocquet, J. F., K. Chhor and C. Pommier (1999). "Barium titanate powders synthesis from solvothermal reaction and supercritical treatment." Materials Chemistry and Physics **57**(3): 273-280.
- Boldrin, P., A. K. Hebb, A. A. Chaudhry, L. Otley, B. Thiebaut, P. Bishop and J. A. Darr (2007). "Direct synthesis of nanosized NiCo₂O₄ spinel and related compounds via continuous hydrothermal synthesis methods." Industrial & Engineering Chemistry Research **46**(14): 4830-4838.
- Burns, J. C., L. J. Krause, D.-B. Le, L. D. Jensen, A. J. Smith, D. Xiong and J. R. Dahn (2011). "Introducing Symmetric Li-Ion Cells as a Tool to Study Cell Degradation Mechanisms." Journal of the Electrochemical Society **158**(12): A1417-A1422.

- Byrappa, K. and M. Yoshimura (2008). Handbook of Hydrothermal Technology.
- Cabanas, A., J. A. Darr, E. Lester and M. Poliakoff (2000). "A continuous and clean one-step synthesis of nano-particulate CeZrO solid solutions in near-critical water." Chemical Communications **0**(11): 901-902.
- Cabanas, A., J. Li, P. Blood, T. Chudoba, W. Lojkowski, M. Poliakoff and E. Lester (2007). "Synthesis of nanoparticulate yttrium aluminum garnet in supercritical water-ethanol mixtures." Journal of Supercritical Fluids **40**(2): 284-292.
- Cao, Y., X. Hu, D. Wang, Y. Sun, P. Sun, J. Zheng, J. Ma and G. Lu (2012). "Flower-like hierarchical zinc oxide architectures: Synthesis and gas sensing properties." Materials Letters **69**(0): 45-47.
- Čapek, R. K., K. Lambert, D. Dorfs, P. F. Smet, D. Poelman, A. Eychmüller and Z. Hens (2009). "Synthesis of Extremely Small CdSe and Bright Blue Luminescent CdSe/ZnS Nanoparticles by a Prefocused Hot-Injection Approach." Chemistry of Materials **21**(8): 1743-1749.
- Carey, G. H., A. L. Abdelhady, Z. Ning, S. M. Thon, O. M. Bakr and E. H. Sargent (2015). "Colloidal Quantum Dot Solar Cells." Chemical Reviews **115**(23): 12732-12763.
- Carp, O., C. L. Huisman and A. Reller (2004). "Photoinduced reactivity of titanium dioxide." Progress in Solid State Chemistry **32**(1-2): 33-177.
- Castro, A. L., M. R. Nunes, M. D. Carvalho, L. P. Ferreira, J. C. Jumas, F. M. Costa and M. H. Florêncio (2009). "Doped titanium dioxide nanocrystalline powders with high photocatalytic activity." Journal of Solid State Chemistry **182**(7): 1838-1845.
- Chan, E. M., R. A. Mathies and A. P. Alivisatos (2003). "Size-Controlled Growth of CdSe Nanocrystals in Microfluidic Reactors." Nano Letters **3**(2): 199-201.
- Chaudhry, A. A., J. Goodall, M. Vickers, J. K. Cockcroft, I. Rehman, J. C. Knowles and J. A. Darr (2008). "Synthesis and characterisation of magnesium substituted calcium phosphate bioceramic nanoparticles made via continuous hydrothermal flow synthesis." Journal of Materials Chemistry **18**(48): 5900-5908.
- Cheary, R. W. and A. A. Coelho (1996). Xfit, CCP14 Powder Diffraction Library, Engineering and Physical Sciences Research Council, Daresbury Laboratory, Warrington, England.
- Chen and R. Fan (2001). "Low-Temperature Hydrothermal Synthesis of Transition Metal Dichalcogenides." Chemistry of Materials **13**(3): 802-805.
- Chen, G., J. Seo, C. Yang and P. N. Prasad (2013). "Nanochemistry and nanomaterials for photovoltaics." Chemical Society Reviews **42**(21): 8304-8338.
- Chen, G., X. Song and T. J. Richardson (2006). "Electron Microscopy Study of the LiFePO₄ to FePO₄ Phase Transition." Electrochemical and Solid-State Letters **9**(6): A295-A298.
- Chen, J. and M. S. Whittingham (2006). "Hydrothermal synthesis of lithium iron phosphate." Electrochemistry Communications **8**(5): 855-858.
- Chen, M., Y. Xie, J. Lu, Y. Xiong, S. Zhang, Y. Qian and X. Liu (2002). "Synthesis of rod-, twinrod-, and tetrapod-shaped CdS nanocrystals using a highly oriented solvothermal recrystallization technique." Journal of Materials Chemistry **12**(3): 748-753.
- Chen, X. and S. S. Mao (2007). "Titanium Dioxide Nanomaterials: Synthesis, Properties, Modifications, and Applications." Chemical Reviews **107**(7): 2891-2959.
- Chen, Z., M. Xu, B. Du, H. Zhu, T. Xie and W. Wang (2014). "Morphology control of lithium iron phosphate nanoparticles by soluble starch-assisted hydrothermal synthesis." Journal of Power Sources **272**: 837-844.
- Cheng, Z., S. Wang, D. Si and B. Geng (2010). "Controlled synthesis of copper sulfide 3D nanoarchitectures through a facile hydrothermal route." Journal of Alloys and Compounds **492**(1-2): L44-L49.

- Cheng, Z., S. Wang, Q. Wang and B. Geng (2010). "A facile solution chemical route to self-assembly of CuS ball-flowers and their application as an efficient photocatalyst." Crystal Engineering Communications **12**(1): 144-149.
- Choi, H., B. Veriansyah, J. Kim, J.-D. Kim and J. W. Kang (2010). "Continuous synthesis of metal nanoparticles in supercritical methanol." Journal of Supercritical Fluids **52**(3): 285-291.
- Choi, H. S. and J. V. Frangioni (2010). "Nanoparticles for Biomedical Imaging: Fundamentals of Clinical Translation." Molecular Imaging **9**(6): 291-310.
- Choi, J., H. Park and M. R. Hoffmann (2010). "Effects of Single Metal-Ion Doping on the Visible-Light Photoreactivity of TiO₂." The Journal of Physical Chemistry C **114**(2): 783-792.
- Choi, W., A. Termin and M. R. Hoffmann (1994). "The Role of Metal Ion Dopants in Quantum-Sized TiO₂: Correlation between Photoreactivity and Charge Carrier Recombination Dynamics." The Journal of Physical Chemistry **98**(51): 13669-13679.
- Choudhury, B. and A. Choudhury (2012). "Luminescence characteristics of cobalt doped TiO₂ nanoparticles." Journal of Luminescence **132**(1): 178-184.
- Choy, K. L. (2003). "Chemical vapour deposition of coatings." Progress in Materials Science **48**(2): 57-170.
- Chung, S.-Y., J. T. Bloking and Y.-M. Chiang (2002). "Electronically conductive phospho-olivines as lithium storage electrodes." Nature Materials **1**(2): 123-128.
- Clark, I. J., T. Takeuchi, N. Ohtori and D. C. Sinclair (1999). "Hydrothermal synthesis and characterisation of BaTiO₃ fine powders: precursors, polymorphism and properties." Journal of Materials Chemistry **9**(1): 83-91.
- Coleman, J. N., M. Lotya, A. O'Neill, S. D. Bergin, P. J. King, U. Khan, K. Young, A. Gaucher, S. De, R. J. Smith, I. V. Shvets, S. K. Arora, G. Stanton, H.-Y. Kim, K. Lee, G. T. Kim, G. S. Duesberg, T. Hallam, J. J. Boland, J. J. Wang, J. F. Donegan, J. C. Grunlan, G. Moriarty, A. Shmeliov, R. J. Nicholls, J. M. Perkins, E. M. Grievson, K. Theuwissen, D. W. McComb, P. D. Nellist and V. Nicolosi (2011). "Two-Dimensional Nanosheets Produced by Liquid Exfoliation of Layered Materials." Science **331**(6017): 568-571.
- Colmenares, J. C., M. A. Aramendía, A. Marinas, J. M. Marinas and F. J. Urbano (2006). "Synthesis, characterization and photocatalytic activity of different metal-doped titania systems." Applied Catalysis A: General **306**(0): 120-127.
- Costa-Fernández, J. M., R. Pereiro and A. Sanz-Medel (2006). "The use of luminescent quantum dots for optical sensing." Trends in Analytical Chemistry **25**(3): 207-218.
- Cui, Y., C. Wang, S. Wu, G. Liu, F. Zhang and T. Wang (2011). "Lotus-root-like NiO nanosheets and flower-like NiO microspheres: synthesis and magnetic properties." Crystal Engineering Communications **13**(15): 4930-4934.
- Curri, M. L., R. Comparelli, P. D. Cozzoli, G. Mascolo and A. Agostiano (2003). "Colloidal oxide nanoparticles for the photocatalytic degradation of organic dye." Materials Science and Engineering: C **23**(1-2): 285-289.
- Cushing, B. L., V. L. Kolesnichenko and C. J. O'Connor (2004). "Recent Advances in the Liquid-Phase Syntheses of Inorganic Nanoparticles." Chemical Reviews **104**(9): 3893-3946.
- Delacourt, C., P. Poizot, S. Levasseur and C. Masquelier (2006). "Size Effects on Carbon-Free LiFePO₄ Powders: The Key to Superior Energy Density." Electrochemical and Solid-State Letters **9**(7): A352-A355.
- Denis, C. J., C. J. Tighe, R. I. Guar, N. M. Makwana and J. A. Darr (2015). "Nucleation and Growth of Cobalt Oxide Nanoparticles in a Continuous Hydrothermal Reactor under Laminar and Turbulent Flow." Crystal Growth & Design **15**(9): 4256-4265.
- Denzler, D., M. Olschewski and K. Sattler (1998). "Luminescence studies of localized gap states in colloidal ZnS nanocrystals." Journal of Applied Physics **84**(5): 2841-2845.
- Devaraju, M. K. and I. Honma (2012). "Hydrothermal and Solvothermal Process Towards Development of LiMPO₄ (M = Fe, Mn) Nanomaterials for Lithium-Ion Batteries." Advanced Energy Materials **2**(3): 284-297.

- Devi, L. G., N. Kottam, B. N. Murthy and S. G. Kumar (2010). "Enhanced photocatalytic activity of transition metal ions Mn²⁺, Ni²⁺ and Zn²⁺ doped polycrystalline titania for the degradation of Aniline Blue under UV/solar light." Journal of Molecular Catalysis A: Chemical **328**(1–2): 44-52.
- Di Benedetto, F., M. Borgheresi, A. Caneschi, G. Chastanet, C. Cipriani, D. Gatteschi, G. Pratesi, M. Romanelli and R. Sessoli (2006). "First evidence of natural superconductivity: covellite." European Journal of Mineralogy **18**(3): 283-287.
- Diebold, U. (2003). "The surface science of titanium dioxide." Surface Science Reports **48**(5–8): 53-229.
- Ding, Y., Y. Jiang, F. Xu, J. Yin, H. Ren, Q. Zhuo, Z. Long and P. Zhang (2010). "Preparation of nano-structured LiFePO₄/graphene composites by co-precipitation method." Electrochemistry Communications **12**(1): 10-13.
- Dunne, P. W., A. S. Munn, C. L. Starkey, T. A. Huddle and E. H. Lester (2015). "Continuous-flow hydrothermal synthesis for the production of inorganic nanomaterials." Philosophical Transactions of the Royal Society of London A: Mathematical, Physical and Engineering Sciences **373**(2057).
- Dunne, P. W., A. S. Munn, C. L. Starkey and E. H. Lester (2015). "The sequential continuous-flow hydrothermal synthesis of molybdenum disulphide." Chemical Communications **51**(19): 4048-4050.
- Dunne, P. W., C. L. Starkey, M. Gimeno-Fabra and E. H. Lester (2014). "The rapid size- and shape-controlled continuous hydrothermal synthesis of metal sulphide nanomaterials." Nanoscale **6**(4): 2406-2418.
- Dunne, P. W., C. L. Starkey, A. S. Munn, M. Sikder, O. Luebben, I. Shvets and E. H. Lester "Transition Metal Doped Anatase Nanocrystals: Continuous-Flow Hydrothermal Synthesis and Photocatalytic Activity." Journal of Environmental Chemical Engineering **4**(3): 2665-2670
- Dunne, P. W., C. L. Starkey, A. S. Munn, S. V. Y. Tang, O. Luebben, I. Shvets, A. G. Ryder, Y. Casamayou-Boucau, L. Morrison and E. H. Lester (2016). "Bench- and pilot-scale continuous-flow hydrothermal production of barium strontium titanate nanopowders." Chemical Engineering Journal **289**: 433-441.
- Ellis, B., W. H. Kan, W. R. M. Makahnouk and L. F. Nazar (2007). "Synthesis of nanocrystals and morphology control of hydrothermally prepared LiFePO₄." Journal of Materials Chemistry **17**(30): 3248-3254.
- Elouali, S., L. G. Bloor, R. Binions, I. P. Parkin, C. J. Carmalt and J. A. Darr (2011). "Gas Sensing with Nano-Indium Oxides (In₂O₃) Prepared via Continuous Hydrothermal Flow Synthesis." Langmuir **28**(3): 1879-1885.
- Erickson, B. E. and G. R. Helz (2000). "Molybdenum(VI) speciation in sulfidic waters: Stability and lability of thiomolybdates." Geochimica et Cosmochimica Acta **64**(7): 1149-1158.
- Esquivel, K., R. Nava, A. Zamudio-Méndez, M. V. González, O. E. Jaime-Acuña, L. Escobar-Alarcón, J. M. Peralta-Hernández, B. Pawelec and J. L. G. Fierro (2013). "Microwave-assisted synthesis of (S)Fe/TiO₂ systems: Effects of synthesis conditions and dopant concentration on photoactivity." Applied Catalysis B: Environmental **140–141**(0): 213-224.
- Etacheri, V., R. Marom, R. Elazari, G. Salitra and D. Aurbach (2011). "Challenges in the development of advanced Li-ion batteries: a review." Energy & Environmental Science **4**(9): 3243-3262.
- Ezhilvalavan, S. and T.-Y. Tseng (2000). "Progress in the developments of (Ba,Sr)TiO₃ (BST) thin films for Gigabit era DRAMs." Materials Chemistry and Physics **65**(3): 227-248.
- Faivre, D. and D. Schüler (2008). "Magnetotactic Bacteria and Magnetosomes." Chemical Reviews **108**(11): 4875-4898.
- Fan, Z., A. O. Yalcin, F. D. Tichelaar, H. W. Zandbergen, E. Talgorn, A. J. Houtepen, T. J. H. Vlught and M. A. van Huis (2013). "From Sphere to Multipod: Thermally Induced Transitions

- of CdSe Nanocrystals Studied by Molecular Dynamics Simulations." Journal of the American Chemical Society **135**(15): 5869-5876.
- Feldman, Y., G. L. Frey, M. Homyonfer, V. Lyakhovitskaya, L. Margulis, H. Cohen, G. Hodes, J. L. Hutchison and R. Tenne (1996). "Bulk Synthesis of Inorganic Fullerene-like MS₂ (M = Mo, W) from the Respective Trioxides and the Reaction Mechanism." Journal of the American Chemical Society **118**(23): 5362-5367.
- Feteira, A., D. C. Sinclair, I. M. Reaney, Y. Somiya and M. T. Lanagan (2004). "BaTiO₃-Based Ceramics for Tunable Microwave Applications." Journal of the American Ceramic Society **87**(6): 1082-1087.
- Fisher, C. A. J., V. M. Hart Prieto and M. S. Islam (2008). "Lithium Battery Materials LiMPO₄ (M = Mn, Fe, Co, and Ni): Insights into Defect Association, Transport Mechanisms, and Doping Behavior." Chemistry of Materials **20**(18): 5907-5915.
- Fisher, C. A. J. and M. S. Islam (2008). "Surface structures and crystal morphologies of LiFePO₄: relevance to electrochemical behaviour." Journal of Materials Chemistry **18**(11): 1209-1215.
- Fonseca de Lima, J., M. H. Harunsani, D. J. Martin, D. Kong, P. W. Dunne, D. Gianolio, R. J. Kashtiban, J. Sloan, O. A. Serra, J. Tang and R. I. Walton (2015). "Control of chemical state of cerium in doped anatase TiO₂ by solvothermal synthesis and its application in photocatalytic water reduction." Journal of Materials Chemistry A **3**(18): 9890-9898.
- Freestone, I., N. Meeks, M. Sax and C. Higgitt (2007). "The Lycurgus Cup — A Roman nanotechnology." Gold Bulletin **40**(4): 270-277.
- Fujishima, A., X. Zhang and D. A. Tryk (2008). "TiO₂ photocatalysis and related surface phenomena." Surface Science Reports **63**(12): 515-582.
- Gao, X., Y. Cui, R. M. Levenson, L. W. K. Chung and S. Nie (2004). "In vivo cancer targeting and imaging with semiconductor quantum dots." Nature Biotechnology **22**(8): 969-976.
- Gao, Y., L. Li, H. Peng and Z. Wei (2014). "Surfactant-Assisted Sol–Gel Synthesis of Nanostructured Ruthenium-Doped Lithium Iron Phosphate as a Cathode for Lithium-Ion Batteries." ChemElectroChem **1**(12): 2146-2152.
- Gaya, U. I. and A. H. Abdullah (2008). "Heterogeneous photocatalytic degradation of organic contaminants over titanium dioxide: A review of fundamentals, progress and problems." Journal of photochemistry and photobiology C: Photochemistry reviews **9**(1): 1-12.
- Ghafarian-Zahmatkesh, H., M. Javanbakht and M. Ghaemi (2015). "Ethylene glycol-assisted hydrothermal synthesis and characterization of bow-tie-like lithium iron phosphate nanocrystals for lithium-ion batteries." Journal of Power Sources **284**: 339-348.
- Gibot, P., M. Casas-Cabanas, L. Laffont, S. Lévassieur, P. Carlach, S. Hamelet, J.-M. Tarascon and C. Masquelier (2008). "Room-temperature single-phase Li insertion/extraction in nanoscale Li_xFePO₄." Nature Materials **7**(9): 741-747.
- Gimeno-Fabra, M., A. S. Munn, L. A. Stevens, T. C. Drage, D. M. Grant, R. J. Kashtiban, J. Sloan, E. Lester and R. I. Walton (2012). "Instant MOFs: continuous synthesis of metal-organic frameworks by rapid solvent mixing." Chemical Communications **48**(86): 10642-10644.
- Goudarzi, A., G. M. Aval, S. S. Park, M.-C. Choi, R. Sahraei, M. H. Ullah, A. Avane and C.-S. Ha (2009). "Low-Temperature Growth of Nanocrystalline Mn-Doped ZnS Thin Films Prepared by Chemical Bath Deposition and Optical Properties." Chemistry of Materials **21**(12): 2375-2385.
- Grange, P. and X. Vanhaeren (1997). "Hydrotreating catalysts, an old story with new challenges." Catalysis Today **36**(4): 375-391.
- Gruar, R., C. J. Tighe, L. M. Reilly, G. Sankar and J. A. Darr (2010). "Tunable and rapid crystallisation of phase pure Bi₂MoO₆ (koechlinite) and Bi₂Mo₃O₁₂ via continuous hydrothermal synthesis." Solid State Sciences **12**(9): 1683-1686.

- Gruar, R. I., C. J. Tighe and J. A. Darr (2013). "Scaling-Up a Confined Jet Reactor for the Continuous Hydrothermal Manufacture of Nanomaterials." Industrial & Engineering Chemistry Research **52**(15): 5270-5281
- Gruar, R. I., C. J. Tighe, J. Muir, J. T. Kittler, M. Wodjak, A. J. Kenyon and J. A. Darr (2012). "Continuous hydrothermal synthesis of surface-functionalised nanophosphors for biological imaging." RSC Advances **2**(26): 10037-10047.
- Guo, Y., J. Wang, L. Yang, J. Zhang, K. Jiang, W. Li, L. Wang and L. Jiang (2011). "Facile additive-free solvothermal synthesis of cadmium sulfide flower-like three dimensional assemblies with unique optical properties and photocatalytic activity." Crystal Engineering Communications **13**(16): 5045-5048.
- Haertling, G. H. (1999). "Ferroelectric Ceramics: History and Technology." Journal of the American Ceramic Society **82**(4): 797-818.
- Hakuta, Y., S. Onai, H. Terayama, T. Adschiri and K. Arai (1998). "Production of ultra-fine ceria particles by hydrothermal synthesis under supercritical conditions." Journal of Materials Science Letters **17**(14): 1211-1213.
- Hayashi, H., T. Noguchi, N. M. Islam, Y. Hakuta, Y. Imai and N. Ueno (2010). "Hydrothermal synthesis of BaTiO₃ nanoparticles using a supercritical continuous flow reaction system." Journal of Crystal Growth **312**(12–13): 1968-1972.
- Hayashi, H., T. Noguchi, N. M. Islam, Y. Hakuta, Y. Imai and N. Ueno (2010). "Hydrothermal synthesis of organic hybrid BaTiO₃ nanoparticles using a supercritical continuous flow reaction system." Journal of Crystal Growth **312**(24): 3613-3618.
- Helmersson, U., M. Lattemann, J. Bohlmark, A. P. Ehiasarian and J. T. Gudmundsson (2006). "Ionized physical vapor deposition (IPVD): A review of technology and applications." Thin Solid Films **513**(1–2): 1-24.
- Hibble, S. J. and G. B. Wood (2003). "Modeling the Structure of Amorphous MoS₃: A Neutron Diffraction and Reverse Monte Carlo Study." Journal of the American Chemical Society **126**(3): 959-965.
- Higuchi, M., K. Katayama, Y. Azuma, M. Yukawa and M. Sahara (2003). "Synthesis of LiFePO₄ cathode material by microwave processing." Journal of Power Sources **119–121**: 258-261.
- Hobbs, H., S. Briddon and E. Lester (2009). "The synthesis and fluorescent properties of nanoparticulate ZrO₂ doped with Eu using continuous hydrothermal synthesis." Green Chemistry **11**(4): 484-491.
- Hong, S.-A., S. J. Kim, K. Y. Chung, M.-S. Chun, B. G. Lee and J. Kim (2013). "Continuous synthesis of lithium iron phosphate (LiFePO₄) nanoparticles in supercritical water: Effect of mixing tee." The Journal of Supercritical Fluids **73**(0): 70-79.
- Hong, S.-A., S. J. Kim, K. Y. Chung, Y.-W. Lee, J. Kim and B.-I. Sang (2013). "Continuous synthesis of lithium iron phosphate nanoparticles in supercritical water: Effect of process parameters." Chemical Engineering Journal **229**(0): 313-323.
- Hong, S. A., S. J. Kim, J. Kim, K. Y. Chung, B. W. Cho and J. W. Kang (2011). "Small capacity decay of lithium iron phosphate (LiFePO₄) synthesized continuously in supercritical water: Comparison with solid-state method." Journal of Supercritical Fluids **55**(3): 1027-1037.
- Hong, S. A., S. J. Kim, J. Kim, B. G. Lee, K. Y. Chung and Y. W. Lee (2012). "Carbon coating on lithium iron phosphate (LiFePO₄): Comparison between continuous supercritical hydrothermal method and solid-state method." Chemical Engineering Journal **198**: 318-326.
- Houas, A., H. Lachheb, M. Ksibi, E. Elaloui, C. Guillard and J.-M. Herrmann (2001). "Photocatalytic degradation pathway of methylene blue in water." Applied Catalysis B: Environmental **31**(2): 145-157.
- Hsu, K.-F., S.-Y. Tsay and B.-J. Hwang (2004). "Synthesis and characterization of nano-sized LiFePO₄ cathode materials prepared by a citric acid-based sol-gel route." Journal of Materials Chemistry **14**(17): 2690-2695.

- Hu, S., W. Chen, J. Zhou, F. Yin, E. Uchaker, Q. Zhang and G. Cao (2014). "Preparation of carbon coated MoS₂ flower-like nanostructure with self-assembled nanosheets as high-performance lithium-ion battery anodes." Journal of Materials Chemistry A **2**(21): 7862-7872.
- Hu, Y., M. M. Doeff, R. Kostecki and R. Fiñones (2004). "Electrochemical Performance of Sol-Gel Synthesized LiFePO₄ in Lithium Batteries." Journal of the Electrochemical Society **151**(8): A1279-A1285.
- Huang, F. and J. F. Banfield (2005). "Size-Dependent Phase Transformation Kinetics in Nanocrystalline ZnS." Journal of the American Chemical Society **127**(12): 4523-4529.
- Huijuan, Z. and Q. Limin (2006). "Low-temperature, template-free synthesis of wurtzite ZnS nanostructures with hierarchical architectures." Nanotechnology **17**(15): 3984.
- Johnson, I. D., M. Lübke, O. Y. Wu, N. M. Makwana, G. J. Smales, H. U. Islam, R. Y. Dedigama, R. I. Gruar, C. J. Tighe, D. O. Scanlon, F. Corà, D. J. L. Brett, P. R. Shearing and J. A. Darr (2016). "Pilot-scale continuous synthesis of a vanadium-doped LiFePO₄/C nanocomposite high-rate cathodes for lithium-ion batteries." Journal of Power Sources **302**: 410-418.
- Joo, J., H. B. Na, T. Yu, J. H. Yu, Y. W. Kim, F. Wu, J. Z. Zhang and T. Hyeon (2003). "Generalized and Facile Synthesis of Semiconducting Metal Sulfide Nanocrystals." Journal of the American Chemical Society **125**(36): 11100-11105.
- Julien, C. M., K. Zaghib, A. Mauger, M. Massot, A. Ait-Salah, M. Selmane and F. Gendron (2006). "Characterization of the carbon coating onto LiFePO₄ particles used in lithium batteries." Journal of Applied Physics **100**(6): 063511.
- Kang, B. and G. Ceder (2009). "Battery materials for ultrafast charging and discharging." Nature **458**(7235): 190-193.
- Kellici, S., K. Gong, T. Lin, S. Brown, R. J. H. Clark, M. Vickers, J. K. Cockcroft, V. Middelkoop, P. Barnes, J. M. Perkins, C. J. Tighe and J. A. Darr (2010). "High-throughput continuous hydrothermal flow synthesis of Zn-Ce oxides: unprecedented solubility of Zn in the nanoparticle fluorite lattice." Philosophical Transactions of the Royal Society A-Mathematical Physical and Engineering Sciences **368**(1927): 4331-4349.
- Khurana, C., O. P. Pandey and B. Chudasama (2015). "Synthesis of visible light-responsive cobalt-doped TiO₂ nanoparticles with tunable optical band gap." Journal of Sol-Gel Science and Technology **75**(2): 424-435.
- Kim, E.-J., J.-H. Kim, A.-M. Azad and Y.-S. Chang (2011). "Facile Synthesis and Characterization of Fe/FeS Nanoparticles for Environmental Applications." Applied Materials & Interfaces **3**(5): 1457-1462.
- Kim, J.-K., J.-W. Choi, G. Cheruvally, J.-U. Kim, J.-H. Ahn, G.-B. Cho, K.-W. Kim and H.-J. Ahn (2007). "A modified mechanical activation synthesis for carbon-coated LiFePO₄ cathode in lithium batteries." Materials Letters **61**(18): 3822-3825.
- Kim, J., Y.-S. Park, B. Veriansyah, J.-D. Kim and Y.-W. Lee (2008). "Continuous Synthesis of Surface-Modified Metal Oxide Nanoparticles Using Supercritical Methanol for Highly Stabilized Nanofluids." Chemistry of Materials **20**(20): 6301-6303.
- Kim, Y.-I., J. K. Jung and K.-S. Ryu (2004). "Structural study of nano BaTiO₃ powder by Rietveld refinement." Materials Research Bulletin **39**(7-8): 1045-1053.
- Koltypin, M., D. Aurbach, L. Nazar and B. Ellis (2007). "More on the performance of LiFePO₄ electrodes—The effect of synthesis route, solution composition, aging, and temperature." Journal of Power Sources **174**(2): 1241-1250.
- Koupanou, E., S. Ahualli, O. Glatter, A. Delgado, F. Krumeich and E. Leontidis (2010). "Stabilization of Lead Sulfide Nanoparticles by Polyamines in Aqueous Solutions. A Structural Study of the Dispersions." Langmuir **26**(22): 16909-16920.
- Kudera, S., L. Carbone, E. Carlino, R. Cingolani, P. D. Cozzoli and L. Manna (2007). "Synthesis routes for the growth of complex nanostructures." Physica E: Low-dimensional Systems and Nanostructures **37**(1-2): 128-133.

- Kumar, S. and T. Nann (2006). "Shape Control of II–VI Semiconductor Nanomaterials." Small **2**(3): 316-329.
- Kwei, G. H., A. C. Lawson, S. J. L. Billinge and S. W. Cheong (1993). "Structures of the ferroelectric phases of barium titanate." The Journal of Physical Chemistry **97**(10): 2368-2377.
- Laffont, L., C. Delacourt, P. Gibot, M. Y. Wu, P. Kooyman, C. Masquelier and J. M. Tarascon (2006). "Study of the LiFePO₄/FePO₄ Two-Phase System by High-Resolution Electron Energy Loss Spectroscopy." Chemistry of Materials **18**(23): 5520-5529.
- Lai, H.-Y. and C.-J. Chen (2009). "Shape-controlled synthesis of iron sulfide nanostructures via oriented attachment mechanism." Journal of Crystal Growth **311**(23–24): 4698-4703.
- LaMer, V. K. and R. H. Dinegar (1950). "Theory, production and mechanism of formation of monodispersed hydrosols." Journal of the American Chemical Society **72**(11): 4847-4854.
- Larson, A. C. and R. B. Von Dreele (1994). General Structure Analysis System (GSAS). Los Alamos National Laboratory Report LAUR 86-748.
- Laurie, Stuart H. (2000). "Thiomolybdates — Simple but Very Versatile Reagents." European Journal of Inorganic Chemistry **2000**(12): 2443-2450.
- Lee, H., M. Yanilmaz, O. Toprakci, K. Fu and X. Zhang (2014). "A review of recent developments in membrane separators for rechargeable lithium-ion batteries." Energy & Environmental Science **7**(12): 3857-3886.
- Lee, J. and A. S. Teja (2005). "Characteristics of lithium iron phosphate (LiFePO₄) particles synthesized in subcritical and supercritical water." The Journal of Supercritical Fluids **35**(1): 83-90.
- Lester, E., G. Aksomaityte, J. Li, S. Gomez, J. Gonzalez-Gonzalez and M. Poliakoff (2012). "Controlled continuous hydrothermal synthesis of cobalt oxide (Co₃O₄) nanoparticles." Progress in Crystal Growth and Characterization of Materials **58**(1): 3-13.
- Lester, E., P. Blood, J. Denyer, D. Giddings, B. Azzopardi and M. Poliakoff (2006). "Reaction engineering: The supercritical water hydrothermal synthesis of nano-particles." Journal of Supercritical Fluids **37**(2): 209-214.
- Lester, E., S. V. Y. Tang, A. Khlobystov, V. L. Rose, L. Buttery and C. J. Roberts (2013). "Producing nanotubes of biocompatible hydroxyapatite by continuous hydrothermal synthesis." Crystal Engineering Communications **15**(17): 3256-3260.
- Li, F., T. Kong, W. Bi, D. Li, Z. Li and X. Huang (2009). "Synthesis and optical properties of CuS nanoplate-based architectures by a solvothermal method." Applied Surface Science **255**(12): 6285-6289.
- Li, X.-L., J.-P. Ge and Y.-D. Li (2004). "Atmospheric Pressure Chemical Vapor Deposition: An Alternative Route to Large-Scale MoS₂ and WS₂ Inorganic Fullerene-like Nanostructures and Nanoflowers." Chemistry – A European Journal **10**(23): 6163-6171.
- Lu, J., Q. Han, X. Yang, L. Lu and X. Wang (2007). "Microwave-assisted synthesis and characterization of 3D flower-like Bi₂S₃ superstructures." Materials Letters **61**(14–15): 2883-2886.
- Lu, J. F., K. Minami, S. Takami and T. Adschiri (2013). "Rapid and continuous synthesis of cobalt aluminate nanoparticles under subcritical hydrothermal conditions with in-situ surface modification." Chemical Engineering Science **85**: 50-54.
- Lu, W., M. Quilitz and H. Schmidt (2007). "Nanoscaled BaTiO₃ powders with a large surface area synthesized by precipitation from aqueous solutions: Preparation, characterization and sintering." Journal of the European Ceramic Society **27**(10): 3149-3159.
- Lu, Z., H. Chen, R. Robert, B. Y. X. Zhu, J. Deng, L. Wu, C. Y. Chung and C. P. Grey (2011). "Citric Acid- and Ammonium-Mediated Morphological Transformations of Olivine LiFePO₄ Particles." Chemistry of Materials **23**(11): 2848-2859.
- Lübke, M., I. Johnson, N. M. Makwana, D. Brett, P. Shearing, Z. Liu and J. A. Darr (2015). "High power TiO₂ and high capacity Sn-doped TiO₂ nanomaterial anodes for lithium-ion batteries." Journal of Power Sources **294**: 94-102.

- Lübke, M., N. M. Makwana, R. Gruar, C. Tighe, D. Brett, P. Shearing, Z. Liu and J. A. Darr (2015). "High capacity nanocomposite Fe₃O₄/Fe anodes for Li-ion batteries." Journal of Power Sources **291**: 102-107.
- Luther III, G. W., S. M. Theberge and D. T. Rickard (1999). "Evidence for aqueous clusters as intermediates during zinc sulfide formation." Geochimica et Cosmochimica Acta **63**(19–20): 3159-3169.
- Luttrell, T., S. Halpegamage, J. Tao, A. Kramer, E. Sutter and M. Batzill (2014). "Why is anatase a better photocatalyst than rutile? - Model studies on epitaxial TiO₂ films." Scientific Reports **4**: 4043.
- Mahdi, M. A., J. J. Hassan, Z. Hassan and S. S. Ng (2012). "Growth and characterization of ZnxCd1-xS nanoflowers by microwave-assisted chemical bath deposition." Journal of Alloys and Compounds **541**(0): 227-233.
- Makwana, N. M., C. J. Tighe, R. I. Gruar, P. F. McMillan and J. A. Darr (2016). "Pilot plant scale continuous hydrothermal synthesis of nano-titania; effect of size on photocatalytic activity." Materials Science in Semiconductor Processing **42, Part 1**: 131-137.
- Mandal, T., G. Piburn, V. Stavila, I. Rusakova, T. Ould-Ely, A. C. Colson and K. H. Whitmire (2011). "New Mixed Ligand Single-Source Precursors for PbS Nanoparticles and Their Solvothermal Decomposition to Anisotropic Nano- And Microstructures." Chemistry of Materials **23**(18): 4158-4169.
- Manna, L., E. C. Scher and A. P. Alivisatos (2000). "Synthesis of soluble and processable rod-, arrow-, teardrop-, and tetrapod-shaped CdSe nanocrystals." Journal of the American Chemical Society **122**(51): 12700-12706.
- Mats, J. and L. Peter (2008). "Perovskites and thin films—crystallography and chemistry." Journal of Physics: Condensed Matter **20**(26): 264001.
- Matsui, K., T. Noguchi, N. M. Islam, Y. Hakuta and H. Hayashi (2008). "Rapid synthesis of BaTiO₃ nanoparticles in supercritical water by continuous hydrothermal flow reaction system." Journal of Crystal Growth **310**(10): 2584-2589.
- McManus, J. S., P. D. Cunningham, L. B. Regan and P. W. Dunne (2012). "The synthesis of organo-soluble anatase nanocrystals from amorphous titania." Chemical Communications **48**(60): 7453-7455.
- Michalet, X., F. F. Pinaud, L. A. Bentolila, J. M. Tsay, S. Doose, J. J. Li, G. Sundaresan, A. M. Wu, S. S. Gambhir and S. Weiss (2005). "Quantum Dots for Live Cells, in Vivo Imaging, and Diagnostics." Science **307**(5709): 538-544.
- Miller, J. D., J. Li, J. C. Davidtz and F. Vos (2005). "A review of pyrrhotite flotation chemistry in the processing of PGM ores." Minerals Engineering **18**(8): 855-865.
- Modeshia, D. R. and R. I. Walton (2010). "Solvothermal synthesis of perovskites and pyrochlores: crystallisation of functional oxides under mild conditions." Chemical Society Reviews **39**(11): 4303-4325.
- Munn, A. S., P. W. Dunne, S. V. Y. Tang and E. H. Lester (2015). "Large-scale continuous hydrothermal production and activation of ZIF-8." Chemical Communications **51**(64): 12811-12814.
- Naik, A. J. T., R. Gruar, C. J. Tighe, I. P. Parkin, J. A. Darr and R. Binions (2015). "Environmental sensing semiconducting nanoceramics made using a continuous hydrothermal synthesis pilot plant." Sensors and Actuators B: Chemical **217**: 136-145.
- Nakamoto, K., J. Fujita, S. Tanaka and M. Kobayashi (1957). "Infrared Spectra of Metallic Complexes. IV. Comparison of the Infrared Spectra of Unidentate and Bidentate Metallic Complexes." Journal of the American Chemical Society **79**(18): 4904-4908.
- Nakamoto, K., Y. A. Sarma and H. Ogoshi (1965). "Normal Coordinate Analyses of Hydrogen-Bonded Compounds. IV. The Acid Carbonate Ion." The Journal of Chemical Physics **43**(4): 1177-1181.

- Nan, C., J. Lu, C. Chen, Q. Peng and Y. Li (2011). "Solvothermal synthesis of lithium iron phosphate nanoplates." Journal of Materials Chemistry **21**(27): 9994-9996.
- Newman, E. J. (1963). "Precipitation of cuprous thiocyanate from homogeneous solution." Analyst **88**(1048): 500-505.
- Ni, Y., F. Wang, H. Liu, G. Yin, J. Hong, X. Ma and Z. Xu (2004). "A novel aqueous-phase route to prepare flower-shaped PbS micron crystals." Journal of Crystal Growth **262**(1-4): 399-402.
- Ni, Y., X. Wei, J. Hong and X. Ma (2007). "Hydrothermal preparation of PbS crystals and shape evolution." Materials Research Bulletin **42**(1): 17-26.
- Nightingale, A. M. and J. C. de Mello (2010). "Microscale synthesis of quantum dots." Journal of Materials Chemistry **20**(39): 8454-8463.
- Ohara, S., T. Mousavand, T. Sasaki, M. Umetsu, T. Naka and T. Adschiri (2008). "Continuous production of fine zinc oxide nanorods by hydrothermal synthesis in supercritical water." Journal of Materials Science **43**(7): 2393-2396.
- Ohno, T., K. Sarukawa and M. Matsumura (2002). "Crystal faces of rutile and anatase TiO₂ particles and their roles in photocatalytic reactions." New Journal of Chemistry **26**(9): 1167-1170.
- Ong, W.-J., L.-L. Tan, S.-P. Chai, S.-T. Yong and A. R. Mohamed (2014). "Highly reactive {001} facets of TiO₂-based composites: synthesis, formation mechanism and characterization." Nanoscale **6**(4): 1946-2008.
- Padhi, A. K., K. S. Nanjundaswamy and J. B. Goodenough (1997). "Phospho-olivines as Positive-Electrode Materials for Rechargeable Lithium Batteries." Journal of the Electrochemical Society **144**(4): 1188-1194.
- Parkin, I. P. and R. G. Palgrave (2005). "Self-cleaning coatings." Journal of Materials Chemistry **15**(17): 1689-1695.
- Pei, B., H. Yao, W. Zhang and Z. Yang (2012). "Hydrothermal synthesis of morphology-controlled LiFePO₄ cathode material for lithium-ion batteries." Journal of Power Sources **220**: 317-323.
- Pelaez, M., N. T. Nolan, S. C. Pillai, M. K. Seery, P. Falaras, A. G. Kontos, P. S. M. Dunlop, J. W. J. Hamilton, J. A. Byrne, K. O'Shea, M. H. Entezari and D. D. Dionysiou (2012). "A review on the visible light active titanium dioxide photocatalysts for environmental applications." Applied Catalysis B: Environmental **125**: 331-349.
- Pérez-Arantegui, J., J. Molera, A. Larrea, T. Pradell, M. Vendrell-Saz, I. Borgia, B. G. Brunetti, F. Cariati, P. Fermo, M. Mellini, A. Sgamellotti and C. Viti (2001). "Luster Pottery from the Thirteenth Century to the Sixteenth Century: A Nanostructured Thin Metallic Film." Journal of the American Ceramic Society **84**(2): 442-446.
- Phuruangrat, A., T. Thongtem and S. Thongtem (2009). "Characterization of Bi₂S₃ nanorods and nano-structured flowers prepared by a hydrothermal method." Materials Letters **63**(17): 1496-1498.
- Plass, R., S. Pelet, J. Krueger, M. Grätzel and U. Bach (2002). "Quantum Dot Sensitization of Organic-Inorganic Hybrid Solar Cells." The Journal of Physical Chemistry B **106**(31): 7578-7580.
- Powell, M. J., P. Marchand, C. J. Denis, J. C. Bear, J. A. Darr and I. P. Parkin (2015). "Direct and continuous synthesis of VO₂ nanoparticles." Nanoscale **7**(44): 18686-18693.
- Prosini, P. P., M. Lisi, D. Zane and M. Pasquali (2002). "Determination of the chemical diffusion coefficient of lithium in LiFePO₄." Solid State Ionics **148**(1-2): 45-51.
- Pumera, M., Z. Sofer and A. Ambrosi (2014). "Layered transition metal dichalcogenides for electrochemical energy generation and storage." Journal of Materials Chemistry A **2**(24): 8981-8987.

- Querejeta-Fernández, A., J. C. Hernández-Garrido, H. Yang, Y. Zhou, A. Varela, M. Parras, J. J. Calvino-Gómez, J. M. González-Calbet, P. F. Green and N. A. Kotov (2012). "Unknown Aspects of Self-Assembly of PbS Microscale Superstructures." ACS Nano **6**(5): 3800-3812.
- Ramaiah, K. S. (1999). "Electrical properties of In doped CdS thin films." Journal of Materials Science: Materials in Electronics **10**(4): 291-294.
- Ramakrishna Matte, H. S. S., A. Gomathi, A. K. Manna, D. J. Late, R. Datta, S. K. Pati and C. N. R. Rao (2010). "MoS₂ and WS₂ Analogues of Graphene." Angewandte Chemie International Edition **49**(24): 4059-4062.
- Rangappa, D., K. Sone, M. Ichihara, T. Kudo and I. Honma (2010). "Rapid one-pot synthesis of LiMPO₄ (M = Fe, Mn) colloidal nanocrystals by supercritical ethanol process." Chemical Communications **46**(40): 7548-7550.
- Rangappa, D., K. Sone, T. Kudo and I. Honma (2010). "Directed growth of nanoarchitected LiFePO₄ electrode by solvothermal synthesis and their cathode properties." Journal of Power Sources **195**(18): 6167-6171.
- Rao, C. N. R. (1993). "Chemical synthesis of solid inorganic materials." Materials Science and Engineering B-Solid State Materials for Advanced Technology **18**(1): 1-21.
- Ravet, N., Y. Chouinard, J. F. Magnan, S. Besner, M. Gauthier and M. Armand (2001). "Electroactivity of natural and synthetic triphylite." Journal of Power Sources **97-98**: 503-507.
- Reibold, M., N. Pätzke, A. A. Levin, W. Kochmann, I. P. Shakhverdova, P. Paufler and D. C. Meyer (2009). "Structure of several historic blades at nanoscale." Crystal Research and Technology **44**(10): 1139-1146.
- Reveron, H., C. Aymonier, A. Loppinet-Serani, C. Elissalde, M. Maglione and F. Cansell (2005). "Single-step synthesis of well-crystallized and pure barium titanate nanoparticles in supercritical fluids." Nanotechnology **16**(8): 1137-1143.
- Reverón, H., C. Elissalde, C. Aymonier, C. Bousquet, M. Maglione and F. Cansell (2006). "Continuous supercritical synthesis and dielectric behaviour of the whole BST solid solution." Nanotechnology **17**(14): 3527.
- Rickard, D. and G. W. Luther (2007). "Chemistry of Iron Sulfides." Chemical Reviews **107**(2): 514-562.
- Roeder, R. K. and E. B. Slamovich (1999). "Stoichiometry Control and Phase Selection in Hydrothermally Derived Ba_xSr_{1-x}TiO₃ Powders." Journal of the American Ceramic Society **82**(7): 1665-1675.
- Rossmann, G. R., R. D. Shannon and R. K. Waring (1981). "Origin of the yellow color of complex nickel oxides." Journal of Solid State Chemistry **39**(3): 277-287.
- Routzahn, A. L., S. L. White, L.-K. Fong and P. K. Jain (2012). "Plasmonics with Doped Quantum Dots." Israel Journal of Chemistry **52**(11-12): 983-991.
- Salavati-Niasari, M., D. Ghanbari and F. Davar (2009). "Synthesis of different morphologies of bismuth sulfide nanostructures via hydrothermal process in the presence of thioglycolic acid." Journal of Alloys and Compounds **488**(1): 442-447.
- Saravanan, K., P. Balaya, M. V. Reddy, B. V. R. Chowdari and J. J. Vittal (2010). "Morphology controlled synthesis of LiFePO₄/C nanoplates for Li-ion batteries." Energy & Environmental Science **3**(4): 457-464.
- Saravanan, K., M. V. Reddy, P. Balaya, H. Gong, B. V. R. Chowdari and J. J. Vittal (2009). "Storage performance of LiFePO₄ nanoplates." Journal of Materials Chemistry **19**(5): 605-610.
- Sasaki, T., S. Ohara, T. Naka, J. Vejpravova, V. Sechovsky, M. Umetsu, S. Takami, B. Jeyadevan and T. Adschiri (2010). "Continuous synthesis of fine MgFe₂O₄ nanoparticles by supercritical hydrothermal reaction." Journal of Supercritical Fluids **53**(1-3): 92-94.
- Sato, S. and J. M. White (1981). "Photoassisted hydrogen production from titania and water." The Journal of Physical Chemistry **85**(5): 592-594.

- Scholes, G. D. and G. Rumbles (2006). "Excitons in nanoscale systems." Nature Materials **5**(9): 683-696.
- Scrosati, B., J. Hassoun and Y.-K. Sun (2011). "Lithium-ion batteries. A look into the future." Energy & Environmental Science **4**(9): 3287-3295.
- Senthilkumar, S. and R. T. Selvi (2008). "Synthesis and Characterization of One Dimensional ZnS Nanorods." Synthesis and Reactivity in Inorganic, Metal-Organic, and Nano-Metal Chemistry **38**(9): 710-715.
- Serpone, N. (1997). "Relative photonic efficiencies and quantum yields in heterogeneous photocatalysis." Journal of Photochemistry and Photobiology A: Chemistry **104**(1-3): 1-12.
- Serpone, N., D. Lawless and R. Khairutdinov (1995). "Size Effects on the Photophysical Properties of Colloidal Anatase TiO₂ Particles: Size Quantization versus Direct Transitions in This Indirect Semiconductor?" The Journal of Physical Chemistry **99**(45): 16646-16654.
- Shaw, W. H. R. and D. G. Walker (1956). "The Decomposition of Thiourea in Water Solutions." Journal of the American Chemical Society **78**(22): 5769-5772.
- Shen, S., Y. Zhang, L. Peng, B. Xu, Y. Du, M. Deng, H. Xu and Q. Wang (2011). "Generalized synthesis of metal sulfide nanocrystals from single-source precursors: size, shape and chemical composition control and their properties." Crystal Engineering Communications **13**(14): 4572-4579.
- Shenghua, L., H. Yu, Z. Ying, S. Xiaohui, Y. Zhengyu and S. Weiyang (2015). "Highly enhanced photoluminescence of AgInS₂/ZnS quantum dots by hot-injection method." Materials Research Express **2**(1): 015901.
- Shi, Y., J. Chen and P. Shen (2007). "ZnS micro-spheres and flowers: Chemically controlled synthesis and template use in fabricating MS(shell)/ZnS(core) and MS (M=Pb, Cu) hollow microspheres." Journal of Alloys and Compounds **441**(1-2): 337-343.
- Shin, Y. H., S.-M. Koo, D. S. Kim, Y.-H. Lee, B. Veriansyah, J. Kim and Y.-W. Lee (2009). "Continuous hydrothermal synthesis of HT-LiCoO₂ in supercritical water." The Journal of Supercritical Fluids **50**(3): 250-256.
- Shiratori, Y., C. Pithan, J. Dornseiffer and R. Waser (2007). "Raman scattering studies on nanocrystalline BaTiO₃ Part I—isolated particles and aggregates." Journal of Raman Spectroscopy **38**(10): 1288-1299.
- Sing, K. S. W., D. H. Everett, R. A. W. Haul, L. Moscou, R. A. Pierotti, J. Rouquerol and T. Siemieniewska (1985). "Reporting physisorption data for gas/solid systems with special reference to the determination of surface area and porosity (Recommendations 1984)." Pure and Applied Chemistry **57**(4): 603-619.
- Smet, P. F., I. Moreels, Z. Hens and D. Poelman (2010). "Luminescence in Sulfides: A Rich History and a Bright Future." Materials **3**(4): 2834-2883.
- Sooklal, K., B. S. Cullum, S. M. Angel and C. J. Murphy (1996). "Photophysical Properties of ZnS Nanoclusters with Spatially Localized Mn²⁺." The Journal of Physical Chemistry **100**(11): 4551-4555.
- Striffler, W. A. and C. W. Bates (1992). "Admittance spectroscopy of CuInSe₂/CdS solar cells prepared by chemical spray pyrolysis." Journal of Applied Physics **71**(9): 4358-4364.
- Sun, P., W. Zhang, X. Hu, L. Yuan and Y. Huang (2014). "Synthesis of hierarchical MoS₂ and its electrochemical performance as an anode material for lithium-ion batteries." Journal of Materials Chemistry A **2**(10): 3498-3504.
- Sustainable-nano.com. (2013). "Surfing Particles: Taking a Ride Using Living Cell Machinery." <http://sustainable-nano.com/2013/04/30/surfing-particles-taking-a-ride-using-living-cell-machinery/>
- Suyver, J. F., S. F. Wuister, J. J. Kelly and A. Meijerink (2001). "Synthesis and Photoluminescence of Nanocrystalline ZnS:Mn²⁺." Nano Letters **1**(8): 429-433.

- Tachikawa, T., M. Fujitsuka and T. Majima (2007). "Mechanistic Insight into the TiO₂ Photocatalytic Reactions: Design of New Photocatalysts." The Journal of Physical Chemistry C **111**(14): 5259-5275.
- Takashi, H., O. Naoto and M. Hiroshi (1994). "Film Thickness Dependence of Dielectric Properties of BaTiO₃ Thin Films Prepared by Sol-Gel Method." Japanese Journal of Applied Physics **33**(9S): 5277.
- Talpin, D. V., J. H. Nelson, E. V. Shevchenko, S. Aloni, B. Sadtler and A. P. Alivisatos (2007). "Seeded Growth of Highly Luminescent CdSe/CdS Nanoheterostructures with Rod and Tetrapod Morphologies." Nano Letters **7**(10): 2951-2959.
- Tan, Z., F. Zhang, T. Zhu, J. Xu, A. Y. Wang, J. D. Dixon, L. Li, Q. Zhang, S. E. Mohney and J. Ruzyllo (2007). "Bright and Color-Saturated Emission from Blue Light-Emitting Diodes Based on Solution-Processed Colloidal Nanocrystal Quantum Dots." Nano Letters **7**(12): 3803-3807.
- Tang, H., K. Prasad, R. Sanjinès, P. E. Schmid and F. Lévy (1994). "Electrical and optical properties of TiO₂ anatase thin films." Journal of Applied Physics **75**(4): 2042-2047.
- Tang, K., D. Chen, Y. Liu, G. Shen, H. zheng and Y. Qian (2004). "Shape-controlled synthesis of copper sulfide nanocrystals via a soft solution route." Journal of Crystal Growth **263**(1-4): 232-236.
- Tauc, J. (1968). "Optical properties and electronic structure of amorphous Ge and Si." Materials Research Bulletin **3**(1): 37-46.
- Tighe, C. J., R. I. Gruar, C. Y. Ma, T. Mahmud, X. Z. Wang and J. A. Darr (2012). "Investigation of counter-current mixing in a continuous hydrothermal flow reactor." Journal of Supercritical Fluids **62**: 165-172.
- Tighe, C. J., R. Quesada Cabrera, R. I. Gruar and J. A. Darr (2013). "Scale up Production of Nanoparticles: Continuous Supercritical Water Synthesis of Ce-Zn Oxides." Industrial & Engineering Chemistry Research **52**(16): 5522-5528
- Tjong, S. C. and H. Chen (2004). "Nanocrystalline materials and coatings." Materials Science and Engineering: R: Reports **45**(1-2): 1-88.
- Toby, B. H. (2001). "EXPGUI, a graphical user interface for GSAS." Journal of Applied Crystallography(34): 210-213.
- Venkateswaran, U. D., V. M. Naik and R. Naik (1998). "High-pressure Raman studies of polycrystalline BaTiO₃." Physical Review B **58**(21): 14256-14260.
- Veriansyah, B., J.-D. Kim, B. K. Min, Y. H. Shin, Y.-W. Lee and J. Kim (2010). "Continuous synthesis of surface-modified zinc oxide nanoparticles in supercritical methanol." Journal of Supercritical Fluids **52**(1): 76-83.
- Wageh, S., L. Shu-Man, F. T. You and X. Xu-Rong (2003). "Optical properties of strongly luminescing mercaptoacetic-acid-capped ZnS nanoparticles." Journal of Luminescence **102-103**: 768-773.
- Walton, R. I., A. J. Dent and S. J. Hibble (1998). "In Situ Investigation of the Thermal Decomposition of Ammonium Tetrathiomolybdate Using Combined Time-Resolved X-ray Absorption Spectroscopy and X-ray Diffraction." Chemistry of Materials **10**(11): 3737-3745.
- Wang, C. and J. Hong (2007). "Ionic/Electronic Conducting Characteristics of LiFePO₄ Cathode Materials: The Determining Factors for High Rate Performance." Electrochemical and Solid-State Letters **10**(3): A65-A69.
- Wang, J. (2005). "Nanomaterial-based electrochemical biosensors." Analyst **130**(4): 421-426.
- Wang, J. and X. Sun (2012). "Understanding and recent development of carbon coating on LiFePO₄ cathode materials for lithium-ion batteries." Energy & Environmental Science **5**(1): 5163-5185.
- Wang, L., L. Chen, T. Luo and Y. Qian (2006). "A hydrothermal method to prepare the spherical ZnS and flower-like CdS microcrystallites." Materials Letters **60**(29-30): 3627-3630.

- Wang, L., W. Sun, X. Tang, X. Huang, X. He, J. Li, Q. Zhang, J. Gao, G. Tian and S. Fan (2013). "Nano particle LiFePO₄ prepared by solvothermal process." Journal of Power Sources **244**(0): 94-100.
- Wang, Q., S. V. Y. Tang, E. Lester and D. O'Hare (2013). "Synthesis of ultrafine layered double hydroxide (LDHs) nanoplates using a continuous-flow hydrothermal reactor." Nanoscale **5**(1): 114-117.
- Wang, Q., X. Wang, W. Lou and J. Hao (2010). "Ionothermal synthesis of bismuth sulfide nanostructures and their electrochemical hydrogen storage behavior." New Journal of Chemistry **34**(9): 1930-1935.
- Wang, X., H. Feng, Y. Wu and L. Jiao (2013). "Controlled Synthesis of Highly Crystalline MoS₂ Flakes by Chemical Vapor Deposition." Journal of the American Chemical Society **135**(14): 5304-5307.
- Weng, X., J. K. Cockcroft, G. Hyett, M. Vickers, P. Boldrin, C. C. Tang, S. P. Thompson, J. E. Parker, J. C. Knowles, I. Rehman, I. Parkin, J. R. G. Evans and J. A. Darr (2009). "High-Throughput Continuous Hydrothermal Synthesis of an Entire Nanoceramic Phase Diagram." Journal of Combinatorial Chemistry **11**(5): 829-834.
- Weng, X., B. Perston, X. Z. Wang, I. Abrahams, T. Lin, S. Yang, J. R. G. Evans, D. J. Morgan, A. F. Carley, M. Bowker, J. C. Knowles, I. Rehman and J. A. Darr (2009). "Synthesis and characterization of doped nano-sized ceria-zirconia solid solutions." Applied Catalysis B-Environmental **90**(3-4): 405-415.
- Whittingham, M. S. (2004). "Lithium batteries and cathode materials." Chemical Reviews **104**(10): 4271-4302
- Wu, B., H. Song, J. Zhou and X. Chen (2011). "Iron sulfide-embedded carbon microsphere anode material with high-rate performance for lithium-ion batteries." Chemical Communications **47**(30): 8653-8655.
- Wu, P. and X.-P. Yan (2013). "Doped quantum dots for chemo/biosensing and bioimaging." Chemical Society Reviews **42**(12): 5489-5521.
- Xia, Q., X. Chen, K. Zhao and J. Liu (2008). "Synthesis and characterizations of polycrystalline walnut-like CdS nanoparticle by solvothermal method with PVP as stabilizer." Materials Chemistry and Physics **111**(1): 98-105.
- Xu, C. B., J. Lee and A. S. Teja (2008). "Continuous hydrothermal synthesis of lithium iron phosphate particles in subcritical and supercritical water." Journal of Supercritical Fluids **44**(1): 92-97.
- Yamada, A., S. C. Chung and K. Hinokuma (2001). "Optimized LiFePO₄ for Lithium Battery Cathodes." Journal of the Electrochemical Society **148**(3): A224-A229.
- Yang, H., X.-L. Wu, M.-H. Cao and Y.-G. Guo (2009). "Solvothermal Synthesis of LiFePO₄ Hierarchically Dumbbell-Like Microstructures by Nanoplate Self-Assembly and Their Application as a Cathode Material in Lithium-Ion Batteries." The Journal of Physical Chemistry C **113**(8): 3345-3351.
- Yang, S., P. Y. Zavalij and M. Stanley Whittingham (2001). "Hydrothermal synthesis of lithium iron phosphate cathodes." Electrochemistry Communications **3**(9): 505-508.
- Ye, C., X. Fang, G. Li and L. Zhang (2004). "Origin of the green photoluminescence from zinc sulfide nanobelts." Applied Physics Letters **85**(15): 3035-3037.
- Yin, W., L. Yan, J. Yu, G. Tian, L. Zhou, X. Zheng, X. Zhang, Y. Yong, J. Li, Z. Gu and Y. Zhao (2014). "High-Throughput Synthesis of Single-Layer MoS₂ Nanosheets as a Near-Infrared Photothermal-Triggered Drug Delivery for Effective Cancer Therapy." ACS Nano **8**(7): 6922-6933.
- Yu, J. H., S.-H. Kwon, Z. Petrášek, O. K. Park, S. W. Jun, K. Shin, M. Choi, Y. I. Park, K. Park, H. B. Na, N. Lee, D. W. Lee, J. H. Kim, P. Schwillie and T. Hyeon (2013). "High-resolution three-photon biomedical imaging using doped ZnS nanocrystals." Nature Materials **12**(4): 359-366.

- Zhang, H. and J. F. Banfield (2009). "Identification and Growth Mechanism of ZnS Nanoparticles with Mixed Cubic and Hexagonal Stacking." The Journal of Physical Chemistry C **113**(22): 9681-9687.
- Zhang, H., B. Chen, B. Gilbert and J. F. Banfield (2006). "Kinetically controlled formation of a novel nanoparticulate ZnS with mixed cubic and hexagonal stacking." Journal of Materials Chemistry **16**(3): 249-254.
- Zhang, H., B. Gilbert, F. Huang and J. F. Banfield (2003). "Water-driven structure transformation in nanoparticles at room temperature." Nature **424**(6952): 1025-1029.
- Zhang, L.-J., X.-C. Shen, H. Liang, S. Guo and Z.-H. Liang (2010). "Hot-injection synthesis of highly luminescent and monodisperse CdS nanocrystals using thioacetamide and cadmium source with proper reactivity." Journal of Colloid and Interface Science **342**(2): 236-242.
- Zhang, Y. C., T. Qiao, X. Y. Hu, G. Y. Wang and X. Wu (2005). "Shape-controlled synthesis of PbS microcrystallites by mild solvothermal decomposition of a single-source molecular precursor." Journal of Crystal Growth **277**(1-4): 518-523.
- Zhang, Z., S. Brown, J. B. M. Goodall, X. Weng, K. Thompson, K. Gong, S. Kellici, R. J. H. Clark, J. R. G. Evans and J. A. Darr (2009). "Direct continuous hydrothermal synthesis of high surface area nanosized titania." Journal of Alloys and Compounds **476**(1-2): 451-456.
- Zhang, Z., J. B. M. Goodall, S. Brown, L. Karlsson, R. J. H. Clark, J. L. Hutchison, I. U. Rehman and J. A. Darr (2010). "Continuous hydrothermal synthesis of extensive 2D sodium titanate (Na₂Ti₃O₇) nano-sheets." Dalton Transactions **39**(3): 711-714.
- Zhao, L.-D., B.-P. Zhang, W.-S. Liu, H.-L. Zhang and J.-F. Li (2008). "Enhanced thermoelectric properties of bismuth sulfide polycrystals prepared by mechanical alloying and spark plasma sintering." Journal of Solid State Chemistry **181**(12): 3278-3282.
- Zhao, N., T. P. Osedach, L.-Y. Chang, S. M. Geyer, D. Wanger, M. T. Binda, A. C. Arango, M. G. Bawendi and V. Bulovic (2010). "Colloidal PbS Quantum Dot Solar Cells with High Fill Factor." ACS Nano **4**(7): 3743-3752.
- Zhao, Y. and C. Burda (2012). "Development of plasmonic semiconductor nanomaterials with copper chalcogenides for a future with sustainable energy materials." Energy & Environmental Science **5**(2): 5564-5576.
- Zhu, J., J. Fiore, D. Li, N. M. Kinsinger, Q. Wang, E. DiMasi, J. Guo and D. Kisailus (2013). "Solvothermal Synthesis, Development, and Performance of LiFePO₄ Nanostructures." Crystal Growth & Design, **13**(11), 4659-4666
- Zhu, Y.-C., Y. Bando and D.-F. Xue (2003). "Spontaneous growth and luminescence of zinc sulfide nanobelts." Applied Physics Letters **82**: 1769.